UNCLASSIFIED

AD NUMBER

AD871427

NEW LIMITATION CHANGE

TO

Approved for public release, distribution unlimited

FROM

Distribution authorized to U.S. Gov't. agencies and their contractors; Administrative/Operational Use; 10 JUL 1970. Other requests shall be referred to Air Force Aero Propulsion Lab, Attn: APIE, Wright-Patterson AFB, OH 45433.

AUTHORITY

Air Force Aero Propulsion Lab ltr dtd 12 Apr 1972

THIS PAGE IS UNCLASSIFIED

REPRODUCTION QUALITY NOTICE

This document is the best quality available. The copy furnished to DTIC contained pages that may have the following quality problems:

- Pages smaller or larger than normal.
- Pages with background color or light colored printing.
- Pages with small type or poor printing; and or
- Pages with continuous tone material or color photographs.

Due to various output media available these conditions may or may not cause poor legibility in the microfiche or hardcopy output you receive.

☐ If this block is checked, the copy furnished to DTIC contained pages with color printing, that when reproduced in Black and White, may change detail of the original copy.

AD 871427

AD No. ____
DDC FILE COPY

AFAPL-TR-70-31

DDC
B

CHARGED DROPLET ELECTROSTATIC THRUSTER SYSTEMS

H. Shelton, C. W. Lear, P. W. Kidd, M. N. Huberman, B. F. Farber, W. F. Krieve

TRW

TECHNICAL REPORT AFAPL-TR-70-31
JUNE 1970

STATEMENT #2 UNCLASSIFIED

This document is subject to special export controls and each transmittal to foreign governments or foreign nationals may be made only with prior approval of

AIR FORCE AERO PROPULSION LABORATORY (APIE)
AIR FORCE SYSTEMS COMMAND
WRIGHT-PATTERSON AIR FORCE BASE, OHIO 45433

250

Statement-2 per Williams.
Air Force Aero Propulsion Laboratory

FOREWORD

This document was prepared by TRW Systems, Redondo Beach, California, under US Air Force Contract No. F33615-69-C-1254. The work was administered by Air Force Aero Propulsion Laboratory, AFIE, Aerospace Power Division, Wright-Patterson Air Force Base, Ohio funds. This work was supported in part by Aero Propulsion Laboratory directions. AFAPL program management and technical guidance were provided by William C. Durson and Jack Gais.

This report describes the work performed from 1 January 1969 to 30 January 1970. The work was performed in the Low Thrust Propulsion Department, which is part of the Technology Laboratory of TRW Systems. Dr. M. W. Huberman was Project Manager.

In addition to the authors' involvement in the project, the following personnel made significant contributions: R. F. Kemp did much of the early pulsed and AC work. Managerial and technical guidance were provided by E. Cohen, Manager of the Low Thrust Propulsion Department. A. Seaton, W. Daley, N. Law and J. Ripley provided invaluable technical support throughout the program. Additional valuable support was also provided by Montano de la Cruz and E. West.

This report was submitted by the authors January 1970.

Publication of this report does not constitute Air Force approval of the report's findings or conclusions. It is published only for the exchange and stimulation of ideas.

Richard P. Leiby

RICHARD P. LEIBY, Maj., USAF
Chief
Propulsion and Power Branch

Attention of Dr. Williams
Air Force Office of Scientific Research (AFSC)
Wright-Patterson Air Force Base, Ohio 45433
A Gately
10 July 1970

NOTICE

When Government drawings, specifications, or other data are used for any purpose other than in connection with a definitely related Government procurement operation, the United States Government thereby incurs no responsibility nor any obligation whatsoever; and the fact that the government may have formulated, furnished, or in any way supplied the said drawings, specifications, or other data, is not to be regarded by implication or otherwise as in any manner licensing the holder or any other person or corporation, or conveying any rights or permission to manufacture, use, or sell any patented invention that may in any way be related thereto.

Copies of this report should not be returned unless return is required by security considerations, contractual obligations, or notice on a specific document.

AFAPL-TR-70-31

CHARGED DROPLET ELECTROSTATIC THRUSTER SYSTEMS

H. Shelton, C. W. Law, P. W. Kidd, M. N. Huberman, B. F. Farber, W. F. Krieve

TRW

TECHNICAL REPORT AFAPL-TR-70-31
JUNE 1970

AIR FORCE AERO PROPULSION LABORATORY
AIR FORCE SYSTEMS COMMAND
WRIGHT-PATTERSON AIR FORCE BASE, OHIO

ABSTRACT

A program to develop and advance the technology needed for practical colloid propulsion flight system is described. A 100-micropound, 1500-second specific impulse, vectorable colloid thruster concept has been developed and tested. Several neutralizer concepts and their interactions with the colloid beam plasma potential are discussed.

Direct thrust measurements have been correlated with time-of-flight calculations for various 100-micropound colloid thruster concepts. Several propellants, including liquid metals, have been investigated. The feasibility of pulsed and AC colloid propulsion has been investigated. Various single-needle colloid experiments were performed.

A preliminary power conditioning approach for a 1-millipound, orthogonally thrust vectorable colloid system has been developed. The anticipated effects of synchronous orbit solar radiation on needle operating temperature have been examined.

Preceding Page Blank

BEST AVAILABLE COPY

SPECIAL NOTE

All results presented in this report, unless otherwise stated, are based on time-of-flight measurements. These measurements are used to calculate thrust, specific impulse, charge-to-mass ratios, mass flow and thruster efficiency. The efficiency in this case is defined as $T^2/2\dot{M}P$ where T and $\dot{M}$ are, respectively, the thrust and mass flow resulting from the time-of-flight calculations and P is the product of the applied needle voltage times the current supplied to the thruster. The time-of-flight calculations neglect the effects of beam spread and an approximate 400-volt loss in the spraying process. The combined inaccuracy due to these two effects, which is impractical to measure in each experiment, is believed, on the basis of periodic experimental observations of beam spread, to be less than 10%. For further evidence in this respect, the reader is referred to the correlation of time-of-flight data with direct thrust and mass flow measurements presented in Section 8 of this report.

CONTENTS

Page

1. INTRODUCTION AND SUMMARY 1

2. THRUST VECTORING 3

2.1 Run 6904-01, Preliminary Single-Needle Experiment . . . 3

2.2 Run 6904-03, 110 Hours, 1500-Second I_{sp}, ~ 3 μlb/Needle 5

2.3 Run 6911-02, 36-Needle Thrust Vectoring Module. 7

3. SINGLE NEEDLE RESEARCH 9

3.1 Single Needle Geometry Studies 9

3.2 Tungsten Needles 14

4. NEUTRALIZATION 19

4.1 Potential Distribution Outside of Engine. 19

4.2 Neutralizer Electron Source 23

4.3 Experimental Tests, 591-Hour Run. 27

4.4 Carburization 31

4.5 Life Tests with Engine. 35

4.6 High Vacuum Life Test 38

5. COLLOID FEED SYSTEM 39

5.1 Introduction. 39

5.2 System Design 40

5.3 System Analysis 45

5.4 System Component Design 52

5.5 System Test Results 59

6. MODULE DESIGN AND TESTING. 63

6.1 Introduction. 63

6.2 Multiple Needle Experiment. 64

6.3 36-Needle Vectorable Module Basic Design. 75

CONTENTS (Continued)

		Page
7.	THRUST MEASUREMENTS	93
	7.1 General	93
	7.2 Thrust Stand	93
	7.3 Experimental Setup	98
	7.4 Experimental Results	101
	7.5 Discussion	102
	7.6 Conclusions	104
8.	THERMAL ANALYSIS OF MODULE	106
9.	PROPELLANT RESEARCH	111
	9.1 CsI, NaI-Glycerol	111
	9.2 KI-Glycerol, 6-Needle Accel Module	112
	9.3 Liquid Metals Research	114
10.	ONE-MILLIPOUND VECTORABLE COLLOID THRUSTER POWER CONDITIONING	122
	10.1 Power Conditioner Requirements	122
	10.2 General Design Considerations for Power Conditioner Selection	123
	10.3 High Voltage Supplies	124
	10.4 Low Voltage Supplies	134
	10.5 Recommended Power Conditioner System	135
11.	AC AND PULSED OPERATION OF A COLLOID SOURCE	137
	11.1 Introduction	137
	11.2 Research Program	137
12.	SLIT GEOMETRIES	163
	12.1 Single Linear Slit	163
	12.2 Double Slit Module	170
	12.3 Annular Slit	197

ILLUSTRATIONS

Figure		Page
1.	Change in Thrust Vectoring, Needle-Extractor Geometry . .	4
2.	Beam Probe Data Run 6904-03	6
3.	Vectored Beam 36-Needle Module at 210 and 500 Hours . . .	8
4.	Tungsten Needle Design.	15
5.	Tungsten Needle Tip	16
6.	Low and High Current Modes - Tungsten Needle.	18
7.	Potential Distribution Throughout the Facility During Neutralizer with a Floating Collector	22
8.	Potential Distribution Around the Needles Illustrating Trajectories of Secondary Particles	24
9.	Neutralizer Power (P), Resistance (R), Heater Current (Ie), and Heat Voltage (Ve) as a Function of Time at Constant Saturated Emission Current (Ie) (Run 6903-01). .	29
10.	Tungsten Filament from Run 6903-01 After Being Broken During Removal from System (90X).	30
11.	Sketch of Shielded Neutralizer Gun (A) and Position in Tank (B)	34
12	Photographs of the Small Impregnated Cathode Gun Structure	37
13.	Colloid Thruster Feed System.	40
14.	Adsorption Isotherms for Ammonia Zeolite Types 5A and 13X	42
15.	Typical Feed System Pressure and Temperature Profiles . .	44
16.	Ammonia Adsorption on Zeolite	47
17.	Zeolite Prototype Test Schematic.	51
18.	Colloid Feed System - Design Layout	53
19.	Inconel Bellow.	54
20a.	Zeolite Pressurizer Components.	57
20b.	Zeolite Pressurizer with Zeolite Charge	57
20c.	Zeolite Pressurizer Subassembly	58
21.	Zeolite Regulator Circuit	58
22.	Assembled Feed System	60
23.	Expulsion Cycle Test.	60

ILLUSTRATIONS (Continued)

Figure		Page
24.	Needle Voltage versus Time, Run 6903-1	66
25.	Needle Current versus Time, Run 6903-1	67
26.	Thrust versus Time, Run 6903-1	68
27.	I_{sp} versus Time, Run 6903-1	69
28.	Efficiency versus Time, Run 6903-1	70
29.	$(\overline{Q/M})$ versus Time, Run 6903-1	71
30.	$\dot{m}$ versus Time, Run 6903-1	72
31.	Typical TOF Trace, 180 Hours, Run 6903-1	73
32.	Extractor Pattern Around Accel Configuration Needles	74
33.	Ripple Pattern in Needle Rim; Magnification 500 X	74
34.	Extractor Vector Position, 36-Needle Module	76
35.	36-Needle Module, Cubicle Component Layout	77
36.	36-Needle Extractored Module	78
37.	Run 6906-05, Baffle Current versus Applied Bias Positive Bias	84
38.	6 Annular-Needle Module Mounted on Thrust Stand	96
39.	Layout of Thrust Stand and TOF Arrangement in Vacuum Tank for Thrust Measurements	99
40.	Geometry of the Thermal Analysis for the 36 Needle Module	106
41.	TOF Trace Obtained with KI-Glycerol Propellant	112
42.	Run 6905-01-5/10 KI-Glycerol Solution	113
43.	TOF Traces for Gallium Ion Beam	115
44.	Liquid Metal Test Station	117
45.	Needle After 300 Hours of Operation with Cesium	120
46.	DC-DC Converter (SWI)	126
47.	DC-DC Converter (PWI)	126
48.	DC-DC Converter (IES)	127
49.	PWI Converter with Multiple Transformer-Rectifier-Filter Configuration	128
50.	SWI Converter	130
51.	Basic PCU System Block Diagram	136

ILLUSTRATIONS (Continued)

Figure		Page
52.	Collector Current Waveforms Following Off-Time Pulses of (a) 0.1, 0.15, 0.2, and (b) 0.4, 0.7 milliseconds	138
53.	Triggered Spark Gap Design	141
54.	50 Hz Single Needle Performance	144
55.	60 Hz Square Wave Performance	145
56.	Photomicrograph of Colloid Needle in Operation	147
57.	Time Required to Form Spherical	148
58.	Microphotograph of Needle after 24 Hours of 1 kHz Operation	154
59.	Waveforms Illustrating Typical 1 kHz Operation	155
60.	Collector Current at Varying Distances From the Needle	157
61.	Honeycomb Pendulum Collector	158
62.	Photomicrograph of Human Hair Perpendicular to Linear Slit (Approximately 30X)	168
63.	Two-Slit Module Schematic	172
64.	Two-Slit Vectored Module	173
65.	Slit Blade Shaping Fixture	175
66.	Potential Field for Double Slit Configuration With Cylindrical Deflector Electrodes	176
67.	Slit Voltage versus Time, 96-Hour Endurance Run, Twin Slit	179
68.	Slit Current Versus Time, 96-Hour Endurance Run, Twin Slit	180
69.	Feed Pressure versus Time, 96-Hour Endurance Run, Twin Slit	181
70.	Specific Impulse versus Time, 96-Hour Endurance Run, Twin Slit	182
71.	Thrust Versus Time, 96-Hour Endurance Run, Twin Slit	183
72.	Mass Flow versus Time, 96-Hour Endurance Run, Twin Slit	184
73.	Average Charge to Mass Ratio versus Time, 96-Hour Endurance Run, Twin Slit	185
74.	Twin Slit Module After 96-Hour Endurance Run, Showing Damage to Deflectors and Effects of Flooding on Extractor Plate	187

ILLUSTRATIONS (Continued)

Figure		Page
75.	Twin Slit Module, Without Extractor, After 96-Hour Endurance Run	187
76.	Twin Slit Module After 96-Hour Endurance Run, Inside Edge of One Slit, Showing Erosion Pattern in Stainless	188
77.	Twin Slit Module, Run 6906-02, Feed Pressure versus Time	191
78.	Twin Slit Module, Run 6906-02, Needle Current versus Time	192
79.	Twin Slit Module, Run 6906-02, Thrust versus Time	193
80.	Twin Slit Module, Run 6906-02, Mass Flow versus Time	194
81.	Twin Slit Module, Run 6906-02, I_{sp} versus Time	195
82.	Twin Slit Module, Run 6906-02, Efficiency versus Time	196
83.	Early Design of Annular Slit	200
84.	TOF Information Run 6909-C4, Platinum Edged Annular Slit, TOF Length is 60 cm, Sweep Speed 20 us/cm	203
85.	Typical Annular Slit Source, Magnified 10X	204
86.	Section Drawing of TRW Annular Slit Design	206
87.	Experimental Single Slit with Two Vectoring Electrodes	212
88.	Time Exposures of Beam from Slit Two Vector Electrodes	213
89.	Average Q/M versus Angle; Probe Measurements from Slit with Two Vector Electrodes	214
90.	Composite Plot of Thrust and Current Densities, Probe Measurements on Two Electrode Vectored Slit	214
91.	Thrust and I_{sp} as a Function of Feed Pressure for Constant Source; Vectored Single Slit	217
92.	Thrust and I_{sp} as a Function of Source Voltage for Constant Feed Pressure; Vectored Single Slit	217
93.	Experimental Single Slit with Three Vectoring Electrodes	218
94.	Time Exposures of Beam from Slit with Three Vectoring Electrodes	220
95.	Experimental Seven Slit Module, Unvectored	221
96.	Annular Needle with Teflon Plug Located in Center Piece	225
97.	Annular Needle with Teflon Hat to Cover Inner Meniscus	225
98.	Top View Looking Down on Extractor Deflector Electrodes, and Annular Needles of 120 μlb Thrust Vectorable Module	229
99.	Side View of 120 μlb Thrust Vectorable Module	229

NOMENCLATURE

A	cross-sectional area contained within tubing wall
A'	cross-sectional area of the Cs within that tubing
c.s.	centistokes
I_{def}	deflector electrode current
I_n	source needle current
I_x	extractor current
I_{sp}	specific impulse
kc	kilocycles/second
L	length of stainless steel feed tubing (Cs experiment)
L'	length of section filled with Cs
lbm	pound mass
lbf	pound force
$\dot{m}$	mass flow rate
psia	pounds per square inch, absolute
$\overline{(Q/M)}$	average charge to mass ratio
$(Q/M)_{eff}$	$\left[\overline{(Q/M)^{1/2}}\right]^2$, i.e., the square of the average of the square roots of the charge to mass ratio
R	electrical resistance along entire length of empty tube (Cs experiment)
R'	resistance along entire tube when length L' is filled with Cs
$R_{L'}$	resistance along length of filled section (Cs experiment)
$R_{L-L'}$	resistance along length of unfilled section (Cs experiment)
T	thrust
TOF	time of flight

NOMENCLATURE (Continued)

V_{def}	deflector electrode voltage
V_n	source needle voltage
V_x	extractor voltage
ρ	resistivity of stainless steel (Cs experiment)
ρ'	resistivity of cesium (Cs experiment)

1. INTRODUCTION AND SUMMARY

TRW Systems, under Air Force Aero Propulsion Laboratory direction and sponsorship, is engaged in the systematic analysis and investigation of charged droplets, or colloids, as a form of electric propulsion. These efforts, initially of a physical research nature, have proceeded to the point where the feasibility of colloid devices has been demonstrated. Concurrent with the technological achievements, systems studies and analyses have been conducted, under both Air Force and TRW support, that have clearly indicated an area of stationkeeping and spacecraft control where colloid propulsion is needed. The present program, "Charged Droplet Electrostatic Thruster Systems," has been directed towards further advancing the needed technology. This report describes and summarizes the specific work performed on this program conducted under Contract F33615-69-C-1254 during the period 1 January 1969 through 30 January 1970.

The work performed encompasses all areas related to the development of practical colloid flight systems. In brief, these areas included thruster neutralization, feed system, power conditioning propellant and fabrication technology. Additional experimental work was performed with AC and pulsed colloid thrusters, liquid metal sources, annular and linear slit thrusters, thrust vectoring geometries, and direct thrust measurements. As part of this program, a special one-volume study entitled "Mission and Spacecraft Interface Requirement for Secondary Propulsion Subsystems and their Impact on Colloid Systems" has been published under separate cover. The objectives of this study were to: (1) select possible Air Force satellite missions and indicate colloid applicability; (2) determine interfaces that exist for a colloid secondary propulsion subsystem (SPS) during integration aboard a future Air Force satellite; and (3) evaluate these interfaces, indicating the areas in which efforts should be concentrated during the next phase of colloid development.

In the present volume, Section 2 describes thrust vectoring experiments designed to demonstrate the feasibility of 1500-second specific impulse vectored operation. Section 3 describes single needle investigations of new needle designs, the use of tungsten needles and

the effects of pump oil contamination on needle operation. Section 4 discusses the use of bare tungsten and activated neutralizers. Theoretical and experimental determinations of the plasma potential distribution in the vicinity of a colloid thruster are presented. Problems associated with neutralizer contamination in a closed system colloid test environment are also discussed.

Section 5 describes the development and testing of a new colloid feed system which utilizes the absorptive properties of zeolite as a pressurant regulator. This concept allows continuous feed pressure control over the entire pressure range between normal feed demand and zero pressure. As a result, it is now possible to (1) maintain constant nominal feed pressure throughout a mission, (2) utilize feed pressure control to compensate for thruster temperature variations and various throttling requirements, and (3) command zero pressure for valveless turnoff.

Section 6 describes the development and testing of a nominal 100-micropound thrust, vectorable, 1500-second specific impulse thruster module. Section 7 discusses the expected needle temperature variations due to solar radiation and energy loss dissipation at typical operation levels in a synchronous orbit. Section 8 describes and correlates simultaneous time-of-flight and thrust measurements performed for three different 100-micropound thruster concepts developed in the course of this program.

Section 9 describes experiments with propellants other than the conventional sodium iodide-glycerol solution. Specific propellants described include potassium iodide-glycerol, a mixture of sodium and cesium iodides in glycerol, liquid gallium and liquid cesium. Section 10 discusses power conditioning concepts for a 1-millipound, orthogonally thrust vectorable, 1500-second specific impulse colloid thruster flight system and presents preliminary weight, size, reliability and efficiency estimates. Section 11 describes experiments with AC and pulsed colloid thrusters and discusses feasibility considerations for these two techniques. Section 12 presents the results of a major program sub-task, the development of various annular and linear slit geometry concepts.

2. THRUST VECTORING

Thrust vectoring experiments were performed with both the standard needles (14-mil I.D.) and the large annular needles (90-mil rim diameter). These experiments led to the development of the 36-needle thrust-vectorable module, and the 6-annular-needle thrust-vectorable module. The annular needle thrust vectoring is discussed in a separate section on slit work.

The goal of increasing specific impulse to 1500 seconds was made even more difficult by the simultaneous thrust vectoring requirement. Since a 1000-second vectorable module was developed and tested during the preceding contract, the 36-needle module was at first proposed using this same geometry. Through experimentation with single-needle thrust vectoring arrangements, several small but very important geometry changes were incorporated into the design. The resulting geometry (Figure 2-1b) made possible long-term 1500-second operation at higher thrusts than had been previously attained because (1) the deflector electrodes reduced the field at the needles, thereby permitting high voltage operation; and (2) the deflector-extractor geometry prevented secondary electron bombardment of the needle, thereby eliminating tar buildup which has been the major cause of life test failure and performance degradation. A record of the more important experiments and the resulting design modifications is presented below.

2.1 RUN 6904-01, PRELIMINARY SINGLE-NEEDLE EXPERIMENT

This was the first run in which it was possible to operate for extended periods at I_{sp}'s of 1500 seconds in the thrust vectorable configuration (Figure 1a.). Two earlier runs terminated when electron emission from the extractor to the deflector electrodes became a problem. The cause of this emission was polishing compound material left in high fields regions on the underside of the extractor hole. The problem was eliminated by carefully cleaning these surfaces.

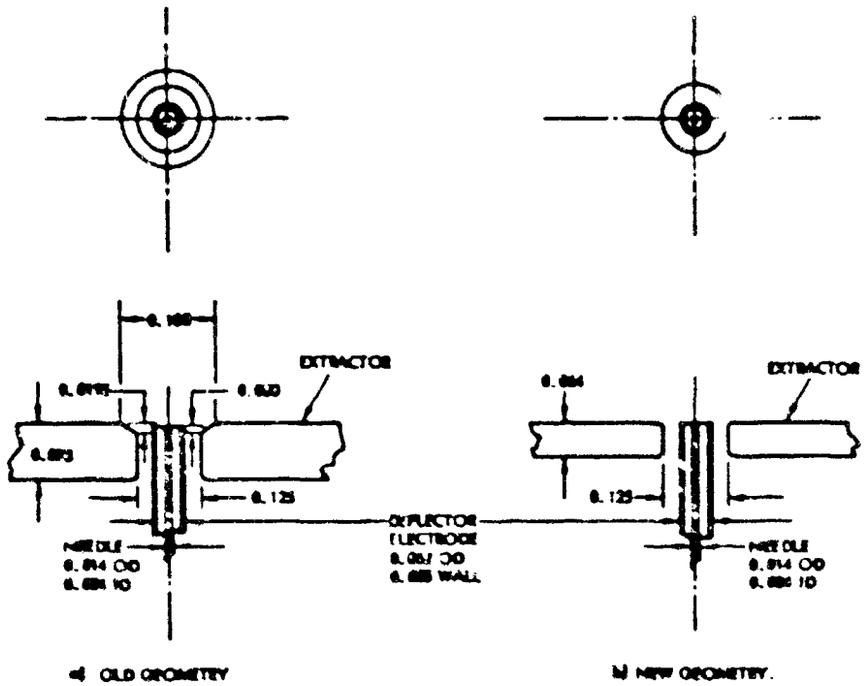

Figure 1. Change in Thrust Vectoring, Needle-Extractor Geometry

During the 8 hours the run was under observation, it ran very well. At 12.6 kv on the needle and deflectors and -1.25 kv on the extractor, I_{sp}'s of 1600 seconds, thrusts of 2.6 μlb, and efficiencies of 75% were obtained. The beam was vectored by adding and subtracting, relative to the needle potential, 1 kv. This produced a total deflection of 8 degrees. The experiment was left to run overnight in the vectored mode. The next morning the needle was found to be shorted to the less positive deflector because of tar accumulation. This rapid tar buildup indicated a need for more thorough investigation of needle-deflector and extractor geometry in future experiments. The run proved that voltages of 10 to [illegible] kv could be used on the needle to produce I_{sp}'s of 1500 seconds or greater when the deflector electrodes were biased symmetrically around the needle potential. This relationship between needle and deflector electrode voltages has been used in all succeeding tests.

2.2 RUN 6904-03, 110 HOURS, 1500-SECOND I_{sp}, ~ 3 μlb/NEEDLE

In this experiment the needle and deflector electrodes were moved forward so that they were mounted flush with the face of the extractor plate. The beveled edge on the downstream side of the extractor hole was eliminated. Instead, the top and bottom edges of the 1/8 inch extractor hole were rounded just slightly to eliminate sharp edges. Figure 1 shows the old and new geometry. The old geometry was believed to be the major cause of tar formation since secondary electrons coming from the beveled surface of the extractor hole were able to strike the needle. This run demonstrated that changing the geometry as described would eliminate tar formation. During 30 hours of this run, the needle was vectored up 3° and down 5°. At other times, the needle deflector electrodes were connected to a common power supply to permit comparison with this configuration and the accel configuration (without split electrodes) used in a 591-hour 6-needle run, No. 6903-01. (See Section 6 for a description of this run).

In the unvectored mode, the needle was kept at 11.7 kv and the deflector electrodes at 12.6 kv. Figure 2 shows probe current versus probe position as it was moved perpendicularly down through the beam. The highest current density is on the periphery of the beam. This hollow beam had a spread of ±15°. When the needle and deflector electrodes were connected to a common power supply, the beam became more uniform within the 15° cone. Accurate probe data of the outer edges of the beam could not be obtained because, at the probe location, the outer limits exceeded the 18-inch tank diameter. Time-of-flight data from this run is recorded chronologically in Table 2-I.

This run showed high I_{sp}, and long-term operation was possible with higher efficiencies and thrust than had previously been possible using the old needle-extractor geometry (without vector electrodes). For this reason, the design was used in the 36-needle module. The final module performance confirmed the results obtained in the single-needle thrust vectoring experiments.

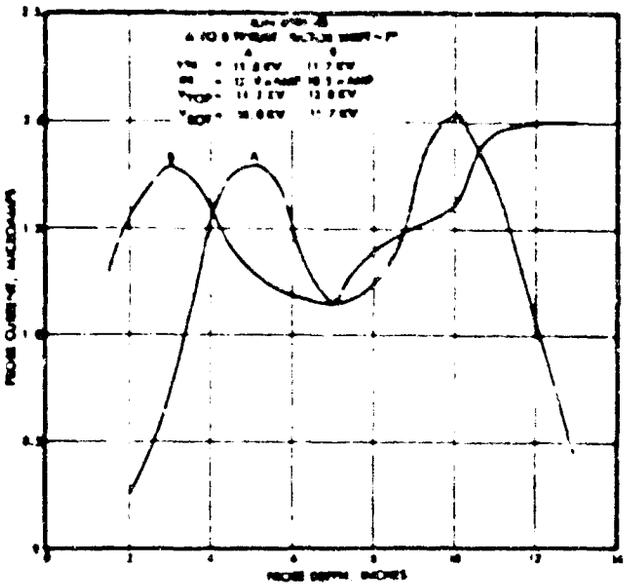

Figure 2. Beam Probe Data Run 6904-03

Table 2-1. Chronological Record of Run 6904-03

Time hr.	P mTorr	V_B kv	I_B 10^{-6} amp	V_{Def} kv	I_{Def} 10^{-6} amp	V_E kv	I_{Def} 10^{-6} amp	I_{sp} amps	$\dot{m}$ 10^{-6} kg/sec	T 10^{-6} lb	η %	$\overline{I_{sp}/\eta}$ sec/kg
0	1.5	12.6	18.0	Top 12.6 Bot 12.5	0 0	-1.6	1.0	No Data	- - -	- - -	- - -	- - -
0	1.5	9.6	9.0	Both 9.6	0	-1.2	0.5	1720	.473	1.66	73	19,000
2.0	1.9	11.7	10.0	Both 12.6	0	-4.3	1.5	No Data	- - -	- - -	- - -	- - -
5.1	1.9	11.7	11.0	Both 12.6	1.0	-4.3	1.0	1750	.893	3.00	79	12,500
26.5	2.0	11.7	10.5	Both 12.6	0	-1.2	0	1683	.884	1.00	79.2	11,600
35.4	2.0	11.7	10.5	Top 13.0 Bot 11.7	0	-4.2	0	No Data	- - -	- - -	- - -	- - -
		Run Overnight in Deflected Mode.										
47.5	2.0	11.7	10.0	Top 13.0 Bot 11.7	-.6 0	-1.2	0.2	Cold Trap Run Dry Overnight. Poor Vacuum in Dynum.				
48.1	2.0	11.7	13.0	Both 12.6	0	-4.2	0.2	1684	.769	2.82	79.5	14,300
53.5	2.0	11.7	12.0	Top 11.2 Bot 14.0	0.5 1.2	-4.2	1.0	Probe Data Taken and Left to Run Overnight.				
89.0	2.0	11.7	12.5	Top 11.2 Bot 14.0	0.3 0.8	-4.2	0.8					
90.1	2.0	11.7	12.0	Both 12.6	0	-4.2	0					
136.0	2.0	11.7	12.0	Both 12.5	0	-4.2	0	1511	.960	3.13	75	12,300
Run Terminated												

NOTE: The current to the deflector electrodes was not from the anode, but from secondary particles coming either from the contractor as a result of positive accelerator bombarding it and/or from the plasma in the chamber, since these electrodes were not shielded from the plasma. There were no indications of beam impingement to the deflector electrodes even during post-operative inspection.

2.3 RLN 6911-02, 36-NEEDLE THRUST VECTORING MODULE

During the 1000-hour test, this module was vectored either up or down for periods of up to 200 hours in duration. Figure 2 shows the vectored beam in three positions: up 7 degrees, down 6 degrees, and straight on. The vectored-up and the unvectored pictures were taken at 210 hours. The vectored-down picture was taken at 500 hours. The maximum attainable vectoring during this test was approximately $\pm 10°$. However, performance at these angles was too unstable to allow photographs to be taken.

During the first 930 hours of the run there was no performance degradation and only after a catastrophic vacuum accident at 930 hours, during which time half of one deflector electrode was burned away, did any change occur in performance or thrust vectoring ability. It appears that the deflector electrodes provided protection for the needles from electron bombardment, as was shown in the earlier single needle tests. Otherwise, there would have been tar buildup and a drop in performance as time progressed. This protection was also evidenced in the 591-hour, 6-needle run. During the 36-needle test, there was electron emission current, at times as high as 35 μamp, coming from the extractor. The deflector electrodes absorbed most of this current and prevented the electrons from polymerizing the propellant on the needles during the run. On the debit side, thrust vectoring complicated module fabrication. The spacing between the deflector electrode supports and the extractor had to be increased, but emission current still became a problem as a film of material coated the extractor (Section 6). It is very likely that had a non-vectorable geometry, similar to that used in the 591-hour, 6-needle test, been also used in this test, these currents would not have occurred.

The net result of these earlier experiments and the life test was that, while electrostatic thrust vectoring still has certain problems related to environment (i.e., the electron emission currents), the concept is feasible and can vector beams through a total angle of at least 13 degrees (as was done in the life test) at I_{sp}'s in the 1400-to 1500-second range for periods of operation in excess of 1000 hours.

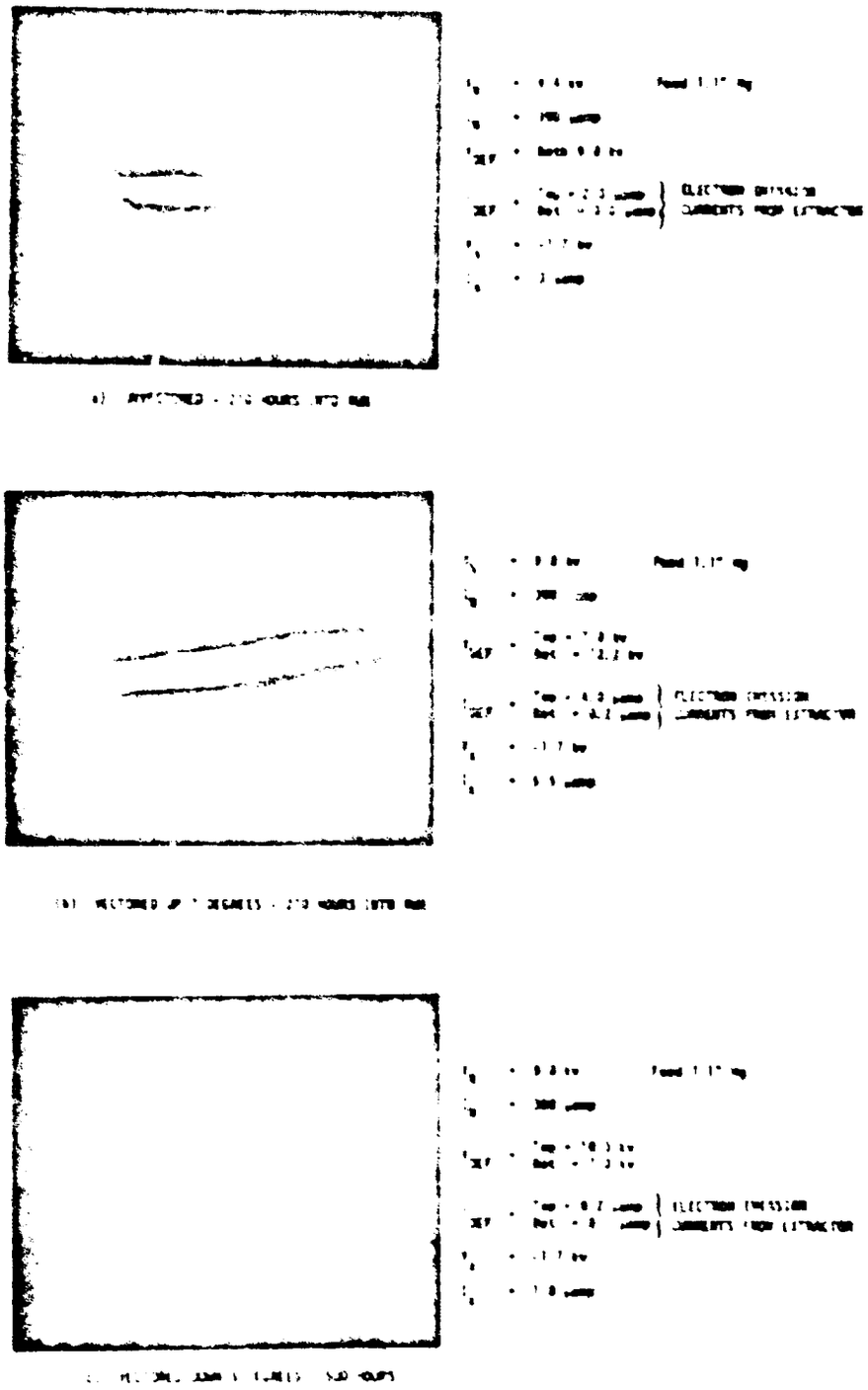

Figure 3. Vectored Beam - 36 Needle Module at 210 and 500 Hours

3. SINGLE NEEDLE RESEARCH

Single needle research was used to investigate new needle designs, study the effects of vacuum system oils on needle wettability, and determine the performance of various propellants. The research on propellants is discussed in Section 9. New needle designs and the effect of pump oils on needle performance are discussed below.

3.1 SINGLE NEEDLE GEOMETRY STUDIES

Two needle types were studied: one was an accel design derived from the thrust vectoring geometry and the other was a conical tungsten needle. (The term "accel" denotes the use of an additional field reducing electrode around the needle to allow operation at higher net acceleration voltages.) An additional single needle experiment with a sandblasted rim is described. The accel design produced excellent performance, but the tungsten needle performed poorly and became baily eroded due to electrolytic etching. Sandblasting had no effect on performance.

3.1.1 Accel Geometry

3.1.1.1 Experiment

Two runs were made using a standard 14-mil O.D., 4-mil I.D. platinum needle onto which a 63-mil O.D., 5-mil I.D. stainless steel (S.S.) tube was soldered. The tube was soldered directly to the needle because it is an expedient method of carrying out experiments in thrust vectoring geometry that require the tube to be operated at needle potentials. The needle rim was placed 7 mils below the rim of the S.S. tube in the first run; in the second run, the needle was placed 2 mils above the rim. In both runs, the S.S. tubes were mounted flush with the extractor surface. These runs provided quantitative information on how needles should be mounted relative to the S.S. tube, and on wetting phenomena at the needle tip due to vacuum system contaminants.

The first run lasted eight hours. Because the needle was mounted below the rim of the S.S. tube, very high voltages were required to produce a colloid beam. At 25 kv, a beam with a $(\overline{Q/M})$ of only 2000 coul/kg could be produced.

For the second run, in order to produce higher fields, the needle was placed 2 mils out of the S.S. tube. In this position, a $(\overline{Q/M})$ of 10^4 coul/kg could be produced at $\dot{m} = 0.65 \times 10^{-9}$ kg/sec, 13 kv needle voltage, and -3 kv on the extractor. The total operating time on the needle was 80 hours (not counting the time spent filling) which included a continuous run of 70 hours.

3.1.1.2 Extractor Geometry

The pattern on the extractor due to both charged and uncharged particle bombardment was particularly informative. It indicated that the potential barriers produced by the new extractor/deflector/needle configuration could effectively protect the needle from secondary electron bombardment. The extractor plate was 40 mils thick with a 1/8-inch hole. The needle tip was flush with the extractor surface. It was felt that with this arrangement secondary electrons from the extractor would have less likelihood of striking the needle and polymerizing the propellant. The pattern on the extractor, formed by the condensation of a film of uncharged particles, and the removal of this film in certain areas by the sputtering action of positively charged particles, supported this thesis. The film coating extended only 1/8 inch outward from the edge of the extractor hole. Outside this area, the surface became clean for another 1/2 inch until the film gradually thickened towards the outer edge of the extractor plate. The localized clean area was interpreted to be the result of a correspondingly localized positive ion bombardment pattern. This indicated that the field between the needle and extractor prevented charged particles from striking the region within 1/8 inch of the hole. Therefore, no secondary electrons were produced in this critical region. The fact that no tar formed on the needle supported the hypothesis that the electrons could no longer bombard the needle tip.

3.1.1.3 Accel Performance

The most important overall conclusion drawn from the experiment was that stable, long-term, high I_{sp} operation could be maintained with the accel configuration when the needle and tube were operated at the same potential. (However, it may be more desirable to operate the tube at higher potentials than the needle to focus the beam and to eliminate any beam impingement on the tube.) This configuration has several advantages. The needle can be operated at much higher voltages than normally used; secondary electrons from the more positively biased vector electrodes cannot reach the needle, and a strong beam focusing effect is produced.

3.1.1.4 Conclusions

This run suggested certain guidelines for needle extractor positioning and the accel configuration:

1) The extractor should not be a thick plate with a beveled hole.
2) The needle should be mounted close to, or flush with, the extractor plane.
3) In the accel configuration, it is desirable to operate with the accel electrode at or above the needle potential.

These guidelines were further tested for validity in the 600-hour, 6-needle accel life test No. 6903-01 discussed in Section 6. The results proved the validity of these guidelines. The design of accel needle and extractor geometry based on these guidelines is shown in Figure 1b.

3.1.2 Sandblasted Needle Tip—Needle Roughness

A single platinum-iridium needle was sandblasted with fine aluminum oxide in an S.S. White industrial abrasive unit. A non-reflecting gray matte finish was produced. No gross operational difference between this needle and polished needles was observed. The ion current peak was slightly higher and the TOF slightly more concave upwards with the sandblasted needle. More work would be needed to prove that these differences are real. It is thus possible that a high polish is not required, although it would intuitively appear that surface roughness should be small

compared to the dimensions of a jet. When wetting problems exist, the high degree of roughness might help in a statistical way in establishing a uniform distribution of jets — a requirement for good efficiency. Gross roughness would reduce efficiency by producing variations in surface electric field intensities for the different emitting jets in addition to possible low field channels through which the fluid could flow, thus causing large angle operation or side tar formation.

3.1.3 Environmental Effects—Studies on Wetting

Performance degradation occurred during the 80-hour accel test. The needle performed well without noticeable degradation the first day of operation. Time-of-flight data indicated high I_{sp} performance with good efficiency. The needle was left to idle overnight at 10 kv with a negative head pressure (I_N < 1 μamp). The liquid nitrogen trap was kept filled during this time. When pressure and voltage were turned up the next morning, performance was not as good as the previous day. Performance continued to degrade during the morning, and the voltage was raised progressively to 18 kv (at a constant -3 kv on the extractor) until a series of arcs occurred, at which time the voltage was reduced. Immediately afterwards, the performance was restored to the previous day's level. The needle was left to run over the weekend. From a chart recording of beam current at constant voltage and feed pressure, it was found that performance did not degrade during the following day and a half. At the end of that time, the cold trap ran dry. In the morning the trap was filled, but whatever happened during the night after the trap ran dry caused, at first, a brief improvement and then a continuous decline in performance for the rest of the run according to TOF data. Since there were no tar deposits or visible films on the needle, it was believed that the degradation was caused by a decrease in the ability of the propellant to wet the needle tip during the period in which the cold trap ceased to function.

The first performance degradation occurred during an idling period (zero feed pressure, reduced needle voltage). At this time the meniscus must have receded into the needle, exposing the surface to contaminants such as pump oil. The following morning, after the feed pressure and voltage had been increased, the current started out lower than the previous day and continued to drop until only 5 μamp could be achieved at 13 kv because of the poor wetting of the platinum rim by the glycerine. By the time the discharges had occurred, and restored performance, it was probable that the trap had been cold long enough to clean up the contaminants within the system. For this reason, there was no performance degradation during the next day and a half until the trap ran dry, thus allowing contaminants to re-enter the system. As a result, the current again dropped to 5 μamp at 13 kv.

In later experiments, operating needles were deliberately exposed to various contaminants. The contaminant that had the most dramatic effect was Dow-Corning 704 silicone oil, which was the diffusion pump oil used during the 80-hour test. In these experiments, when the oil was evaporated onto the needle, an immediate drop in Q/M was observed. Thus, it is not unreasonable to believe that the performance degradation during the 80-hour test occurred because the chamber became contaminated with this oil when the trap warmed up.

Attempts were made to find a wetting agent that, when mixed with the glycerol, would allow the propellant to wet a thin film of silicone diffusion pump oil. Four materials were tested. Tween 21, Tween 80, Alkaterge C and Lecithin. None produced permanent wetting but all did promote wetting to some degree.

An experiment in which Octoil was evaporated on an operating single needle produced the same results as were obtained with DC 704; i.e., a reduction of current (at a fixed voltage) after exposing the needle to a few monolayers of oil. After cessation of the oil exposure, more than an hour was required for partial recovery. Before exposure, the needle had good wetting characteristics as tested by current recovery to the

original value after a 10-second voltage-off. After exposure to oil and partial recovery, the current after a 10-second voltage-off period was close to normal because the liquid had been forced further out on the partially non-wetting rim; however, within a few minutes, the current returned to a lower value. This confused a hope that switching the diffusion-pump oil to Octoil would reduce the wetting problem and perhaps even eliminate the need for continuous liquid nitrogen trapping.

3.2 TUNGSTEN NEEDLES

Two runs using tungsten needles were made. The first was operated with CsI as the glycerol dopant; the second was operated with the standard NaI-glycerol solution. In both cases, the performance was poor and the needles became eroded.

A tungsten single needle (Figure 4) manufactured by the Precision Research Corporation was operated for 24 hours using a 3/10 mixture of CsI-glycerol as propellant. This same propellant has been used with platinum needles and performed as well (in short term tests—no long term tests have been made as yet) as the 3/10 NaI-glycerol solution. Results of the tungsten needle tests were not very encouraging, although it is felt that a change in the needle geometry will improve performance. Electrolytic erosion was apparent after only 24 hours at relatively low currents (2-4 μamp). The low needle currents were apparently the result of low fields in the droplet forming region. This is inferred from the fact that time-of-flight data taken at 10 kv indicated low charge-to-mass ratios (∿ 2000 coul/kg). The eroded area (Figure 5) also indicated that the emitting region was confined to an area somewhat down inside the needle which, from the geometry of the needle (Figure 4), should be a region of low field.

Additional tests were made using NaI-glycerol to confirm the susceptibility of tungsten to electrolytic etching. The tungsten needle was run for approximately 24 hours using a 3/10 mixture of

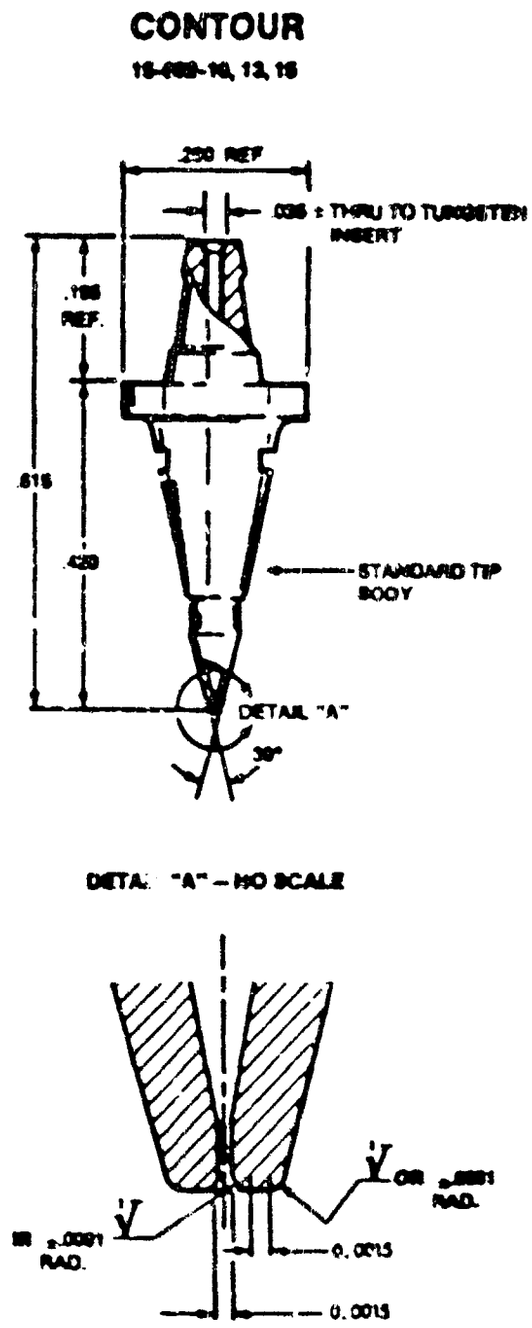

Figure 4. Tungsten Needle Design

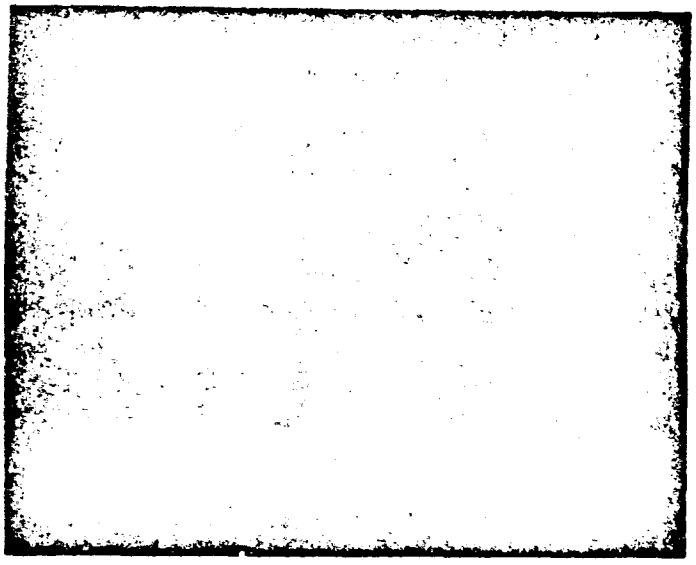

(a) 900 x Magnification of Tungsten Needle Tip Showing Eroded Area Around Needle Hole

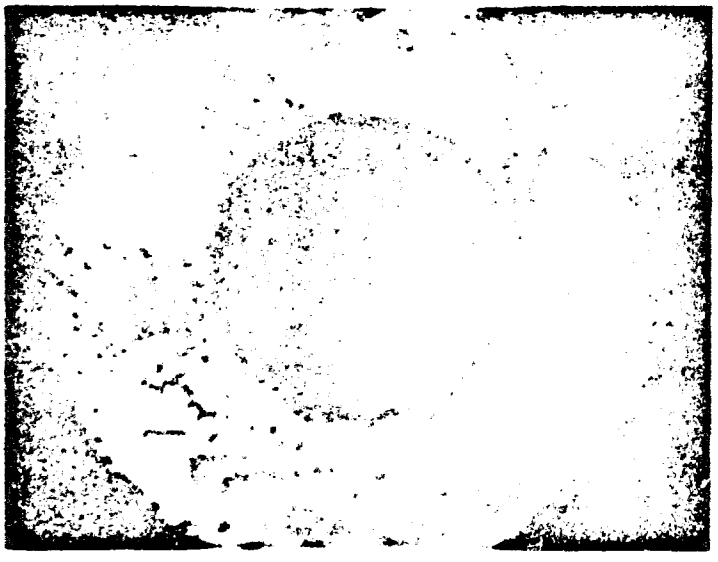

(b) 1000 x Magnification of Tungsten Needle Tip (Uneroded Needle) 4 Mil Across, 1.5 Mil Hole

Figure 5. Tungsten Needle Tip

NaI-glycerol. The operating voltages were kept at approximately $V_N = 6.4$ kv, $V_{ex} = 1.4$ kv. The needle current fluctuated between 2 and 50 μamperes. After operation it was found that the needle tip had changed shape due to electrolytic erosion.

The needle had been purposely electroetched in an $NaOH-H_2O$ solution prior to installation. The electroetch had several effects on the geometry: it produced a polished surface making it easier to detect erosion; it increased the hole size to twice its former diameter; it gave the hole a flared-out shape similar to the standard needle design; and it produced a narrower rounded rim. After the run it was found that flattening and broadening of the rim were the major erosion changes that occurred. This erosion was much more evenly spread than in the previous run, but nevertheless quite prevalent. The fact that one can electroetch tungsten is a tip-off that tungsten might be susceptible to electrolytic erosion. The tungsten needles erode too rapidly to be of practical use in a colloid thruster.

An interesting aspect of this needle operation was that it was bi-stable, alternating between a very low current, low Q/M, efficient mode and very high Q/M, high current (because of a large ion peak), inefficient mode. Figure 6 shows time-of-flight traces for these two modes. The low current mode would generally shift into the high current mode after a few moments. The high current could generally be dropped back to low value by a time-of-flight off pulse. These two modes were probably caused by different stable wetting positions on the needle. These positions could be caused by either geometry effects or by surface contamination. In any event, the low current mode produced a very narrow beam while the high current resulted in wider beam spread. In the past, low current, low Q/M, narrow beams have been caused by jets formed inside the needle below the rim, while the higher Q/M beams with greater spread came from the jets on the rim. A similar situation possibly occurred here, the low current mode being unstable due to overfeeding, causing the meniscus to grow and eventually moving out onto the rim.

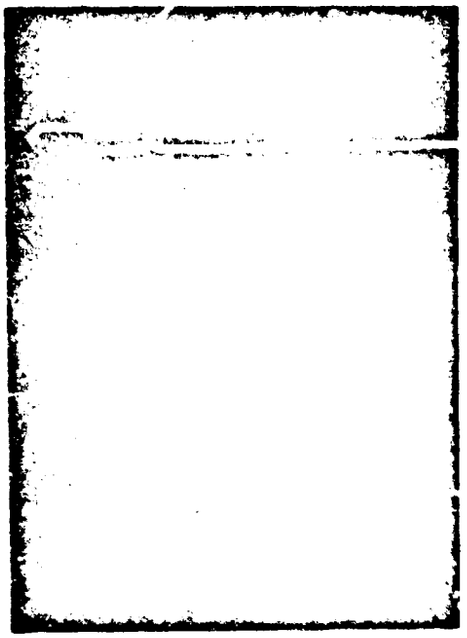

3/10 NaI-glycerol

P = 20" Hg

Vm = 4.4 kv

Vx = -1.4 kv

Top Trace: Low current mode I_m = 2 μamps. Scope set at 0.1 μamp/cm and 100 μs/cm

Bottom Trace: High current mode I_m = 27 μamp. Scope set at 1 μamp/cm and 10 μs/cm

Figure 6. Low and High Current Modes—Tungsten Needle

4. NEUTRALIZATION

4.1 POTENTIAL DISTRIBUTION OUTSIDE OF ENGINE

A negative potential exists adjacent to the extractor even in the presence of a beam, and a neutralizer placed at such a position cannot emit electrons (unless the beam partially stalls, producing a positive plasma which raises the potential at the neutralizer and extracts the necessary electrons). We have calculated this sheath thickness (the distance from about 1/4-inch in front of the extractor electrode to the plasma boundary) and compared it with experimental data from a moveable emissive probe.

4.1.1 Theory

Let 360 microamperes be emitted from a 36-needle array with a specific impulse of 1000 seconds, 75% efficiency, and a 20-degree half angle. Further, let the excess negative voltage applied to the extractor be 500 volts (i.e., if negative 1000 volts were necessary to prevent electron tunneling, then -1500 volts is applied). The positive charge density within the sheath which is responsible for the potential increase from -500 volts to the plasma potential at zero volts is estimated from the linear charge density $\rho_e = \frac{1/2\ i}{2/3\ v} = 2.7 \times 10^{-8}$ coul/meter, and an average area through which the beam passes of 1.5×10^{-3} M^2 (1-1/2 in. square), to be $2.7 \times 10^{-8}/1.5 \times 10^{-3} = 1.8 \times 10^{-5}$ coul/M^3. Poisson's equation ($dE/dx = \rho/\varepsilon_o$) predicts a parabolic potential distribution within the sheath of the form $\Delta V = 1/2\ \rho/\varepsilon_o\ (\Delta X)^2$ where ΔX is the sheath thickness and ΔV is the 500 volts across the sheath. Then, in the sample case, $\Delta X = (2 \times 500 \times 8.85 \times 10^{-12}/1.8 \times 10^{-5})^{1/2} = 2.2 \times 10^{-2}$ meter or a little less than one inch. We shall see that the sheath distance, as experimentally determined, was about this dimension. An exposed neutralizer close to the beam edge would have to be placed approximately 1 inch in front of the engine. For a single module with no undue amount of negative extractor beyond the needles and a ground shield between

the neutralizer and both the edge of the beam and the extractor, the neutralizer could be closer to the engine. Electrons then would be emitted outward, loop around and join the beam beyond the sheath.

4.1.1.1 Plasma Potential

The small potential variation within the plasma is governed by the positive charge distribution and the electron temperature. This temperature and the reason for it are uncertain. It is likely caused by the energy of the neutralizing electrons, which in space is governed by the perveance between the neutralizer and the beam, and might be equivalent to about 10 volts (100,000°K). In a ground test system with no neutralizer where all the particles strike a surface at a single potential, the temperature might be only about a volt, caused by the energy of the secondaries. If the beam strikes surfaces at two potentials, the temperature is much greater — caused by the energy of the secondaries coming from the more negative electrode.

Expressing the temperature of the electrons as a voltage V_T, and assuming equilibrium, then $\rho_e = \rho_+ = \rho_o^{V/V_T}$.

So the potential between two points of positive charge density ρ_1 and ρ_2 is $\Delta V = \ln \rho_1/\rho_2$. For example, three times further down the beam, where the charge density has dropped by a decade, the voltage is 2.3 V_T more negative. This field accelerates positive ions created within the beam, away from the engine. If they were directed towards the engine, they would be further accelerated across the sheath and cause severe tar problems. Conversely, negative ions (or attached electrons) are accelerated towards the engine but bounce off the sheath (as do electrons).

4.1.2 Experimental Probing of Potential

An emissive probe (small hair pin of fine tungsten wire heated to thermionic emission) was used to sense the potential within the sheath and plasma of a 36-needle module operating at 360 microamperes. By heating with 1/2 wave AC and viewing the incidence of a small emissiv

current during the period of no heating current on an oscilloscope, the potential could be determined to within about 0.1 volt. The sheath distance was found to be close to 1 inch from the extractor electrode. This sheath distance increased with an increase of negative extractor voltage, or decrease of current, or increase of specific impulse and remained the same with a pressure change. All of this is in accord with theory.

The plasma potential and its large variation when the beam hit both a wall at zero volts and a screen at plus 30 volts well illustrated the high electron temperature that results when "hot" electrons are ejected into the plasma. ("Chamber" neutralization was being used with no thermionic neutralizer.) When the +30 volts was removed, the plasma potential dropped from a value that varied around +27 volts to a very nearly constant +1.50 volts.

These results are illustrated in Figure 7. In this instance a floating collector is assumed at positive 25 volts with respect to a zero volt neutralizer filament. This floating potential would be greater if the filament were farther from the edge of the beam or more extensive shielding were employed. In an electron diode with an area equal to the spacing squared or when rapid dilation is possible, the current is about 2.3 microamperes x $V^{3/2}$ or 360 microamperes at about 28 volts. A current of electrons exactly equal to the positive beam current flows to the floating collector keeping the voltage constant. The electrons that provide the exact space-charge neutralization at all points within the beam are trapped within a boundary that is everywhere more negative than the plasma potential. In this laboratory situation these electrons have no net drift velocity, but a high random velocity. These are the electrons that are in thermal equilibrium with each other (but not with the ions) and establish the potentials within the plasma. Very cold electrons would all flow to any point that was even a few millivolts more positive than the rest and would maintain a very uniform potential.

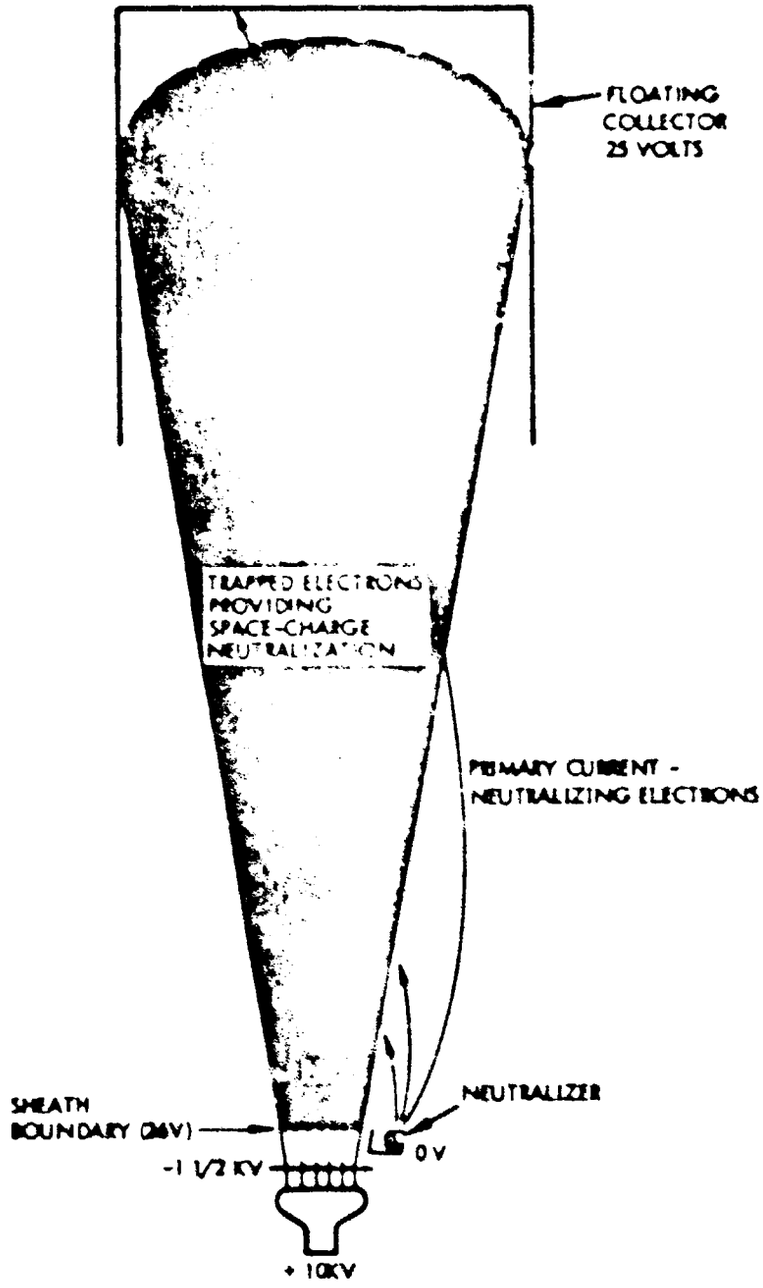

Figure 7. Potential Distribution Throughout The Facility During Neutralization With A Floating Collector

The inch-wide sheath whose potential is negative so that no electrons from the plasma can penetrate it is shown. If this sheath were much wider because of, for example, less current density, the neutralizer would be subjected to less positive potential and the plasma and floating potential would have to rise to attract the necessary electron current.

4.1.3 Potential Distribution Around the Needles

The sheath was probed up to a distance about halfway from the plasma to the thruster. The potential distribution outside these areas, i.e., around the saddle point and the needles as shown in Figure 8, is an approximation since no electrolytic tank or computer was used. The main uncertainty is the potential and position of the saddle point. The potentials towards the plasma follow from the parabolic distribution and the near-planar boundaries.

A sketch of this type is a great aid in visualizing the charged particle trajectories originating at various points within the space beyond the needles. For example, an electron-ion pair created at rest at point A by interaction of a constituent of the beam with a gas molecule will have the electron directed at the interior of the needle as shown by the dotted line and will accelerate the ion harmlessly towards the collector. If, however, a similar pair is created beyond the saddle point (the most negative point in front of the needle) at point B, the ion is accelerated toward the engine while the electron is directed to the collector. This is the cause of the extractor current that increases with pressure. These ions are deflected away from the round equipotentials surrounding the needle and strike the extractor electrode. If the deflecting potential is larger (as when deflectors are used) the ions might harmlessly strike the outer flat surface of the extractor and the resulting secondary electrons that are liberated go to the collector (making a negative undershoot on the TOF). When the ions strike the rounded portion of the extractor aperture, the producing electrons can bombard the critical rim area of the needle. There might

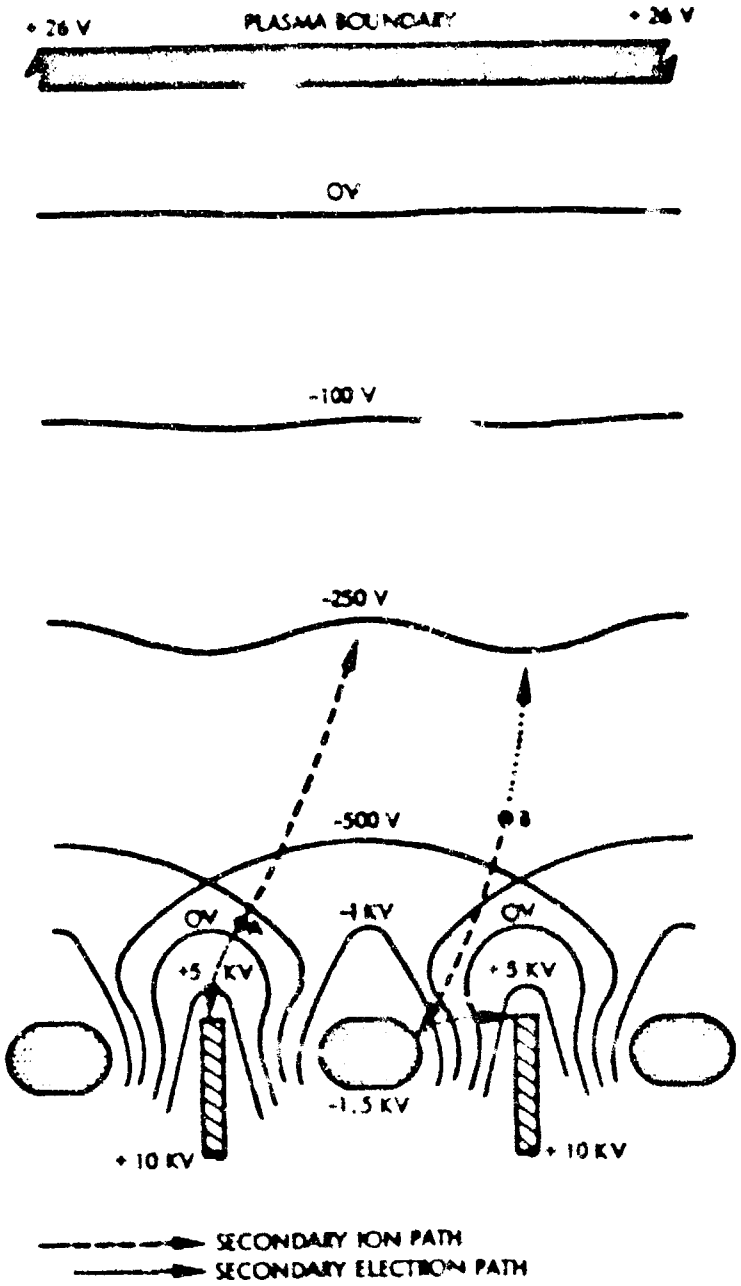

Figure 8. Potential Distribution Around the Needles Illustrating Trajectories of Secondary Particles

also be negative ions ejected which, if tar formation is not too far advanced, can clean the tip. There has been much experimental evidence of this. The needles often appear cleaner than surrounding electrodes which have the same incident efflux of material from the collector. Microscopic examination has shown that erosion of the platinum is greatest where the propellant has not wetted.

4.2 NEUTRALIZER ELECTRON SOURCE

The electron source must supply an electron current equal to the positive beam current at a power expenditure less than that needed to produce the thrust. 20% should be an upper limit with less than 10% being a desirable goal. For low thrust (~100 micropounds) engines operating at about 400 microamperes and 10 kilovolts (4 watts), the neutralizer would have to produce 0.4 milliampere with 0.8 to 0.5 and less watts. This cannot be achieved from a tungsten filament with 10,000 hours of life. (It can be achieved by a tungsten filament with a life in excess of 2,000 hours. Also, a 10,000-hour tungsten filament can supply 1 milliamperes at 3 watts and so can meet the power requirement of larger engines or ones operating substantially above 10 kilovolts.) These goals can easily and simply be achieved by a barium-oxide coated filament with 10,000-hour life (in space). This source will have reduced life when used in ground testing stations, cannot be reused after testing, and must use statistical methods for assuring reliable, long-lived operation when first put in operation in space.

Efforts during this program were directed towards developing the most efficient tungsten filament (although admittedly of poorer efficiency or shorter life than desired) for ground testing colloid engines and studying the chemical interaction with materials encountered in the testing facility. Also, experience was gained testing a type of barium cathode less efficient than the oxide coated filament but more rugged and less sensitive to poisoning in the testing chambers—the barium impregnated cathode.

4.2.1 Tungsten Emitters

The emission efficiency (ma/watt) increases with temperature and is about 0.85 ma/watt at 2300°K. The emission current density is 40 ma/cm^2 at this temperature so a current of only 1 ma requires a short, thin wire. At this temperature 1/16 mil of tungsten is evaporated from the surface in 10,000 hours - the maximum amount that a 2-mil-diameter wire can be reduced without failure. A 1-inch long, 0.002-inch diameter tungsten wire at 2300°K will have a life of 10,000 hours, will emit 2 ma from an active length of about 1.5 cm which will radiate 2.4 watts, and allowing 0.6 watt for the two end losses, will require about 3 watts. The generous 0.6 watt end-loss assumption (somewhat justified by experiment) bears heavily on the reason why an efficient tungsten emitter cannot be constructed for less than 1 watt power expenditure.

Since the evaporation rate of tungsten goes as the 1.65 power of the electron emission, the life testing of a filament can be accurately accelerated. If the emission is increased by a factor of 10, and the filament lasts 250 hours, its life at rated emission current would be $250 \times (10)^{1.65} = 11,250$ hours. So as not to degrade the life of a filament, the design current must not be exceeded by more than about 5%.

4.2.2 Oxide-Coated Filament

Although the present research has not been involved with this type of cathode, it is recommended that it be considered for space application, especially if a small (<1 mlb) thruster is considered. Also, since the efficiency, life and reliability are extremely sensitive to the control of trace impurities in the materials used, it is recommended that the emitters be purchased from a reputable supplier. The thruster manufacturer would test the emitters separately for life in a high vacuum and also in position on the operating engine to determine performance.

The emitter would consist of a wire about 1 inch long and 0.003 inch diameter of special alloy of nickel or platinum with trace reducing materials in solution coated with a barium-strontium-calcium carbonate

mix in a nitrocellulose binder. The emitter in this condition would be quite rugged and would withstand exposure to atmospheric conditions. Upon heating in space, before the colloid engine is turned on, the binder would first evaporate and then the carbonate would decompose (liberating CO_2) to the oxide. During the life of the cathode, trace materials would diffuse to the metal-oxide interface and produce free barium, which keeps the cathode active. Two disadvantages of this cathode over the tungsten filament are the possible need for higher initial power to activate and the lack of a predictable relationship between emission current and heater current. With tungsten, if the heater current is right, emission capability must be right. With the oxide cathode, if the heater current is right, the emission might be zero or insufficient because of poisoning or lack of activation or depletion of barium.

4.2.3 Impregnated Cathode

Ba-Sr-Ca-Al_2O_3 is melted into the pores of a porous tungsten disc swaged into a molybdenum cylinder enclosing a heater. This cathode can stand more abuse than the oxide cathode. It can be exposed to moist air for extended times even after use with only temporary degradation of emission. As with any indirectly heated cathode, the excellent power efficiency possible from the emissive material alone is degraded by the increased area of the nonactive side walls and the radiant power lost out the back from the hotter heater. Careful radiation shielding and potting the heater helps, but it is still difficult to reduce the heating power below 1 watt. A standard "button" cathode of about 1/8 inch diameter with reasonable heat shielding that was used required about 5 watts, but had a huge emission capability (> 100 ma).

4.3 EXPERIMENTAL TESTS, 591-HOUR RUN

Previous tests had established the long life of a tungsten filament in a high vacuum, and its adequacy as a neutralizer for a colloid engine. Trouble had been experienced with deterioration by products from the

colloid engine. Therefore, the neutralizer run during most of the 591-hour life test (Run #903-01) consisted of a 0.6 inch length of 0.002 inch tungsten wire completely enclosed in a small aluminum box except for a small slit aperture looking at the side of the beam. The purpose of this arrangement was to completely shield the filament from direct impingement from either the source or collector.

The neutralizer was heated by a 50-percent duty cycle 1-kc square wave. Performance data was periodically recorded at 50, 100 and 150 amperes. Between readings, the heater power was adjusted to give 100 amperes emission current.

Figure 9 shows performance as a function of operating time (472.4 hours total). There is a discontinuity in the curves due to a vacuum accident at 200 hours. A temporary power failure caused the bleedgate to close and the neutralizer remained on as the chamber pressure rose to well over the 10^{-5} torr range for approximately 90 minutes.

The filament, which had become quite brittle, broke in handling during post-test removal. Figure 10 is a photograph of the filament taken after the test, in which the effects of considerable grain growth offset can be observed. An X-ray diffraction scan indicated that considerable W_2C had been formed. There was no observable decrease in filament diameter.

The filament had been suspended between two nickel support posts in a slightly stressed configuration to allow for thermal expansion. Evidently, as Figure 10 indicates, this technique did not work well. Subsequent filaments employ a bowed or spiral filament configuration.

Figure 9 shows that the resistance at constant emission current initially increased with time and then dropped to a much lower value after the vacuum accident. This is believed to have resulted from filament being carburized by thermal decomposition of incident glycerol. This has a two-fold effect in that the carbide has a higher resistivity than pure tungsten and, in addition, the carbide's higher work function

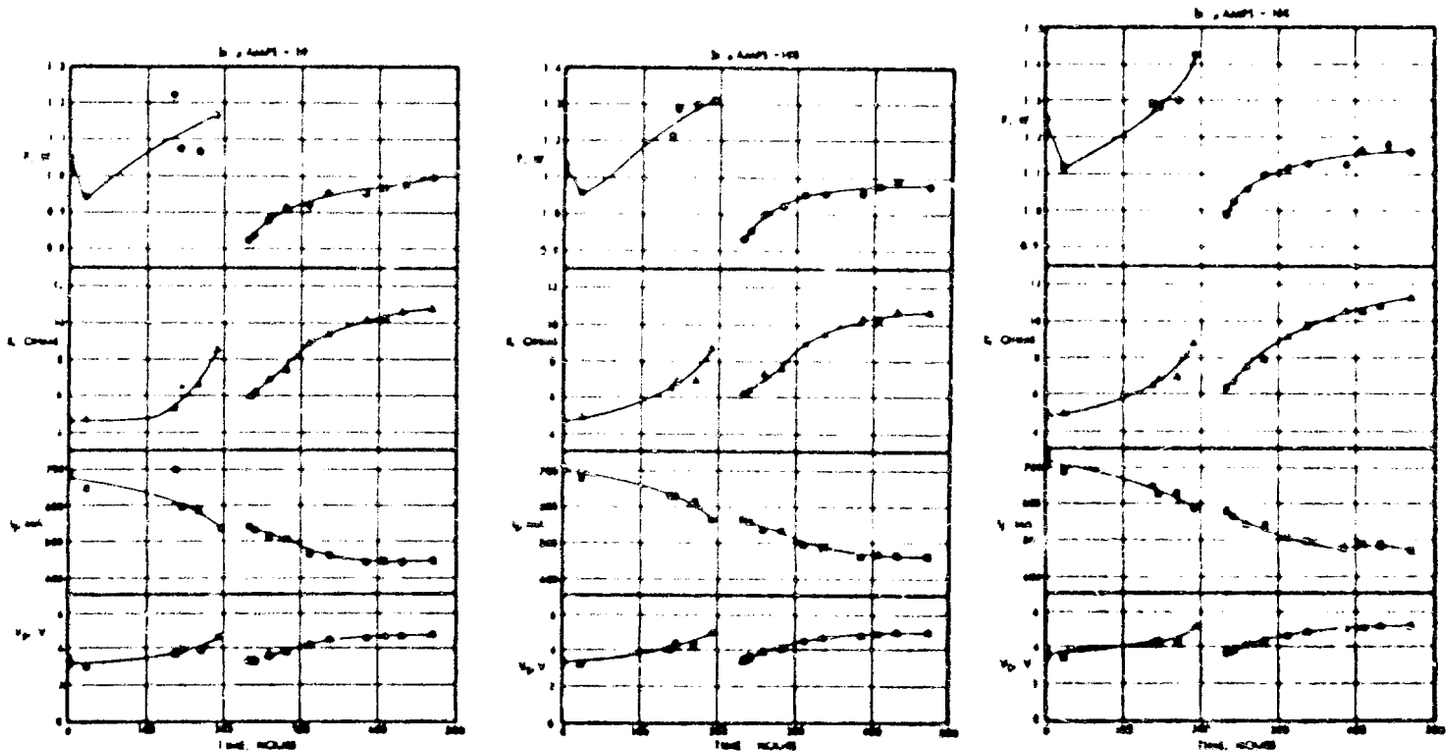

Figure 9. Neutralizer Power (P), Resistance (R), Heater Current (I_e), and Heat Voltage (V_e) as a Function of Time at Constant Saturated Emission Current (I_e) (Run 6903-01)

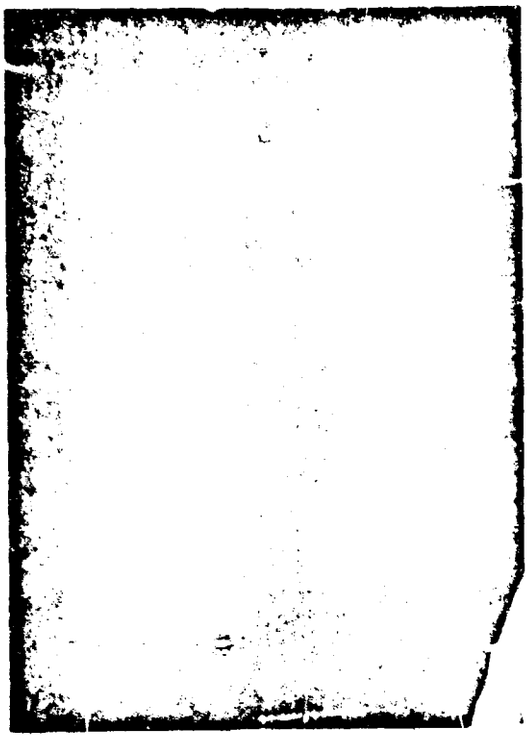

Figure 10. Tungsten Filament from Run 6903-01 After Being Broken During Removal From System (90X)

requires a higher operating temperature and, hence, higher resistivity for a given emission current. Oxygen exposure during the vacuum accident removed the carbon at the filament surface, reducing the work function to that of pure tungsten. The resistivity was still higher than at the beginning of the test since the filament interior was still partly carburized. As the test proceeded, the resistance continued to rise again as both the surface and interior were further carburized. The graphs suggest that a steady-state equilibrium was being approached. Unfortunately, the test duration was not adequate to definitely establish the existence of a horizontal asymptote.

The power versus time curves are more difficult to explain. The fact that lower power was required at the end of the test than during the early stages is believed due to the lower thermal conductivity of the carbide s[illegible]e, for short filaments, and losses are a large part of the power budget. Quantitative calculat[illegible]s need to be performed, however, to confirm this explanation. The initial drop-off in power at the beginning of the test is most likely due to the delay time in attaining thermal equilibrium of the support structure and to initial changes in surface emissivity and work function.

4.4 CARBURIZATION

Studies of the carbiding of tungsten filaments in a system with an operating colloid engine have shown the following:

1) Glycerol is emitted from the needle tip normal to the thrust direction.
2) A large fraction of the carbiding materials is condensed by liquid nitrogen.
3) High temperatures and low hydrocarbon arrival rates will evaporate the cracked carbon and maintain the central part of the filament carbide free. However, there are always cooler regions near the support that will carbide.
4) When operating in oxygen, the carbon is very efficiently removed as carbon monoxide.

The first point was established by operating two filaments very close to an operating single needle. One filament had its axis pointed at the needle rim and the other had its surface normal to the needle rim. Both filaments were out of the beam. The filament whose surfaces faced the needle tip showed a resistance increase of 0.35% per hour while the other filament (axis towards the needle and hence protected from glycerol from the needle) showed no resistance increase. A later experiment with the entrance of an ionization gage close to the side of a 36-needle module failed to find a trace of glycerol ejected 90° from the axis of the needle.

This experiment and later ones confirmed definitely that higher temperatures will reduce the carbiding rate, due presumably to the evaporation of the cracked carbon. The vapor pressure of carbon from graphite is 10^{-6} torr at 2150°K and 10^{-4} torr at 2400°K; however, the adsorption energy is most likely higher for tungsten and tungsten carbide. In light of the experimental evidence, and these large vapor pressures at electron emitting temperatures, it seems safe to assume evaporation. The carbon might migrate down to a slightly cooler carbided region where it might then evaporate.

The next experiment was designed to find out how much of the carbiding gas was condensable at liquid nitrogen temperature. A filament was mounted in a copper enclosure that could be cooled. The vacuum resulting from a single operating needle was degraded by reducing the pumping speed of the system. When the carbiding rate was established, the enclosure was cooled. The carbiding rate stopped. This indicated that the arrival rate of hydrocarbons dropped below the carbon evaporation rate or the rate that oxygen (due to negligibly small leak) or H_2O evolving from the insulators would remove the carbon. It was feared that methane or other untrapped gases generated at the collector would produce an excessive carbiding even when the filament was completely trapped.

The next experiment was performed in the large tank with an eighteen needle array. The filament was in an enclosure with a single aperture that could face different portions of the tank including completely trapped regions outside the liquid nitrogen shrouds. This experiment confirmed all previous hypotheses. Carbiding rates corresponded to resistance increases of about 1% per hour at indicated pressures of about 3×10^{-6}. This was at low temperatures (to prevent evaporation of carbon). When facing completely trapped regions, the carbiding rate dropped to 0.2% per hour at low temperatures of about 1800°K. This small finite carbiding rate was due to non-condensable gasses such as methane and ethane.

An opportunity was taken during this test to confirm quantitatively a previous observation: the very rapid conversion back to pure tungsten by oxygen (or water vapor) of a carbided filament. This was done and a calculation showed that 100% of the oxygen molecules that struck the filament, stuck (sticking coefficient = 1.0, not 0.03 as on pure tungsten) and removed two carbon atoms ($2C+O_2 \rightarrow 2CO$), freeing four tungsten atoms to return to metallic tungsten ($2W_2C \rightarrow 4W + 2C$).

These experiments were performed to prove that a tungsten neutralizer shielded from the needles and operating in space would not have a carbiding problem, and, further, to provide techniques for constructing a tungsten wire neutralizer that could be used for ground tank tests that could survive for long durations. We feel these experiments have adequately answered these questions.

4.4.1 Cooled Gun

For a time the presence of non-condensable hydrocarbon gases such as ethane was not known, so attempts were made to design guns utilizing directly heated tungsten filaments that would allow complete shielding by liquid nitrogen cooled wall from the engine and beam. Since then, measurement with a mass spectrometer has identified such gases (methane and ethane). Therefore, some other method must be used when a tungsten

filament neutralizer is operated in a ground testing facility. One of the early configurations that was devised prior to obtaining this knowledge is shown in Figure 11. This design took advantage of the vacuum system cold walls needed to maintain vacuum during colloid life testing. The electrons were attracted into the beam by a large cylindrical anode placed between the beam and the filament. Electrons were prevented from striking the anode by interposing a planar strip of mica that charged to the exact potential of the filament opposite it. This eliminated the bothersome effects of the voltage gradient across the engine, beam, or collector when mounted in the position shown in Figure 11 When the filament is heated by AC as it must be to prevent migration of tungsten atoms and life reduction, the mica will no longer be as effective. Also, the necessity of an extra potential is a serious disadvantage.

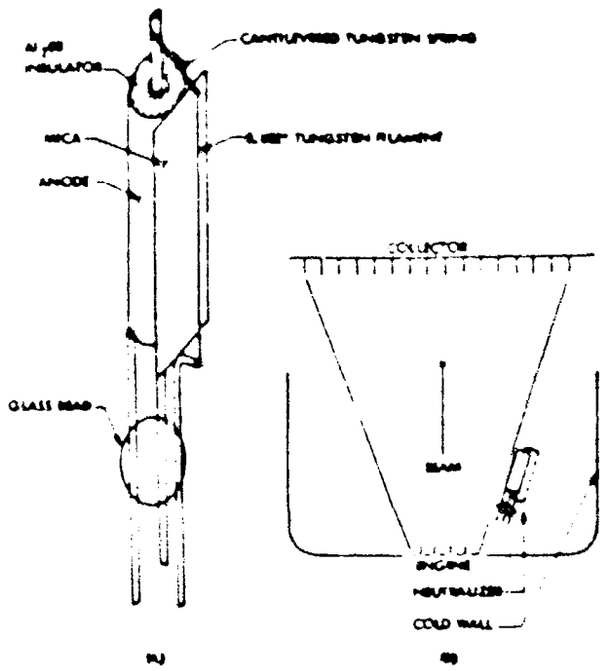

Figure 11. Sketch of Shielded Neutralizer Gun (A) and Position in Tank (B)

4.4.2 Scheme to Prevent Carbiding

Carburization is easily detectable by a resistance increase. In the experiments with carburization, rate-of-resistance increases of 0.1 to 4 percent per hour were easily measured. Detecting the elimination of this increase or its reversal is a simple matter. A scheme that has been very successfully tested to eliminate this carbiding is to introduce a small leak of oxygen. The partial pressure of oxygen needed is usually less than 10% of the total pressure in the system and so has negligible effect on other aspects of the engine's operation. It is strongly felt that quite a wide range of oxygen partial pressure will prevent carbide formation without tungsten mass loss by volatilization of WO_3. Surface migration of carbon atoms and the unity sticking coefficient of oxygen on tungsten carbide in conjunction with only a 0.03 sticking coefficient on clean tungsten should allow a much longer life tungsten filament in a variable combination of oxygen and hydrocarbon gas than in a small part of either gas alone. This hypothesis has not been tested, but when this scheme was used for 950 hours on the colloid microthruster experiment, the resistance change was about 3% for not too critical an oxygen adjustment. This 3% was probably true evaporation.

The filament would be placed behind a shield to prevent possible efflux of material from the engine or beam. The collector would be as far away as possible. Diffusion pumps of as high a speed as feasible would be used to reduce methane and liquid nitrogen cooled walls used to reduce the condensibles. Then, oxygen would be used to eliminate the residual carbiding rate. This would allow the tungsten filament neutralizers to be placed on the engine as they would be in space and tested in a ground test facility.

4.5 LIFE TESTS WITH ENGINE

Two neutralizers were installed in the high pumping speed system with the 36-needle vectorable modules. One was a 0.8 inch spiral of 0.002 inch tungsten carefully mounted parallel to a plane electrode placed 3/4 inch in front of and to the side of the module. The relative arrangement was such that the entire structure was just outside the edge

of the beam. The plane electrode shielded the filament from looking directly at the needles. The electrode was connected to one side of the filament. This successfully neutralized a 360-microampere beam when the filament was 50 volts positive with respect to the plasma. Because of the electron drain problems with the engine, and the almost daily removal of the module, little time was accumulated on the filament and it was accidentally destroyed.

An impregnated cathode was also in the system. It was a larger-than-necessary, higher power unit that was ordered off-the-shelf while awaiting smaller units that were being fabricated. It was considered mandatory to quickly determine if impregnated cathodes were compatible with a hydrocarbon atmosphere. It was expected that a low hydrocarbon partial pressure would not carbide the cathode but would crack on the surface and reduce the aluminate, causing a very active cathode but one with a reduced life. It was further felt that this was a very tolerable solution to any engineer's demand that the same neutralizer be tested with the engine, then be stored in humid air, and then be launched and have a satisfactory life in space. This would be because testing, although reducing the life of the cathode from, for example, 12,000 hours to 500 hours, would use 20% of the material in a 100-hour test, still leaving 10,000 hours when operated in hydrocarbon-free space. The tests with the colloid engine did prove that no poisoning occurred, but the tests were too short to indicate any life reduction. This cathode, too, was carelessly damaged and was not available during the longer runs. Two smaller impregnated cathodes arrived from the vendor. One was mounted in a close-spaced gun structure where the electrons are accelerated through a high transmission photo etched grid. This gun, shown in Figure 12, has not yet been tested. It is expected to have more than 1 milliampere capability with less than 1 watt input power.

Side View

Front View

Figure 12. Photographs of the Small Impregnated Cathode Gun Structure. The Cathode is 0.035 Inch In Diameter.

4.6 HIGH VACUUM LIFE TEST

The configuration that had been planned for a life test with an engine was placed in an ion-pumped high vacuum system. It was run for 1300 hours at over 0.600 ma emission current at 1.45 watts with a barely perceptible resistance increase of about 0.4%. This gives a projected life of 30,000 hours based on an end life at 12% resistance increase. At 1300 hours, the filament was changed to 1.9 watts, giving 6 ma of emission and an accelerated life test. It is expected to have a life of 1500 hours. At 2 ma it takes 1.65 watts and would have a life of 10,000 hours; at 4 ma it takes 1.75 watts and would have a life of 3,000 hours.

5. COLLOID FEED SYSTEM

5.1 INTRODUCTION

The objective of this phase of the program was to develop a feed system for colloid thrusters that does not require a propellant flow control valve. The feed system was to be a positive expulsion type which supplies propellant to the thrusters at a nominal operating pressure of 0.50 psia. In the absence of the flow control valve, the feed system must have the capability of modulating the pressure for ON-OFF thruster operation. During periods of thruster operation, the feed system supplies propellant at the nominal operating pressure level; however, when the thrusters are off, the propellant pressure must be reduced to a level equal to or less than the surface tension retaining pressure developed by the propellant in the thruster needles. At this pressure level no propellant is expelled from the needles when the thruster potential is off. It is also desirable for the feed pressure to be independent of both the amount of propellant expelled and the prevailing ambient temperature. The design requirement that the feed system maintain a slight, non-zero pressure on the propellant during no flow conditions was imposed to preclude bubble formation within the stored propellant. Void formation could occur after propellant is expelled from the system if the storage vessel is not restrained from returning to its original volume during zero pressure OFF operation. This was desired in order to avoid the possibility of voids presenting gas bubble nucleation points caused by residual noncondensible material dissolved in the propellant.

The nominal volume of propellant stored in the feed system [illegible] to be 3940 cc (12.6 lb). This represents a total impulse of 18,900 lb-sec at 1500 seconds specific impulse, equivalent to approximately 10,000 hours operation at a 500 mlb thrust level. The final system, however, had considerably more volume to allow the manufacturer to use existing tooling. This resulted in a considerable cost savings. All materials in contact with the propellant were to be metal. The metals to be selected were those demonstrating compatability with the propellant. No organic materials were allowed to contact the propellant. This requirement was established to eliminate the potential both for outgassing into the propellant of absorbed gases and for propellant contamination caused by reactions resulting from long-term contact with an organic material.

An overall operating temperature range of 10° to 50°C was established for the feed system. This temperature range is characteristic of that encountered on operational spacecraft.

5.2 SYSTEM DESIGN

The schematic diagram, Figure 13, shows the basic feed system selected to meet the program objective and requirements. The system consists of a propellant storage vessel, a pressurizing device, a pressure control system, a filter and a squib valve for system isolation prior to operation.

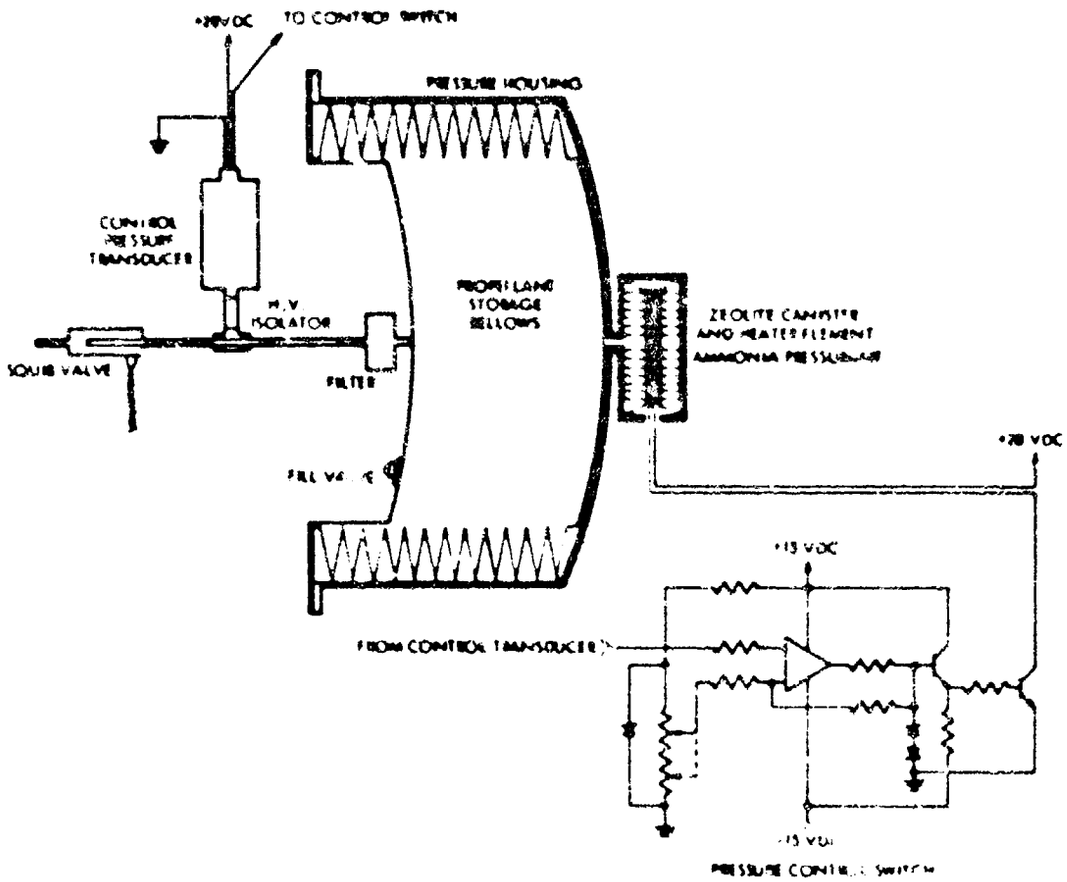

Figure 13. Colloid Thruster Feed System

5.2.1 Propellant Storage Vessel

Because of the propellant volume and materials limitation requirements, a metal bellows was selected as the propellant storage vessel. The propellant is stored inside of the bellows to achieve maximum expulsion efficiency. With this configuration, the bellows convolutions expand when filled and collapse as propellant is expelled. At complete expulsion, residual propellant in the convolution section of the bellows is minimized. If propellant storage were exterior to the bellows, the bellows would be compressed when the system was filled. As propellant was expelled, the bellows convolutions would separate, this decreasing the expulsion efficiency.

The bellows is confined in a hermetically sealed housing so that the propellant can be pressurized by a gas.

5.2.2 Propellant Pressurization

The pressurization mechanism selected for the feed system utilizes the equilibrium pressure associated with an adsorbed vapor on a solid surface. This type of pressurization concept is similar to that of a volatile liquid or solid in which the vapor phase of the substance provides the working fluid. In both the adsorbed or volatile fluid systems, the pressure exerted by the vapor phase is a function of the condensed phase temperature. Thus, for both systems, it is necessary to have a region of controlled temperature to achieve pressure control. A volatile fluid system requires the temperature of the controlled area to be lower than the minimum anticipated throughout the entire pressurant storage volume. This is to avoid condensation of the working fluid in other cold spots which would result in loss of pressure control. This requires either heating the entire system relative to its environment or using refrigeration for local cold spot control. The adsorbed vapor system does not have this limitation since it is now possible for the material on which the vapor is adsorbed to be maintained at a temperature above the surrounding pressurant storage volume. The adsorbent material temperature, and therefore propellant feed pressure control, can be maintained with a localized heater element. Such a heat source is simpler, more reliable, and more efficient than a cooling unit.

The adsorbent material selected for the feed system was Linde Molecular Sieve, which is an artificial zeolite. The working fluid was ammonia.

This combination minimized the weight and volume of adsorbent required for a given volume and pressure requirement. The vapor pressure of ammonia at 10°C, the minimum temperature requirement, is 89.2 psia. This pressure is in excess of that required for a colloid feed system, thus eliminating condensation problems. Adsorption isotherms for ammonia on zeolite are shown in Figure 14. Carbon dioxide/zeolite is another possible combination; however,

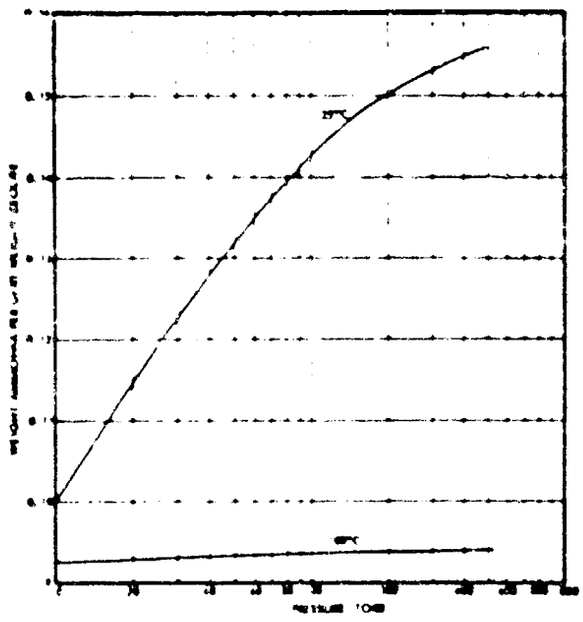

Figure 14. Adsorption Isotherms for Ammonia Zeolite Types 5A and 13X

approximately twice the amount of zeolite is required to achieve the same operating characteristics as for the ammonia/zeolite system.

5.2.3 Pressure Control

The pressure control unit selected for the feed system is similar to that used for the ACSKS ammonia feed system, Reference 5-1. A high output, absolute pressure transducer is used to sense the propellant feed pressure. The output voltage of this transducer is used as the input to a level detector circuit. The output signal from the level detector controls the conducting state of a switch in the heater element/power supply circuit. The heater

element is located within a canister containing the zeolite adsorbent. During operation, the feed pressure is regulated by controlling the zeolite temperature with the heater element. Pressure increase is accomplished by increasing the zeolite temperature to desorb ammonia. This desorbed ammonia increases the quantity of vapor in the chamber surrounding the bellows, and therefore, the pressure on the bellows. The increased pressure on the bellows increases the propellant feed pressure. The feed pressure is decreased by allowing the zeolite to cool which results in removal of vapor from the bellows chamber by readsorption of ammonia on the zeolite.

As propellant is expelled from the system, the pressure exerted by the ammonia on the bellows must increase to maintain a constant feed pressure, because of the increased spring force of the bellows as it is depressed. In addition, the volume occupied by the ammonia increases as the propellant is expelled. Because of these two factors, the average temperature of the zeolite increases as propellant is expelled. The typical feed system pressure and temperature profiles during system operation are shown in Figure 15.

The propellant feed pressure is controlled at two levels. The upper pressure control level corresponds to the flow condition and the lower level to the system no-flow state. These two levels are achieved by supplying two separate reference voltages to the pressure control level detector. The pressure change from one level to the other is made by switching from the one reference voltage to the other. The pressure control bandwidth at each control level is the result of hysteresis in the level detector circuit and thermal response characteristics of the heater element and zeolite adsorbent.

5.2.4 Propellant Conditioning and Retention

During normal spacecraft operation, the feed system supplies propellant to thrusters operating in a gravity-free vacuum environment. On the ground, however, the system is exposed to the ambient atmosphere and gravity. Air and atmospheric moisture both have a high solubility in the propellant. The presence of these materials in the propellant will deteriorate thruster performance. Thus, it is necessary to isolate the propellant from the atmosphere. Also because of high specific gravity of the propellant, certain spacecraft orientations can result in high hydrostatic heads relative to the

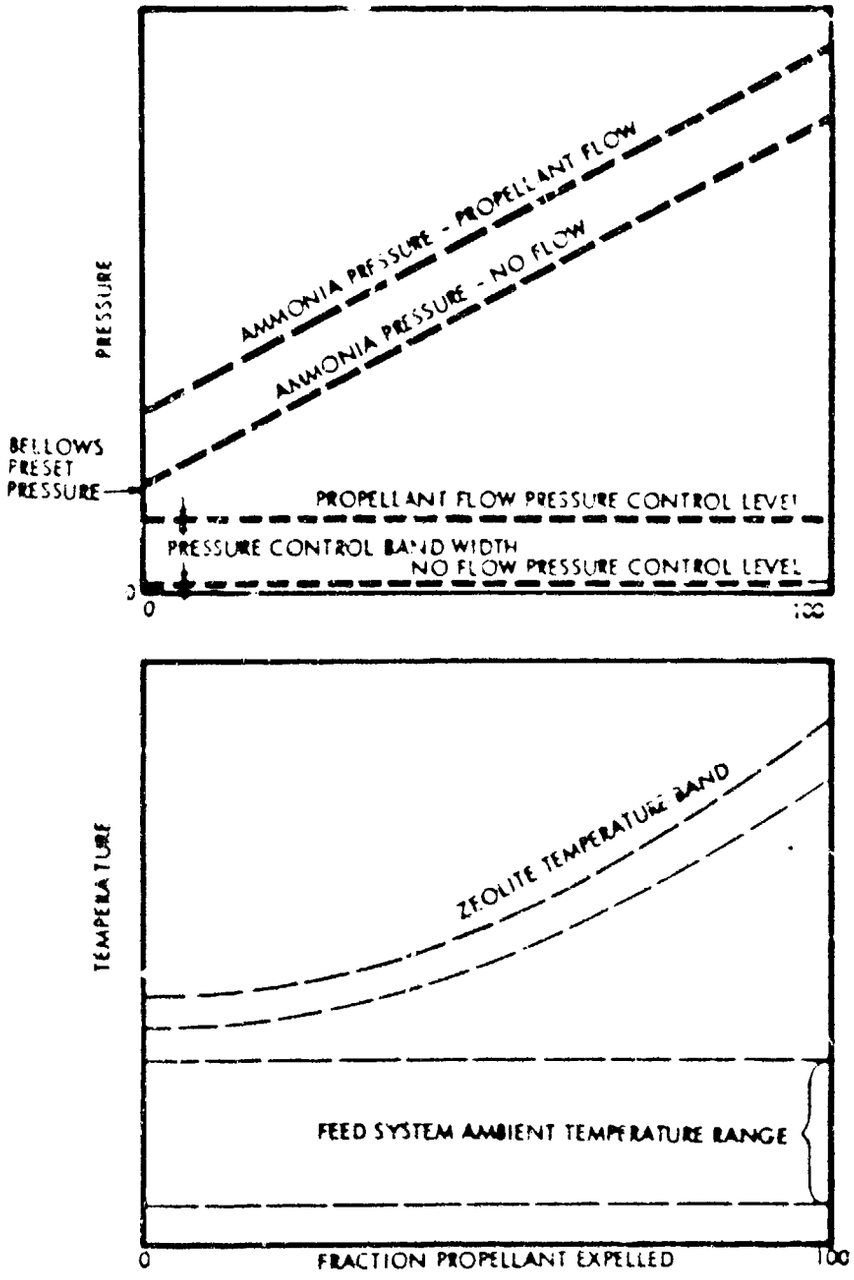

Figure 15. Typical Feed System Pressure and Temperature Profiles

thruster nozzles. In addition, during launch, hydrostatic heads will develop independent of the orientation. The propellant, therefore, must be retained to avoid expelling propellant through the thruster during the launch and prelaunch periods. In order to eliminate these problems an explosively actuated, normally closed squib valve was selected for prelaunch propellant isolation and retention. Under normal operation, the squib valve would be opened prior to thruster operation in space. The use of a squib valve in the propellant distribution system does not preclude functional checkout of the feed system prior to launching. The various operating characteristics of the feed system can be checked without expelling propellant. Latching solenoid valves were also considered for this purpose; however, the development time and cost were beyond the scope of this program.

A porous metal filter was positioned at the outlet of the propellant storage vessel. The purpose of the filter was to remove particulate material that might have accumulated in the propellant from the bellows storage vessel. The filter would be more effective if it were placed downstream of the squib valve to remove the particulate generated by the squib valve. However, the control pressure level would have to be set to compensate for the pressure drop through the filter if it is located in the downstream position. Because this pressure drop varies with flow rate and temperature, the feed pressure to the thrusters would vary. In the present design, particulate matter generated by the squib valve is removed by the thruster filters.

5.3 SYSTEM ANALYSIS

The zeolite/ammonia pressurizing unit was analyzed with respect to the conditions encountered in the colloid feed system. The results of these analyses were used to determine: (1) quantity of zeolite required to perform the pressurization, (2) operating temperature range of the zeolite, (3) system power requirements, and (4) dynamic response characteristics. A series of experiments was performed to verify analytical results and to determine operational behavior.

5.3.1 System Static Analysis

As propellant is expelled from the storage bellows, the volume and pressure of the vapor phase pressurant increases. This means that the mass of ammonia in the vapor phase increases. The increase in vapor phase

mass is accomplished by depleting the adsorbed phase. The quantity of zeolite and its maximum operating temperature are determined by the amount of pressurizing vapor required. This in turn is determined from the bellows characteristics and the propellant feed pressure.

The bellows selected for the feed system had the following characteristics:

- Effective cross sectional area - 66 square inches
- Overall length - 6 inches
- Spring constant - 0.5 psi/inch

The bellows travel needed to displace 3940 cc of propellant was 3.64 inches. This movement corresponds to a spring pressure of 1.84 psi. When incorporated in the feed system, the bellows is depressed 1.0 inch by the surrounding pressure housing. Because of this bellows preset, an ammonia pressure of 0.5 psia is required before a propellant feed pressure starts to develop. Without this preset pressure, any small ammonia pressure over the zeolite deflects the bellows and expells propellant. Thus, in this case, the ammonia pressure has to be essentially zero when the bellows is filled with propellant and the system is in the OFF condition. This results in prohibitively low OFF temperatures.

For the above stated bellows characteristics, the ammonia pressures required for system operations are:

• Full propellant loading	0.1 psia OFF 1.0 psia ON
• At complete expulsion	2.34 psia OFF 2.84 psia ON

The total weight of ammonia available for delivery by the zeolite is determined from (1) the free volume in the pressure housing surrounding the bellows when all of the propellant has been expelled, and (2) the pressure difference between the cases of full propellant loading with no flow and complete expulsion with full flow. The free volume is approximately 6000 cc and the pressure difference is 2.34 psi. This corresponds to 0.697 gm of ammonia. The data shown in Figure 16 are used for calculating the required weight of zeolite to supply this ammonia.

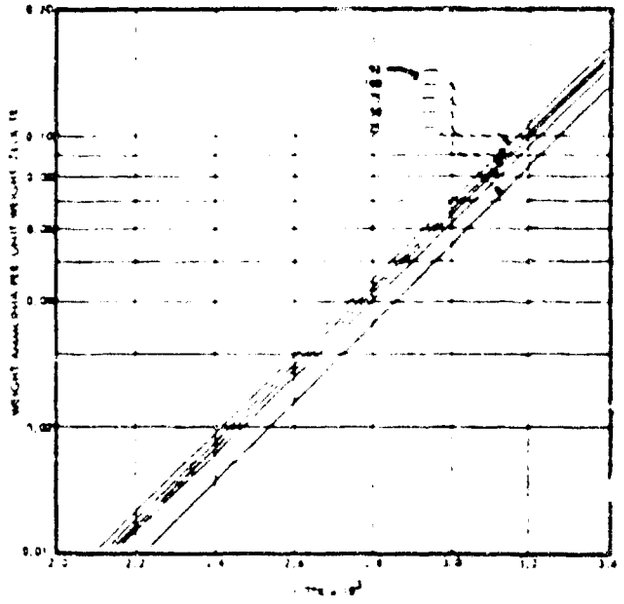

Figure 15. Ammonia Adsorption on Zeolite

For a more detailed solution to the problem, the dynamic characteristics of the system must also be considered. The heat of adsorption of a material is in the range of the heat of sublimation and vaporization of that material. For thin adsorbed layers, the heat evolved during adsorption is similar to that evolved during sublimation. As the adsorbed layer becomes thicker, the heat evolved during adsorption approaches the heat of vaporization. The relation for the adsorption process is

$$\frac{d}{d\left(1/T\right)} \ln P = \frac{A}{R} \qquad (1)$$

where

P = pressure

T = absolute temperature

A = constant corresponding to the heat of sublimation

R = universal gas constant

This relationship and the data presented in Figure 15 are sufficient to characterize the ammonia/zeolite system. A maximum zeolite temperature of 120°C was arbitrarily selected. This temperature would be necessary to

pressurize the system during propellant flow at complete expulsion. The ammonia pressure at these conditions is 2.84 psia (142 torr). From Figure 15 the weight of ammonia adsorbed per gram of zeolite of this end point is 0.0300 gm. The weight of ammonia available per gram of zeolite is 0.0205 gm. The total weight of zeolite to supply the 0.570 gm ammonia is 28 gm.

5.[illegible].2 System Dynamics Analysis

Dynamic response of the system determines the time for the system propellant feed pressure to change from one level to the other. Turn-ON time is the time required for the feed pressure to increase from the no-flow level to the full-flow pressure control level. Turn-OFF time is the time required for the pressure to decay from the flow to the no-flow level. Except for tightly bound monolayers, the adsorption and desorption of vapors from zeolite is an extremely rapid process (reference 5-2). Therefore, because of the temperature dependence of the pressure over the zeolite, the pressure response characteristics of the system are a direct function of the system thermal response characteristics.

Factors that influence the thermal response of the system are:

- Heat capacities of the zeolite, heater element, and associated structural material of the zeolite canister
  - Heat of adsorption and desorption of ammonia
  - Thermal loss from the zeolite canister
  - Power input to the zeolite

The equation that describes the thermal response of the system is:

$$\left[\sum_i \left(C_{p_i} M_i\right) + \frac{dm}{dT} A\right] \frac{dT}{d\theta} = q_{in} - q_{Loss} \qquad (2)$$

where

C_p = specific heat

M = mass

m = mass of ammonia

T = temperature

A = Adsorption heat

θ = time

q_{in} = power input

q_{Loss} = thermal loss rate

Subscript i refers to the ith component of the zeolite canister. The term $\left[\sum_i (C_{p_i} M_i)\right]$ represents heat capacity of the zeolite canister, zeolite, and heater element. This term is essentially constant over the entire operating range of the system. The term $\left[\frac{dm}{dT} A\right]$ represents heat required for desorbing the ammonia per unit temperature change of the zeolite. The change in mass (dm) results in a pressure change (dP) in the pressurizing fluid. The relationship is

$$dm = C_o V \, dP \qquad (3)$$

where

C_o = constant

V = pressurized volume

The pressurized volume, V, is a linear function of the fraction of propellant expelled. Because of this volume variation, the response of the system will change as propellant is expelled. This same condition would exist in a volatile fluid pressurization system. Equations (2) and (3) can be combined and the resulting equation:

$$\frac{dP}{dt} = \frac{1}{AC_o V} \left[q_{in} - q_{loss} - \sum_i (C_{p_i} M_i) \frac{dT}{dt}\right] \qquad (4)$$

gives the relationship between the pressure response and the system thermal characteristics. This equation is valid for both increasing and decreasing ammonia pressure. The relationship between temperature and pressure can be determined from the data in Figure 16, the system dimensions, and the zeolite mass. When the system is filled with propellant, the relation $\frac{\Delta P}{\Delta T}$ for the turn ON and OFF cycle is approximately 0.045 psi/°C. At complete expulsion, the same relationship is 0.035 psi/°C. These values are based on the assumption that the zeolite bulk is at an isothermal condition. The pressure response of the system is then

$$\frac{dP}{dt} = \frac{1}{\left[AC_o V + \frac{1}{K(V)} \sum_i (C_{p_i} M_i)\right]} (q_{in} - q_{loss}) \qquad (5)$$

where K(V) is the functional relationship of $\frac{\Delta P}{\Delta T}$ with respect to the pressurized volume, V. As can be seen from equation (5), the pressure response

characteristics of the feed system are influenced by:

- Stored propellant volume
- Pressurizing chamber void volume
- Thermal mass of the zeolite canister
- Power input
- Thermal loss rate
- Quantity of zeolite

For the assumed system design, the values of $\frac{dP}{d}$ are:

- Full tank

$$\frac{dP}{d} = 10.8 \times 10^{-4} \ (q_{in} - q_{loss}) \quad \text{psi/sec}$$

where

P = pressure in psi

= time in seconds

q_{in} = power input from heater in watts

q_{loss} = thermal loss rate from system in watts.

- Empty tank

$$\frac{dP}{d} = 6.79 \times 10^{-4} \ (q_{in} - q_{loss}) \quad \text{psi/sec}$$

The thermal loss rate from the system can be adjusted so that it will vary between 2.0 and 2.7 watts over the ambient temperature range of the feed system surroundings and the temperature range of the zeolite. By using a 5 watt heater element, the response characteristics of the system for turn ON and turn OFF are:

- Full tank

  Turn ON - 2.3 to 3.0 minutes

  Turn OFF - 2.6 to 3.5 minutes

- Empty tank

  Turn ON - 3.6 to 4.8 minutes

  Turn OFF - 4.1 to 5.5 minutes

The average power consumed by the feed system is that equivalent to the thermal loss rate, an average of approximately 2.4 watts. Peak power of 5 watts will be used when the heater element is ON.

5.3.3 System Prototype Tests

A series of experiments was performed to determine actual performance characteristics of a zeolite-ammonia pressurization system. These experiments included tests to verify the pressure-temperature adsorption characteristics of the ammonia-zeolite system and the system response characteristics. A schematic diagram of the test layout is shown in Figure 17. Line and ballast volume were calibrated so that the quantity of ammonia stored in them could be determined from a pressure measurement. The line volume was used to represent the void volume in the pressure housing of the feed system when the bellows was filled with propellant. The combination of the line and ballast volumes was used to represent the pressure housing volume at complete propellant expulsion. Although the volumes were smaller than in the actual feed system, the volume ratios were nearly the same and the quantity of zeolite used was scaled proportionally. The ballast volume was 1970 cc, the line volume 630 cc, and the weight of zeolite was 17.1 gm.

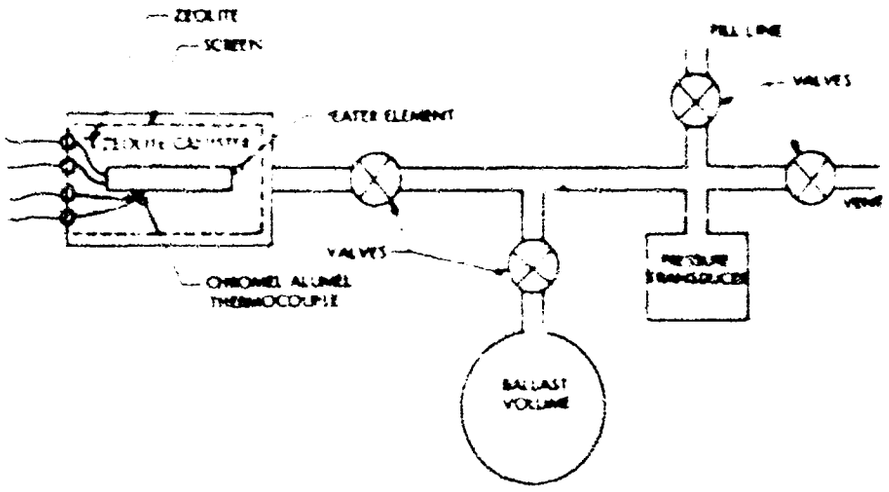

Figure 17. Zeolite Prototype Test Schematic

The results of the adsorption characteristics tests were, within experimental error, identical to the data shown in Figures 15 and 16. There was a difference between the results of the response tests and the calculated response data. The relationship, $\frac{\Delta P}{\Delta T}$, as determined experimentally was

[illegible] psi/°F and was independent of expelled propellant fraction. The calculated values were [illegible] psi/°F for the filled tank and [illegible] psi/°F when the propellant had been expelled. Although agreement between experimental and calculated values of $\frac{dP}{dT}$ is good under the condition of [illegible] propellant expulsion, the variation was large for the full tank condition. This large variation was probably caused in part by some mismatch in scaling the volume for the full tank condition and to temperature gradients in the zeolite. Fins were incorporated in the zeolite canister of the feed system to minimize thermal gradients.

The resulting response characteristic values based on the prototype test data are:

- Full tank

$$\frac{dP}{d} = 7.68 \times 10^{-6} (q_{in} - q_{loss}) \text{ psi/sec}$$

- Empty tank

$$\frac{dP}{d} = 6.36 \times 10^{-6} (q_{in} - q_{loss}) \text{ psi/sec}$$

5.4 SYSTEM COMPONENT DESIGN

A complete feed system was designed, fabricated and assembled using the results of the analysis described in the previous sections of this report.

The initial intent of the colloid feed system fabrication and assembly phase was to produce a demonstration system having the characteristics developed in Section 5.2. The complete design layout is shown in Figure 18.

The bellows dimensions are 9.66 inch OD by 8.56 inch ID (Figure 19). This gives an average storage cross-sectional area of approximately 56 in^2. The bellows material is Inconel 718. The bellows, as delivered, has a surface oxide which was formed during the anneal processing cycle. A complete removal of this oxide coating is not possible without jeopardizing the Inconel 718 corrosion resistance properties. Instead, a hot caustic-permanganate bath is used to remove any loosely adherent oxide. The remaining oxide is a thin, tightly adhering film. This surface condition represents the maximum corrosion resistant state for the bellows material.

The welding of the bellows to the end flanges proved to be a difficult problem. This was due in great part to having too loose a fit between the

Figure 18. Colloid Feed System - Design Layout

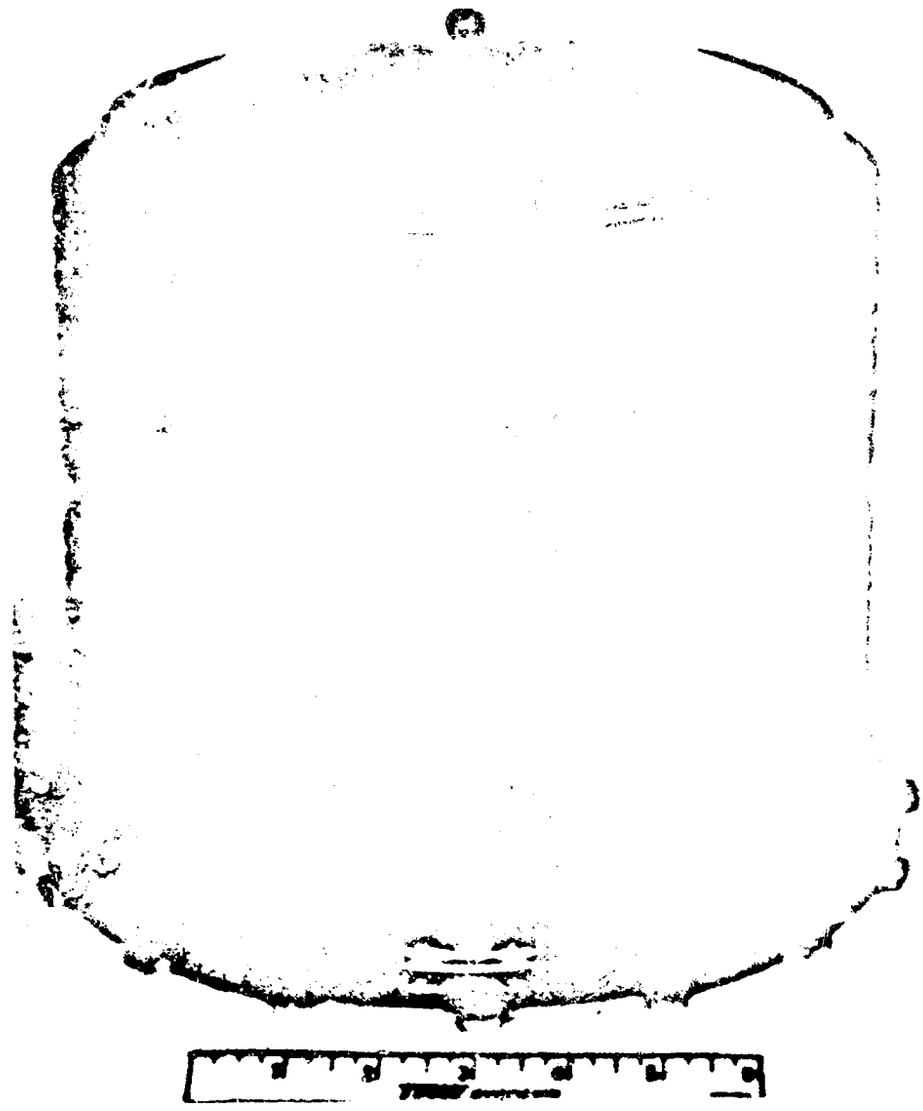

Figure 19. Inconel Bellows

mating parts. It was fortunate that two bellows had been ordered, since repeated attempts to perfect welding procedures resulted in considerable damage to the first bellows. This was after a series of operations including an initial electron beam weld, an attempt to bridge remaining gaps by the use of filler material in conjunction with electron beam welding, a further attempt to bridge the gap [illegible]ding material during a tungsten-inert (TIG) gas weld operation, and finally torch brazing with a gold-nickel alloy. The welding of the second bellows was finally accomplished by the use of an intermediate ring. The bellows was first TIG welded to a ring placed over the periphery of the bellows tip. The ring was then TIG welded to the flange. There was a leak in the area of the final weld; however, it was closed by peening the weld. In addition, the area was covered with torr seal low vapor pressure epoxy resin to ensure the leak would not recur.

The transducer selected for the system has a 0 to 5 psia pressure range with a 5-volt maximum output. It has an approximate 1-volt offset at zero pressure. Although time was not available on the present program, on an actual flight system suitable electrical isolation techniques will be required if a pressure readout is desired.

The squib valve selected has an explosively-operated cam that shears a metal diaphragm. No internal voids are created as a result of actuation. The residue of the explosive actuation is isolated from the propellant by the press metal lit of the cam.

The system response characteristics create no extraordinary demands on the pressure control logic. The control logic consists of a first stage level detector used to drive a switching stage for the zeolite heater element power. The input to the level detector is the output of the pressure transducer which monitors the feed system exit pressure. The level detector operates at two pressure levels, full feed and propellant cut-off pressures. The pressure level change is accomplished by switching the reference voltage to the level detector. It is anticipated that when the feed system is integrated into an actual propulsion system the pressure level control will be referenced to thruster beam current. This will automatically maintain constant mass flow at constant needle voltage.

The zeolite pressurizer assembly is shown in Figure 57. The total charge is 34.3 grams of type 5A zeolite. The canister is 2-3/8 inches long by 1-3/8 inches in diameter. Aluminum is used throughout the assembly. The unit is sealed by TIG welding. The heater assembly consists of a 157-ohm Nichrome V heater element wire packaged in MgO insulation. contained within a 2-inch long by 1/4-inch diameter Inconel sheath. The total weight for the filled subassembly is 0.25 lb.

A schematic of the pressure regulator switching circuit is shown in Figure 58. The circuit utilizes an operational amplifier with positive feedback for voltage level detection. The output of the amplifier is used to drive a two-stage switch which actuates the zeolite heater element. The output voltage of the amplifier is set at either plus or minus 5 volts at the base of the first stage switch, T_1, by the back-to-back zener diodes, D_2 and D_3. The reference voltage on the amplifier at pin 3 is set by both the resistance value in parallel with the zener diode D_1, and the voltage on the base of T_1. For the condition in which the pressure of the feed system is within the required deadband, the output of the control transducer, which is connected to pin 2 of the operational amplifier, will be above the reference voltage at pin 3. The output of the amplifier is a negative 5 volts at the base of switch T_1. With a negative bias, the switch will not conduct. When the feed pressure decreases the output of the transducer will decrease, and the voltage at pin 2 will decrease. When the voltage at pin 2 reaches the value at pin 3, the amplifier output becomes positive. This causes the reference voltage at pin 3 to assume a new higher value which is above the voltage at pin 2. The positive output from the amplifier causes a positive base voltage on switch T_1 and it will conduct. When it is conducting, the base voltage on switch T_2 becomes positive and it also is conducting. This turns the heater element on. The ammonia pressure then rises, thus increasing the pressure and the output signal of the control transducer. The potential at pin 2 of the amplifier will increase until it reaches the new voltage level at pin 3. When it reaches this value, the amplifier output becomes negative, the switches become nonconducting, and the heater element is turned [illegible] With the negative amplifier output, the potential at pin 3 will assume its original lower voltage, which is below that at pin 2. The switching deadband of the circuit is determined by the magnitude of the voltage change at pin 3 for the cases of positive and

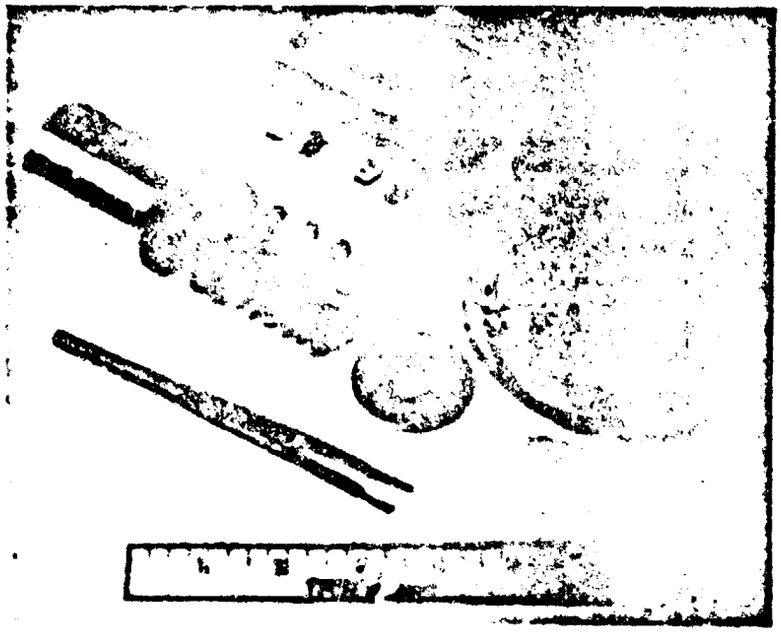

Figure 20a. Zeolite Pressurizer Components

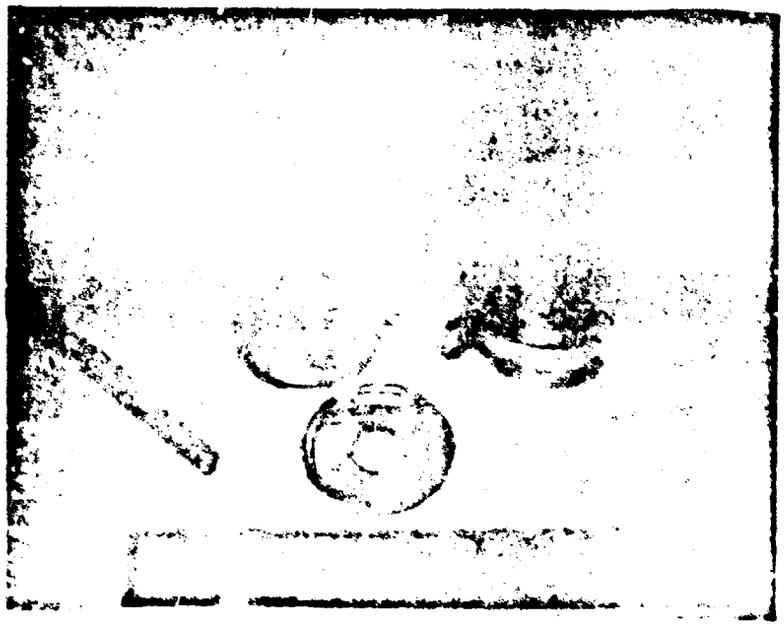

Figure 20b. Zeolite Pressurizer with Zeolite Charge

Figure 20c. Zeolite Pressurizer Subassembly

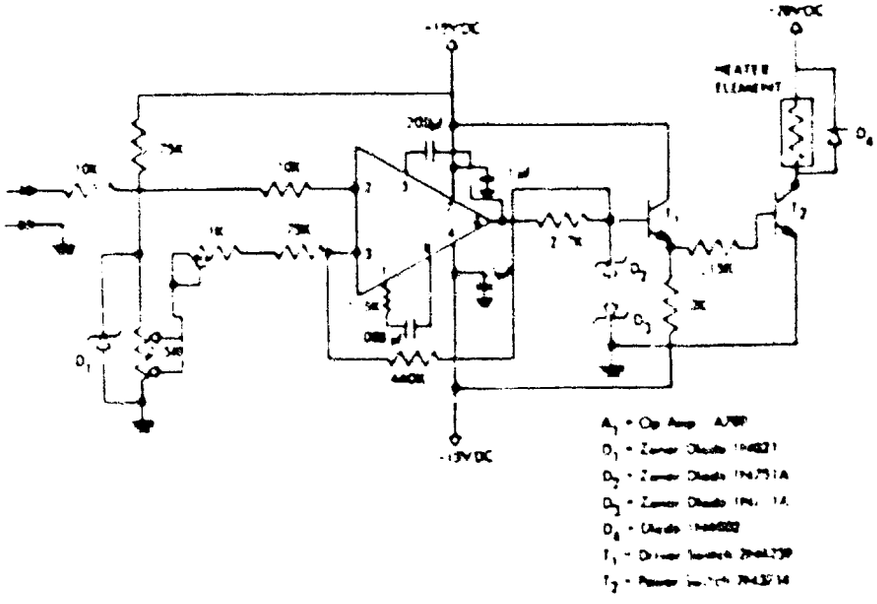

Figure 21. Zeolite Regulator Circuit

negative amplifier output. This voltage differential can be varied by adjusting the 1 K pot in series with pin 3. The pressure levels at which switching occurs are varied by adjusting the pick-up position of the 0.5 pot.

5.5 SYSTEM TEST RESULTS

The dry weight (non optimized) of the system (excluding stand-off insulators and electrical shielding) is 7.5 lbs. The total system volume is 9.8 liters. Figure 22 is a photograph of the assembled system. The system was filled with 5500 cc (equivalent to 17.6 lbs. of propellant) of glycerol, and zeolite pressurizer charged with ammonia. The filled system was dynamically tested during a 2-week period in which it was cycled five times between the full ON (0.5 $\pm$0.03 psi) and full OFF (0.03 $\pm$0.015 psi) positions. The power requirements at this time were 2 watts for the ON position and 1 watt for OFF. However, the response times were longer than originally intended; 6 minutes for OFF-ON cycle, and 12 minutes for ON-OFF cycle. Two factors contributed to the longer times:

(1) The system was designed for operation in vacuum. It was more convenient for laboratory testing, however, to operate on work benches, outside of vacuum, where all parts are accessible. This resulted in a stronger thermal coupling of the zeolite canister to its environment. This situation was later partially corrected by insulating the canister.

(2) A second problem was the gravity head present during ground testing. The normal testing position of the system is such that the zeolite subsystem must provide an additional 0.5 psi pressure compensation, which is approximately equal to the overall design feed pressure. This causes both a greater response time (approximately double) and greater power requirements.

The system was then run through an entire expulsion cycle lasting approximately one month. The test set up is shown in Figure 23. The feed system is shown mounted on a ring stand assembly in the center of the figure. The two 4-liter flasks at the right of the photograph were used to receive the propellant efflux. Since the feed system is referenced to zero absolute pressure it is necessary to maintain the flasks evacuated during the expulsion cycle.

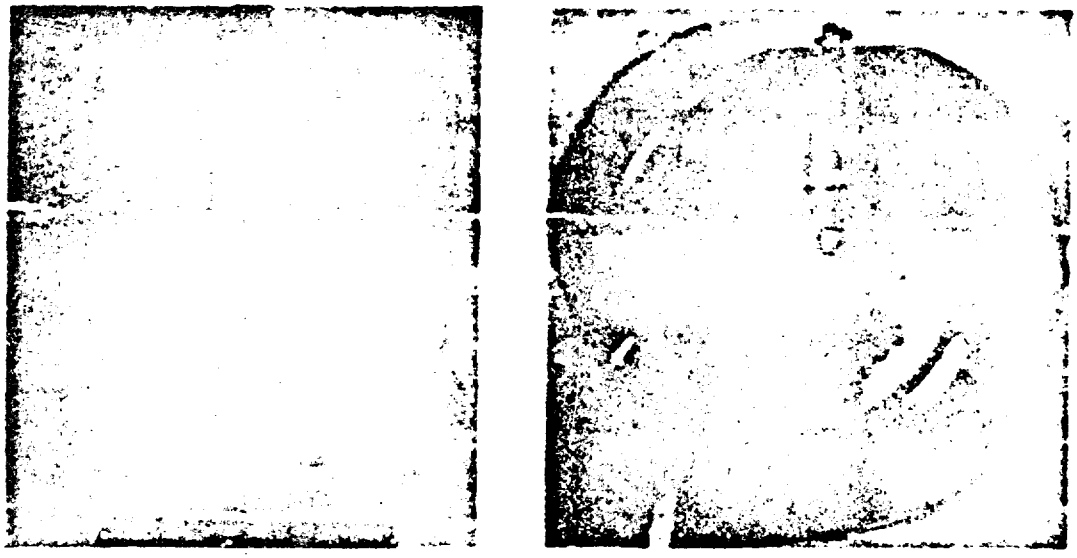

Side View Bottom View

Figure 22. Assembled Feed System

Figure 23. Expulsion Cycle Test

The metal weight and cardboard resting on top of the system were required to minimize convection currents and to hold down the thermal insulation which was inserted to simulate vacuum thermal conditions. The chart recorder at the far left shows the pressure drop caused by an ON-OFF cycle shortly before the photo was taken.

During the test total propellant expelled was 5200 cc. Thus, the system had a 94.5% expulsion efficiency. Twelve ON-OFF cycles were carried out during the test. The time required for ON-OFF cycle varied between 5 and 7 minutes. The OFF-ON cycle time depended on input power and percentage depletion. At full expulsion, the power requirement rose to 13.5 watts for a 16-minute ON time. Future feed system designs will be directed at reducing this value, by further optimization of the zeolite canister design and amount of ammonia loading. Vacuum environmental testing will also be instituted to minimize thermal loss. Moreover, it is presently anticipated that most missions will employ a valve, thus removing the requirement for a rapid cycle time. This in turn allows stringent thermal isolation techniques to minimize steady-state power dissipation.

REFERENCES

5-1 Technical Report AFAPL-TR-68-14, "Attitude Control and Stationkeeping Subsystem Program, Final Report," W. F. Krieve, TRW Systems Group, March 1968.

5-2 The Adsorption of Gases and Vapors, Vol. I, Physical Adsorption. Brunauer, Stephen; Princeton University Press, New Jersey, 1943.

6. MODULI DESIGN AND TESTING

6.1 INTRODUCTION

The main effort in this task was to determine the best approach for covering the 1-micropound to 1-millipound thrust range at a specific impulse range of 1000-2000 seconds and source efficiency greater than 70%. A modular design approach, which emphasized the inherent reliability of colloid propulsion, was chosen. A 36-needle module square array was developed as the fundamental building block for this concept. There were three major advantages to this approach:

1) Scalability. The modular concept emphasizes a major advantage of the colloid thruster concept, viz., its ease of scalability to suit particular thrust level requirements. Thus, the 36-needle module can be a basic building block designed to satisfy a wide variety of specialized mission tasks up through the millipound range.

2) Reliability. Intermodular isolation techniques can be utilized to eliminate the chance of a single needle malfunction jeopardizing the entire system. This is based in part on the knowledge that the initial failure mode of a needle is not a dead short, but, rather, a sudden increase in beam spread, extractor current and needle arcing. Once these warning signals occur, it is possible to prevent further damage by stopping the mass flow, perhaps through the aid of a squib valve.

3) Simplified Fabrication, Development and Test Procedures. All initial development and testing for a given mission can be performed with a single 36-needle module. This results in a considerable easing of fabrication and vacuum system requirements in the earlier stages of the program.

Initially, it was planned to first develop one 36-needle module with a design goal of 2 μ lb/needle thrust, and then build a multiple array of these modules for high thrust level operation. During the course of the program, it was found that the 36-needle module was capable of producing 100 micropounds of thrust. However, a vacuum contamination problem developed which made it necessary to redesign the module to

minimize the contamination-induced leakage currents. This problem, which was a result of backscattered material during prolonged high thrust operation, made the task of prolonged life testing in existing facilities exceedingly difficult as thrust levels were raised. As a result, after discussion between TRW and AFAPL personnel, it was decided to concentrate efforts during the remainder of the program on further development, redesign and evaluation of the basic 36-needle, 100 μlb thrust module. A total of three modules were built, the latter two incorporating extensive design changes based on information gained from the original prototype. These two modules were then tested separately, rather than in tandem, in order to allow life testing of one module to proceed simultaneously with direct thrust measurements of the other. As a result of these experiments, a 1000-hour life test was completed (twice the 500-hour program goal) in addition to direct measurement of the 100-micropound thrust and its correlation with simultaneous time-of-flight measurements (Section 8).

6.2 MULTIPLE NEEDLE EXPERIMENT

In order to test the proposed module electrode configuration at high voltages and high I_{sp}'s for extended periods, and to provide preliminary confirmation of the basic design concept, 6 needles with 63-mil O.D., 53-mil I.D. stainless steel tubes soldered to them were mounted in a 37-needle module. The stainless steel tubes acted as field modifying electrodes. The needles were mounted flush with the downstream side of the extractor. The extractor was a 30-mil-thick stainless steel with no bevel on the extractor holes. This configuration duplicated the needle-deflector electrode conditions when the needle and deflectors were operated at the same voltages but with separate supplies. Under moderate vectoring conditions, the $\pm \Delta V$ applied to the deflectors was small enough so that the above situation, i.e., $V_n = V_{deflector}$, was approximately true. Therefore, this configuration provided a quick, reliable, preliminary test of accel performance and endurance.

This test was finally terminated after 591 hours to free the facility for other experiments. The module performed exceptionally well, operating at 1500 seconds I_{sp}, 80 percent efficiency and 17

micropounds thrust during the entire run with no performance degradation. Time-of-flight data from Run 6903-01 are shown in Figures 24 through 30. Figure 31 is a typical time-of-flight trace made during this run. The needles remained tar free. This was probably the most important outcome of the test. The run indicated that the guidelines developed in the single needle work for needle - extractor positioning and accel configuration are valid and necessary to ensure efficient, long-lived operation. There were two vacuum system accidents during the run, neither of which resulted in any thruster deterioration.

An extractor pattern (Figure 32) caused by the interaction of positive particle sputtering and neutral particle condensation could be seen about each extractor hole. Streaks in these patterns radiated outward from the needle. These streaks were clean areas in the deposits around each hole. They appeared to be due to shadowing by dirt particles lying on the extractor, that had intercepted material produced near the needle tip. This indicated that the area around the needle was the source of a material that enhanced the accumulation of deposits around the extractor hole. Later ionization gauge measurements (described in the following section) of the neutral molecular density in the vicinity of the 36-needle module indicated that the beam fraction not included in the main thrust was less 0.7% of the total mass flow.

The extreme stability of this run made it possible for the emitting jets to remain undisturbed along the needle rim for long periods of time, resulting in a ripple pattern along the needle rim (see Figure 33). This pattern was apparently caused by electrolytic etching of the areas directly beneath the emitting jets. The arrangement of the ripple patterns on the various needles suggests that a jet will shift its position after it has etched a certain depth groove. If this shifting of the jets occurs as supposed, the etching effect will be spread over the entire needle rim, thereby greatly reducing the erosion rate over the needle rim as a whole. The etching may not be prominent on pure platinum. These needles were platinum-iridium. The etching may have been the result of chloride impurities within the sodium iodide bulk, since chlorides are the most electrolytically active materials as far as platinum is concerned. The questions of immediate concern are:

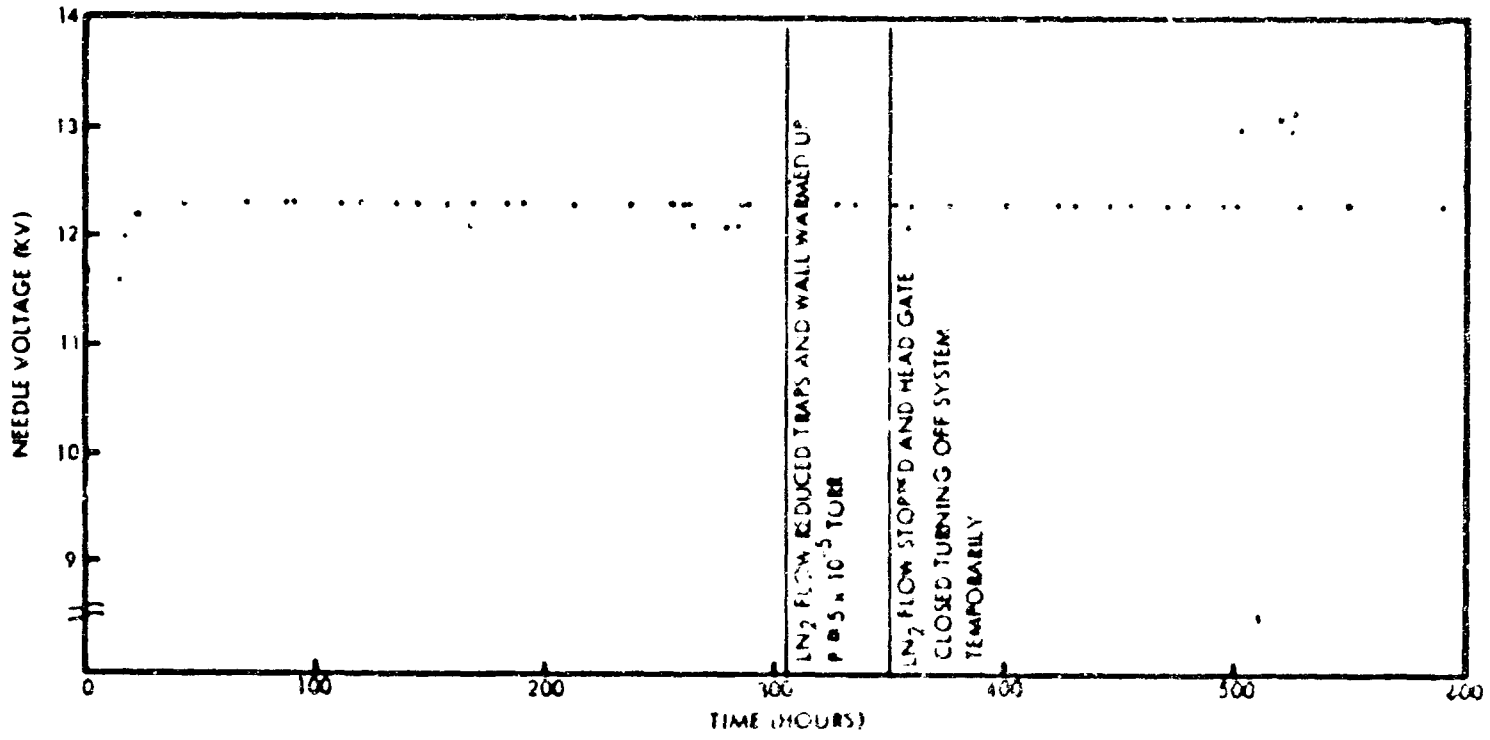

Figure 24. Needle Voltage versus Time Run 6903-01. Note that two vacuum accidents occurred during the life test and are noted on each of the Figures 6-1 through 6-7 at 310 hours. The needle voltage was raised to 13 kv for 24 hours towards the end of the run in order to raise the thrust above 3 μlb/needle at 1500 seconds. This was done from approximately the 510th hour to the 535th hour. During much of this time, the thrust was 4 μlb/needle. The module operated smoothly at this higher voltage and thrust level until the 535th hour at which time it became unstable and consequently the voltage was returned to 12.3 kv and the ṁ reduced. Vex was kept at -1.25 kv.

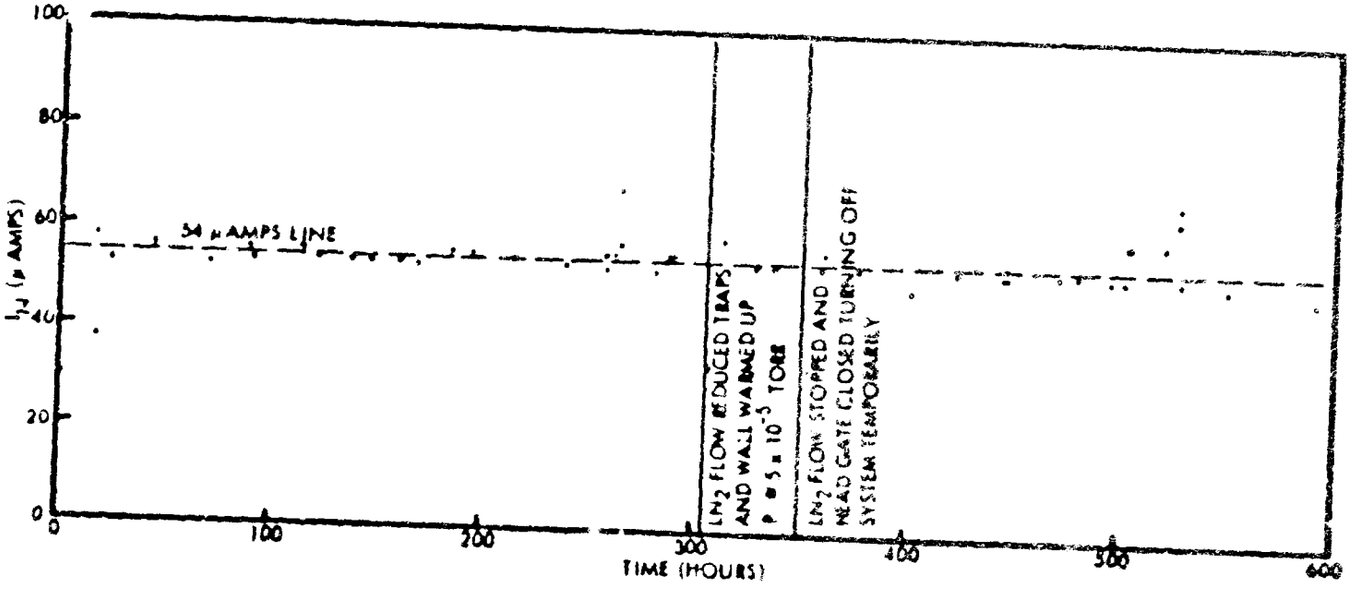

Figure 25. Needle Current versus Time Run 6903-01. Note that at each of the vacuum accidents the needle current dropped to a very low value because of a non-wetting contaminant condensing on the needle tips which caused a much lower $(\overline{Q/M})$

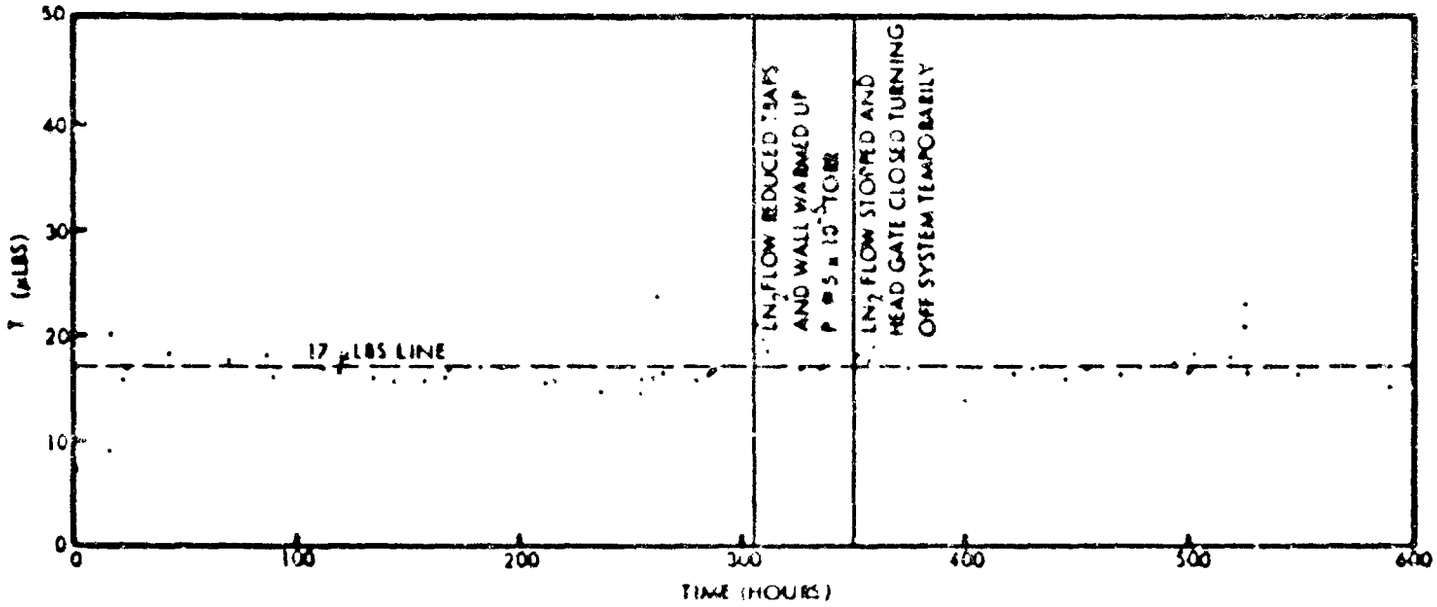

Figure 26. Thrust versus Time Run 6903-01. Six needles were used in the module.

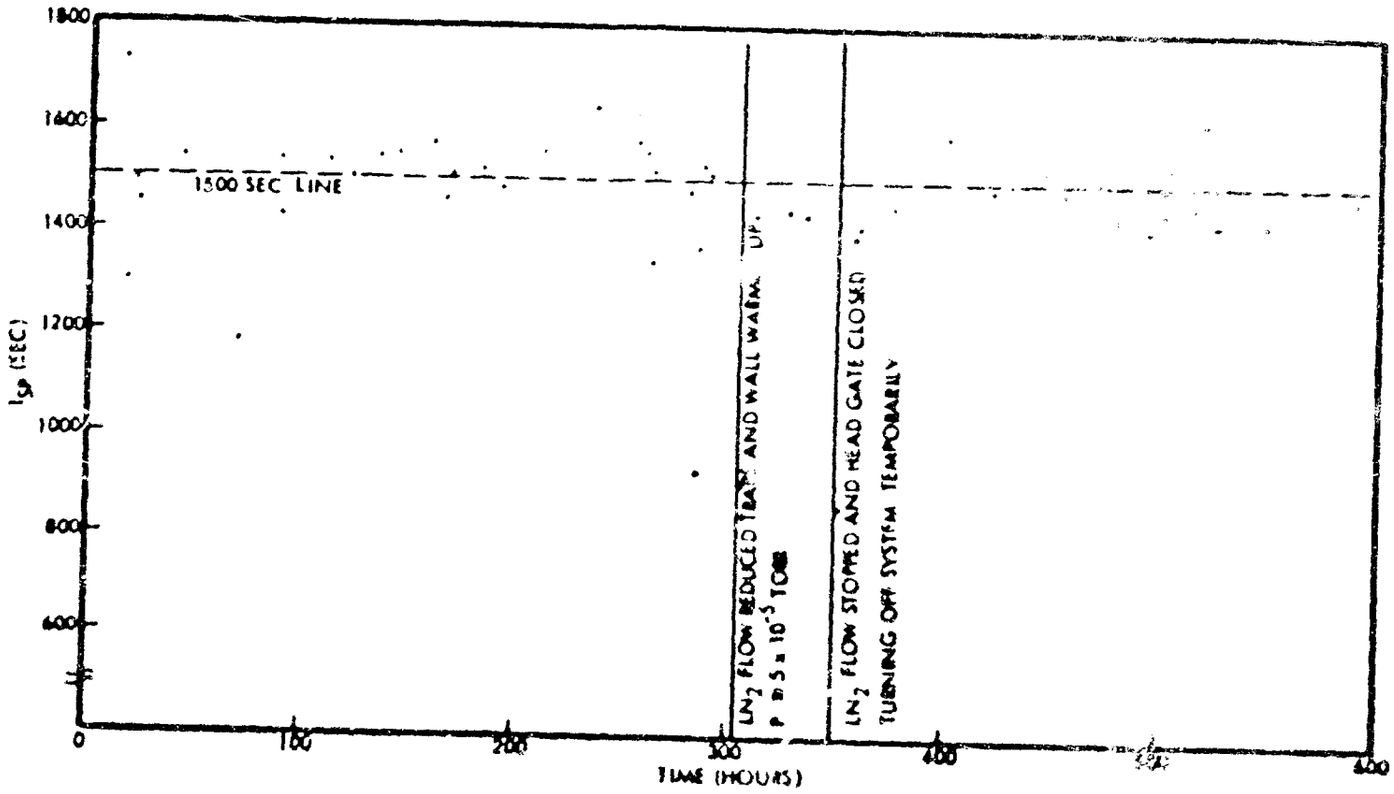

Figure 27. I_{sp} versus Time, Run 6903-01

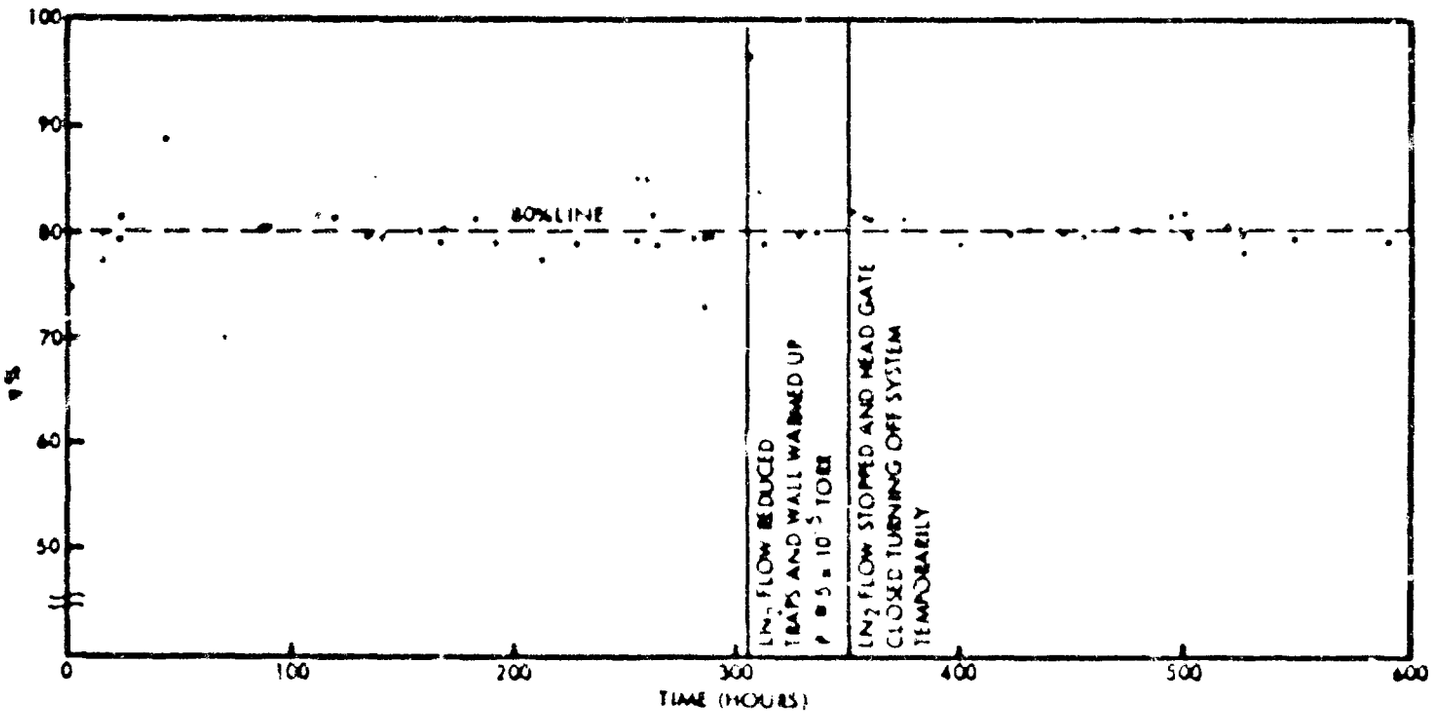

Figure 26. Efficiency versus Time, Run 6903-01

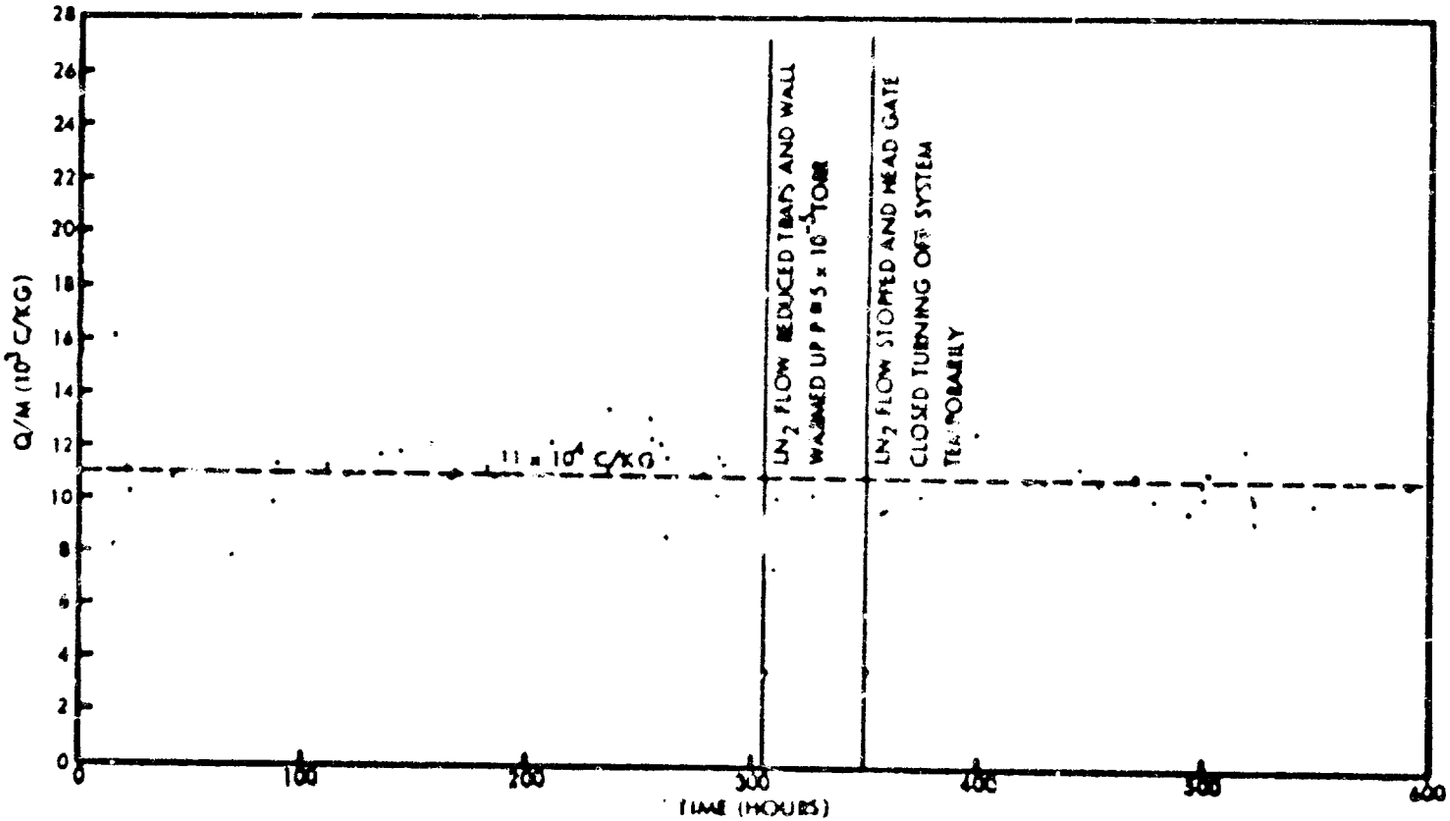

Figure 29. $(\overline{Q/M})$ versus Time, Run 6931-01

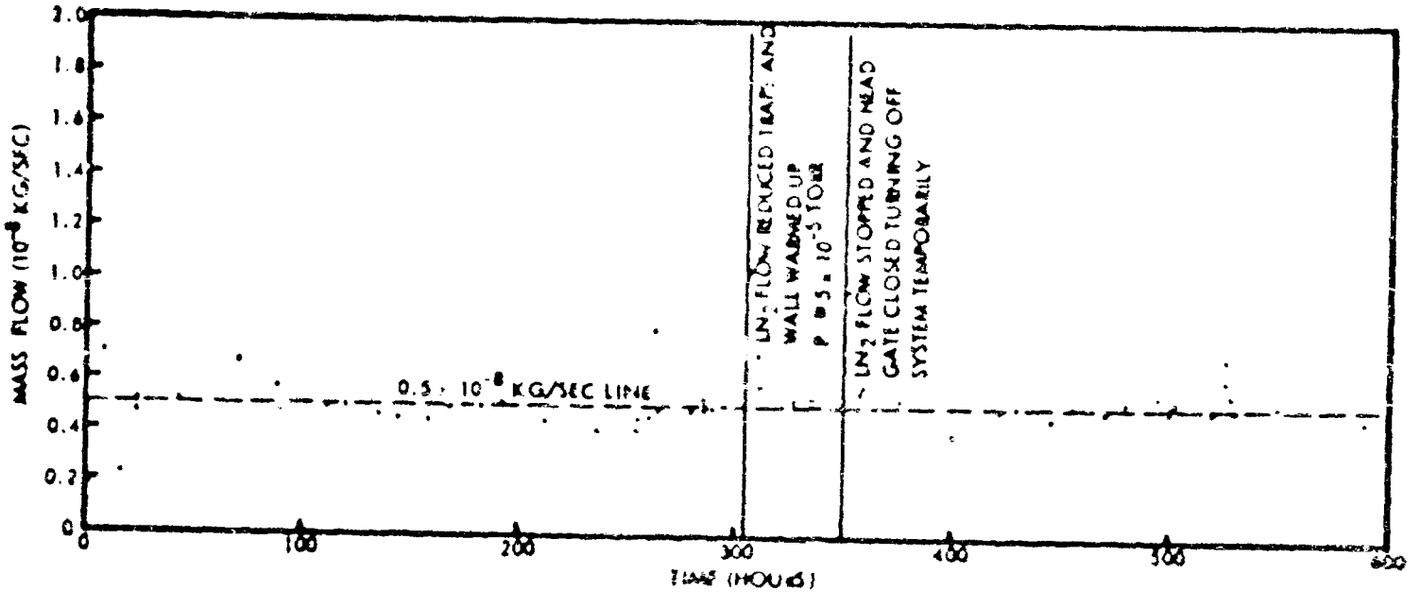

Figure 30. $\dot{m}$ versus Time, Run 6903-01

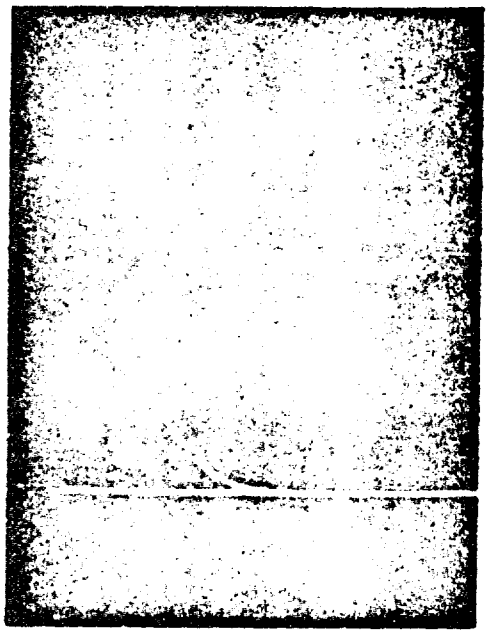

		Voltages	Currents
T.O.F. Data:	I_{sp} = 1520 sec	V_s = 12.3 kv	I_s = 55 μa
	T = 16.9 μlb	V_e = -1.15 kv	I_e = 0.1 μa
	η = 81%	V_c = 0	I_c = 20 μa
	Q/M = 11,200 coul/kg	V_d = Tubes Brazed to Needles	I_d = 0

Figure 31. Typical TOF Trace, 180 Hours, Run 6903-31
(50 microseconds/cm horizontal d = 187 cm)

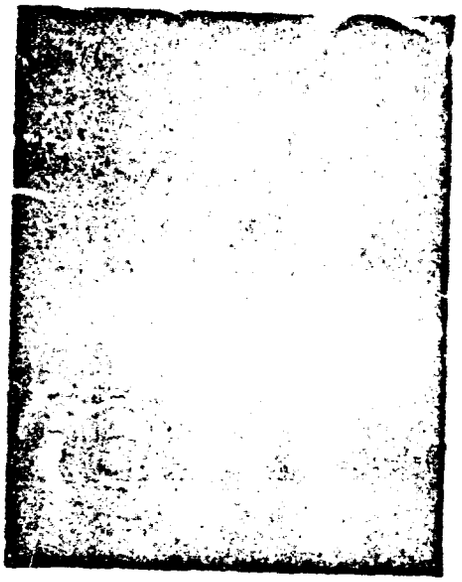

Figure 32. Extractor Pattern around Accel Configuration Needles (Note dark streaks radiating outward from needle tip)

Figure 33. Ripple Pattern in Needle Rim; Magnification 500 X

(1) how rapidly does the etching occur, and (2) how will it affect lifetime? Additional experiments are needed to answer those questions quantitatively but qualitatively it appears that, under similar operating conditions, a 5000 to 10,000 hour life per needle is possible.

6.3 36-NEEDLE VECTORABLE MODULE BASIC DESIGN

Figures 34 and 35 are basic module assembly drawings. Figure 36 shows photographs of the final module. Individual needles are the conventional 4-mil I.D. x 14-mil O.D. TRW platinum-iridium design. The needles are soft soldered into stainless steel needle holders in order to enhance mechanical integrity and thermal control. Ethylene propylene rubber (EPR) O-rings provide individual seals with the plenum chamber. EPR was chosen on the basis of its compatibility with both glycerol and methyl ethyl ketone cleaning solution. Swelling problems caused by the latter resulted in the abandonment of the originally planned Viton seals.

The needles are arranged in a 1/4-inch spacing square array. The square pattern was chosen in preference to the slightly more dense hexagonal geometry in order to simplify thrust vectoring. The vector electrodes are fabricated from 304 stainless steel, 0.063-inch O.D., half cylinders brazed into underlying horizontal steel support bars. Thus, each needle is contained within a pair of concentric parallel half cylindrical vector electrodes. The needle tips, ends of the vector electrodes, and front of the extractor plates are all coplanar to within a few mils. One of the main problems encountered in fabricating the module was that of obtaining accurate alignment of these members. Another critical consideration, discussed later, was the length of the vector plates parallel to the needle axis, since this determined the spacing between the vector electrode support structure and the underside of the extractor plate. Originally, this distance was 1/16 inch, which, under clean vacuum conditions, was easily able to withstand up to 20 kv test potential difference. It was found, however, that after one or two days of actual engine operation, leakage currents were initiated between the two structures due to field emission from the underside of the extractor plate. For this reason, the distance between

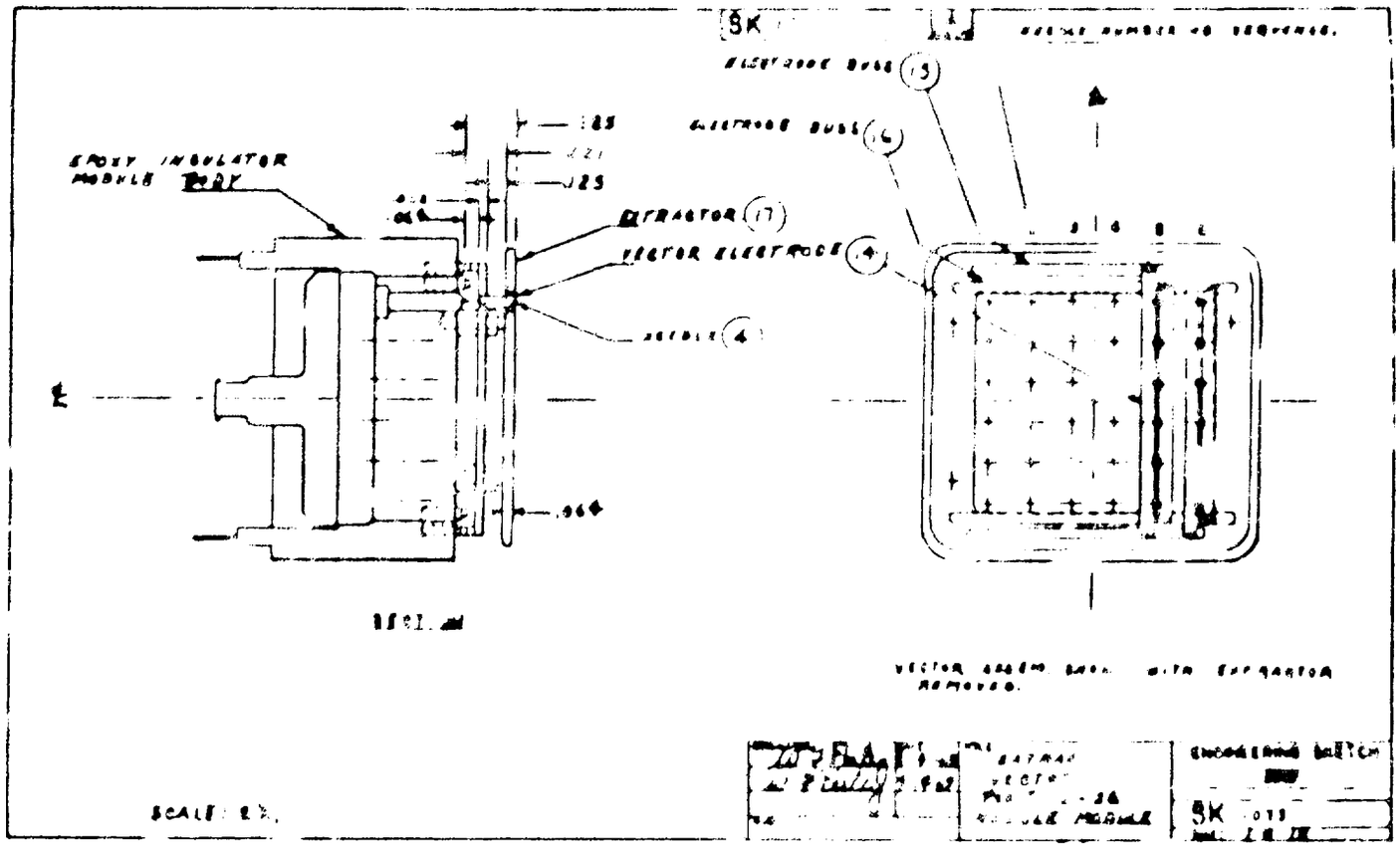

Figure 34. Extractor Vector Position, 36-Needle Module

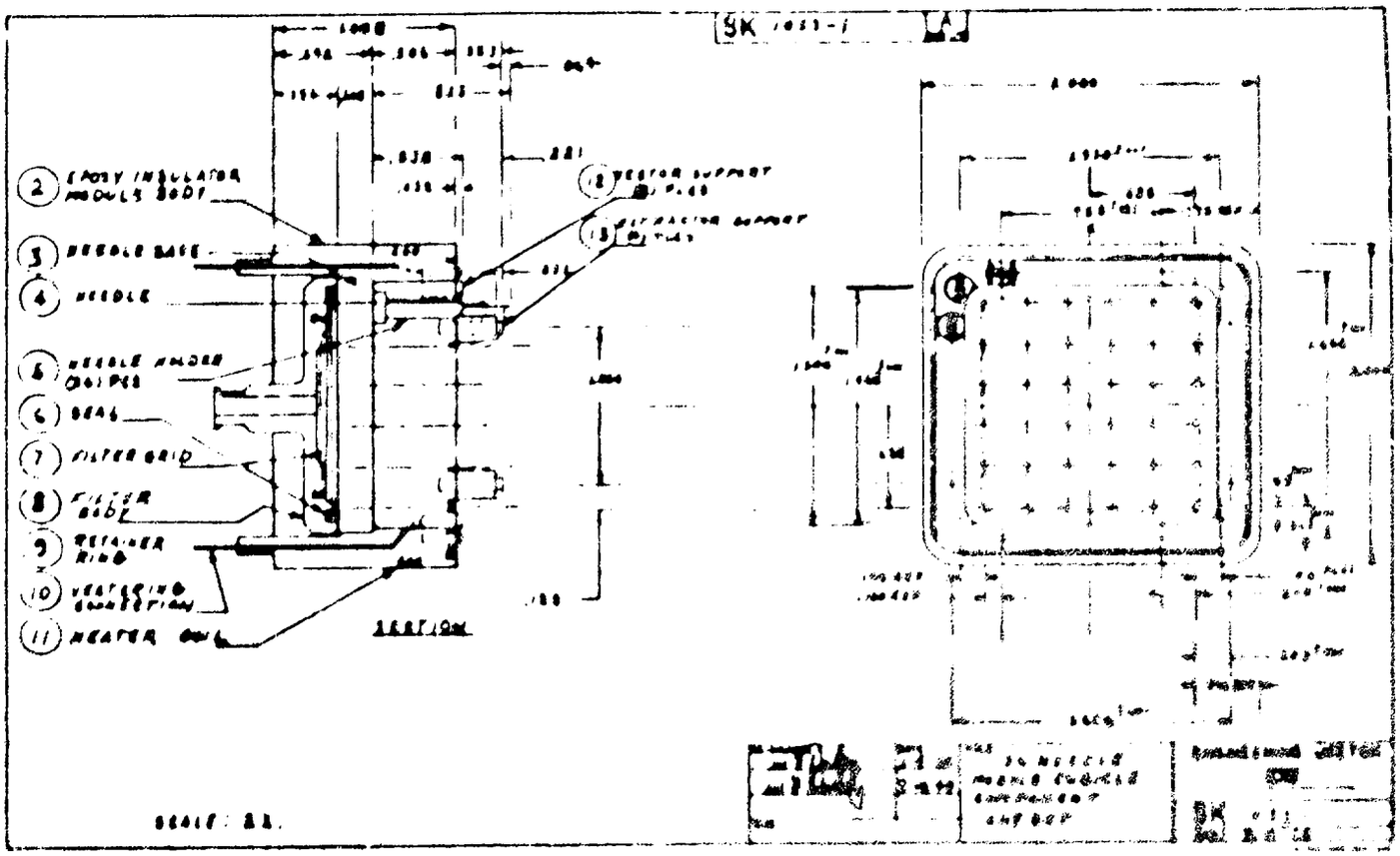

Figure 33. 36-Needle Module, Cable's Component Layout

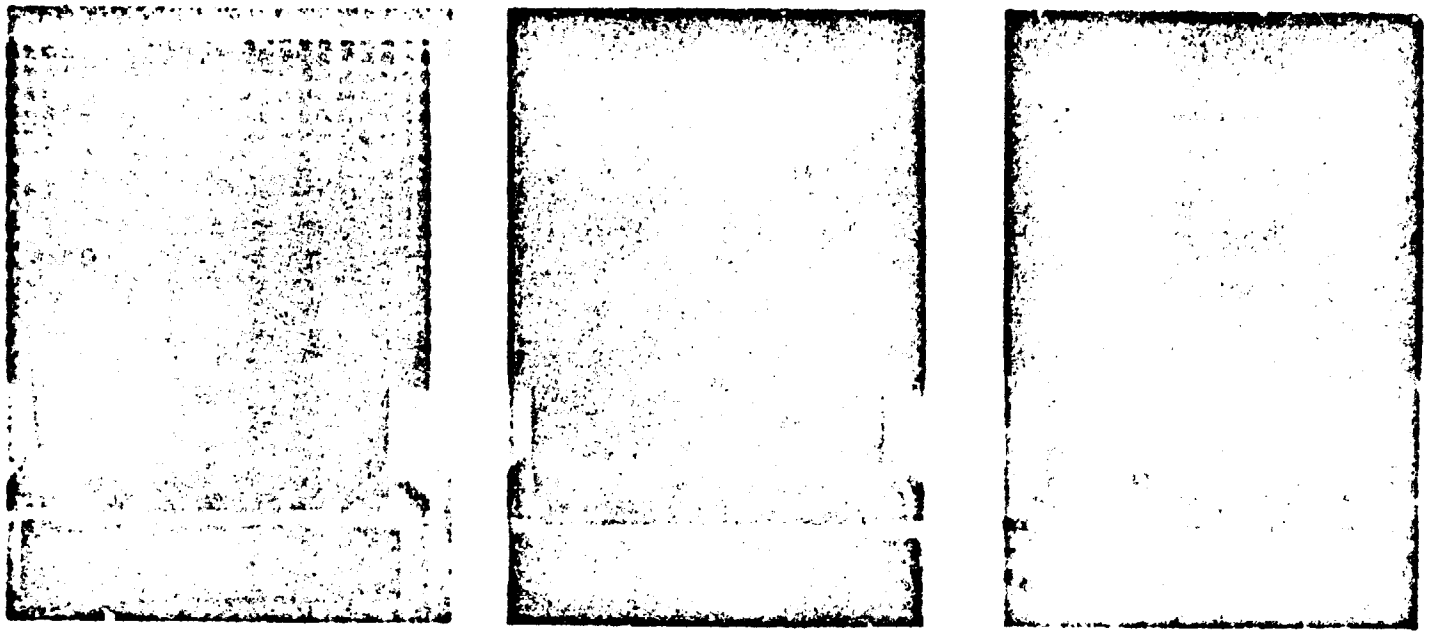

Rear View Front View Side View

Figure 36. 36-Needle Vectored Module

the two was increased to 1/8 inch with a resultant equivalent lengthening of the vector electrode plates. This also required redesign of the module holders, base plate and overall module support structure to accommodate the new dimensions.

The extractor was made from 0.064-inch-thick, 21-6-9 stainless steel, which was selected in the design revision because of its suitability for electropolishing. This was deemed desirable in order to minimize extractor surface roughness in a further attempt to solve the field emission problems. The original extractor utilized 0.040-inch-thick, 304 stainless steel.

The module was potted in an epoxy support base which also encapsulated the extractor and vector electrode structural support posts and high voltage feedthroughs. A thermistor temperature sensor and 10 ohm thermal control heater elements were also potted within the structure. For this reason, Emerson and Cuming Stycast 2850 FT, a special purpose thermally conductive electrically insulated casting resin, was employed as the potting compound. This material has a thermal conductivity of 10.7 Btu/ft^2/hr/$^\circ$F/in, electrical resistivity of 5×10^{14} ohm-cm at 77°F, and dielectric strength of 280 volts/mil. Less than 1/2 watt heater power was required to maintain the module at operating temperature when using an LN_2 shroud.

The modal plenum chamber was a two-part demountable structure which allowed disassembly for cleaning and also for insertion of an internal Millipore filter and subassembly.

6.3.1 Module Performance

6.3.1.1 Preliminary Runs

The first 36-needle vectored array experiments took place in a 4x8 foot chamber which utilizes a 10-inch diffusion pump system. This allowed an assessment of the vacuum loading effects on a 10-inch pumping system and a basis for comparison with later tests in a newly installed 24-inch system, in addition to providing preliminary module operation data and identifying trouble spots.

The first time the module was turned on, it was allowed to run for 2-hours. Discharges at the rear of the module prevented exceeding 15 kv needle voltage during that time. The trouble was diagnosed as

electron streaming around to the high voltage connections at the rear of the module. The front of the module, however, was extremely quiet. No needle arcing was observed, and operation was very smooth when the back end was quiet. After 2 hours, it was decided to terminate the test, open the vacuum chamber, and install a more complete baffle around the module.

The module was removed from the chamber, cleaned and reinstalled. After modifying the test system as described above, a new run was initiated. This run, which was allowed to proceed for approximately 30 hours, was again plagued by arcing at the rear of the module. Once again, performance in the front of the module was extremely smooth; no arcs observed. Most of the efforts during the run were devoted to isolating causes of the breakdown problems. It soon became apparent that discharges were occurring between the main high voltage lead and the grounded thermocouple wires.

In addition to causing erratic needle voltage behavior, these discharges prevented adequate thermal control. There were also discharges between the deflector leads and the ground shield screen encasing the rear of the module. The extractor lead feedthrough was also breaking down. Fortunately, these were all relatively straightforward problems required, as later tests proved, more stringent insulation and spacing requirements for the various lead wires inside the vacuum system.

Although most of the efforts in this run were devoted to chasing down the above problems, three time-of-flight photos were taken and the results are presented below.

	4	5	6
V_n(kv)	9.8	10.5	11
V_x(kv)	-1.5	-1.0	-1.5
I_n(ma)	370	350	300
P(in. Hg)	1.0	1.5	0
I_x(μA)	2	.5	0
I_{def}(μA)	0	0	0
η(%)	82	82	78
I_{sp}(sec)	1590	1422	1800
Thrust (μlb.)	83	95	65

(continued)	4	5	6
q/m(c/kg)	15,000	11,900	18,000
$\dot{m}$(μgm/sec)	24	30	16.5

The results were roughly in the operating region that had been anticipated, although it was still hoped to exceed 100 μlb. at 1500 seconds I_{sp} once the operational difficulties were cleared up.

The first runs in the 4x8 foot chamber with the 24-inch pumping system achieved 26- and 49-hour durations, during which various performance parameters were measured. The shorter run (4906-07) was terminated because one of the needles was sparking. This failure was later attributed to faulty deflector electrode positioning relative to the needle.

The 49-hour run (6707-01) was terminated because of extractor-deflector leakage currents. Subsequent attempts to run the module failed due to continued extractor-deflector breakdown during pre-run hi-pot tests. This problem was believed to be caused by some small initial arcing that resulted from buildup of backscattered materials on the extractor surface.

Apart from the leakage problem, the module performed beautifully. Table 6-1 lists the time-of-flight calculations at various operating points. It can be seen that specific impulses up to greater than 2000 seconds were obtained at reasonable thrust levels. The mass utilization efficiencies went a little lower than had been hoped for, due in part to higher than usual operating temperatures resulting from a breakdown in the laboratory temperature controller.

6.3.1.2 Vacuum Loading

During these runs it was found that the best vacuum attainable by the 10-inch system with LH_2 in the shroud was 10^{-5} torr. If we assume complete dissociation of each propellant molecule into seven noncondensible molecules ($4H_2$ + 3 CO), or perhaps five ($2CH_3$ + CO + O_2 + H_2), a mass flow rate of 30 gm/sec at 10^{-5} torr results in noncondensible gas generation rates of the order of 1000 l/sec, which approaches the

Table 6-1. 36-Needle Module Initial Test Time-of-Flight Results

P in. Hg	V_n kv	I_n μa	V_{def} kv	I_{def} μa	V_{xtr} kv	I_{xtr} μa	T °C	I_{sp} sec	I μlb	R μq/sec	η %	q/m c/kg
					Run 6906-07							
1.5	11.4	368	11.4	0	-1.5	0	25	2242	66	14	79	26,000
1	11.4	378	11.4	0	-1.5	2	29	1746	86	22	74	27,000
1	10.8	350	10.8	0	-1.9	2		1935	63	[illegible]	70	24,000
1	10.7	362	10.7	0	-1.9	2	26	1745	70.0	15	70	19,800
1	10.0	420	10.0	0	-2.9	7.5	29	1602	87	25	72	17,000
1	10.0	352	10.0	0	-2.9	6.2	26	1800	63	16	70	20,000
1	11.0	390	11.0	0	-2.9	6.5	26	1940	71	16	70	24,000
1	12.0	422	12.0	0	-2.9	6.5	26	2155	75	16	75	29,000
					Run 6907-01							
2	11.0	352	11.0	0	-1.7	0	26	1380	97	33	75	11,000
1.4	11.5	333	11.4	0	-1.7	0.5	28	1335	93	27	77	12,840
1.5	11.5	262	12	0	-1.7	0.4		1276	79	28	73	9,000
0.8	11.5	220	12	0.5	-1.7	0.5		1520	53	14	69	14,000
2.9	11.5	345	12	0.3	-1.7	0.1	28	1140	120	48	75	7,000
1.1	12	320	12	.5	-1.7	0.5		1690	78	21	75	15,000
1.1	12	320	12	0.5	-1.9	2.0		1705	76	20	74	16,000
1.1	12.2	302	12	0.5	-1.9	1	26	1813	64	16	69	19,000

overall pumping speed of the 10-inch system (~ 2000 l/sec). Thus, the pumping speed requirement and propellant mass flow correlated as anticipated. Subsequent module tests in the new 24-inch pumping system, which has approximately 4-1/2 times greater pumping speed, achieved 1.8×10^{-6} torr, thus providing further correlation.

As a measure of the ambient plasmas created within the chamber under these operating conditions, positive voltage biases were applied to the upper baffle plate through which the thruster fired. The resulting volt-ampere curve is shown in Figure 37.

6.3.2 Leakage Current Experiments

At this time an extensive program was initiated to diagnose and prevent drain currents between the extractor and the vector electrodes. The following facts were uncovered. No current was present before the run, even when voltages 50% in excess of operating values were applied for many hours. Once the drain currents began, they increased somewhat with voltage. They also remained at quite low voltages. The current fluctuated about a value that increased with time. There were occasional large current increases followed by an abrupt drop back to the lower mean value. Changing the back-scattered material from the collector by a factor of four (by moving the collector closer) caused no correlated change in these currents.

One device that was found to decrease, and even temporarily stop, these currents was to admit a high gas pressure of about 1×10^{-4} torr into the system. At this pressure, about one out of every thousand electrons in transit would create an ion which could come back and alter the negative electrode by sputtering so as to render it nonemitting. Burn marks on the vector electrodes, a faint blue fluorescence, a bright fluorescence were willemite was painted on the electrodes, and the distribution of current between the two vectoring electrodes with applied voltages, all confirmed that the current consisted of electrons from the extractor to the vector electrodes and sometimes a small current to the manifold. This electron current was field-enhanced, but in no way followed the Fowler-Nordheim law for field emission. Two explanations are possible: the current

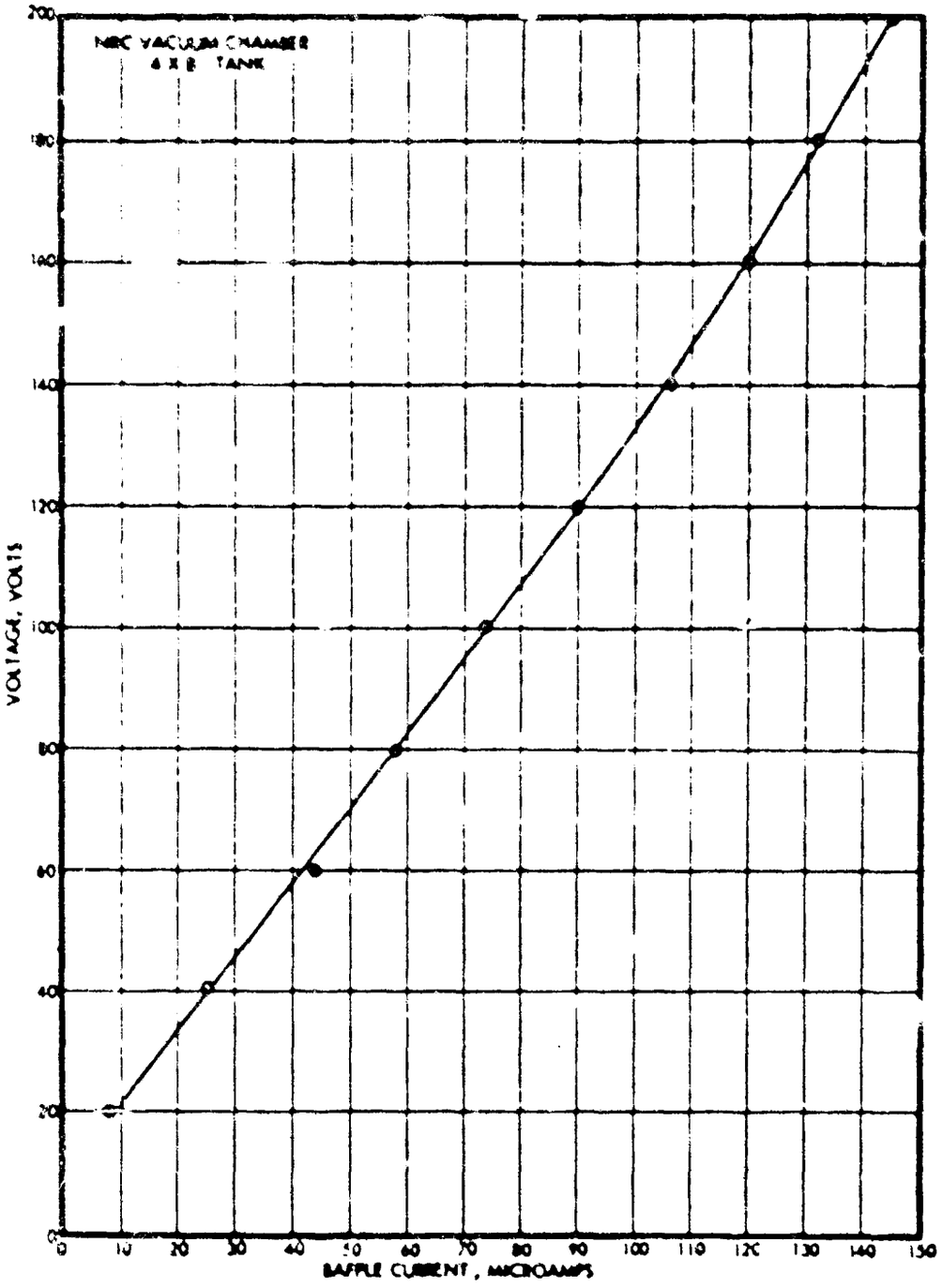

Figure 37. Run 6906-05, Baffle Current versus Applied Bias Positive Bias

might have consisted of thousands of smaller currents, each of which individually increased as predicted by the Fowler-Nordheim law but burned themselves out (without initiating an arc) to be replaced by another source at a higher voltage; or the field-emitting points were poor conductors and the IR drop reduced the field, thereby stabilizing the current. The latter view is in accord with an observation from single-needle AC work; it was observed often, that after AC operation when the needle was dry due to either a needle blockage or the fluid having been rapidly evaporated out of the end of the needle by a discharge, field emission occurred during negative voltage peaks. These field emission currents disappeared and were replaced by normal needle current when the liquid propellant again wetted the tip of the needle. If there was a connection between these two currents, it was that remnants of the propellant on a negative electrode in a high electric field produced, quite faithfully, electron currents.

In an attempt to prevent this current, efforts were made to smooth the negative electrode by careful mechanical and electrical polishing. It was found that electropolishing the original 304 stainless steel extractor resulted in considerable pitting. For that reason, a change was made to the small-grained 21-6-9 stainless steel. Also, some experiments were performed to determine if changes in the mechanical polishing procedures could improve the subsequent electropolished finish. These, however, were unsuccessful.

Since roughening by micro-arcs has also been observed, experiments were performed with copper extractors, which could be easily fabricated and electropolished in addition to having a higher thermal diffusivity which would lessen the localized damage due to inadequate heat dissipation. This improved the situation, but did not completely eliminate the drain currents. The main purpose of these experiments was to look for a correlation between the initiation of breakdown and organic contamination of the electrode surfaces.

The entire module, including the copper extractor, was inserted into an ultra-high vacuum ion pumped system which was free of any pump oil contamination. It was found that full voltage could be maintained prior to introduction of glycerol into this system. No leakage current

was observed.

The thruster was then reinserted into the regular 24-inch diffusion pump system for a performance check. After a short period of operation, the breakdown began once again. The thruster was then pulled out, and reinserted into the ultra-high vacuum system with only minimal cleaning being performed. It was found that the thruster could no longer stand high voltage and that the breakdown problem initiated in the previous test continued.

The module was then removed and thoroughly cleaned of all contamination and once again tested in the ion pumped system. It was found that it could now successfully withstand high voltage. A small thimble of glycerol was then placed in the system in the vicinity of the thruster, and after pumpdown, the high voltage test was repeated. In this instance the breakdown phenomenon once again took place, thus indicating that the problem was definitely connected with organic surface contamination.

This problem, which is aggravated by having to test within a confined chamber, will have some impact on future thruster design. The reason it only recently became apparent is connected with the fact that we have become more sophisticated in designing to critical tolerances, higher voltages, and more stringent performance demands. We have, in fact, begun to push the limits of technology in this area. Previous designs required only 8 kv, 1000 seconds impulse, no vector electrodes, and were not as highly optimized with respect to volume and weight requirements. The original 36-needle design was an attempt to push all aspects of this technology to its limits and, as such, conformed very closely to conventional requirements for avoiding high voltage vacuum breakdown. It is now apparent that an extra margin of safety is required to compensate for the deleterious effects of organic contamination. For this reason, the module was redesigned to provide larger tolerances in these critical areas.

6.3.3 <u>Measurement of Sideward Emission Glycerol From a Colloid Emitter</u>

Some evidence has indicated the possibility of appreciable

glycerol emanating sideways from a colloid engine. Carbiding of filaments at various orientations with respect to a single needle has been compatible with this hypothesis. Extractor deposition patterns have enforced the supposition. Tar formation on the central needles in an array was another possible indication of high atom density in front of the engine in accord with glycerol evaporation.

To further investigate this point, the glass tubulation of an ionization gauge was positioned within an inch of the center of an operating 36-needle module. It was expected that an increase of gauge reading of about 1×10^{-5} torr would result when the tubulation was moved to this position, due to the expected glycerol arrival rate. The change observed was only about 2×10^{-7} torr. This suggests that the glycerol side loss is in reality practically nonexistent, since analysis of the pumping speed of the tube, cracking rates of the filament of the gauge, and gauge constants for CO and H_2 suggest that the gauge reading will be roughly twice the equilibrium pressure associated with the arrival rate. This point was checked in a separate experiment where the gauge and its tube were placed immediately above a pool of glycerol. In this instance, the ionization gauge response to the normal glycerol surface evaporation was clearly evident.

The 2×10^{-7} torr observed with the module was thus equivalent to an arrival rate of $2 \times 10^{13}/cm^2/sec$. Assuming a constant density hemispherical emittance, the total efflux would be about 4.10^{-4}/sec or 6×10^{-8} grams/sec. The total $\dot{m}$ is ~ 36×10^{-6} grams/sec, so the neutral glycerol efflux is probably less than 1/6 of 1% of the total mass flow — a negligible value.

6.3.4 1000-Hour Life Test

Two new modules incorporating the previously discussed design changes were built. This allowed thrust measurements (Section 8) to be performed on one thruster while a life test was in progress in the other. The life test was performed in a 4 x 8 system incorporating an Edwards 24" diffusion pump and liquid nitrogen cryowall at the rear of the chamber. Two neutralizers tested with this thruster are

described in Section 4.5 Concurrent thrust vectoring experiments are reported in Section 2.3. A 35-inch-diameter honeycomb time-of-flight collector was placed 1.92 meters from the module. The suppressor bias was -20 volts and the screen +12 volts throughout the test. Table 6-2 lists the time-of-flight results obtained at various times during the test.

For the first 180 hours, the thruster performed perfectly. The performance improvement due to the design changes was clearly apparent. Module operation was extremely stable, with no trace of flashing, arcing or needle glow at the front. Over the first few days, the thruster was gradually brought up to its nominal 100-micropound thrust range. This was done slowly out of caution rather than being due to a lack of thruster response. It was possible to attain 1500 seconds I_{sp} at less than 11-kv voltage. Extractor currents of the order of 1 microampere or less were drawn during this period. Time-of-flight efficiencies were of the order of 70%. It was found during this period that the best operation was obtained at a module temperature of 27°C. After 180 hours, high leakage currents appeared between the extractor and bottom vector electrodes. The current meters for both these electrodes were pegged full scale (25 μ amp). While this was a considerably longer trouble-free duration than had been previously attainable, it was evident that the leakage problem still existed.

At this point, three steps were taken to cure the problem. Firstly since previous experience had demonstrated that increased vacuum pressure reduced the drain currents, a deliberate leak was used to raise the pressure to 2×10^{-5} torr, a factor of ten increase. Secondly, the feed pressure was cut in half to 1" Hg. Thirdly, the beam was vectored by lowering the lower electrode bias voltage, thus decreasing the potential drop between the extractor and deflector to 9 kv total. These steps not only produced an immediate reduction in the drainage currents, but also had a cumulative beneficial effect. Unfortunately, the tungsten neutralizer, which had been inadvertently left running, was burned out by the added gas. By its 189th hour of the test, the vacuum was restored to the low 10^{-6} torr range and per-

Table 6-2. 1000-Hour Test Data

Time Sec	[illegible]	V_o kv	I_o amp	$V_{def}(V_1/V_2)$ kv	$I_{def}(I_1/I_2)$ amp	V_{def} kv	[illegible] amp	Module Temp °C	Chamber Pressure torr	I_{sp} sec	R Ω/□	F gal	[illegible]	[illegible] g/lb g/sec
1.5	1.5	16.0	330	16.5/16.5	0.0/0.0	-1.0	0.1	35	4×10^{-6}	1403	1.45×10^{-6}	67.6	69.0	15,167
17.0	1.5	16.1	325	16.5/16.5	0.0/0.0	-1.0	0.1	35	1.4×10^{-6}	1707	1.11×10^{-6}	61.0	66.5	20,229
21.7	1.0	16.5	320	11.5/11.5	0.0/0.0	-2.1	0.6	35	1.0×10^{-6}	1560	1.09×10^{-6}	67.0	67.0	16,004
22.1	1.0	16.4	330	11.5/11.5	0.0/0.0	-2.1	0.7	36	2.6×10^{-6}	1562	1.96×10^{-6}	66.0	66.0	16,796
25.0	2.3	16.0	365	16.5/16.5	0.0/0.0	-2.1	1.0	37	2.2×10^{-6}	1337	1.05×10^{-6}	69.6	71.2	11,977
36.6	2.3	16.0	365	16.5/16.5	0.0/0.0	-2.1	1.0	37	2.2×10^{-6}	1304	2.05×10^{-6}	66.0	71.9	13,000
41.3	2.7	16.2	330	11.0/11.0	0.0/0.0	-2.1	0.5	37	2×10^{-6}	1400	2.03×10^{-6}	71.0	70.6	17,231
43.6	2.3	16.0	365	16.5/16.5	0.0/0.0	-2.1	0.0	37	2.2×10^{-6}	1305	2.03×10^{-6}	65.0	75.0	12,000
45.0	2.2	16.3	465	11.0/11.0	0.0/0.0	-2.1	0.0	37	2.3×10^{-6}	1445	2.10×10^{-6}	96.5	73.4	17,54
50.3	2.3	16.3	495	11.0/11.0	0.0/0.0	-2.1	0.0	37	2.3×10^{-6}	1415	1.96×10^{-6}	95.0	70.0	13,246
63.7	2.2	16.3	460	11.0/11.0	0.0/0.0	-2.1	0.0	37	2.1×10^{-6}	1430	2.02×10^{-6}	92.5	70.0	13,700
71.0	2.3	16.2	465	11.0/11.0	0.0/0.0	-2.1	0.5	37	2.1×10^{-6}	1405	2.11×10^{-6}	90.5	71.6	13,320
71.5	2.2	16.5	415	11.5/11.5	0.1/0.0	-2.0	0.5	37	2.3×10^{-6}	1430	2.17×10^{-6}	97.3	70.3	13,305
72.9	2.0	16.5	380	11.5/11.5	0.1/0.0	-2.0	0.5	38	2.5×10^{-6}	1463	2.04×10^{-6}	90.5	71.3	15,040
74.0	2.0	16.5	430	11.5/11.5	0.1/0.0	-2.0	0.6	38	2.4×10^{-6}	1434	2.10×10^{-6}	500.3	73.3	13,210
76.1	2.0	16.5	430	11.4/11.4	0.1/0.0	-2.0	0.6	37	2.6×10^{-6}	1454	2.10×10^{-6}	99.3	75.6	13,341
96.3	2.0	16.3	430	11.4/11.4	0.1/0.0	-2.0	0.6	36	2.4×10^{-6}	1443	2.14×10^{-6}	98.5	71.3	13,305
98.6	2.0	16.4	430	11.3/11.3	0.1/0.0	-2.0	0.6	30	2.0×10^{-6}	1435	2.10×10^{-6}	99.0	72.5	13,344
121.6	2.0	16.4	432	11.3/11.3	0.1/0.0	-2.0	0.6	37	2.3×10^{-6}	1443	2.08×10^{-6}	96.7	[illegible]	13,040
146.6	2.0	16.4	433	11.4/11.4	0.1/0.0	-2.0	0.7	37	2.0×10^{-6}	1413	2.10×10^{-6}	100.3	[illegible]	12,950
161.5	2.0	16.3	433	11.3/11.3	0.1/0.0	-2.0	0.7	37	2.4×10^{-6}	1382	2.16×10^{-6}	100.3	70.6	12,350
181.6	2.0	16.4	430	11.3/11.3	0.1/0.0	-2.0	0.7	37	2.4×10^{-6}	1433	2.08×10^{-6}	98.5	71.5	13,040
186.6	2.0	16.3	433	11.3/11.3	0.1/0.0	-2.0	0.7	37	2.0×10^{-6}	1320	2.00×10^{-6}	96.5	73.3	14,020
196.7	2.0	16.4	430	11.3/11.3	0.1/0.0	-2.0	0.7	37	2.4×10^{-6}	1403	2.02×10^{-6}	97.5	71.0	[illegible]
200.3	1.1	16.0	366	6.0/16.4	4.0/1.0	-1.0	11.0		1.2×10^{-6}	1730	1.34×10^{-6}	60.0	57.0	21,000

Note: $V_1/V_2(I_1/I_2)$ refer to upper and lower deflector electrodes, respectively.

Table 6-2. 1000-Hour Test Data (Continued)

Time Hrs	P Torr	V_a kv	I_a ma	$V_{def}(V_1/V_2)$ kv	$I_{def}(I_1/I_2)$ ma	V_{def} kv	I_{def} ma	Module Temp °C	Chamber Pressure mm	I_{cp} ma	N kg/mm	T °K	η %	η/η_0
215.7	1.8	9.0	436	7.3/10.1	0.6/0.0	-1.6	2.5	28	2.0×10^{-6}	1521	3.36×10^{-6}	96.6	60.0	11.340
218.8	1.5	9.1	425	7.3/10.1	0.6/0.0	-1.6	2.1	30	2.6×10^{-6}	1455	2.61×10^{-6}	83.6	60.3	16.250
233.7	1.5	9.1	430	7.3/10.1	1.0/1.0	-1.6	3.0	28	1.9×10^{-6}	1446	2.65×10^{-6}	83.9	60.0	15.830
259.6	1.8	9.7	410	10.1/10.1	0.1/0.0	-1.6	0.5	27	3.0×10^{-6}	1490	[illegible] $\times 10^{-6}$	86.8	59.5	15.250
264.5	1.8	9.6	530	11.0/11.0	0.1/0.1	-1.6	0.5	27	3.0×10^{-6}	1475	2.66×10^{-6}	84.7	60.3	15.730
286.0	1.8	9.2	410	11.1/11.1	0.1/0.1	-1.6	0.5	27	3.0×10^{-6}	1460	2.81×10^{-6}	87.3	67.0	16.170
311.0	1.7	9.7	405	11.1/11.1	1.0/0.2	-1.6	2.5	33	3.3×10^{-6}	1432	3.12×10^{-6}	96.2	68.7	16.890
329.0	1.5	9.7	370	9.6/7.9	2.0/0.6	-1.7	3.0	33	2.2×10^{-6}	1505	1.92×10^{-6}	66.0	69.5	19.130
332.0	0.3	8.2	345	5.6/7.0	3.0/0.2	-1.7	4.0	33	0.5×10^{-7}	1450	0.81×10^{-7}	55.9	57.6	19.500
386.6	1.3	8.5	325	7.3/9.6	2.3/0.1	-1.6	4.0	33	2.1×10^{-6}	1350	1.80×10^{-6}	64.5	69.2	15.860
404.4	1.0	8.9	394	9.6/7.5	0.6/1.5	-1.0	4.0	27	1.0×10^{-6}	1479	1.39×10^{-6}	76.3	68.6	17.363
462.7	1.3	8.5	325	6.3/7.3	0.0/0.0	-1.4	4.0	3	2.0×10^{-6}	1315	2.19×10^{-6}	64.6	67.8	16.860
480.9	1.5	9.0	350	7.3/10.0	3.3/0.1	-1.7	3.0		2.0×10^{-6}	1365	2.41×10^{-6}	72.8	64.0	16.300
623.6	1.0	9.5	325	7.3/10.0	2.0/0.1	-1.3	4.0	28	1.3×10^{-6}	1715	1.35×10^{-6}	51.1	61.8	34.042
630.6	0.0	8.2	350	7.3/9.8	2.0/0.0	-1.7	4.0	30	1.2×10^{-6}	1629	1.46×10^{-6}	56.1	67.6	30.000
652.8	0.0	9.5	300	7.3/9.5	3.0/0.3	-1.3	3.0	36	1.1×10^{-6}	1516	0.96×10^{-6}	41.8	66.2	30.230
652.7	1.2	8.7	330	7.3/9.8	1.0/0.3	-1.7	4.0			1360	2.36×10^{-6}	76.3	66.3	13.790
676.4	1.5	8.8	360	7.3/9.9	1.0/0.1	-1.7	3.0	36	1.5×10^{-6}	1308	3.17×10^{-6}	96.5	66.5	15.530
687.3	1.1	8.0	360	7.3/10	2.0/0.2	-1.3	3.0	40	2.0×10^{-6}	1425	2.06×10^{-6}	64.5	60.0	16.000
698.0	1.3	8.3	360	7.3/9.8	1.0/0.2	-1.7	3.0			1356	2.50×10^{-6}	75.1	72.5	16.000
364.0	1.1	9.5	385	7.7/10.3	3.0/0.3	-1.7	3.5			1370	3.16×10^{-6}	75.3	70.0	17.000
363.3	1.1	9.6	365	8.0/10.3	1.0/0.2	-1.7	1.0			1153	3.54×10^{-6}	87.3	63.0	18.023
363.0	1.3	9.4	380	10.3/8.6	0.3/0.3	-1.7	0.6			1360	2.64×10^{-6}	86.6	60.1	16.410
364.5	1.1	9.8	380	10.3/7.0	0.3/0.1	-1.3	0.6			1390	2.52×10^{-6}	77.1	60.6	15.983
369.4	1.1	9.0	370	7.0/10.3	0.3/0.1	-1.7	0.5			1460	2.14×10^{-6}	50.9	63.0	17.274
521.5	1.1	9.5	330	7.0/10.3	0.3/0.1	-1.7	0.5			1750	1.30×10^{-6}	37.6	67.1	23.300
526.6	1.1	9.6	320	8.0/0.6	2.3/4.2	-2.0	9.0	30	2.2×10^{-6}	1363	2.07×10^{-6}	63.3	69.0	15.490

Note: $V_1/V_2(I_1/I_2)$ refer to upper and lower deflector electrodes, respectively.

Table 6-2. 1000-Hour Test Data (Continued)

Elapsed Time Hrs	P_{-Hg}	V_a kv	I_a ma	V_{def}/V_1 kv	I_{def}/I_1 ma	V_{def}/V_2 kv	I_{def}/I_2 ma	Ambient Temp °C	Chamber Pressure torr	I_{sp} sec	θ kg/mm	T mlb	η %	P/η w/kg
130.4	1.1	8.7	120	9.2/8.6	4.5/3.0	-2.0	11.3		2.1×10^{-6}	1390	2.00×10^{-6}	[illegible]	70.3	15,360
343.5	1.1	8.7	120	9.2/8.6	5.0/3.0	-2.0	10.0			1430	1.82×10^{-6}	58.1	68.6	16,490
543.9	8.8	9.0	300	9.4/9.0	3.0/4.0	-2.0	9.0			1630	1.34×10^{-6}	47.4	66.3	21,514
560.6	8.7	9.5	143	9.7/9.7	5.0/4.5	-2.0	11.0	29	1×10^{-6}	2130	0.37×10^{-6}	18.9	54.3	30,000
590.1	6.1	9.3	130	9.7/9.6	1.5/3.2	-2.0	7.0	29	0.8×10^{-7}	2430	0.25×10^{-6}	16.5	54.5	47,000
617.0	8.9	8.5	100	9.6/9.6	2.2/3.0	-2.0	5.0	29	1.6×10^{-6}	1495	0.50×10^{-6}	32.3	68.6	18,500
666.0	8.9	8.3	110	8.7/8.6	1.8/1.0	-2.0	6.5	29	1.5×10^{-6}	1433	1.23×10^{-6}	30.0	70.3	17,000
672.5	1.3	9.6	300	8.3/10.0	0.3/2.0	2.0	5.0	29		1600	1.90×10^{-6}	30.1	60.1	19,230
673.0	1.3	9.6	300	8.3/10.0	0.3/2.5	-2.0	9.0	29	3×10^{-6}	1615	1.66×10^{-6}	67.0	60.2	25,650
689.7	2.3	9.6	300	8.4/10.1	1.0/3.5	-2.0	8.0	29	3×10^{-6}	1636	1.98×10^{-6}	[illegible]	68.0	19,000
690.5	1.6	9.6	300	8.3/10.1	0.3/3.0	-2.0	6.5	29	3.1×10^{-6}	1502	2.12×10^{-6}	74.5	60.0	18,630
714.2	1.4	9.6	300	8.3/10.1	0.2/4.5	-2.0	6.0	29	3.3×10^{-6}	1534	2.20×10^{-6}	76.3	60.0	17,430
722.7	1.3	9.6	300	8.3/10.1	0.2/4.0	-2.0	7.0	29	2.2×10^{-6}	1613	2.06×10^{-6}	72.6	60.0	19,120
738.6	1.3	9.6	300	8.3/10.1	0.3/2.5	-2.0	6.0	29	2.3×10^{-6}	1574	2.03×10^{-6}	70.1	63.7	19,630
746.6	1.0	9.6	300	8.2/10.0	1.0/3.2	-2.0	3.0	29		1663	1.20×10^{-6}	45.4	70.0	21,000
761.0	0.5	9.7	270	8.4/10.2	1.5/2.5	-1.7	3.0			2130	0.62×10^{-6}	30.3	66.3	33,130
769.3	1.0	9.1	150	8.0/10.0	0.5/1.0	-1.5	1.7		2.2×10^{-6}	1630	1.36×10^{-6}	35.5	60.0	20,720
797.0	0.7	9.3	200	8.2/10.1	0.0/1.5	-1.5	2.0		1.8×10^{-6}	1940	1.08×10^{-6}	[illegible]	60.0	27,367
804.9	0.6	9.3	160	7.9/9.9	1.2/7.0	-1.5	1.0		1.6×10^{-6}	2400	0.52×10^{-6}	29.4	71.8	46,343
835.5	1.0	9.5	270	7.9/10.0	0.6/4.5	-1.7	6.5			1815	1.60×10^{-6}	50.5	66.6	20,000
838.5	1.1	9.0	400	7.5/9.6	0.0/3.0	-1.7	5.5	29	2.5×10^{-6}	1560	2.00×10^{-6}	72.1	60.3	19,130
839.7	1.6	9.0	270	8.3/9.5	0.0/1.4	-1.7	4.0			1336	2.46×10^{-6}	73.5	64.0	13,050
861.6	1.4	9.0	270	8.3/9.6	1.0/4.0	-1.7	[illegible]		3.2×10^{-6}	1400	2.42×10^{-6}	74.6	66.3	12,000
877.8	1.4	9.1	300	8.3/9.4	0.0/1.0	-1.7	3.0	29	3.5×10^{-6}	1442	2.33×10^{-6}	74.3	70.0	13,630
894.0	1.6	9.0	300	8.3/9.5	0.0/1.0	-1.7	2.5			1300	2.96×10^{-6}	84.4	70.5	14,530
900.6	1.6	9.5	400	8.3/10.0	0.0/0.7	-1.7	2.3	29	2.6×10^{-6}	1513	2.36×10^{-6}	77.6	64.0	17,000
905.3	1.6	9.5	400	8.4/10.0	0.3/0.5	-1.7	1.5	29	2.6×10^{-6}	1543	2.34×10^{-6}	76.3	67.0	17,050
931.3	1.6	9.5	130	8.7/10.3	0.2/0.1	-1.7	0.5	29	2.0×10^{-6}	1290	1.31×10^{-6}	51.5	66.6	11,560
953.5	1.3	9.7	130	8.6/10.3	0.2/0.1	-1.7	0.2	29	1×10^{-6}	1323	1.13×10^{-6}	53.7	67.2	11,050
960.0	1.7	9.5	150	8.7/10.3	0.1/0.1	-1.7	0.2	29	1.2×10^{-6}	1670	1.00×10^{-6}	63.7	69.3	8,000
1000.0	1.6	9.5	150	8.7/10.2	0.2/0.1	-1.7	0.1		1.34×10^{-6}	1230	1.36×10^{-6}	42.6	70.3	8,030
1001.0	2.0	11.1	200	9.3/11.3	1.5/1.29	-1.7	10.11			1050	3.31×10^{-6}	57.1	50.1	5,941

Note: $V_1/V_2(I_1/I_2)$ refer to upper and lower deflector electrodes, respectively.

formance had returned to 60 μlb at 1795 seconds I_{sp}. By the 215th hour, the thrust could be increased to 94 μ lb at 1300 seconds specific impulse. Deflector drain currents had decreased to less than 1 microampere.

The module continued to perform well, with thrusts in the mid-80 μ lb region until the 320th hour, at which time the drain currents returned. The curative process was repeated, except this time, air was bled in for only one hour. By running at reduced mass flow and thrust, 0.8 x 10^{-8} kg/sec and 34 μ lb, it was possible for the module to once again cure itself. For the rest of the test, the thruster was run at various thrust levels and specific impulses as shown in Table 6-2. There was occasional periods when the deflector current increased slightly and the module was temporarily throttled back to clear up the problem. The module was usually run with the beam vectored down, although occasionally it would vector in the opposite direction.

One more serious leakage problem occurred as the result of a vacuum system accident after 930 hours. In this instance, the liquid nitrogen supply ran out while the thruster was running overnight unattended. As a result, the vacuum system main valve closed and a safety interlock automatically reduced the feed pressure to zero. However, the interlock for the power supplies failed and the system remained at high voltage. This resulted in a continuous breakdown arch back through the feed pressurization line and from the vector electrodes to the extractor. By the time the situation was discovered in the morning, half of the vector electrode and portions of several others had been badly eroded. Although previous to the accident there had been no evidence of tar formation, heavy tar encrustations were now apparent in half the needles. Moreover, the mass flow rate was considerably reduced, indicating needle plugging. It was possible to restart the engine and complete the test. However, performance was reduced to the order of 30-40 μ lb thrust and 1000 to 1300 seconds I_{sp}. At 1001 hours, the thrust was temporarily returned to 97 μ lb and [illegible]6 seconds. The operation was unstable at this point due to the tar and deflector damage, and the run was terminated.

7. THRUST MEASUREMENTS

7.1 GENERAL

A cross flexure thrust stand was used to measure thrusts in the 100 μlb range for three modules: (1) the 9-needle, thrust vectorable annular module, (2) the 36-needle, thrust vectorable module, and (3) the 6-needle annular module. Whenever possible, thrust stand and time-of-flight data were taken simultaneously. The following text includes a description of the thrust stand, experimental setup, method of measurement, experimental results (Tables 7-1, 7-2, and 7-3), a discussion of those results, and a comparison of time-of-flight and direct thrust measurements.

7.2 THRUST STAND

In order to accurately measure 100 micropounds of thrust, a test stand with high load-to-precision ratio ($\sim 5 \times 10^6$ lbm/lbf) capability was required. This imposed severe sensitivity restraints on test stand design. Provisions for electrical power, command links, and signal lines to the thruster system under test had to be made without compromising accuracy requirements. The test stand had to operate in the vacuum chamber environment needed for thruster evaluation, and be isolated from mechanical vibrations and noise generated by pumping equipment or other facility disturbances.

The thrust stand used for this purpose is shown in Figure 36. It is a balanced beam suspended on two pairs of crossed flexural members. The beam pivots about the line located by the points where the flexural members cross. A wire-wound flat coil is rigidly attached to the beam at the pivot point and is located between the pole pieces of a stationary permanent magnet. The thrust device is attached to the balanced arm and becomes an integral part of the suspended system. Counterweights are positioned on the balance arm below the pivot line of the thrust stand to adjust the restoring force of the suspension system and the moment of inertia of the suspended assembly. All power and signal leads required during thruster operation are connected to the thrust stand

Table 7-1. Thrust Measurement for 6 Annular Needle Thrust Vectorable Module Thrust Stand and TOF Data

V_a (kv)	I_a (μamp)	V_s (kv)	I_s (μamp)	V_{def} (kv)	I_{def} (μamp)	Feed Pressure (inches of Hg)	Thrust (μlb) Stand	Thrust (μlb) TOF	Z (μgm/cm²) Visual Measurement	Z (μgm/cm²) Recorder Measurement	Z (μgm/cm²) TOF	I_{sp} (seconds) Stand*	I_{sp} (seconds) TOF	Thrust Efficiency (%) Stand*	Thrust Efficiency (%) TOF
9.0	316	-1.0	0	-1.0	0	1.95	73	38	44	47	40	700	760	56	63
9.0	323	-1.0	0	-1.0	0	1.96	71	61	—	45	40	720	760	55	66
9.65	300	-1.0	0	-1.0	0	1.96	82	97	48	43	49	870	890	55	64
8.4	300	-1.0	0	-1.0	0	1.00	75	78	43	43	35	790	1030	52	67
11.0	320	-2.0	0.5	3.41	0	2.00	108	96	45	38	36	1150	1210	71	67
12.6	400	-2.0	0.5	3.41	0	2.90	121	114	—	33	44	1030	1160	56	58

*In calculation of I_{sp} and efficiency, the average of visual and recorder was used.

Table 7-2. Thrust Measurements for 36-Needle Thrust Vectorable Module Thrust Stand and TOF Data

V_n (kv)	I_n (μamp)	V_x (kv)	I_x (μamp)	V_{def} (kv)	I_{def} (μamp)	Feed Pressure (inches of Hg)	Thrust (μlb) Stand	Thrust (μlb) TOF	$\dot{m}$ (μgm/sec) Visual Measurement	$\dot{m}$ (μgm/sec) TOF	I_{sp} (seconds) Stand	I_{sp} (seconds) TOF	Thrust Efficiency (%) Stand	Thrust Efficiency (%) TOF
6.03	213	-1.55	6.0	4.4	0.5	1.15	45	—	30		680		54	
6.03	213	-1.55	6.0	4.4	0.5	1.25	41		22		840		60	
6.61	306	-1.55	7.5	4.95	1.0	1.5	56		32		835		52	
6.67	332	-1.55	8.2	4.96	1.5	1.5	58		32		920		53	
6.58	320	-1.55	7.5	4.96	1.5	1.5	57	62	32	27	799	1000	48	60
9.65	360	-1.70	8.0	9.65	10.0	2.0	100	83	46	31	1050	1270	63	68
LEFT RUNNING OVERNIGHT														
9.83	360	-1.70	3.0	9.83	0.0	2.0	83	70	35	23	1000	1440	56	90
9.83	360	-1.70	3.0	9.83	0.0	2.0	83	61	35	27	1000	1370	56	60
8.00	221	-1.70	3.6	8.00	0.0	2.0	53	57	30	33	750	1120	50	70
8.06	226	-1.70	3.6	8.00	0.0	2.0	64	56	35	36	830	1140	66	72
10.00	403	-1.70	6.9	10.0	0.3	2.6	112	102	51	38	1000	1230	64	66
10.00	403	-1.70	7.0	10.0	0.3	2.6	111	107	51	44	1000	1130	63	66
9.30	243	-1.70	3.0	9.30	0.0	1.1	42	43	12	12	1360	1630	70	67
9.33	246	-1.70	3.0	9.33	0.0	1.1	46	44	12	13	1700	1600	76	67

a. Front View

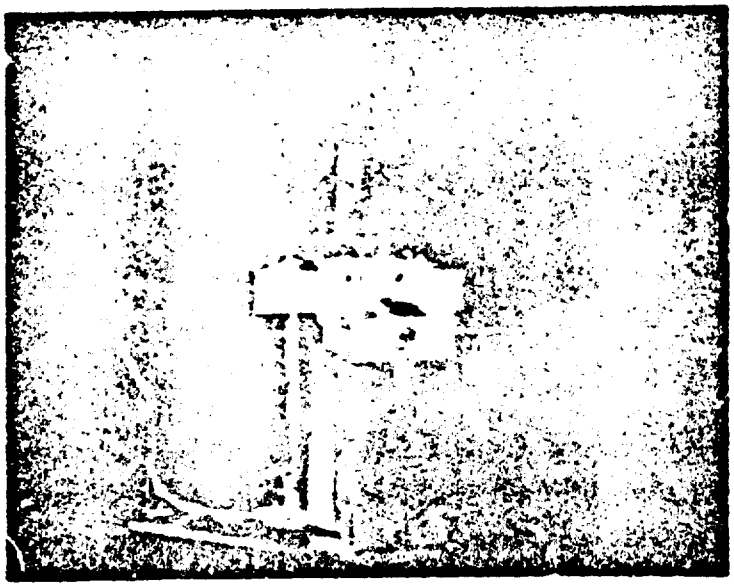

b. Rear View

Figure 38. 6 Annular-Needle Module Mounted on Thrust Stand (Propellant Reservoir, Capillary Feed Tube and Gas Pressurant Tube are Visible).

Table 7-3. Thrust Measurements for the 6 Annular Bundle Module Thrust Stand and TOF Data

V_D (kv)	I_D (amp)	V_E (kv)	I_E (amp)	Feed Pressure (torr of Kr)	Thrust (mN) Stand	Thrust (mN) TOF	θ (mm/sec) Generator Measurement	θ (mm/sec) TOF	I_{sp} (seconds) Stand	I_{sp} (seconds) TOF	Thrust Efficiency (%) Stand	Thrust Efficiency (%) TOF
11.5	230	-1.7	0.5	2.1	61	73	32	32	850	1075	66	80
12.1	200	-1.6	0.5	2.1	75	84	31	36	1500	1180	58	[illegible]
11.3	200	-1.8	0.5	2.0	60	79	33	37	950	970	61	73
11.3	223	-1.8	0.5	1.6	78	94	40	42	730	910	58	70

coincident with the pivot line. The power leads are attached to the stand on one side of the balance arm, and signal leads on the other. The crossed flexures are isolated electrically from both the balance arm and ground and may be used for high-current, low-voltage leads.

During operation, thrust generated by the thruster will cause the balance arm and the coil to rotate about the pivot point. Deflection of the arm is monitored by the change in resistance of a magnetic sensitive resistor (Mistor) that is rigidly attached to the balance arm and located in the field of the permanent magnet. The Mistor is one leg of a bridge circuit. The direction of rotation of the stand is sensed by the polarity of the bridge output.

For measurement of steady-state thrust level, the thrust stand is used as a null-balance device. When the stand is deflected by the thrust force, the Mistor bridge becomes unbalanced. A current is applied to the coil, either manually or by a feedback system. The coupling of the magnetic field of the permanent magnet and that induced by the coil current exerts a force that counters the thrust force. The coil current required to return the arm to its null position is proportional to the thrust level. The device is calibrated for steady-state thrust by measuring the current required to restore the null balance with known steady-state torques.

7.3 EXPERIMENTAL SETUP

The thrust stand and time-of-flight arrangement is shown schematically in Figure 39. The nominal distance from the module to the time-of-flight collector was 1.5 meters. The module and feed system were mounted on top of the thrust stand balance beam. Figure 38a. shows the thrust stand with the 6-needle annular module mounted 25 cm above the pivot line. Figure 38b. is a view from the back of the module. Some of the module shielding has been removed to make the module and feed system visible. The bundle of wires coming in from the left contains the Mistar and deflection coil wires. The bundle on the right contains the three thruster leads (needle, extractor, and deflector voltage) and the feed pressure tube (24-mil O.D., 15-mil I.D. SS). The feed pressure tube was used to pressurize the propellant reservoir on the stand.

The thrust stand was calibrated by placing a weight equivalent to 100 μlb (45.4 milligrams) at a point equal in distance to the thruster lever arm (~25 cm) from the pivot. The current required to return the balance arm to its original position was then measured. The calibration obtained was in amp/gm. In addition to the null technique, a deflection versus thrust calibration was made. This differed from the null technique in that the amount of deflection caused by the 100 μlb weight was measured and then the amount of coil current required to cause an equal deflection was measured. Since this later calibration agreed with the null calibration, it was felt that thrust measurements could accurately be measured in the 100 μlb range by measuring beam-off, beam-on deflections. This technique was used in most thrust measurements because it was quicker and simpler to use than the null technique.

The sensitivity of the thrust stand, as a physical pendulum, is related to its period. The longer the period the greater the deflection for a given thrust torque. Gravity is the major restoring torque since careful placement along the pivot line and use of the thinnest and fewest number of power, signal and feedlines have reduced the torque effect of these wires to a minimum. Experience has shown that a period of 6

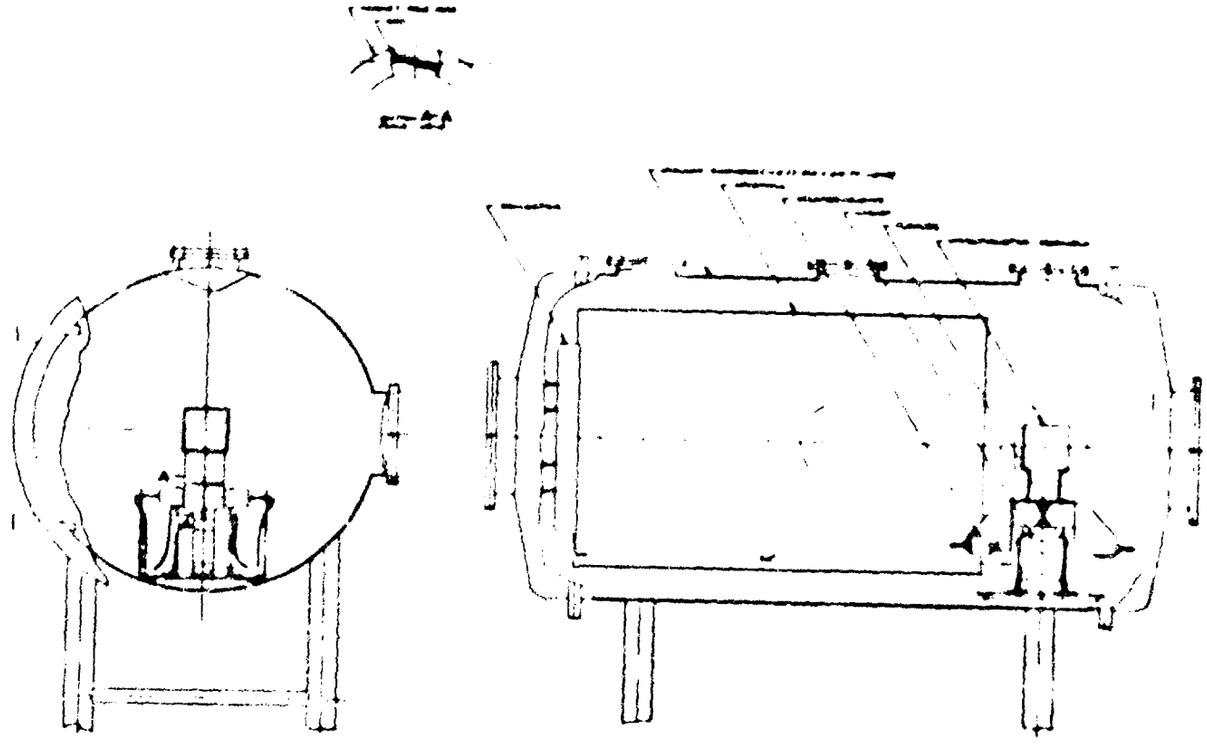

Figure 19. Layout of Thrust Stand and TOF Arrangement in Vacuum Tank for Thrust Measurements

seconds will produce an accuracy of 10% at 100 μlb. Accuracy is determined by the amount of deflection of the balance arm for a given force and the error in reading repeated deflections. The major cause for error in deflection readings is a hysteresis in the return of the balance arm to its original position. This is caused by the pliable insulation on the various wires and feedthroughs remembering their former positions. Another cause of error peculiar to the electrostatic thruster is the deflecting force on the arm due to electrostatic images on the vacuum tank walls. This effect is minimized by careful shielding of the thruster and by dropping the voltage to half its total value when the colloid beam is turned off for thrust measurements. This reduces the image forces to 1/4 of what they would be had the voltage been turned completely down, since this force varies with the square of the voltage.

Mass flow rate data were obtained in two ways: by visually following the propellant height in a capillary tube, and by recording the deflection versus time shift of the balance arm as propellant was used up. In the first technique, vertical sections of the capillary tubing connecting the reservoir to the module were calibrated for volume versus length. The movement of the meniscus down or up these tubes with time was measured with a cathetometer viewing the meniscus through a window in the vacuum system. In the second technique, the position of the balance center of gravity provided a measure of the propellant depletion in the reservoir. The resultant shift in the balance equilibrium position, as measured by a chart recorder, thus provided a measure of the propellant flow.

Time-of-flight data were taken coincident with the thrust measurements. Traces were taken preceding each thrust measurement. A flat honeycomb time-of-flight collector and two biased screens was used. The screen closest to the collector was biased -100 volts. The other screen was biased +50 volts. The flight path differed slightly from run to run but was nominally 1.5 meters.

7.4 EXPERIMENTAL RESULTS

The first module tested, the 6-needle thrust vectorable annular module, was run on the thrust stand for 8 hours. Six separate thrust measurements were made ranging from 70 to 120 μlb. The first four measurements were made with the deflectors connected in common with the extractor voltage V_x, to permit operation at lower needle voltages, V_n. The last two data points were made in normal configuration with the deflector voltage intermediate between V_n and V_x. Mass flow was measured visually and from the slope of the balance arm deflection versus time display on a chart recorder. The time-of-flight and thrust stand data are given in Table 7-1.

Data from the second module tested, the 36-needle thrust vectorable module, are listed in Table 7-2. This module was operated on the stand for 30 hours. Sixteen thrust measurements were made covering the range from 40 to 110 μlb. Only visual mass flow rate measurements were made because the propellant reservoir was centered over the pivot line. This was done because, during the previous run, the stand shifted so rapidly with time it had been difficult to obtain thrust data before the chart recording had gone off scale. This change was a mistake because thrust stand deflection with propellant usage permits a rapid measurement of $\dot{m}$ and provides an independent check on our visual $\dot{m}$ measurements. In later measurements, the propellant lever arm was placed one-half as far from the pivot line as in the first thrust experiment. This kept the chart recorder from moving off scale too fast but still permitted taking $\dot{m}$ calculations from slope.

Data from the 6-needle annular module, the third tested, is shown in Table 7-3. This module did not perform well. It was difficult to obtain stable currents due to poor wetting and needle-extractor arcing. These data are the least accurate because of the unstable operation of the module. In addition, some of the high voltage leads coming into the balance beam along the pivot line were later found to have been loose. When these wires were loose they caused a torque on the balance as voltages were applied to the module. This torque was found to be

variable. The effect could not be eliminated from the beam-off, beam-on deflections. All $\dot{m}$ data were obtained from the thrust stand deflection with time. No visual $\dot{m}$ measurements were made because the reservoir was slightly overfilled and the propellant meniscus never dropped into the capillary tube. Had this module performed better, it would have been run long enough to bring the meniscus down into the capillary.

7.5 DISCUSSION

The first two modules performed well, providing stable operation while on the thrust stand. The third module did not perform well and there were uncertainties in thrust stand operation (see the preceding section). Therefore, it is felt the data from the first two runs (Table 7-1 and 7-2) provide the best comparison of TOF and thrust stand measurements.

Thrust stand accuracy is felt to be within 10% at 100 μlb and proportionately less at lower thrusts. Electrostatic image forces had a very small effect on balance arm deflection (less than 1% at 100 μlb in the first two experiments).

The uncertainties of the time-of-flight technique result from several unrelated factors. They are (1) the use of flat collector, (2) not subtracting the energy loss from V_a when calculating the various performance parameters, and (3) the difficulty of accurately reading the tail end of the TOF trace where the current approaches zero.

A flat collector exaggerates the $\dot{m}$ values because of beam spread. The greater the spread, the greater the exaggeration. This effect should be relatively minor with a narrow beam (±10 degrees) at high I_{sp} operation (> 1000 seconds). At lower I_{sp}, this effect becomes more important because low I_{sp} beams almost always (in a well wetting module) have wide beam spread (±30 degrees).

The effect of energy loss has been measured at ~4% for a colloid beam operating at 10 kv (Ref. 7-1). Not including this in the time-of-flight calculations should produce slightly higher thrusts, mass flow rates, and efficiencies.

Whenever the current sensitivity in the oscilloscope was purposely increased to more accurately observe the tail end of the trace, the resulting calculations progressed asymptotically towards higher $\dot{m}$, higher thrust, lower efficiency, and lower I_{sp}.

The sum effect of these errors become apparent when TOF and thrust stand data are compared. The thrust stand data indicated, generally, higher thrusts, lower I_{sp}'s, higher $\dot{m}$, and lower efficiencies than the TOF data. The differences are not too great. In Tables 7-1 and 7-2, the agreement between TOF and thrust stand values of thrust is close. Out of 16 comparisons, one differed by [illegible]%, one by 18%, and two by 11%. All the rest agreed to within 10%. The thrust stand measured higher thrust in 10 out of 16 cases. It also indicated higher $\dot{m}$ in 12 out of 16 comparisons. The thrust efficiencies were lower in 13 out 16 times.

These results suggest that an inability to accurately read the last part of the TOF trace explains most of the difference between the TOF and thrust stand data. The importance of the tail end of the TOF trace can be seen from the TOF equation for $\dot{m}$,

$$\dot{m} = \frac{4V}{L} \int_0^{t_0} t\, I(t)\, dt$$

Here, any additional I(t) is weighted by multiplying it by t. Obviously, if I(t) approaches zero slowly, but is so close to zero that it cannot be differentiated from zero, then an error in $\dot{m}$ can occur when I(t) is assumed to be zero earlier than it should.

A very interesting outcome of the thrust measurements was that thrust efficiency appeared to go up with increased I_{sp} (or more accurately with increased $\overline{Q/M}$). This effect will have to be verified in later experiments because it is contrary to what is indicated by TOF data. If it is true, then the high ion peak at high Q/M operation is more than offset by a reduction in the slow low Q/M particles.

The data in Table 7-3 for the third module tested are anomalous compared to Tables 7-1 and 7-2 since the thrust and $\dot{m}$ values were lower than the TOF values. However, as mentioned before, this module behaved erratically, making it difficult to obtain data. The scatter in the data is a result of unreliable behavior.

The relatively low I_{sp}'s (less than 1500 seconds) are the result of not having time to analyze the data during the tests and are not indicative of module capabilities. In the first two tests, we worked well within the limits of voltage operation and could have adjusted the voltage and feed pressure for 1500 seconds operation at 100 μlb.

7.6 CONCLUSIONS

The TOF and thrust stand thrusts agree, on the average, to within 10%. The low TOF $\dot{m}$ values (compared to thrust stand values) may be the result of our inability to accurately follow the TOF trace when it is very close to zero. Careful attention to this part of the trace will bring the TOF and thrust stand data closer together. High Q/M, high I_{sp} (i.e., high voltage) operation improves the thrust efficiency over low I_{sp}, low Q/M operation.

Additional tests must be made to verify, by experimental repetition, the above conclusions. The use of thrust stands in long-term tests appears to be impractical because of the bulkiness of the stand and its need for a constant, room-temperature environment. TOF techniques will continue to be used. It may be desirable to use a logrithmic amplifier to improve the accuracy of the TOF readings by making the tail end of the TOF trace more visible.

REFERENCES

7-1. M. H. Haberman, "Measurement of Energy Dissipated in Electrostatic Spraying Process," February 1970, J.A.P. (To be published)

5. THERMAL ANALYSIS OF MODULE

A simplified heat transfer analysis was undertaken on the critical components of the module to determine the effects of solar radiation and thrust beam energy loss on the temperature at the needle tip. The region investigated is shown in Figure 40, and consisted of the extractor plate, the needles, the module base and the needle holder. For the purpose of the analysis, the needle holder was taken as part of the module base, whose temperature is controlled at 305°K.

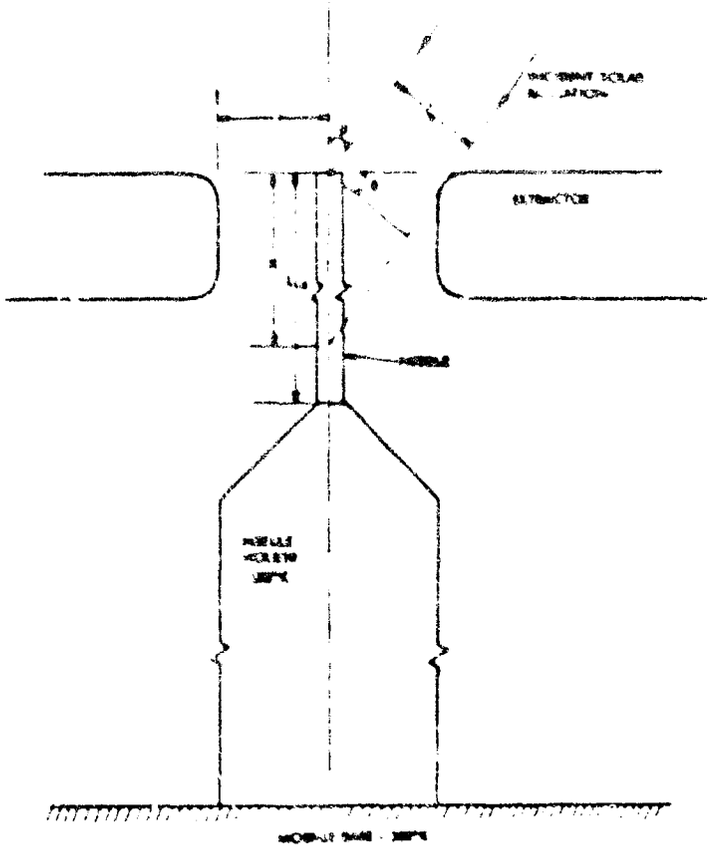

Figure 40. Geometry of the Thermal Analysis for the 36-Needle Module

Module temperature control is accomplished with the combined use of a module heater and a thermal conductance to a radiator or the relatively cold spacecraft structure. This is desired because the glycerol propellant viscosity is highly temperature-dependent. Thus, the average needle temperature will significantly affect mass flow rate. The 36-needle colloid thruster module is designed to operate with a propellant temperature of 25°-27°C. The purpose of the analysis was to determine the deviation of the needle temperature from the design value due to the effects of solar radiation and energy loss.

The study showed that the needle will normally operate about 3.5°C above the control temperature of the module base. It was further found that almost all this temperature difference is due to the energy loss mechanism, and the effects of solar radiation are insignificant. The energy loss is roughly proportional to needle current, and is subject to control and observation; therefore, the needle temperature is also.

Thermally, the needle was assumed to behave like a point mass radiator with a thermal conductance to the base determined by the total needle length. Since almost all of the heat input is due to energy loss and occurs at the tip of the needle, this appears to be a good assumption. The radiation areas were computed according to the actual exposed surface area of a bare needle. The shielding effect of deflector electrodes was not taken into account. Since the effects of radiation were found to be so small in this study, it is reasonable to assume that the deflectors would have a temperature close to the control temperature, and would tend to draw the needle temperature down by shielding.

The case studied was that of the greatest illumination incident on the needle. Because of this, and because of the omission of the deflectors, it was in some sense a "worst case." The problem of needle illumination can be posed by referring again to Figure 40. Neglecting such effects as dependence of emissivity on angle of incidence, the effective irradiated area of a needle of diameter d is given by:

$$A_e = d\,L_e$$

where L_e is the effective length shown in Figure 5?, and must satisfy

$$L_e = x \sin \theta$$

If θ is less than some critical angle θ_c, x is constrained to be its maximum value, the needle length L_n. If $\theta > \theta_c$, the constraint is on the extractor hole radius and

$$L_e = r \cos \theta$$

which is the condition shown in the figure. Two expressions for effective area account:

$$A_e = d\, L_n \sin \theta, \quad \theta < \theta_c$$

$$A_e = dr \cos \theta, \quad \theta > \theta_c$$

For a 14-mil needle and a standard extractor, the following parameters were used.

d = 0.0356 cm, needle diameter

r = 0.159 cm, extractor hole radius

L_n = 0.586 cm, needle length above holder

The maximum effective area occurs when the above two expressions for A_e are equal. This occurs at θ_c.

θ = 13°, critical incidence angle

$A_e(\theta_c)$ = 0.0055 cm^2, maximum effective area

In writing the extractor heat balance equations, the radiative heat transfer between the module base and the extractor was assumed to take place as between two plane surfaces of equal emissivity. Heat conduction between the two takes place through four stainless steel studs. The balance equations appear as follows.

Radiation to space + radiation to module + conduction to module = absorbed incident solar radiation.

$$\sigma \epsilon_x A_x T_x^4 + \sigma A_x (1/\epsilon_x + 1/\epsilon_m - 1)^{-1} (T_x^4 - T_m^4)$$

$$+ k_s A_s \quad (T_x - T_m)/L_s = R \cos \theta_c \; \epsilon_x A_x$$

σ = 5.67×10^{-12} watts/cm^2 - °K^4, Stefan Boltzmann constant

ϵ_x = 0.10, emissivity of extractor, for aluminum

ϵ_m = 0.10, emissivity of module base

k_s = 0.222 watt/cm - °C, thermal conductivity of stud

L_s = 0.64 cm, stud height

A_s = 0.149 cm^2, total stud cross section

A_x = 70.4 cm^2, net extractor area

R = 0.140 watt/cm^2, incident solar radiation in near-earth environment

Using a module temperature of T_m = 305°K, the above equation was solved for $T_x - T_m$ (the conduction term) by a method of successive approximations. The resulting extractor temperature was T_x = 308.3°K, or about 3.3 degrees above the base temperature. The following power distribution was found.

Incident solar radiation = 0.0136 watt/cm^2

Heat conducted to module = 0.00844 watts

Radiation to module = 0.00011 watts

Radiation to space = 0.00511 watts

The heat exchange between extractor and needle is too small to influence this balance, as the solution of the needle heat balance equations shows. In formulating these equations, it was assumed that the radiative view factor from the needle to both the extractor and the module base is equal to one--only an approximate assumption in the latter case. The needle energy loss was based on an assumed voltage drop of 400 volts and a nominal needle current of 10 microamperes. The balance equations are formed as follows.

Radiation to extractor + radiation to module + conduction to module = energy loss + incident solar radiation.

$$\sigma \epsilon_n A_{np} (T_n^4 - T_x^4) + \sigma \epsilon_n A_{np} (T_n^4 - T_m^4)$$

$$+ k_s A_{sc} (T_n - T_m)/L_s = E + R \epsilon_n A_p$$

ϵ_n = 0.035, needle emissivity, for polished platinum

k_n = 0.70 watt/cm^2 - °C, needle conductivity, for platinum

A_{np} = 0.0657 cm^2, needle perimeter area, $\pi d L_n$

A_{nc} = 0.092x10^{-3}cm^2, needle cross section

E = 0.004 watt/needle, energy loss

The needle cross section was found for a standard 14-mil needle, and the perimeter area was calculated assuming an exposed portion of the needle above the needle holder of 0.231 inch in length. The above equation was solved for $T_n - T_m$ in a similar manner to the extractor equation. The resulting needle temperature was found to be T_n = 308.6°K, about 3.6° above the base temperature. The following power distribution was found.

Heat conducted to needle = 0.004 watt/needle

Radiation to needle = 0.05 x 10^{-3}

Radiation to extractor = 0.417 x 10^{-5}

Energy loss = 0.004 watt

Incident solar radiation = 0.244 x 10^{-4}

Based on the extractor area of 20.4 cm^2 for the 36-needle module, the average radiation density from the needles to the extractor is 0.74 x 10^{-5} watt/cm^2. This is a small fraction of any of the power inputs to the extractor which have been accounted for, and its neglect is justified.

9. PROPELLANT RESEARCH

In addition to NaI-glycerol (3 gms NaI to 10 gms of glycerol), the standard colloid propellant, the following propellants have been tested using platinum needles (14 mil O.D., 4 mil I.D.):

- KI-glycerol (3 gms KI to 10 gms of glycerol)
- CsI, NaI-glycerol (3 gms NaI, 3 gms CsI to 20 gms of glycerol)
- Liquid gallium
- Liquid cesium

The KI-glycerol and NaI, CsI-glycerol propellants did not perform as well as NaI-glycerol. The gallium ion species was identified as Ga^{+}. The cesium ion species was identified as Cs^{+} and the mass utilization measurements indicate that at least 77% of the mass is utilized in the ion beam. In addition to the items reported in this section, work with NaOH-glycerol is reported in the section describing pulsed and AC work.

9.1 CsI, NaI-GLYCEROL

A mixture of cesium and potassium iodides in glycerol was run for about 400 hours. Initial results were good, indicating efficiencies greater than about 80% for specific impulses of 1000 seconds. The ion peak indicated only one species - heavier than with NaI-only operation. Later operation degraded, and massive charred deposits were found around the needle. Also, erosion of the platinum-iridium needle was noted. Although operating conditions were admittedly poor (not trapped, short flight path, needle not beyond the extractor, and often times insufficient negative voltage on the extractor), evidence is mounting that heavier ions such as potassium and cesium cause more tarring and possibly even needle erosion. The mixture was made by mixing equal volumes of 3/10 (30 grams/100 cc glycerol) of CsI-glycerol with a resistivity of 3900 ohm-cm and a viscosity of 416 centistokes (c.s.) and 3/10 NaI with 4700 ohm-cm and 1500 centistokes. The resulting mixture had a viscosity of 656 c.s. and a resistivity of 4200 ohm-cm. All resistivities and viscosities were measured at 25°C.

9.2 KI-GLYCEROL, 6-NEEDLE ACCEL MODULE

A 170-hour run was made using KI/glycerol. Thrusts of close to 4 μlb/needle were maintained at 83 percent efficiencies and 1400 seconds I_{sp}. In general, the KI propellant produced lower Q/M and therefore lower I_{sp} beams for equivalent voltages, mass flow and thrust. There was almost no low peak on the time-of-flight (TOF) traces (Figure 41).

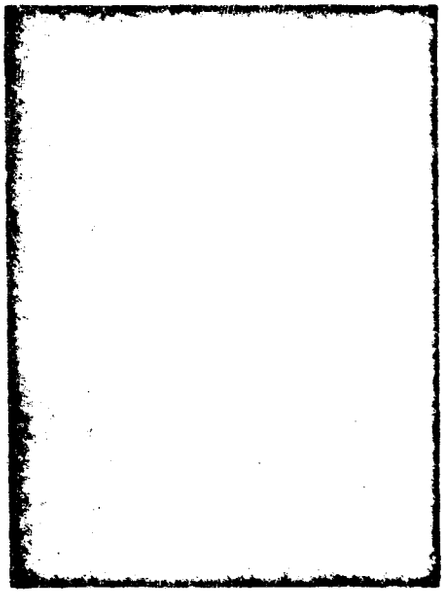

Figure 41.. TOF Trace Obtained With KI-Glycerol Propellant

I_{sp} = 1380 seconds

η = 82%

T = 22 μlb

$\dot{M}$ = 7.2×10^{-9} kg/sec

(Q/M) = 8.0×10^{-3} coul/kg

V_B = 13.8 kv

V_x = -1.5 kv

I_B = 57 μamp

I_x = 0.0

TOF length = 1.82 meters

2 screen shields. The one closest to collector biased -19 volts, the other biased +12 volts.

Scope scales: 5 μamp/cm, 50 μsec/cm

$\dot{M}$ and T based upon I_B

Beam spread less than ± 10°

Data not corrected for beam spread.

The KI-glycerol solution was a 3 gms KI to 10 ml of glycerol mixture. The viscosity was 575 centistokes and the resistivity was 2300 ohm-cm at 25°C.

After opening the tank, it was noticed that the needles were almost completely covered with KI crystals (see Figure 42). These crystals were apparently formed during the 90 post-operational hours the module remained in vacuum during a long holiday weekend. There had been no deterioration during the prior 170-hour test, so it is unlikely that these crystals were present during the run. In addition they were easily visible and would have been noticed through the vacuum view port had they formed during the run. This crystal growth by evaporation of glycerol from the solution at the needle tip could be a problem during extended shutdown periods. Experiments will have to be made to determine how best to operate the colloid thrusters during extended zero thrust periods.

Figure 42. Run 6905-01 - 3/10 KI-Glycerol Solution. KI Crystal Growth on Needles After Setting 90 Hours in Vacuum With Beam Off, i.e., Zero Voltage and Zero Feed Pressure

9.3 LIQUID METALS RESEARCH

9.3.1 Gallium Experiment

Swatik[1] of the University of Illinois found that spraying gallium-indium eutectic produces only dimers and tetramers but no singly charged ions. Since an error in the ion species might account for the apparent difference in the mass carried by the ion beam and the amount of mass used as determined in past experiments by weighing, it was decided to more carefully identify the ion species. A longer TOF length, 56 cm versus 20 cm, was used to improve accuracy. The sweep speed of the oscilloscope was calibrated against known frequencies and the delay in amplifier response, approximately 1/4 microsecond, was subtracted from all time of flights.

As in past experiments, a hollow platinum needle with a 60° conical tip tapered from the 14 mil O.D. to a 4 mil I.D. was used to introduce the gallium into the high field at the needle tip. The needle and high voltage lead-ins were carefully shielded to prevent collection of secondary electrons. The gallium was introduced into a chamber behind the needle before installation. Some gallium was forced through the needle and then the needle tip was coated with a thin film of gallium and gallium oxide by drawing the tip through a bath of oxide-covered gallium. This last step was necessary to ensure good wetting of the needle which provides a foundation for the emitting cone of liquid metal at the needle tip.

The gallium needle was operated for several hours before being weighed to ensure that a stable ion current could be maintained and that any mass lost in the initial start-up procedure would not be counted in the final weighing. After the initial startup, the needle was cooled to freeze the gallium, then carefully removed without disturbing the emitting tip, weighed and then replaced. The needle was operated in a horizontal position to eliminate hydrostatic head.

---

[1] D. S. Swatik, University of Illinois, "Production of High Current Density Ion Beams by Electrohydrodynamic Spraying Techniques," 14 May 1969.

A positive feed pressure was required to maintain a steady current. If the feed pressure were removed, the current would steadily diminish over a period of several hours until emission stopped. This phenomenon had been observed in the past and was caused by a gradual disappearance of the emitting cone as the gallium receded into the needle tip. At a pressure of 0.8 inch of Hg, 6.20 kv was required to maintain a current of 65 μamps (V_x = -400 volts). At higher pressures, up to approximately 3 inches of Hg, the current would increase, for a fixed voltage, with increased pressure. Above 3 inches, large drops of gallium could be seen being pulled off from the needle tip and the current would pulse.

The ion species determined from the TOF traces shown in Figure 43 are within 5% of the Q/M value for singly charged gallium ions; i.e., $1.27 \times 10^{+6}$ coul/kg measured versus $1.35 \times 10^{+6}$ coul/kg actual value of the ionic specific charge for Ga^{+}. From this data and experiments made in May-June 1968, it appears that the only ion species to within 1 percent

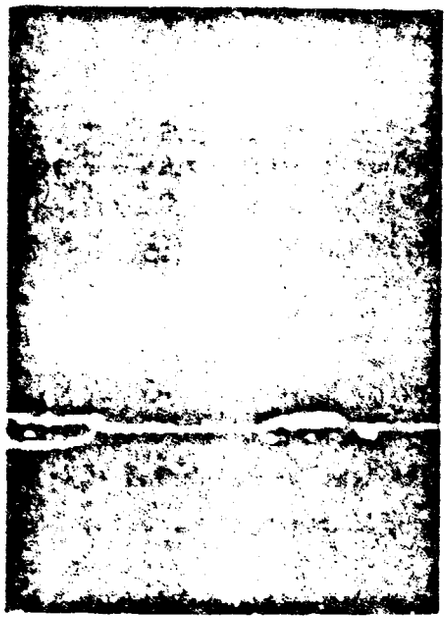

Figure 43. TOF Traces for Gallium Ion Beam
V_n = 7.17 kv Scope Settings: 1 μs/cm, 1 μamp/cm
I_n = 63 μamp TOF Length: 56 cm

of the total ion current is Ga^+. As in earlier experiments, more mass was lost than could be accounted for in the ion beam. In the present experiments, the ratios of measured mass flows to those calculated from an assumed 100% ion current were 3.1 and 4.6. The difference in the ratios may be caused by two factors: (1) imperfect shielding from secondary electrons (collecting electrons on the positive electrodes would produce higher needle currents than were actually going into ions and would tend to lower the mass utilization ratio), and (2) a feed pressure dependence in the mass utilization ratio, although this has not specifically been tested for, as yet. The surrounding surfaces, shadowed from gallium atoms that might return after striking the collector or walls of the tank but in direct line of sight with the needle tip, were coated with gallium. This source of coating could only have been the needle and could not have been in the form of high [illegible] ions which would have sputtered the surfaces clean rather than coating them.

9.3.2 Cesium

9.3.2.1 Liquid Metal Test Station

The liquid metal test station for cesium (Figure 44) is designed to provide clean cesium to a needle for time-of-flight analysis. A view port permits visual observation of the emitting needle. Oxygen contamination is kept at a minimum by using a leak-free system capable of 10^{-8} mm of Hg vacuum after bakeout. Both the upper and lower systems can be baked out to reduce water vapor evolution from the glass. In addition, an LN_2 trap is used to trap residual H_2O in the system. Low-dewpoint, oxygen-free nitrogen provides the feed pressure. A cesium boiler distills cesium into the stainless steel feed line connected to the needle. As the cesium in the feed line is used up, the total resistance of the line changes. This change in resistance is used to calculate mass usage. By keeping a record of the needle current levels for long enough periods, the TOF data ion species can be used to determine the mass ejected in the ion beam and compared with the mass usage

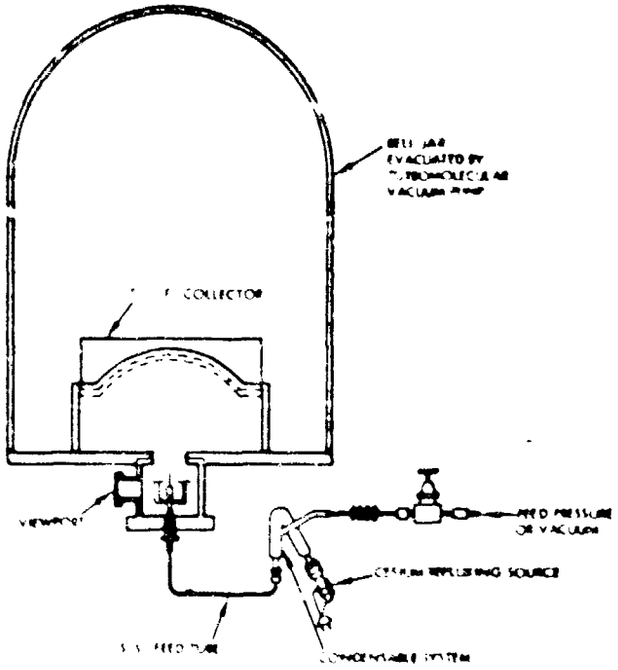

Figure 44. Liquid Metal Test Station. A turbo-molecular pump capable of producing a vacuum in the 10^{-8} torr range is used to pump out the bell jar. The feed system is made from glass and stainless steel tubing. The feed system can be baked out. The cesium is distilled from a boiler into the glass tubing just above the 1/8 inch O.D., 1/16 inch I.D. stainless steel tubing. The cesium is then forced through the stainless steel tubing by nitrogen gas pressure (the nitrogen is dried by passing it through tubing immersed in an LN_2 dewar). A view window for microscopic observation of the needle tip is used to take photographs of the emitting cone on the needle tip. A time-of-flight collector, situated above the needle tip, is used to analyze the ion species, mass flow and specific impulse of the beam. The resistance of the Cs filled stainless steel tube varies as the cesium is used up. This resistance change is used to determine mass usage.

calculated from the resistance change in the feed line. Resistance measurements of the cesium-filled tube have checked out to within 2% of the calculated value. Introducing cesium reduces the resistance to approximately half the value for the empty feed tube. The mass change is reflected by a change in the feed tube resistance. As the cesium content is depleted, the length of the cesium-filled region within the tube can then be calculated from the resistance change by the following:

Let

- L = length of stainless steel feed tubing
- L' = length of section filled with cesium
- ρ = resistivity of stainless steel
- ρ' = resistivity of cesium
- A = cross-sectional area contained within tubing wall
- A' = cross-sectional area of the cesium within the tube
- R = electrical resistance along entire length of empty tube
- R' = resistance along entire tube when length L' is filled with cesium
- $R_{L'}$ = resistance along length of filled section
- $R_{L-L'}$ = resistance along length of unfilled section

The following relationships hold:

$$R = \frac{\rho}{A} L \qquad (1)$$

$$R' = R_{L'} + R_{L-L'} \qquad (2)$$

$$R_{L-L'} = R\left(1 - \frac{L'}{L}\right) \qquad (3)$$

$$R_{L'} = L' \left(\frac{\rho}{A}\right) \left(\frac{\rho'}{A'}\right) \left(\frac{\rho}{A} + \frac{\rho'}{A'}\right)^{-1} \qquad (4)$$

Experimentally we measure R' in order to calculate L'. Equations (2) and (3) yield:

$$R_{L'} = R' - R\left(1 - \frac{L'}{L}\right) \qquad (5)$$

Combining (4) and (5) yields:

$$L' = L\left(1 - \frac{R'}{R}\right)\left(1 + \frac{L\rho'}{RA'}\right) \qquad (6)$$

or, more simply:

$$L' = \left(1 - \frac{R'}{R}\right)\alpha \qquad (7)$$

where

$$\alpha = L\left(1 + \frac{L\rho'}{RA'}\right) \qquad (8)$$

where α is a constant independent of the amount of cesium in the tube.

R' is measured by passing a 1-ampere current through the tubing and measuring the voltage drop across it. The mass flow is then determined by the change in L':

$$\Delta L' = -\frac{\alpha}{R}\,\Delta R' \qquad (9)$$

The needle current versus time is recorded to determine the total mass carried by the beam as predicted by the charge-to-mass ratio. These two determinations are then compared to determine the net mass utilization.

9.3.2.2 Experimental Results

Steady cesium ion currents of up to 550 microamperes have been obtained by ion field emission from a hollow Pt needle. The ion species has been identified as singly charged cesium. The TOF traces indicate at least 98% of the beam consists of this one ion species.

The cesium ions originate from emission points along the rim rather than the tip of a liquid metal cone as with liquid gallium. The beam spread varied from 45 to 60 degrees as the current was increased from 225 to 550 microamperes. At 550 microamperes the extractor current was 50 microamperes.

The first needle currents were achieved using a standard colloid needle placed in the system by mistake. A platinum needle (14 mil O.D., 4 mil I.D.) of the type used in the gallium experiment (i.e., the outside of the tip tapered down in a cone to the 4-mil I.D.) was used later. The difficulty of getting a stable, well-wetted tip on which to form an emitting cone is greatly reduced with this type of needle.

After the needle was replaced, the cesium needle was operated for more than 300 hours. Currents were generally kept between 100 and 200 μamp, although currents as high as 500 and as low as 60 μamp were obtained. The mass utilization was measured by comparing the mass as calculated by dividing the total coulombs used in the beam by the Q/M for a cesium ion, with that calculated from the resistance change in the feed line as the cesium in it is used up. This data indicated that at least 72% of the mass was turned into ions. The chance for better mass utilization in future measurements is good because there were several periods of over-feeding during which microscopic drops of cesium could be seen coming from the needle. This of course tended to lower the mass utilization factor.

The needle current was close to being independent of voltage from 3 to 5 kv for the present needle geometry (See Figure 45) and wetting conditions. For example, decreasing the voltage from 4.2 to 3.3 kv decreased the current only 15 μamp, from 165 μamp to 150 μamp. The current depended on the feed pressure more than the voltage.

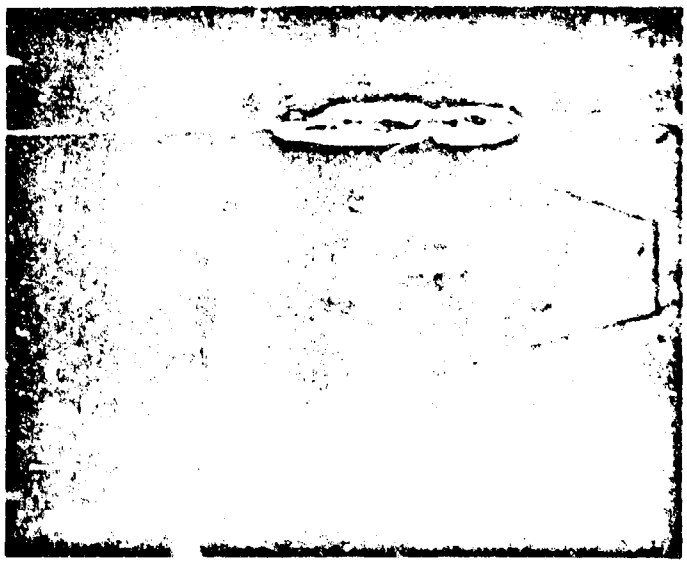

Figure 45. Needle After 300 Hours of Operation with Cesium. Inked in Line Indicates Original Shape.

9.3.2.3 Conclusions

Examination of the needle after more than 300 hours of operation indicated a general erosion of the needle tip (Figure 45) occurred. There have been reports of platinum-cesium reactions in contact ion thrusters when platinum was used to braze the tungsten ionizer pieces together. Available metallurgical data for platinum-cesium compounds is very sketchy. It is felt that needle materials such as tungsten or stainless steel would be better suited for long-term operation with cesium.

These preliminary experiments with Cs indicate that the potential of cesium as a high I_{sp} thrust source is good although the I_{sp} is too high for many colloid missions. The thrust per needle of < 5 μlb and the low power loss needed to produce ions as compared to contact or Kaufman type engines make it a highly attractive alternative to these devices in the microthruster range. The I_{sp} at 3000 volts is 6500 seconds.

10. ONE-MILLIPOUND VECTORABLE COLLOID THRUSTER POWER CONDITIONING

10.1 POWER CONDITIONER REQUIREMENTS

A preliminary study has been made of the power conditioning requirements for a typical 1-millipound thrust, 1500-second specific impulse, two-axis vectorable colloid thruster system. The power conditioning unit (PCU) converts the 28-vdc spacecraft bus voltage to the various levels necessary for operating the Millipound Vectorable Colloid Thruster (MVCT). It contains, as a minimum, the following supplies and functions:

- High voltage needle supply
- Extractor supply
- Four vector electrode supplies
- Neutralizer heater supply
- Two temperature controllers

The high voltage needle supply must provide a ±2% regulated, low-ripple DC voltage in the range of 11 to 14 kv DC. (Output voltage setting is to be adjustable in 500-volt steps.) Maximum output power rating, at 14 kv DC, is 70 watts. Short-circuit protection is required to protect the power conditioner in the event of thruster arcing.

An extractor supply is required at a regulated voltage level equivalent to -10 percent of the needle supply voltage. Wattage required is essentially negligible. As with the needle supply, short circuit protection is required during periods of thruster arcing.

Each of the four vector electrode supplies provides a variable regulated output voltage ranging from 0 to 6 kv DC. Each pair of supplies is connected to provide a reversible polarity output to one pair of vector electrodes with the individual outputs referenced to the needle potential. An external low-level analog command signal establishes the resultant output for each pair, thereby controlling beam deflection. The output wattage of the vector supplies is very small, but short-circuit protection must be provided in the event of thruster arcing.

Output needle supply current is sensed to provide an indicator of mass flow. This signal is furnished to the feed system temperature controller, contained within the PCU, which acts to control feed system pressure. An estimated 2 watts is controlled in this function.

The second temperature controller contained within the PCU provides high accuracy control of the needle module temperature. A predetermined set point is established and compared with the signal derived from a thermistor located at the thruster. Approximately 1 watt of thruster heater power is required.

10.2 GENERAL DESIGN CONSIDERATIONS FOR POWER CONDITIONER SELECTION

The selection of a particular overall approach for the PCU yielding minimum weight, maximum efficiency and high reliability rests primarily on the particular circuit approach utilized for providing the high voltage needle power, since this output comprises the bulk of the total delivered power. Two special characteristics of this load are the requirement for a very high step-up ratio of the primary source voltage to the required needle voltage level, and the occasional presence of intermittent output arcing.

The step-up, accomplished through conventional techniques involving a primary power switching transistor and a high ratio transformer, presents the problem of high reflected capacity on the primary side. This capacitance primarily derives from a complex combination of transformer stray capacitances, such as secondary layer-to-layer capacity and winding-to-winding capacity, the total of which is multiplied by the square of the step-up ratio when reflected to the primary circuit. The high transformer turns ratio also results in a unit yielding relatively high leakage inductance due to the need for added insulation to stand-off the high voltage between primary and secondary. These factors combine to adversely affect power switch operation. During turn-on, for example, following either an output short or normal equipment start, a high charging current flows through the transistor into the discharged reflected capacity. Since the power transistor initially sustains the full input voltage in this condition, a severe transient stress occurs

which may fall beyond the "safe area" capabilities of the device. During turn-off, the effect of high leakage inductance manifests itself in the generation of high, and possibly excessive, transient voltage levels across the power transistor.

Output arcing represents an overload condition ranging anywhere from zero impedance up to the rated load value during which protection of critical semiconductor components must be assured. This arcing is high in EMI content and may couple through output transformer windings to the primary power circuitry through common mode impedances resulting in severe stresses being placed on the power switches. The charging of output filter capacitance to the high output voltage required, subsequent to the cessation of an arc (or during equipment turn-on), may, depending on circuit choice, also unduly affect power switch stress.

Other factors influencing the selection of a basic high output voltage circuit configuration are: the relative ease in implementing redundancy should reliability considerations so dictate, and the influence of the primary current switching waveform (as affected by basic circuit choice) on system input filter size and weight.

For any PCU system approach selected for this application, a relatively large number of parts will be required to implement all the various functions and requirements. This, along with the need for isolation of the very high voltages developed by the PCU (through insulation spacing requirements, etc.), will result in a disproportionate system weight for the amount of output power processed when compared to other systems supplying loads at conventional voltage levels.

10.3 HIGH VOLTAGE SUPPLIES

10.3.1 Description of Candidate Converter Circuits

There are three candidate regulated DC-DC converter approaches capable of providing the high voltage requirements (needle, extractor, and vector electrode supplies) of the PCU:

- Square wave inversion type (SWI)
- Pulse width inversion type (PWI)
- (IES) or energy-loading type

Block diagrams are shown in Figures 46, 47, and 48.

The SWI type consists basically of an input filter, a fixed frequency switching modulator (buck type line regulator), and an unregulated DC-DC converter stage (fixed frequency square wave inverter-transformer-rectifier-output filter). Output voltage is sensed and compared with a voltage reference in an operational amplifier which, in turn, controls the switching modulator stage via a duty-cycle generator. A frequency standard provides the timing function for the inverter and modulator stages. Overload protection for the converter is obtained through a separate control loop by controlling the duty-cycle generator from a signal sensing converter output current.

The PWI type consists of an input filter, a switching power modulator of the pulse-width inversion type, a transformer, rectifier and output filter. It is characterized by high efficiency and low weight due to the combination of regulation and inversion functions within one power switching stage. Sensing and control of output voltage and overload protection are implemented in a similar manner to that described for the SWI type converter.

The IES, an energy ladling type DC-DC converter, consists of an input filter followed by a form of switching power modulation wherein an inductive element stores and delivers energy cyclically to an output filter and the load. The transformation function is also achieved in the inductive element. This system is characterized by high efficiency and lightweight with an added advantage that, during output faults, the power switching element within the modulator is not subjected suddenly to the fault load.

A variety of operating modes and output voltage sensing, control, and power switch drive configurations are available, their choice depending on the particular type of application involved. A separate control loop providing overload protection is not required in this type of converter since it is inherently achieved. A more detailed description of the basic operation of the IES converter is given in Appendix A.

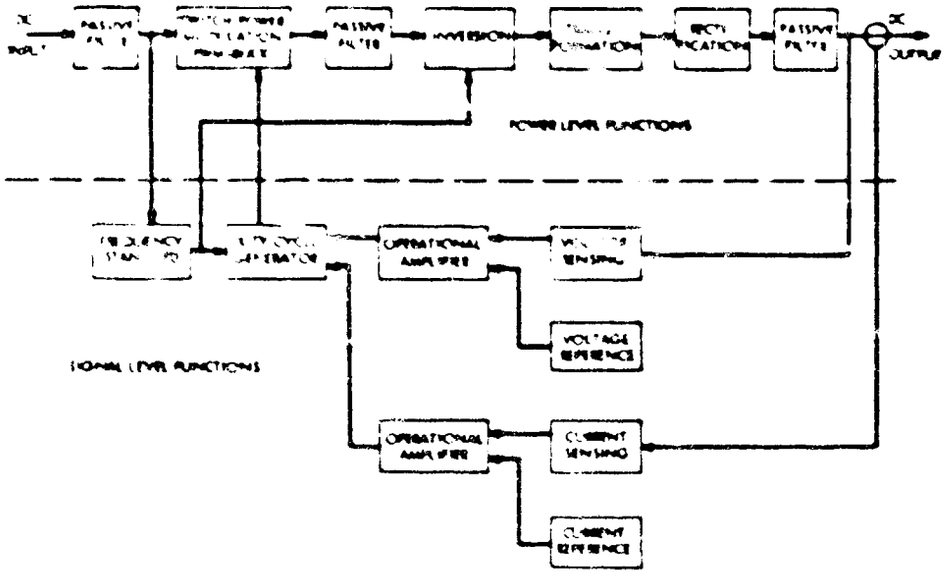

Figure 46. DC-DC Converter (SWI)

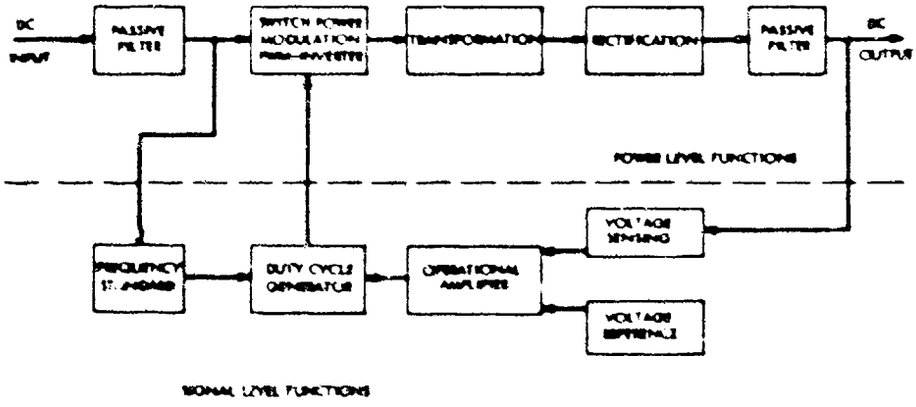

Figure 47. DC-DC Converter (PWI)

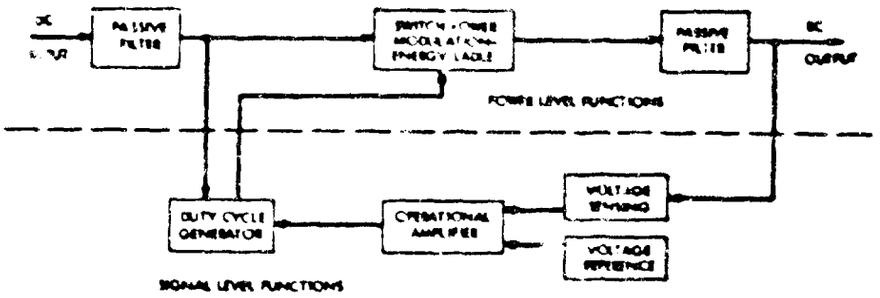

Figure 48. DC-DC Converter (IES)

10.3.2 Circuit Tradeoffs for Needle Supply

The general design considerations noted in Section 2 indicate some of the i[illegible]tant factors to be considered in the following paragraphs in comparing t[illegible] elative merits of the three basic converter approaches for satisfying the high voltage needle o[illegible]put requirements of the RVCT power conditioner.

10.3.2.1 Step-up Ratio

In either the SWI or PWI converter approaches, the high voltage transformer-rectifier-output filter configuration is an important consideration. The utilization of a multiple configuration, wherein several individual transformers and rectifiers are cascaded to develop the high output voltage, offers the advantage of a significant reduction in reflected stray capacitance when compared to the single output circuit configuration. The 14 kv needle output can be provided by using five transformers with primary windings connected in parallel and individual secondaries connected to separate-series-connected, output rectifier-filter combinations. Figure 49. shows a simplified schematic of a PWI unit.

The determination of the amount of reflected capacitance reduction, though appreciable, is difficult to assess in the general case owing to the specialized nature of construction techniques available for use in the design of minimum-weight, high-voltage transformers. Significant reductions in magnetic winding insulation voltage stress (and, to a lesser exte[illegible], leakage inductance) in the individual transformers of the multiple

scheme, due to the decreased turns ratios achieved, may not be fully realized since the interwinding insulation must stand-off the full output voltage, resulting in added weight over the single output circuit configuration. Despite this limitation and that of a higher part count, the use of a multiple configuration in either FWI or SWI converter approaches is desirable to obtain a large reduction in primary circuit reflected capacity.

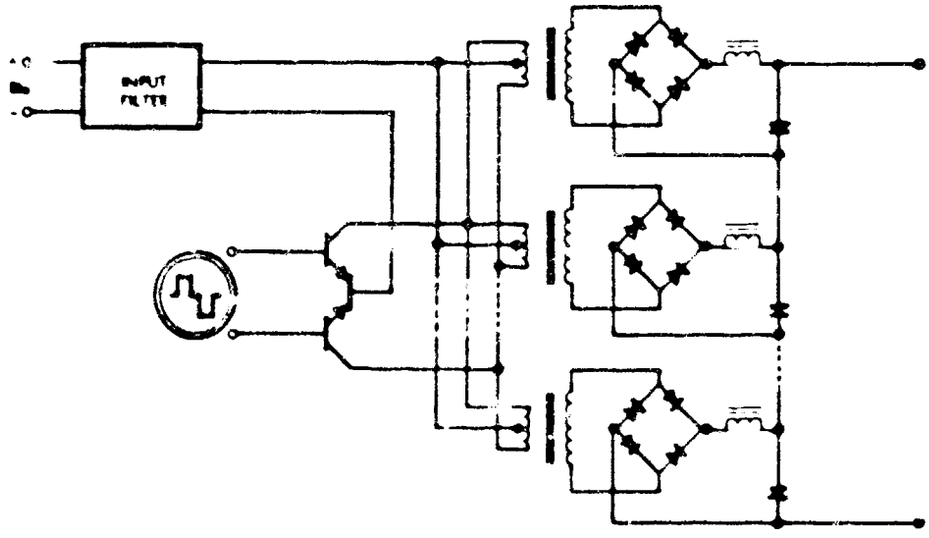

Figure 49. FWI Converter with Multiple Transformer-Rectifier-Filter Configuration

The IES or "energy-ladling" converter utilizes an inductive element, a single transistor power switch and an output diode and capacitor to simultaneously achieve conversion, regulation and transformation functions. (See Figure A-1a, Appendix A.) The output voltage is a function of both the inductor primary-to-secondary turns ratio and the transistor on-time to off-time ratio. Because of the added flexibility offered through the selection of a suitable on/off ratio, a high output voltage can be obtained with a much-reduced magnetic device turns ratio, thereby eliminating any need for a multiple output circuit configuration.

A sharp reduction in turns ratio, obtained in this manner, does not necessarily lead to a corresponding reduction in the effect of primary reflected stray capcity. In a converter designed to operate with a

rectangular, or actually, trapezoidal primary current waveform, a leading-edge current spike occurs during the transition from the switch "off" to "on" state. This arises from a combination of the effects of reflected capacity (as it is brought to a full reversed charge) and output diode recovery. By designing an IES converter to operate with a triangular primary current, these effects are essentially eliminated. In this case, at the onset of the turn-on period, the output diode current has decayed to zero thus allowing full recovery and the reflected capacitance is essentially discharged to zero and does not have to experience the otherwise full voltage excursion at the transition. Thusly, the effect of stray capacitance is further reduced over that achieved through the reduction in turns ratio.

10.3.2.2 Efficiency

Certain basic problems exist in the basic IES converter for which corrective measures are required to achieve the high efficiency desirable in electric propulsion applications. These relate to the energy storage inductor power loss (a function of leakage inductance and instantaneous primary current), power transistor switching loss, and output rectifier recovery. Special circuit modifications have been developed which overcome these basic problems, enabling the attainment of high efficiency in this converter approach. These, briefly, consist of added passive networks which (1) recover inductive switching energy to minimize energy storage inductor power loss, and (2) phase transistor current and voltage during switching to obtain essentially zero transistor switching loss. Output rectifier recovery loss, not peculiar to the IES approach, can be effectively eliminated by proper circuit configuration such that diode forward current goes to zero before voltage reversal to the blocking state is initiated. This technique requires the use of the triangular primary (and secondary) current previously indicated. Of itself, the diode recovery loss may be tolerable but because of the effect of the recovery current transient reflected into the primary winding (which induces both large current demands on the power transistor during off-to-on transitions and ringing), it is advisable to utilize the triangular current technique

where maximum efficiency is to be obtained. The higher peak stress level that must be tolerated in the power transistor, along with an increased input filter weight (over that required when rectangular or trapezoidal currents are drawn from the power source) must, in the final analysis, be balanced against the minimization of recovery problems (and reflected capacity) through the use of triangular waveforms.

The PWI and IES converters are inherently more efficient than the SWI type because the primary source power must, in the latter, pass through two, rather than one, saturated semiconductors. (Figure 50, shows a simplified schematic of the SWI converter with a multiple output circuit configuration). For the needle supply application, efficiencies of approximately 93 percent may be obtained in the former types with the aid of specialized design techniques and modifications. The efficiency of both the PWI and SWI converters is penalized from the effects of transformer half-cycle to half-cycle volt-second unbalance and inverter transistor storage time. These two factors result in increased inverter switching losses. In the PWI converter, the dwell period acts to preclude the occurrence of the latter effect (except under low input line voltage conditions). The net difference in efficiency in these two converter systems (PWI and SWI) can range from 5 to 8 percent.

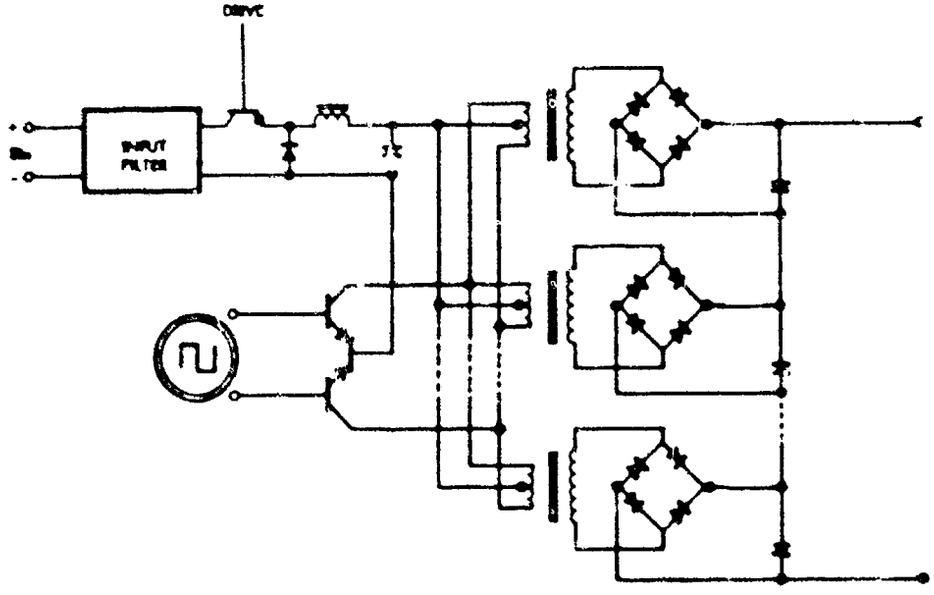

Figure 50. SWI Converter

As with the IES converter, recovery losses in the output rectifier diodes of PWI or SWI converters, especially high voltage types, represent a significant loss factor largely due to the effect of diode recovery time on the switching characteristics, hence losses, of the inverter transistors. This effect is more pronounced in the SWI type than in the PWI type.

10.3.2.3 Overload Protection

A particular advantage of the IES and PWI converter approaches in thruster applications is the fact that fast build-up of output current, and consequent surge stress in primary switching elements, is prevented. In the former, the primary and secondary windings of the energy storage inductor are never directly coupled with the result that the power transistor in series with the primary does not experience any sudden increase in current during severe converter overload or short circuit conditions. In the PWI converter the output filter inductor limits the fast buildup of output current. For these converters relatively simple and slow-acting overload protective measures can be utilized. By contrast, the SWI converter approach requires a separate, fast-response, control loop for overload protection of the inverter transistors. This entails extra parts for an output current sensor and an operational (feedback) amplifier.

10.3.2.4 Weight

Total part count is a primary factor in comparing the weight of the various converter approaches. In this regard, the IES converter has an inherent advantage arising from the fact that its power stage is single-ended rather than push-pull and that a multiple output circuit configuration and a separate, fast-response, overload control loop are not required.

Another factor is the total combined weight of required converter magnetic components. Both SWI and PWI converters require the use of an averaging or L-C type filter; in the former, it is connected after the pre-regulator power switching transistor, while in the latter, it is connected following the output rectifier. In the IES converter, the energy storage inductor combines both transformation and filtering

functions. Generally, therefore, the energy storage inductor of an IES converter will weigh more than the output transformer alone in the other converter types. However, in applications where high voltage is involved, insulation becomes a critical factor in establishing component weight. For the needle output requirement, preliminary calculations have indicated that the weights of an energy storage inductor for an IES converter and a multiple (five transformer) combination as used in either a PWI or an SWI converter would be approximately the same (1.25 lb). Further, in the case of the PWI converter, the output filter choke contributes significantly to total part weight since it is required to stand-off the full output voltage. Even in a multiple output circuit configuration (Figure 49), each filter choke, nominally designed for a winding voltage stress equal to the output voltage divided by the number of seriesed units, must stand-off the full output voltage to ground.

Offsetting somewhat this advantage in favor of the IES converter approach is the additional weight that would be required in the converter input filter when operating on a triangular current basis. Output filter capacitance weight is also increased over that required for an SWI converter. On balance, for this application, the IES converter should yield the least total part weight.

10.3.2.5 Reliability

The reliability of a correctly designed IES-type converter is basically superior to that of other converter types, not only because of the relatively small part count inherently required, but also because of the manner in which stresses in all the critical semiconductor elements are controlled under all conditions of converter operation. Operational redundancy, if required, is easily implemented by connecting several "energy-ladling" circuits into a common output capacitor.

10.3.3 Recommended Converter Approach

From the preceding tradeoff discussion, it is seen that the IES converter approach has the greatest potential for providing the combined characteristics of high efficiency, high reliability and low weight for the high voltage supplies of a vectorable colloid thruster PCU.

The figures previously cited for efficiency of the various converter approaches represent those attainable with optimum circuit design techniques and the best space-qualified parts and materials available. Little is gained in trading off additional converter weight for increased efficiency. In the present output voltage and power range, the components which are normally traded off (such as magnetic devices) represent a relatively small percentage of total converter losses.

Converter weight, normally only a function of part count and heat transfer requirements, is, in large measure, greatly dependent on high voltage insulation requirements and, in a non-redundant configuration, would probably not vary more than 20 percent for any of the converter types considered.

Using part failure rate data developed from recent TRW satellite operating experience, the part count necessary to supply the colloid thruster high-voltage requirements in any of the converter approaches discussed is such that a reliability goal of > 0.98 for 10,000 hours can be achieved in a non-redundant configuration. A reliability-weight tradeoff, therefore, is not applicable.

10.3.4 Vector Electrode and Extractor Supplies

The IES converter approach is ideally suited for supplying vector electrode and extractor output requirements. Functionally, the requirements are for high voltage bias supplies, normally providing a negligible output current yet requiring overload protection.

The extractor supply can be simply derived from the needle supply IES converter by the addition of an extra winding on the energy storage inductor and an output rectifier and capacitor. Obtained in this fashion, the extractor output voltage can be designed as a fixed percentage of the needle supply voltage with the requisite ripple, regulation and overload protection features.

In the case of the vector electrode supplies, four variable output voltage IES converters, controlled in a unique manner, can be operated independently to provide, in pairs, the required reversible polarity

deflection controls. Each converter would produce a regulated output voltage up to maximum of about 1 watt, in response to an external analog command signal. Above this level, the average output power decreases since the converter becomes, effectively, a constant current source; overloads or short circuits do not reflect an increasing power source drain. In normal operation, the level of quiescent, or no-load current drawn can be maintained very low with the use of a recently developed power switch control technique featuring automatic adjustment of the converter on/off ratio.

The vector electrode outputs are referenced to a fixed 3-kv level below the needle potential. For any required deflection, the output of each pair of converters, individually variable over a zero to 6 kv range, is connected so as to provide any potential within a band of ±3 kv about the needle potential. For zero degrees deflection, individual converter output is 3 kv, resulting in zero voltage potential between the two deflection plates and between the deflection plates and the needle.

10.4 LOW VOLTAGE SUPPLIES

Three low-voltage supplies are required for the colloid thruster power conditioning unit. These are the neutralizer, the feed system temperature controller and the needle module temperature controller. Total power output for all three supplies amounts to less than 10 percent of total PCU power.

Neutralizer heater power is efficiently and simply controlled utilizing an AC output, series saturable reactor circuit. With this type of control, a constant average output current is maintained with a constant low-level input current control signal. Also, this circuit provides a desirable soft-start capability; i.e., during neutralizer turn-on, output current is allowed to build up slowly to the desired level. Circuit efficiency is a function of the operating frequency and weight goals. Typical values fall between 91 and 95 percent for the low output power level required (3 w).

High-accuracy temperature control circuits, either proportional or on-off types, can be easily implemented utilizing, for the most part, integrated circuits, and they have slight impact on PCU system efficiency and weight.

For the feed system temperature controller, the input signal is derived from sensing needle supply output current. The DC current monitor circuit can be best implemented as a DC output series saturable reactor circuit. AC power for both the current monitor and the neutralizer heater control can be simply obtained from a small (5 w) inverter circuit producing a square wave output. Total estimated weight for the low voltage supplies is approximately 0.3 pound using a 1 kHz inverter. Estimated power loss is less than 3 watts.

10.5 RECOMMENDED POWER CONDITIONER SYSTEM

From the tradeoff discussion of the preceding paragraphs, a basic PCU system that reflects the best compromise in obtaining desired efficiency, weight and reliability characteristics, can be recommended. As stated previously, the implementation of the needle output supply, which provides the bulk of the required power, at very high voltage, is the key consideration. For this, the IES converter, primarily on the grounds of reliability and efficiency, should best provide the specified requirements.

The recommended PCU system is shown in block diagram form in Figure 51. Included are the IES converters for providing all the high voltage outputs, the neutralizer heater control, the temperature controllers and an input line filter.

The filter enables the PCU to meet system EMC requirements by preventing large current excursions from being reflected to the input terminals. It also attenuates audio frequency disturbances present on the input line. Telemetry outputs are not shown.

From preliminary calculations, the weight and size of the PCU can be approximately 6 pounds and 250 cubic inches (6" x 7" x 6"), respectively. Total system efficiency, also based on preliminary calculations, is 88 percent. Reliability for a 10,000 hour mission life, using latest space-use failure rate data, is calculated to be 0.990.

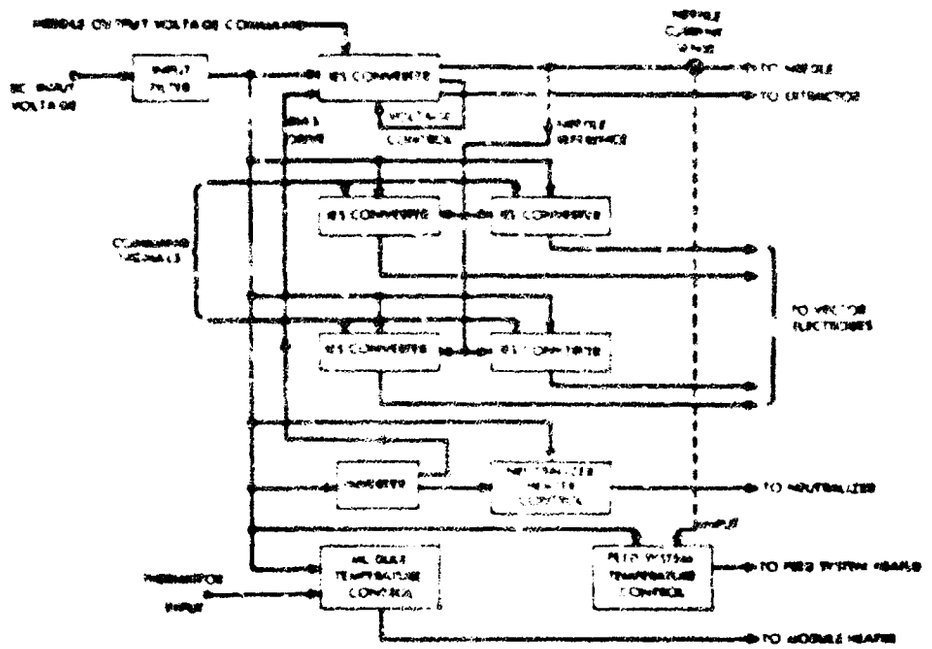

Figure 51. Basic PCU System Block Diagram

11. AC AND PULSED OPERATION OF A COLLOID SOURCE

11.1 INTRODUCTION

This research was undertaken to extend present knowledge about the operation of a colloid source on AC and pulsed voltages. Studies at AFAPL (Ref. 11-1) had already been performed with sinusoidal voltage for a range of frequencies. Studies at IBM had shown successful pulsed operation. The main directions of effort were: (1) to develop a method to measure faithfully the instantaneous needle current, (2) to investigate the jet formation and collapse time by studying the needle current response to a pulsed voltage on the extractor, (3) to develop a low capacity spark gap that would allow time-of-flight (TOF) analysis on both positive and negative cycles, (4) to perform the experiments in a system that would allow continuous observation under a microscope, (5) to use phase-synchronized stroboscopic illumination to observe jet formation and collapse during the applied voltage cycle, (6) to recognize problems associated with large capacitive currents and handle them by resonance techniques, and (7) to extend the frequency beyond 50 kHz. The chronological progress of the research is presented in this section.

11.2 RESEARCH PROGRAM

During the first month of the AC and pulsed colloid research effort, a new AC diagnostic test station was completed and put in operation. A balanced differential attenuation circuit for direct oscilloscope recording of instantaneous true needle current was built and tested.

Two experimental runs were then made. The first tested the use of the differential attenuator with AC modulation signals; the second tested the use of a triggered spark gap as a time-of-flight switch.

Sine wave signals from 140 Hz to 2 kHz frequency and up to 2400 v (peak-to-peak) amplitude were applied to the extractor of a single-needle colloid module. The needle voltage was +7 kv; the extractor bias was -600 v, and the average needle current was 7-9 μa. As expected, strong non-linearities in needle current response were noted. The most interesting results were obtained for maximum amplitude signals of 140

and 320 Hz. At the lower frequency, needle current appeared to stop completely for about 3 milliseconds and returned in a series of four "steps" over the next 2 milliseconds. At the higher frequency, complete interruption lasted for a little over 1 millisecond, and the turn-on was much smoother. It appeared that as modulating signals, rectangular pulses of varying duration would be more revealing than sine waves.

For the second run, rectangular pulse trains of varying duration and repetition rate were applied to the extractor. The pulse trains were amplified to approximately 1500 v peak amplitude using a vacuum-tube and step-up transformer circuit. In order to compensate for the tilt in pulse waveform at the output of the transformer, a lag network was incorporated in the amplifier input. This allowed the pulse shape to be sustained at maximum amplitude for about 2 milliseconds before onset of transformer saturation. Figure 52 shows current as measured at the TOF collector (approximately 2 μa). The vertical scale is 1 μa/division; the horizontal scale is 1 millisecond/division. The three traces in the upper frame show turn-on after off-time pulses of 0.1, 0.15, and 0.2 milliseconds, respectively, and in the lower frame after pulses of 0.4 and 0.7 milliseconds.

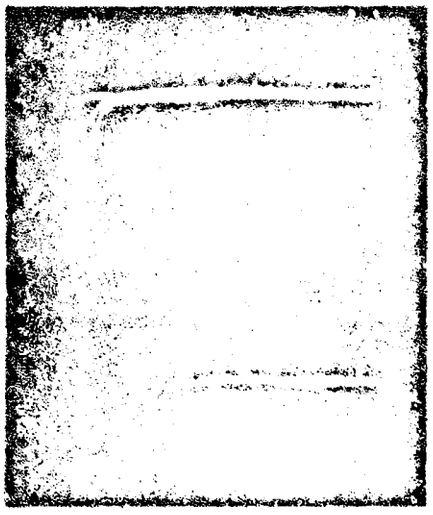

Figure 52. Collector Current Waveforms Following Off-Time Pulses of (a) 0.1, 0.15, 0.2, and (b) 0.4, 0.7 milliseconds. Horizontal scale is 1 millisecond/division.

These results are important for two major reasons. First, they show that the current can be completely stopped by only a fractional reduction of the voltage. This will make the power-conditioning for pulsed operation simpler and more efficient. Secondly, they give clear insight into the mechanisms of formation and collapse of the jets. It appears that minor collapse occurs in 0.1 ms, extensive collapse in 0.5 ms and almost complete collapse in 1 ms. Complete reforming of the jet takes about 3 ms, dependent on the degree of collapse and most likely the degree of over-voltage. The 50-millisecond readjustment period mentioned under the pulsed work is probably associated with the fluid motion under the jets. These time scales are consistent with later observations of jets forming and collapsing below 100 Hz while remaining stable throughout the cycle at higher frequencies.

For the initial attempts at time-of-flight measurement of beam characteristics, a commercial spark gap, type GP-22 (EG&G), was used inasmuch as it was readily available. With a negative trigger spike applied to the gap, an additional 0.005 μfd capacitance was required at the needle to enable the gap to fire completely. Even then, a significant delay and considerable jitter were observed so that the resulting TOF trace was not a good indication of beam conditions at the instant of the trigger pulse.

A small triggered spark gap was then built using two metal hemispheres of about 1/3 cm radius with air dielectric. The trigger electrode was centered in the grounded electrode. Gap spacing was adjusted to give the most reliable triggering in the working range of needle voltages. Additional capacitance was not required in order to allow this gap to fire. As with the larger gap, the trigger arc was followed after a measurable time interval by transfer of the arc to the main gap which then switched off the needle voltage. The smaller gap reduced this time interval from something over 100 microseconds to about 8 microseconds.

Using the balanced attenuator circuit as well as collector current readout, more measurements were made of needle current response to step reductions in accelerating potential. The following quantitative results were observed: from an initial 7.6 kv accelerating potential, a step reduction (positive voltage step on extractor) of 1000 volts brought the needle current to zero after 1 millisecond; a 2 kv step stopped it in half that time; and a step of less than 1 kv could not completely interrupt the current. Once interrupted, the current took from 2 to 6 milliseconds from the end of the pulse to restore itself, depending on pulse amplitude and duration. The turn-off interval was also dependent to a minor extent on propellant feed pressure.

Better impedance matching between the audio amplifier and the step-up transformers improved both the amplitude and rise time of the modulation signals. When AC and square-wave signals of ± 5 kv peak amplitude were applied to the needle, collector current pulses were noticeable, but new difficulties were revealed in the attenuator circuit. In particular, with continuously varying needle voltages, redistributions of electric charge on insulating surfaces (particularly at points of transient high-field conditions) gave rise to micro-arcs. These arcs became a severe source of noise in the output signal at peak needle voltages over about 3 kv. The attenuator circuit was then rebuilt, giving more attention to symmetry and electric field considerations. A new step-up transformer was designed to enable operation at up to ± 10 kv, AC or square wave, at frequencies of 100 Hz or higher, with either single or bipolar modules.

Continued work on the spark gap, resulting in the design shown schematically in Figure 53, further reduced the response time. The design consists of two spherically curved surfaces, one grounded and the other connected to the thruster needle. The trigger electrode is coaxially located in the grounded electrode. The gap electrodes are formed by rounding the ends of two 3/8 - 16 bolts positioned inside a threaded Plexiglas block. The ground electrode screw is drilled to accept a 3-mm glass tube which acts as a containing insulator for the trigger electrode wire, and also extends the length of the trigger spark so as to instantaneously shorten the effective gap spacing. The main

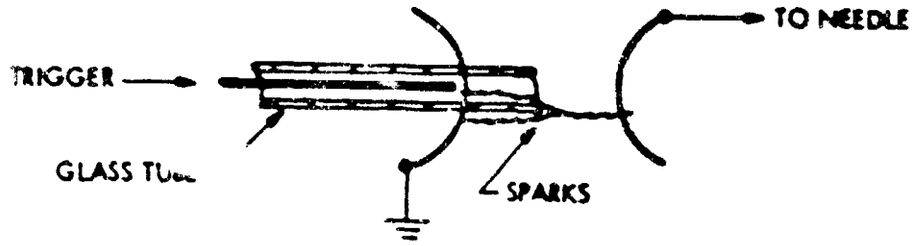

Figure 53. Triggered Spark Gap Design

gap spacing is adjusted to about 0.2 inch, which is sufficient to hold off 10 kv. The end of the trigger wire is brought flush with the surface of the grounded electrode, and the end of the glass tube is extended to about halfway between the main electrodes. Trigger spark polarity is typically made the same as the needle electrode, so that at the instant of the trigger spark, the breakdown first propagates from trigger to ground electrode, then the main discharge occurs in the short gap between the trigger spark plasma and the needle electrode. This design adds very little extra capacitance to the needle circuit, and triggers reliably from a few hundred volts to over ±10 kv.

A 15-kv trigger pulse for the gap is provided by an E.G.G. type TR-69 transformer driven by a Type 2N4102 Silicon Controlled Rectifier (SCR). A transistor amplifier stage triggers the SCR from either a push button or an electrical timing pulse. The time delay from input pulse to main gap breakdown is a fairly stable 3 μsec. Thus it is possible to trigger the gap from the start of an oscilloscope sweep and record collector current beginning approximately 3 microseconds prior to the time-of-flight spark. The onset of the main time-of-flight trace is signalled by a small noise pulse superimposed on the trace.

A special transformer was wound using a 1.5 x 1.5 square stack of EI-150 (0.014 thick) laminations as the core, and having 280 turns, No. 27 wire and 20,000 turns, No. 42 wire center-tapped, as primary and secondary. The entire unit was vacuum potted in epoxy. When driven by the 600-ohm output of a 30-watt McIntosh audio amplifier, it delivered 10 kv (rms) between each end of the secondary and the center tap at 70 Hz. With a suitable lag network between the input to the audio amplifier and a square-wave generator, it was possible to control the tilt in the output waveform down to about 60 Hz square waves (depending on amplitude).

Square-wave rise time for a 10-kv amplitude (20-kv excursion) is 120 microseconds (167 volts per μsec slewing rate), measured with one end of the secondary grounded, center tap open. Similarly, the maximum sine-wave frequency for 10 kv peak output was about 1200 Hz. This transformer considerably extended the needle voltage capability.

11.2.1 NaOH - Glycerol Propellant

A propellant mixture of 1 gm NaOH to 25 ml glycerol was used with a platinum needle of 0.014 inch O.D., with DC, AC, pulsed, and square-wave needle voltages. No quantitative data could be taken because of the very erratic nature of the beam performance. Operation on DC was characterized by sudden bursts of current of varying amplitude, each with an approximately exponential decay. With each burst, a yellowish glow appeared at the needle tip. All time-of-flight traces showed a pronounced ion peak.

The difference between the performance of NaOH doped glycerol seen here and that reported by Burson (Ref. 11-2) is thought to be due to formation, in our case, of gas bubbles within the platinum needle, whereas this apparently was not a problem with the steel needles. Analysis of the time-of-flight data showed in one case a significant colony of droplets with a velocity of about 77 km/sec and average charge-to-mass ratio of 2.95×10^5 coul/kg. The nearest quantized value of 3.22×10^5 corresponds to one Na^+ with 3 glycerols. Some other typical numbers for overall traces were: positive half cycle - I_{sp} = 2988 sec, $(Q/M)_{eff}$ = 47,637 c/kg; negative half cycle - I_{sp} = 2435 sec, $(Q/M)_{eff}$ = 31,647. It might be well to try a smaller concentration of NaOH doping at some future date. However, in order to establish a firm base for comparison of AC and pulsed operation with DC operation as seen elsewhere in our laboratory, it was decided to return to the use of NaI - glycerol at this time.

11.2.2 Sine-Wave and Square-Wave Operation, NaI - Glycerol

Following a brief run under DC conditions, comparisons were made of needle operation at 50 Hz sine wave, 500 Hz sine wave, and later at 60 Hz square wave. During the DC operation, several TOF traces were made to determine the character of the beam as a function of voltage. It was

found that the relative fraction of extremely fast particles was negligible for needle voltages below about 4 kv, and increased rapidly with voltage above that point. Consequently, the operating voltage for the 50 Hz sine wave was kept below the point where a large fraction of fast particles would appear. Figure 54 is a sketch of the needle voltage wave form (V) showing a solid line during the time current appeared, the current waveform (i), and two values calculated from TOF pictures — thrust (f), and I_{sp}. Current (and hence thrust) appeared from about 60 degrees to 130 degrees during the positive half cycle and between 237 degrees and 307 degrees during the negative swing. Specific impulse and average thrust were typically lower on the negative side. The average thrust over the entire cycle was 6.01 μlb_f.

At 500 Hz the performance as indicated by TOF pictures was radically different. The current pulse duration was still about 70 degrees of phase angle, but shifted about 10 degrees later in the cycle than at 50 Hz. TOF traces showed a predominance of fast particles until very late in the cycle, when the current and voltage were both low. The pictures did not look particularly promising, and were not analyzed in detail.

Operation of the needle with approximately 60 Hz square wave is shown in Figure 55. The upper trace in the upper frame is needle voltage at 4 kv/division; the lower trace is collector current. In the lower frame, the collector current signal is superimposed on the needle current signal derived from the balanced attenuator circuit. TOF traces taken at various times during the cycle gave the results shown in Table 11-1. The average value of thrust over the cycle is 6.11 μlb_f.

Data reported in Table 11-1 were taken at intervals during a three-day period following an initial startup. When not set for operation in some other mode (for exploration or data taking), the mode of operation was 60 Hz square wave. Total continuous operating time in this mode was probably more than 50 of the last 58.5 elapsed hours of this period.

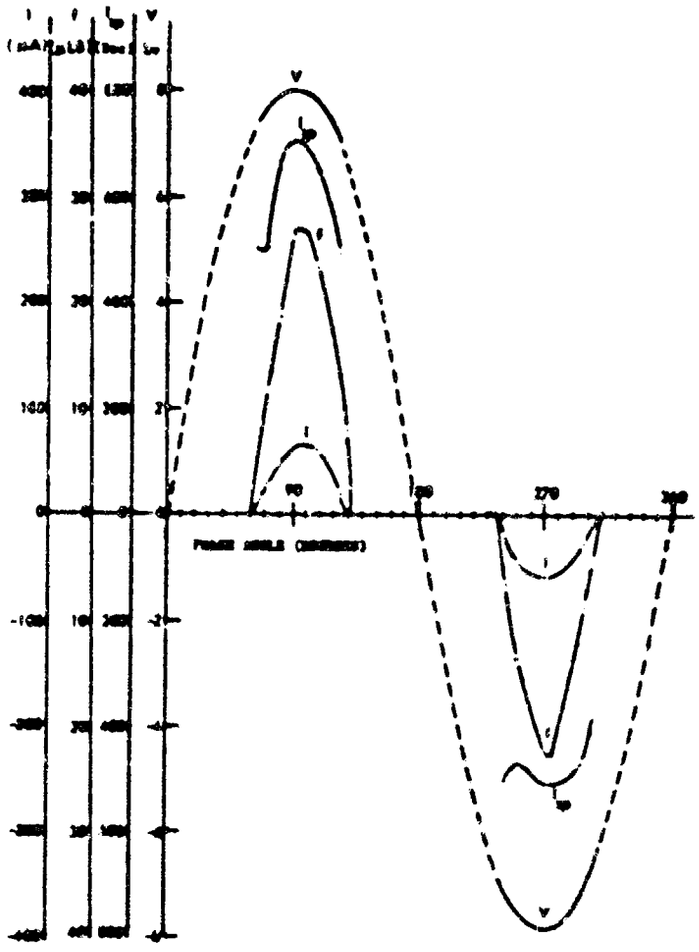

Figure 54. 50 Hz Single Needle Performance

Figure 55. 60 Hz Square Wave Performance - Upper Frame Needle Voltage (Upper Trace) and Collector Current (Lower Trace) versus Time; Lower Frame Collector and Needle Currents Normalized and Superimposed.

Table 11-1. TOF Results for 60-Hz Square Wave

t (msec)	I_{sp} (sec)	f (lb_f)	(q/m) (coul/kg)	V_n (kv)	I (μA)	$\dot{m}$ (μg/sec)	η (%)
1.0	437	4.6	1508	6.1	8	5.3	92
2.0	648	5.4	3301	6.1	18	5.4	71
3.0	790	7.2	4915	6.1	28	5.7	74
4.0	815	6.7	5230	6.1	28	5.3+	72
6.0	733	8.2	4230	6.1	30	7.0	74
7.5	754	6.3	4546	6.0	24	5.3+	74
9.0	310	7.7	755	-6.1	-16	21.0	55
11.0	414	7.1	1352	-6.1	-22	16.0	52
12.0	621	5.6	3042	-6.1	-23	7.5	55
14.0	738	6.1	4293	-6.1	-25	5.8	66
15.0	745	5.4	4375	-6.1	-22	5.0	67

Following the approximately 50 hours of operation at 60 Hz square wave, the needle and extractor were removed from the vacuum system for examination. A considerable deposit of dark material was seen on both the needle and extractor plate. Some roughening of the surface of the needle rim was also noted. A 50-hour run was then made using a new needle and extractor plate and DC operation to verify that these effects would not occur during normal DC operation in this facility.

11.2.3 Pulsed Mode Operation

In TRW Report 07131-6019-R0-00, Colloid Microthruster Experiment No. 17, pulsed operation at 1 pulse per second, 250 msec pulse duration was reported. There was an initial period of about 70-80 msec during which current amplitude was low and consisted of fast particles. Following an additional few milliseconds, needle performance resembled that of DC operation. Using the high-voltage transformer, we were able to generate 8 msec pulses within a 40-msec period. TOF traces indicated that we were always within the initial turn-on transient.

11.2.4 Pulsed Operation — Off Time versus Feed Pressure

An additional facility, made available for use on this project, featured a small stainless steel box that served as a needle mounting chamber. The box is of about 5 inch square cross section by 9 inches long and is fitted with three 3-inch-diameter plate glass windows through which the needle and extractor plate may be viewed while in operation. Using a short-range telescope (at 20 to 50X magnification), several photomicrographs were made of the array of jets at the rim of an operating needle. One such picture is shown in Figure 56. The axis of the needle and propellant feed tube were mounted horizontally so that it is possible to achieve zero (or slightly negative) feed pressure. A number of experimental observations were made as described in the following.

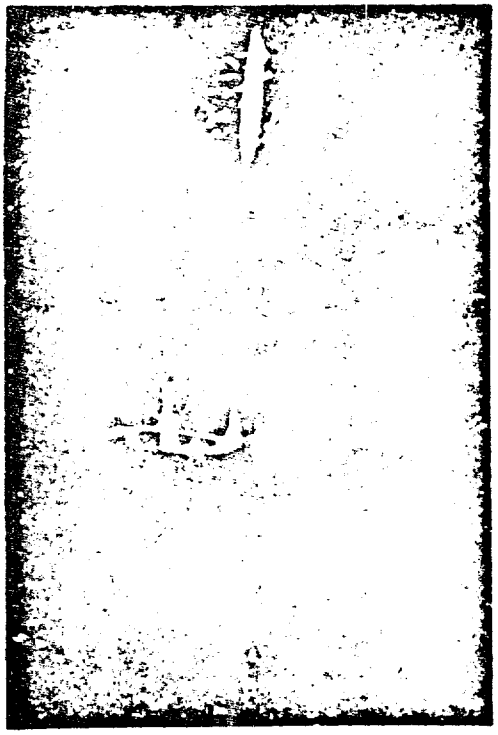

Figure 56. Photomicrograph of colloid needle in operation. Total accelerating voltage = 6 kv. Current is 11 μA. Optical focus is on the near rim of needle and shows about a dozen current sources. By adjustment of optical focus, about 30 such jets were counted around the rim of the needle.

Measurements were made which gave an estimate of the maximum safe voltage off time in pulsed operation as a function of feed pressure and operating voltage. The results of these measurements are shown in Figure 57. Following voltage turn-off, the first effect observed was a structural collapse of the spraying jets. Following this, the fluid filled the needle tip, then formed in sequence a positive meniscus, a hemispherical meniscus, and finally a large drop which wet the outside of the needle, sagged, and dropped away.

The point in this sequence considered to be a maximum safe standby condition for a non-operating needle is the hemispherical meniscus, inasmuch as, at this point, capillary forces within the drop are at their maximum. Fortunately, there is a way of determining the moment when a given meniscus size has been arrived at, although determination of the exact droplet volume is not very precise. The method consists of applying a very low value of needle voltage (about 1/3 operating value) to the needle. This voltage is then carefully adjusted so that the droplet of desired size is unstable under the action of the electric field and a portion of it is pulled off and accelerated. The measurement is the time

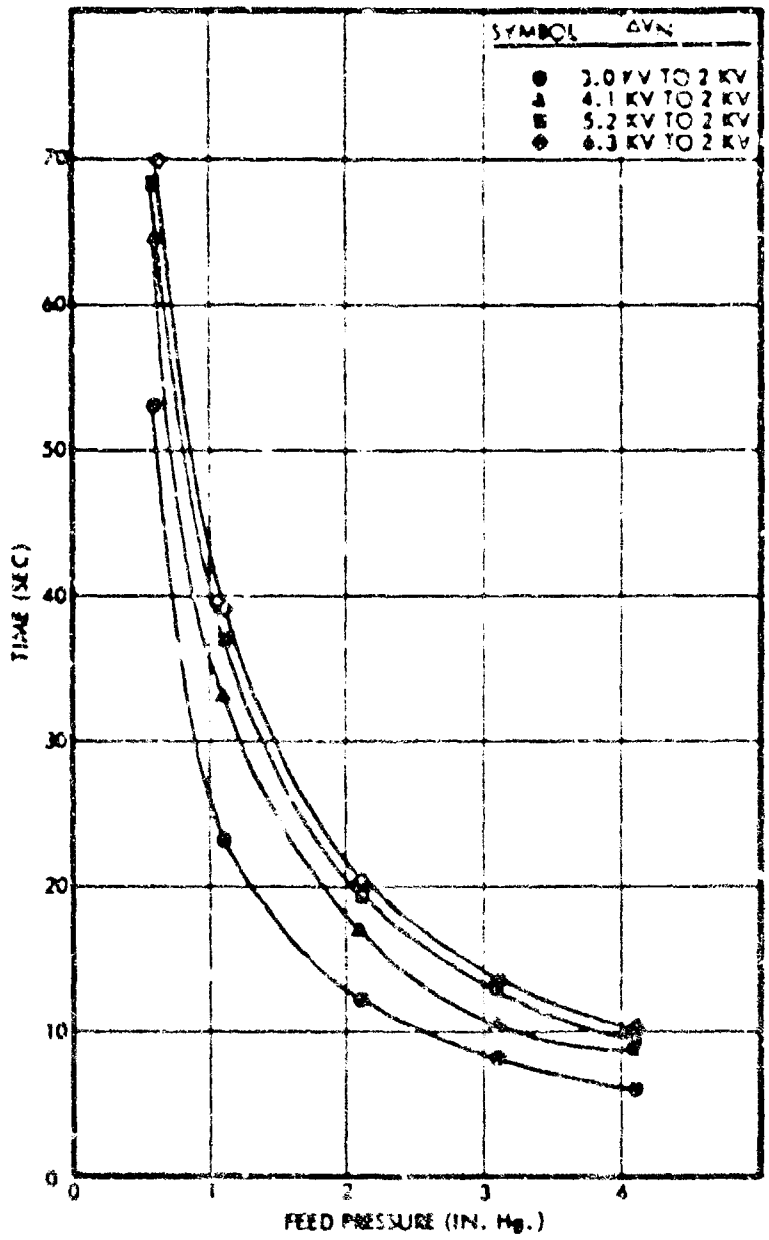

Figure 57. Time required to form spherical drop at the needle tip following a step reduction in needle voltage below the value for normal operation. Longer times are required for higher initial voltage, indicating there is less fluid within the rim of the needle at higher voltages. These plots are a measure of the maximum safe off-time in pulsed operation.

interval from reduction of needle voltage (from operating value to this lower point) until the first large droplet is expelled. Three sets of measurements are plotted in the figure indicating that the depth within the needle tip to which the (negative) meniscus is drawn also varies with needle accelerating voltage.

11.2.5 AC Operation — Phase Angle Dependence of Jets

Observations of the jet structure at the rim of a needle in AC operation were made in a manner so that the phase angle dependence could be observed. This was accomplished by illuminating the needle tip with a stroboscopic flash unit triggered at a slightly different frequency from that of the AC voltage applied to the needle tip. Both the needle voltage waveform and the strobe trigger pulse were observed on an oscilloscope so that the phase angle of the light flash could be determined.

Observations were made over the frequency range of 40 Hz to 500 Hz. At the lowest frequency, the collapse of the jets between successive alternations of the needle voltage was almost complete and formation of new jets required a large fraction of each half cycle. At somewhat higher frequencies, the collapse was only partial with the greatest collapse occurring just after the zero crossing of voltage. Jet structure during positive alternations resembled very closely that during negative alternations. At frequencies above a few hundred cycles per second, the jet structure seemed not to collapse noticeably between positive and negative alternations. Resonance effects were not observed. Apparently the damping was of a high order. It appeared that the dynamic effects observed were related only to magnitudes and frequencies of electric field and fluid mechanical forces, inasmuch as no evidence of effects due to the polarity of the electric field were observed.

11.2.6 Experimental Modifications

Problems associated with capacitive currents were becoming excessive as we proceeded to higher frequency operation. Higher frequencies (to about 3 kHz) were achieved with the original transformer by using a higher

power driving amplifier. Previously, the needle current would fall at the higher frequencies because the amplifier could not supply the higher currents associated with the charging and discharging of the distributed capacities, and the voltage would fall and become triangular with negligible time at the peak voltage. The new amplifier corrected this, but the higher frequency operation caused problems associated with the capacitive current drawn by the propellant in the glass feed line. This current caused gas generation, was variable, and could not be nulled out so as to get a meaningful measurement of the true needle particle current from the divider circuit. Also, small stray capacitances in the divider produced improper voltage division at all frequencies so direct needle-current measurements were obscured. A few modifications were effected to help the situation. The glass feed tube was replaced with a low capacity metal line. A dummy capacity was used in a bridge circuit to simulate the needle so the divider output would not read reactive currents. The dividers were redesigned. However, for high frequency and for square-wave operation, it was still difficult to accurately measure the current from the needle. The registered hole TOF collector was installed and operated with the needle in position to be observed through a microscope with constant front light or strobed back light.

Later, a transformer technique was developed for direct observation of needle current during AC operation. The originally intended method of measuring the actual instantaneous needle current (not current collected by a TOF collector) utilized accurately compensated attenuators across a series load resistor in the needle circuit. The reduced differential voltage was monitored by an oscilloscope. It was found, however, that it was impossible to balance out the large total needle voltage fluctuation (~6 kv) sufficiently enough to see the small voltage drop across the load resistor. The scope adjustments would drift. The attenuators were not exactly identical at all frequencies. Also, there existed a capacitive needle current hundreds of times the value of the emitted current. This was due to the capacitance of the needle assembly and the attached feed system.

These problems were surmounted by using a specially designed current transformer. The primary is 4,000 turns center-tapped, wound on a Teflon bobbin. The AC voltage is applied to the center tap, the needle to one side, and an adjustable, high-voltage tuning capacitor to the other. The 500-turn secondary is terminated with 25 Ω and connected to the 1 mv/cm input of an oscilloscope. Ten microamperes in the primary causes 40-microampere flow through the 25-ohm secondary load, thus producing 1 millivolt and 1-cm scope deflection. It was found desirable to shunt a 200 K Ω resistor across the primary, to damp [illegible] oscillations due to the distributed capacity and leakage inductance.

The transformer is mounted in oil in a non-metal box. The low frequency response is limited by an L/R time constant of about 0.01 second (12% and 25Ω). High frequency response is limited by leakage inductance and distributed capacity to about 8 microseconds.

11.2.7 Outside Needle Wetting

Wetting on the side of the needle during AC was investigated. Propellant would leak out onto the side, then bubble and be pulled off as jets at 90°. The bubbling was probably due to hydrogen evolution resulting from electrolytic action caused by electrons striking the fluid surface. This wetting was not as severe with square wave operation at the same frequency or DC operation, and was less severe at higher frequencies. It was surmised that the modulation of the force proportional to K^2 somehow sloshed the liquid over the side as the jets formed and collapsed. For square wave operation, K^2 was a constant except for the brief switching time. For higher frequency AC operation, the jets did not collapse.

11.2.8 Needle Current Versus TOF Collector Current

It was found that gas generated within the liquid at the tip resulted in erratic operation if the net needle current was negative or if electrons bombarded the liquid during positive operation. To eliminate electron bombardment, a negative voltage was applied to the accelerator (just as in positive DC operation). This increased the field during

positive operation, causing an unbalance of current (sometimes the negative current was zero). A constant negative bias was applied in series with the AC voltage to balance the net current to almost zero (slightly positive to prevent gas formation). These equal currents were indicated by the current transformer output as well as a DC meter in series with the needle. An untried alternate solution to the above would have been to use an AC extractor bias 180° out of phase with the main needle voltage.

The currents measured on the TOF collector did not generally agree with those indicated by the needle current monitor. The collector indicated less negative current. Since the collector had registered holes and variation of the biases had no effect, this discrepancy was real and not understood. We feel it was associated with beam spread since it is known that the collector did not catch the entire beam. There was also evidence of low angle beam scattering off adjacent walls into the collector. It is probable that scattered negative particles preferentially lose their charge. It is hard to believe that the negative half cycle has a higher beam spread since stroboscopic visual observation of the needle has shown that at moderately high frequencies there are no changes in emitting jet structure between positive and negative half cycles. If, however, some of the negative needle current was from the sides of the needle (typically quite dirty during AC operation), then the collector might have been accurately indicating a smaller quantity of negative colloid particles.

11.2.9 Typical AC Operation

Extended AC operation has always resulted in a pitted needle with foaming liquid, crystals, and tar on the outside. It was hoped that careful operation without over-voltage, and with proper potentials to prevent gas formation, would prevent these effects. However, repeated restarts preceded by careful polishing of the needle and DC startup has always produced outside wetting and material growth during AC operation. The pitting, however, was reduced and probably was a result only of arcing which can be controlled.

11.2.10 AC Power Requirements

A second high-voltage transformer was designed to operate between 100 Hz and 10 kHz. The transformer dimensions were roughly 6x7x8.5 inches. It weighed 35-40 pounds, including encapsulation. The high power required to generate high voltage at high frequency without power factor correction (resonating) initially was not fully recognized. The failure to achieve high voltage at high frequency was blamed on the transformer. Unfortunately, the capacitive load that is driven is much larger than the distributed capacity of even our old transformer, so the new transformer with lower distributed capacity did not lessen the power required. The original 30-watt amplifier could achieve only a few hundred cycles at 6 kv rms. A 200-watt amplifier allowed extension to over a kilocycle. However, this amplifier failed, and the only amplifier at hand was 90 watts, which was just adequate to achieve about 1 kHz and 6 kv rms. The amplifier, when supplying a capacitive load, must dissipate all the stored energy on the power tube anodes, thus limiting tube life. The obvious answer to this problem was to reduce the load and to shunt an inductance across the amplifier output. The load was reduced by reducing leads to inconveniently short lengths, eliminating the meter, spark gap, and current transformer (and dummy capacity). We constructed an inductance to reduce the load on the amplifier, and in this manner were able to work comfortably at 1 kHz and extend the measurements to 5 kHz, with the new transformer in conjunction with the 90-watt McIntosh amplifier.

11.2.11 1-kHz Operation

Long-term 1-kilocycle sinusoidal operation of a 0.014 inch O.D. platinum needle using 3/10 KI-glycerol propellant was typified by growth of material on the needle exterior (Figure 58) and poor efficiency. The poor efficiency was due to the beam's high ionic component. This is illustrated in Figure 59 where tracings were made of polaroid pictures of the scopeface. Trace (b) tells the story: the current consisted of an initial burst of high specific impulse particles with mostly ions as analyzed in the time-of-flight trace in (c). Most of the mass flow is represented by the current in a trailing shoulder.

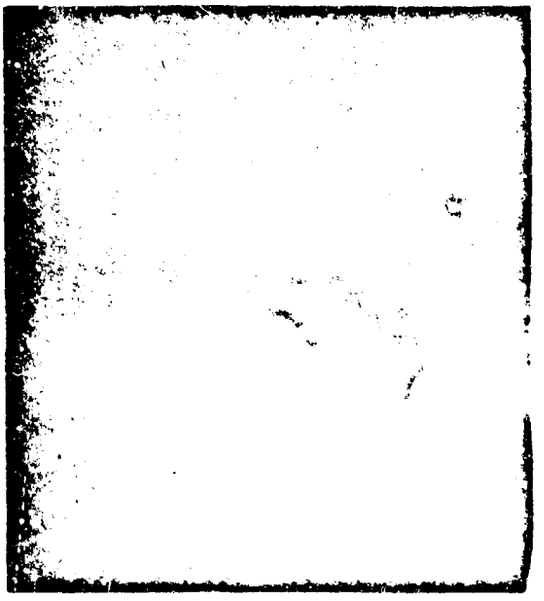

Figure 58. Microphotograph of needle after 24 hours of 1 kHz operation.

The efficiency during this period was high as seen by the trace in (d). The story during negative operation is similar, as seen in the latter half of trace (b) and the time-of-flight traces in (e) and (f). This operation was not peculiar to 1 kHz; with the needle in the condition that produced the traces of Figure 59, operation at all lower frequencies to 50 cycles produced the familiar spike and shoulder pattern similar to trace 11-8 (b).

11.2.12 50-kHz Operation

Using a 50- to 2000-turn transformer on a ferrite core with an air-gap in oil, and reducing the capacity of the needle current to 20 pf, the system was successfully run at 50 kHz. At this frequency, detailed time-of-flight analysis is impossible because the currents are not of long enough duration to steady-state populate an appreciable volume and the slow particles of a given pulse are soon overtaken by the fast particles of the next pulse. Also, it was necessary to remove our time-of-flight

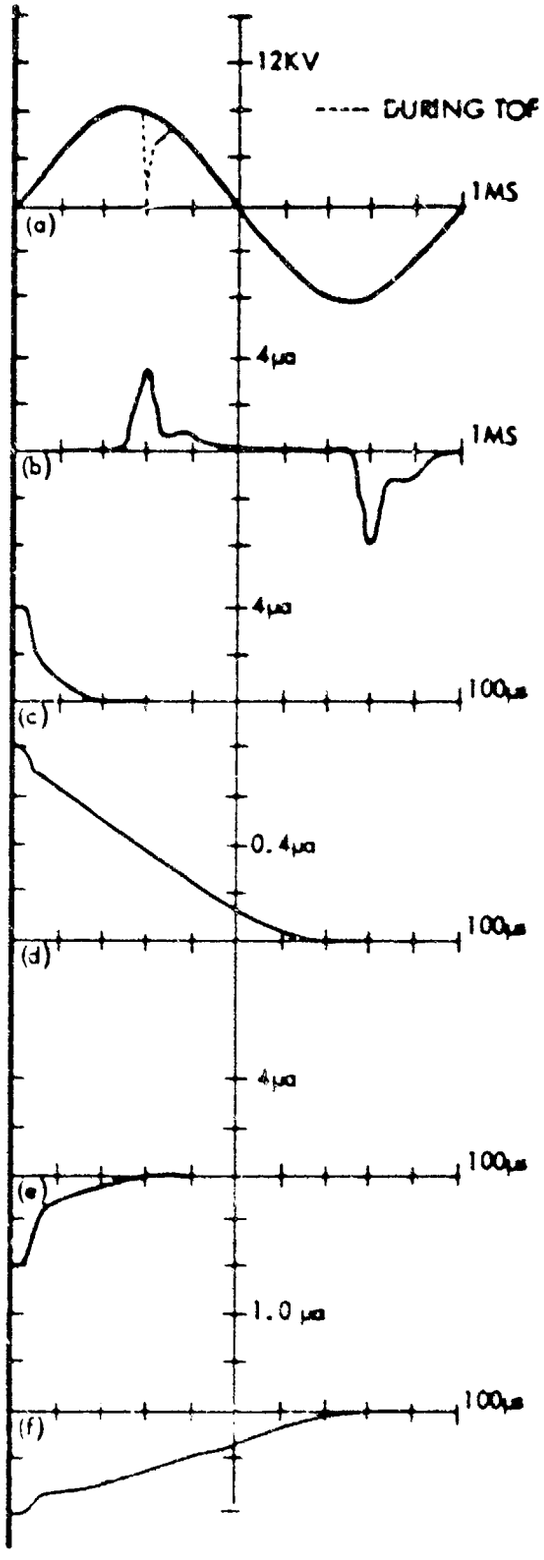

Figure 59. Waveforms illustrating typical 1 kHz operation, (a) needle voltage (b) current on TOF collector (no zaps) (c) TOF taken at peak of positive current showing mostly ions (d) TOF taken on positive shoulder (e) TOF at negative peak (f) TOF on negative shoulder. Collector distance is 30 cm.

circuit to reduce the capacity. However, qualitative observations could be made. The operation was very similar to lower frequencies if not smoother. Collector current secondary electron ratios indicated fast ion peaks as at lower frequency. Visually, the jets around the rim were similar and very stable. Outside wetting still occurred, but possibly at a slower rate. The net current still had to be balanced by including a negative voltage in series with the AC needle voltage to offset the negative extractor voltage used to trap electrons during positive operation.

Some information was gained by observing the collector current as a function of collector distance. These currents are shown in Figure 60. A phase shift is seen. This shift of about 8 microseconds in 60 cm indicates that most of the recorded current consisted of bursts of fast ions familiar to us from the DC work.

An attempt to analyze the Q/M's by a massenfilter was abandoned after an experiment yielded currents too low to read over the noise. An electrostatic analyzer (whose resolution was degraded in an attempt to increase the current) was placed in front of a massenfilter and the whole instrument pivoted to look at the needle from various angles. The hope had been to analyze the charge-to-mass distribution, at various voltages (or phases) as selected by the electrostatic energy-analyzer, both positive and negative.

11.2.13 Direct Thrust Measurement

Figure 61 shows the front and back of a swinging honeycomb collector used to measure the thrust of a needle working at 50 kHz. The magnet was used for damping, and the mirror on the back used to measure the angular deflection. A telescope with cross-hairs in the eyepiece focussed on the reflected image of a millimeter scale at a 144 cm distance This produced a millimeter displacement of image for a 1-1/2 micropound thrust.

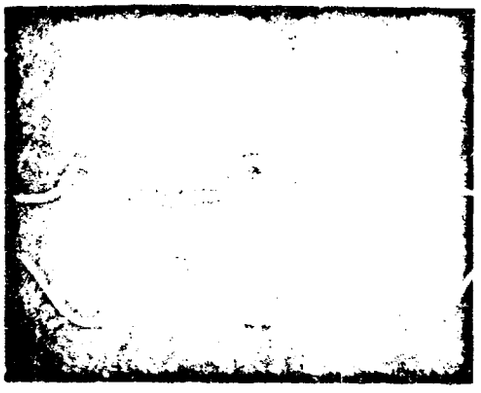

Figure 50. Collector current at varying distances from the needle.
(a) 12 inch,1 microamp/division
(b) 23 inch,1 microamp/division
(c) 34 inch,0.1 microamp/division
5 microsecond/division.

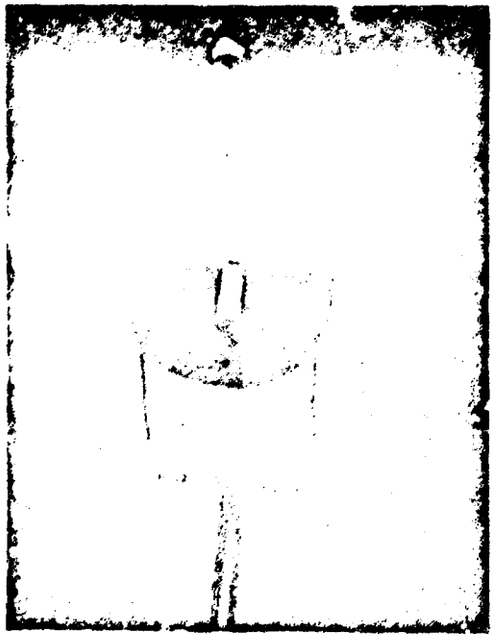

(a) Front View

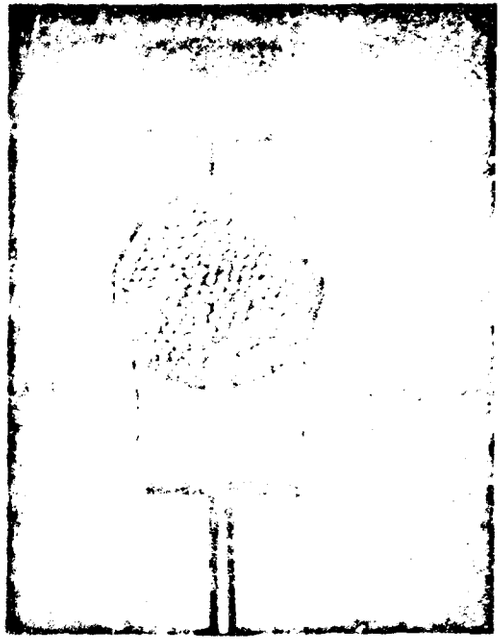

(b) Rear View

Figure 61. Honeycomb Pendulum Collector

Thrusts were first measured with the needle operating DC from 1.5 micropounds to 3 micropounds at currents from 9 to 15 microamperes, voltages of 5-1/2 to 7-1/2 kv, and feed pressures from 0.7 to 3.2 inches of mercury. When the needle was operated at 50 kHz and the same feed pressure that gave 3 micropounds DC thrust at 15 microamperes and 6.2 kv, the thrust produced was 0.3 micropound at 6.5 kv peak, 1.4 micropounds at 7.75 kv peak, and 3 micropounds at 9.75 kv peak. Previous experience with AC operation would suggest that the currents would be quite large at this highest voltage — suggesting a poor efficiency.

Little was learned from the thrust measurement except perhaps the obvious: almost as much thrust can be achieved as one wishes by overdriving a needle with more voltage, but the efficiency and life are degraded to unacceptable levels.

11.2.14 Maximum Pulse Periods

Propellant accumulated in the needle during the OFF period is rapidly used up during the ON period. The position of the fluid will then change during operation, the amount depending on the size of the needle (storage capacity) and the amount of mass used during the ON time. The operating characteristics will alter with the position of the fluid. During the pulse, the current and $\dot{m}$ decrease and the specific impulse increases. A tolerable change of these parameters that does not materially alter the overall thrust efficiency occurs when about 1 microgram of propellant per 0.014 inch O.D. needle is used in each pulse. This mass is used in about 1 second when the needles are operating at the maximum current density consistent with long life and at a specific impulse of 1000 sec. This mass represents only a small amount of propellant present at the tip of the needle—about a 1 mil depth charge. This 1-second ON time would be adequate for a satellite spinning as slowly as 15 revolutions per minute for a duty cycle of 25%. For a slower spinning satellite, or as a longer pulse for any other reason, the current density could be reduced, or larger needles could be used (the storage time should go as the square of the needle dimension).

11.2.15 Minimum Pulse Periods

Optical viewing of the jets around the rim of the needle shows them completely collapsing during the OFF time. When the voltage is reapplied, a time approaching 50 milliseconds is required before the jets are all formed and the operation becomes stable. During this transition period, some jets do not yet experience field reduction due to the presence of adjacent jets. This produces excessively fast particles and large numbers of molecular ions. High average efficiencies thus require the ON period be long enough for this low efficiency transition period to be negligible. A long ON period, exceeding 0.15 seconds for instance, then puts a lower limit on the duty cycle of operation. For example, at 1 pulse per second (60 ppm) the efficiency is seriously degraded for a duty cycle below 15%. For 120 ppm, the duty cycle should be over 30%.

11.2.16 Power Conditioning

Pulsed power supplies used in the laboratory for expediency have been simple utilizing a series resistor and a shunt tube to lower voltage and stop emission, but have been inefficient powerwise. For space application, a lightweight efficient unit is required. The main concern in the design of the unit is to rapidly remove the voltage without wasting energy or using heavy, power-consuming devices such as vacuum tubes or thyratrons. Fortunately, a colloid engine can be turned off for the required time by reducing the voltage by about 25%. This allows a conventional DC power supply, 6 kv for example, in series with a rapidly ON-OFF cycled 2-kv supply. The 2-kv supply would use a moderately high frequency, square-wave bridge rectifier circuit so that a small filtering output capacity would be needed. The voltage would be dropped to zero by stopping the square wave input to the step-up transformer and firing a string of series high-voltage SCR's across the output to discharge the filter capacity. Energy loss due to stored magnetic flux in the transformer can be eliminated by starting and stopping the square-wave drive in the middle of its conduction period. The energy lost in discharging a 2500 pf filtering capacitor (approximately 1% ripple at 1 kc and 1 ma) from 2 kv is only

5 millijoules and is negligible when operating at low repetition rates mainly because of the low voltage. Turn-on characteristics and voltage control during the ON time might be used to improve the colloid engine's operation and efficiency, but otherwise the regulation, control, provision for varying input conditions, etc., are conventional.

REFERENCES

11-1. W. C. Burson, Jr., and R. C. Herrem, Jr., "Alternating Current Operation of a Colloid Source," AIAA Paper No. 69-495, AIAA 5th Propulsion Joint Specialist Conference, June 9-13, 1969.

11-2. W. C. Burson, Jr., "Research on Electrohydrodynamic Charged Droplet Beams," AFAPL-TR-67-109, Wright-Patterson Air Force Base, Ohio, October 1967.

12. SLIT GEOMETRIES

12.1 SINGLE LINEAR SLIT

Work accomplished on the single slit module this year was a direct continuation of work done on the 1967 program. Only six runs were made with the module, and work was suspended in July. These runs totaled 340 hours operating time, the longest being 140 hours.

A significant technological advance was achieved by the use, for the first time, of slit edges of platinum - 20% iridium alloy, a substance with much greater machinability than pure platinum. Some of the slit fabrication problems were greatly reduced by this step, and over 50 hours of running time demonstrated its resistance to electrochemical erosion.

The highest thrust density achieved from a slit geometry this year came from a single slit run - 60 μlb/inch at 1700 seconds and 70% efficiency. This is probably a good upper limit for present technology, although higher thrusts have been achieved. The 60 μlb/inch number was obtained for 4 hours of relatively trouble free operation. During the same run, the module ran for 40 hours at 40 μlb/inch and 1650-second I_{sp}.

Thrusts reported here and elsewhere in this section are uncorrected for beam divergence and energy loss, a correction of 8-10%.

At the beginning of the program, the linear slit geometry (LSG) effort was faced with three basic problems to overcome. These were:

1) Excessive beam divergence. The LSG normally runs at about 20° half-angle beam spread. This is about twice the desired goal. A half-angle of 10° was observed once, but was never repeated.

2) High source voltage. Voltage requirements are still on the order of 15 kv for this geometry. No way has been found to solve this problem other than adequate high voltage power conditioning.

3) Low thrust density. While the LSG has yielded a much higher thrust density than the standard needle, the goal of obtaining a reliable 100 μlb/inch has not been realized.

During the early part of the year another problem developed. The extremely fine tolerances on the slit edges, and the softness of the platinum, made the fabrication of new slits and the refinishing of old slits an

extremely difficult process. The problem was alleviated somewhat by the platinum-iridium slit edge, but no truly systematic fabrication techniques were ever worked out. Some attempts were made along this line with the double slit, and these are discussed in Section 12.2. All of the aforementioned problems require further solution before LSG flight systems can be seriously proposed.

12.1.1 Run 6812-04; Low Beam Spread

Work began in December of 1968 when the single slit module was run in the CMA test station to determine the effects of varying deflector geometry. The nominal deflector setting on the single slit had been, in the past, ±0.040 inch on either side of the slit edge and 0.025 inch in front of it. For this run, the deflectors were set at ±0.017 inch on either side of the slit edge, and 0.007 inch in front of it.

The slit was run for approximately 2 hours, at a net feed pressure of 2 inches of Hg and a voltage of 14 kv. The deflectors were set at 2.5 kv and 6 kv, to compensate for a thrust vector error. The reason for the error was apparent. After the run, the lateral deflector displacements were measured again and found to be 0.021 inch and 0.012 inch. The drain current to extractor and both deflectors was negligible. Over the duration of this run, the beam current ranged from 60 to 70 microamperes current. The extractor voltage was varied between -1 kv and -3 kv, and the effect of this variation on performance was not noticeable. The thrust efficiency was 65%; specific impulse was 2,000 seconds; thrust was 10-13 micropounds; mass flow rate was 2.6 to 3.0 micrograms/second; and average Q/M was 20,000 to 26,000 c/kg.

The important result obtained here was that placing the deflector electrodes closer together apparently has the effect of narrowing the beam spread. The nominal half width of the beam was observed to be about 10°, and 90% of the current fell within these limits. The total beam spread was about a third of that which had been observed previously. These are all rough measurements based on visual observations.

12.1.2 Run 6812-07; 142 Hours at 2000 seconds I_{sp}

Run 6812-07 was made using the same slit that was used for several extended runs. The placement and positioning of the slit edge relative to

the deflector electrodes and extractor edge were on previously used. The test was again run in the CHA system with a horizontal 1.5 x 4 foot chamber. Several additions were made to provide a shutdown capability in case of overcurrent operation. An automatic feed pressure pumpback system activated by a sensitive overcurrent relay prevented fluid from shorting out the electrodes in case an arc or sudden current surge activated the overcurrent relay. During the run, the slit performed very well with no degradation except during the last few hours when the slit accidentally became overfed. At that time an obstruction in the feed plenum which had required an increase in feed pressure from 4.5 to 13 inches of Hg gave way. For twelve hours subsequently, the slit ran at 3 times its normal mass flow. The overfeed produced excessive beam spread (±20° as compared to the ±15° during the previous 130 hours), with resulting beam impingement on the deflection electrode, extractor, and ground plane. Post-operative inspection revealed tar formation along the emitting edge of the slit. It was felt that this tar formed during the period of excessive beam spread. The slit had, until that time, operated very smoothly and with a relative narrow beam. After the period of overfeed, the beam spread remained ±60°, even at reduced $\dot{m}$. The feed plenum was found to have been plugged with a gel-like material (as yet unidentified, but possibly silicone grease) and fine fibers. It was this material that gave way during the period of increased feed, resulting in the overfeed.

During the run the slit was operated at 16 kv, the deflector electrodes at 6 kv, and the extractor at -1 kv. Except for the period of overfeed, the I_{sp} was kept above 2000 seconds. The slit was operating steadily at the fairly high thrust level of 25 μlb/inch from the 19th to the 100th hour.

In more detail: The first 10 hours were run with 1.2 inches of Hg feed pressure. At this pressure the current was 40 ±4 μamp. The thrust was approximately 6.2 μlb (8.5 μlb/in); the efficiency was 65%, and the $\dot{m}$ averaged 1.25 μgm/sec. During the first 3 days of operation, the slit was idled overnight at negative head pressure with V_{slit} = 13 kv. The idling time was not counted in the total running time. After idling overnight, the slit was operated for 8 hours at 1.3 inches and a slit current of 30 μamp. After the last idling period, at the 19th hour, feed pressure was set at 4.5 inches of Hg and left at that pressure until the 125th hour.

From the 19th to the 100th hour, the current ran steadily at 60 μamp ±5 μamp. The thrust stayed at 15 μlb (25 μlb/in), η =63%, and ṁ stayed at 3.6 μgms/sec. After the 100th hour, the feed path gradually plugged up and the current dropped to 36 μamp. The pressure was then increased to 9 inches and, four hours later, to 13 inches. The current returned to 60 μamp, the thrust to 15 μlb, and the ṁ to 3.6 μgm/sec (all the values previously obtainable at 4.5 inches). The slit ran stably for the remainder of the day, but during the night the plug opened up causing the slit to overfeed. By morning, ṁ had risen to 1.1 μgm/sec, and the beam spread had increased irreversibly to ±80°.

Had a filter been placed in the line, the problem of overfeed would not have occurred and it seems likely that 200 hours could have been attained.

12.1.3 Run No. 6905-02; Platinum-Iridium Slit Edges

The single slit module was rebuilt with slit edges made of platinum-20% iridium. The original extractor and copper vane deflectors were used. The deflectors were set at 0.030 inch on either side of the slit edges, and at approximately the same height. The module was installed in the 6 inch vacuum system, the main objective of the run being to test the erosion characteristics of the slit edges.

The total running time was approximately 30 hours. During its normal operating hours, the slit behaved extremely well. The slit voltage was run at 13 kv for the first 15 hours, and 14.5 kv for the last 15. There was no extractor or deflector drain current.

During the first half of the run, the slit voltage was 13.5 kv and the current was 45 μamp. Feed pressure was held at just under 2 inches and the deflector voltage was about 6 kv. Under these conditions the efficiency was 60 percent; the I_{sp} was 1262 sec; thrust was 30 μlb/in; flow rate was 10 μgm/sec/in; and average Q/M was 9,500 c/kg.

During the second half of the run the slit voltage was set up to 14.6 kv, and the feed pressure was dropped to 0.5 inch. This held the slit current constant at 45 μamp. All other conditions remained the same. These settings succeeded in raising the I_{sp} to 2200 seconds, but the thrust went down to 20 μlb/in.

The module was set to zero feed pressure and allowed to idle overnight, and over most of the weekend. At the end of the weekend, a failure was discovered in the form of a massive current drain to both deflectors. When the module was opened, there was no sign of direct impingement to the deflectors, and the slit edges while somewhat tarred, were not overly damaged.

Closer inspection revealed that the lead solder bond between the stainless and the platinum part of the slit bond had eroded away electro-chemically. This left a gap where the gasket spacer did not seal, and allowed propellant to leak out the sides of the module. This was the probable cause of the short failure. As a corrective measure, the eroded gap in the lead solder was then filled with epoxy, as in previous modules.

It was also found that the platinum-iridium slit edges had eroded, leaving a jagged edge of 1/2 to 1 mil roughness. This was apparently a result of arc damage, since the following run showed the material was not subject to electro-chemical etching.

12.1.4 Run No. 6906-01; 52 Hours on the New Edges

The single slit with platinum-iridium edges was refinished. The deflectors were set at 0.027 inch on either side of the slit center, and 0.030 inch in front of the slit. With these few changes the slit module was reinstalled in the 6 inch vacuum system to run another erosion test on the slit edges.

The performance of the slit was excellent. At least some of the improvement can be ascribed to the repositioning of the deflectors. It was also noted that the slit edge radius was somewhat larger than usual - on the order of 1/2 mil. Figure 62 is a photomicrograph of the edges of a similar slit, with a human hair across the field of view for comparison. The hair is 0.004 inch thick.

Most of the run was made at low thrust and high specific impulse, although the thrust was elevated toward the end of the run. Table 12-1 is a performance summary for this run.

The first 20 hours were spent at 12.5 kv slit voltage and 0.75 inch Hg feed pressure. (The operating conditions are given in column 1.) The linear thrust density was 10 μlb/in. When the feed pressure and voltage were increased, a maximum thrust density of 53 μlb/in was obtained.

Near the end of the test, a rough measurement of the beam profile was made with a current probe which could move laterally with respect to the slit. The current distribution was found to be double peaked, with the peaks occurring at 17° above and 10° below the horizontal. The lower peak had less current density than the upper. Some allowance must be made for the fact that the pumping area was on the bottom of the tank and near the probe, but these measurements indicate a larger beam spread than has been observed visually. The current density at zero degrees was practically negligible.

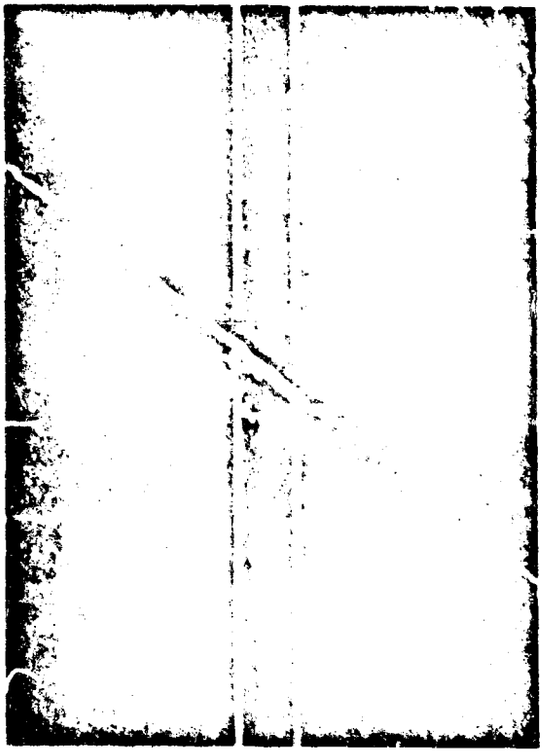

Figure 62. Photomicrograph of Human Hair Perpendicular to Linear Slit (Approximately 30 x)

Table 12.1 Single Slit Run 6906-01

Time (hr)	21.5	23	24	45	50	52
Voltage (kv)	12.6	13	13.2	13.6	14.8	14
Feed Pressure (in.)	0.75	0.75	0.75	0.7	1.5	2.7
Current (μamp)	70	104	85	75	128	180
Thrust (μlb)	9	12.5	11	9.5	18.7	31.7
Flow Rate (μgm/sec)	1.6	1.7	1.7	1.4	3.0	6.8
Efficiency (%)*	60	56	64	61	61	58
Specific Impulse (sec)	2640	3270	2970	2990	2860	2120
Q/M (c/kgm)	45,000	60,000	50,000	52,000	43,000	27,000

*Hunter Beam Efficiency

12.1.5 Run 6907-02; High Thrust Densities

In July, the single slit module was installed in the 4 feet x 8 feet tank for a life test. The test was not completed because of excessive deflector drain, resulting from an attempt to run at elevated performance.

This slit was given a slightly rounded edge (0.001 inch radius) since previous results indicated a performance improvement by this means. The deflectors were positioned nominally 0.025 inch on either side of the slit edge, and the edge was 0.030 inch behind the plane of the deflector edges. The edges were of Pt - 20% Ir.

This run lasted about 40 hours, most of which was spent at an elevated thrust level. The average thrust level for the run was 40 μlb/in at an I_{sp} of 1650 seconds and 70% beam efficiency. The highest thrust level achieved was 60 μlb/in or 37 μlb at 1700 seconds and an efficiency of 70%. Feed pressure was kept at 2.5 inches, slit voltage 16.5 kv, extractor voltage -1 kv and deflector voltages 5 kv. The extractor current was less than a microampere, and the needle current was nominally 80 μ amp.

Deflector breakdown occurred quite early, about 10 hours into the run. It became a serious problem after about 35 hours, and at 40 hours caused the run to be terminated. The ambient pressure in the chamber during this breakdown period was between 2×10^{-6} and 3×10^{-6} torr. The characteristic problem here is the difficulty of finding a deflector spacing large enough to prevent breakdown to the slit, yet small enough to provide effective focusing and reduce beam divergence.

12.1.6 Run 6907-04; Attempted Endurance Run

The single slit module was reinstalled in the 4 feet x 8 feet tank for a second try for an endurance run. The goal was 300 hours. The test was automatically shut off after 75 hours. The shutdown occurred at midnight, and the exact cause is not known. Either a bad vacuum or a control power relay failure is suspected.

The deflector-to-slit spacing was increased to 0.035 inch on either side for this run. The slit edges were again round to about 0.001 inch radius. All other geometry was identical to that of the previous run.

Nominal operating conditions for this run were a feed pressure of 3 inches, slit voltage of 18 kv, extractor voltage of -1 kv, and deflector voltage of 3 kv. For these conditions, the slit ran with a current of 45-55 μamp. Thrust was nominally 12 μlbs at an I_{sp} of 2,000 seconds and a beam efficiency of 60%.

The run started at a lower feed pressure, 1.5 inch, and a higher thrust, 13 μlbs and 1700-second I_{sp}. After 6 hours the module was turned off, allowed to idle over a weekend, and restarted on Monday. The remainder of the run saw a gradually decreasing thrust. This may not have been significant. On the eve of the last day, the feed pressure was increased by 1/2 inch and more current was applied to the module heater. This may have given rise to failure through overpressure in the vacuum tank, as the flow rate increased. The general tendency before that time was toward decreasing mass flow and higher $\overline{q/m}$, as the feed pressure was held constant at 3 inches.

At this time, linear slit tests were discontinued in order to concentrate on the promising aspects of annular slit development to be discussed in Section 12.3.

12.2 DOUBLE SLIT MODULE

At the beginning of the year, one of the basic problems facing the program was how to modularize the LSG. A feasibility demonstration of the multiple linear slit module was dramatically accomplished with the first testing of the double slit module in February.

The fabrication of this slit was, in itself, a significant technological achievement, entailing a difficult flow impedance match between the two slits, generally close machining tolerances, and a most difficult match of the geometries of the two sets of emitting edges. These formidable tasks exposed several difficult fabrication problems, and provided considerable insight into their possible solution. Beyond this, the year's operating experience on the double slit module has definitely proven the basic concept. In general, performance characteristics were unchanged by proximity and remained similar to those of the single slit. The one exception was increased difficulty in guarding against return electrons due to the decrease in extractor area surrounding the slits. This was successfully accommodated by raising the extractor voltage.

The problem areas of the double slit module include all those mentioned for the single slit in the last section. In addition, two other problems are more bothersome for the double slit than for the single slit:

1) Tar formation. The buildup of tar, crystals and gelled propellant may become extremely heavy on the slit edges, especially during erratic operation. This strongly suggests an overabundance of backstreaming electrons from the exhaust plasma to the slit edges, caused perhaps by an incompletely effective negative bias.

2) Breakdown between slit edge and deflector. Possibly initiated by the same backstreaming electron phenomenon, this breakdown problem may also be a function of the new electrode design used on the module.

The overall design of the module is shown in Figures 63 and 64. The slit spacing was chosen to be 3/8-inch. Insofar as fabrication is concerned, it is felt that the slits may be packed as close together as 1/4-inch separation. Both slits are fed from a common propellant plenum. A compression set screw acts from a common yoke to apply a force against the slit blades sufficient to keep them sealed

Because of its simplicity and ease of fabrication, a new deflector electrode design was tried on this module. The deflectors were 20-mil tungsten rods, held in place on either side of the slit edges by two mylar insulation bars. These bars can be seen on either end of the slit

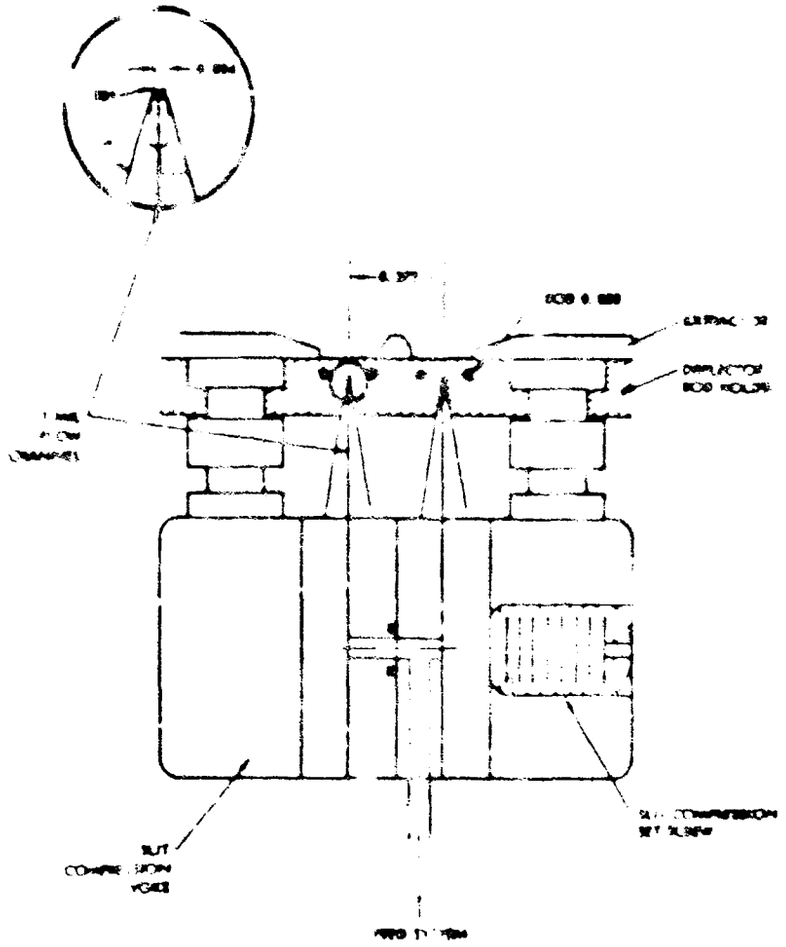

Figure 63. Two-Slit Module Schematic

a. Edge View

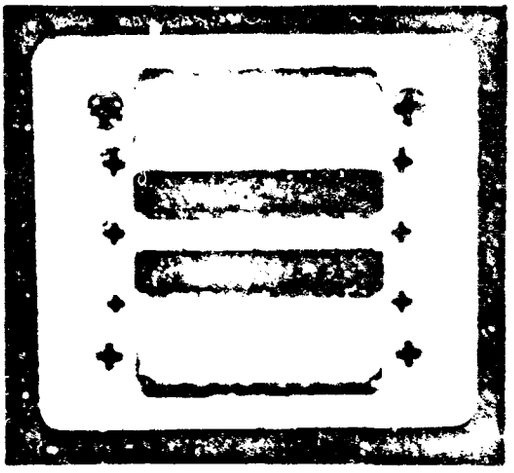

b. Front View

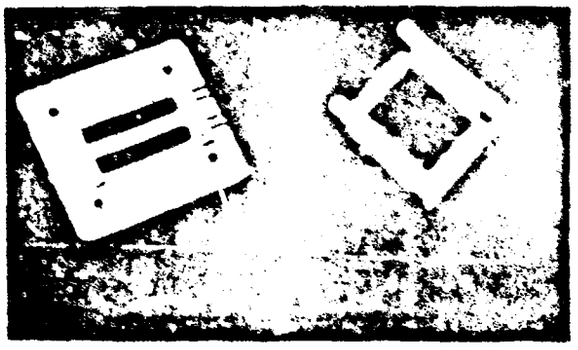

c. Prior to Assembly

Figure 64. Two-Slit Vectored Module

openings at the rear of the extractor plate (Figure 64c). The design proved quite successful, except for the occurrence of the usual problem of deflector-to-slit high voltage breakdown.

12.2.1 Fabrication Techniques

Some time was spent on this module in an effort to develop some uniform standards for finishing slit edges. The point was reached in slit development where fabrication procedures were becoming a real problem. No truly repeatable methods have emerged whereby a uniform edge may be put on a slit, and the process of finishing a slit edge is still costly and time consuming. A number of varied techniques have been tried in an attempt to systematize the process.

The first technique tried was the use of precision machine milling. Figure 65 shows the fixture that was assembled. Two dowel pins were used to align a slit blade with respect to a carefully positioned aluminum block. This block was then to be precisely aligned with respect to a modified precision end mill which would then machine the proper bevel angle at the blade edge. This attempt failed, and the reasons for the failure are thought to be twofold. First, the platinum on the slit edges is too soft to be easily machineable. This difficulty is compounded by the fact that the tool was forced to machine stainless steel simultaneously with the platinum. The result was an apparent dulling or fouling of the tool, and the platinum tended to "tear out" rather than machine smoothly. These difficulties can be somewhat alleviated by using a platinum-iridium edge, and by finding a way to keep the tool off the stainless and only on the platinum.

The second cause for failure was apparently that a 10° angle is too narrow to try to cut a true edge. Up to now, no accurate measurements have been made of the slit angle right at the edge. Judging from the results here, it seems probable that previous slits have had angles somewhat greater than 10° right at the edge. Increasing the local angle may ease fabrication procedures, and may even improve beam focusing somewhat, owing to less local field divergence.

12.2.2 Initial Trials

Two preliminary runs were made in the 6 inch CBA Test Station, for purposes of observation and preliminary performance evaluation.

The first run was aborted by excessive arcing between deflectors and extractor, which was felt to be due mainly to poor extractor design. Later, propellant leakage out the sides of the slits was caused by a poor gasket seal. This module was harder to seal than the old single slit module. The problem was corrected by using a slightly thicker seal.

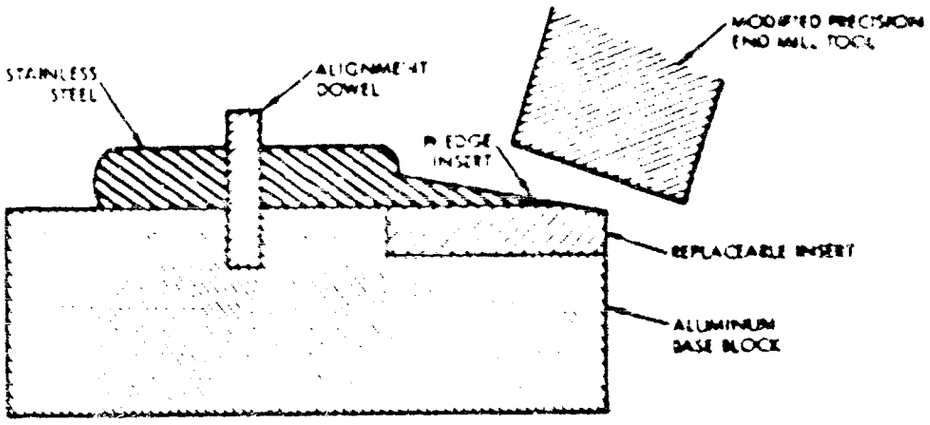

Figure 65. Slit Blade Shaping Fixture

The second run was successful. The module was operated for about 6 hours, at a feed pressure of 1 inches of Hg and a slit voltage of 16 kv. The deflectors were held at nominally 7 kv, with a 3-kv differential to compensate for a thrust vector error. The total slit current was 77 μamp.

The beam pattern was observed and found to be very similar to that of a single slit. The beam spread was ±25°. The collector glow was slightly darker in the middle, more intense above and below, corresponding to emission from the top and bottom edges of the slits. The collector current was smooth, just as for the single slit, and the arcing problem had diminished greatly. Some breakdown occurred between deflectors and extractor, but this could be partially corrected by raising the (negative) extractor voltage to increase the negative potential barrier. This prevented electrons from raining back down into the deflector-slit area and initiating inter-electrode discharges. This may possibly be further corrected by using broader, plate-shaped deflector electrodes instead of the cylindrical geometry.

Figure 66 shows the potential field resulting from a computer study of the twin LSG. The figure shows half a slit, the lower boundary being the centerline of symmetry. The upper boundary is also a symmetry boundary on which the normal component of electric field vanishes. Thus, the boundary conditions are such that the configuration is repeated, as a reflection, above the upper boundary. The potential field map points out the problem, which was experienced in the above run, of the lack of an effective negative potential barrier. This problem was not seen in similar computer studies of the single slit where a potential barrier did exist. The disappearance of the barrier is a result of the close packing between slits, and the consequent reduction of extractor area.

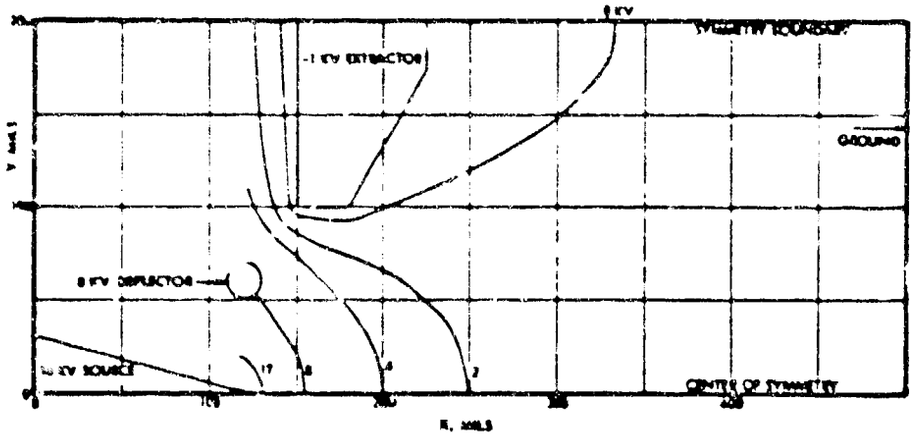

Figure 66. Potential Field for Double Slit Configuration with Cylindrical Deflector Electrodes

12.2.3 Run 6903-09; First Performance Data

The twin slit module was installed in the NRC 4 foot x 8 foot tank for a performance test. The module ran nicely at nominal conditions for 50 hours. The run was terminated when excessive warmth caused the slit to flood. The failure was attributed to irregular control of liquid nitrogen in the tank shrouds. There was no indication of slit failure. In particular there was no indication of any leakage problem in the slit gasket, which had been degrading earlier performance.

The module was supplied with a heater to provide temperature control in the relatively cold 4 foot x 8 foot tank environment. However, other than that available from multi-needle modules, there was no data on temperature versus power input, so the exact operating temperature was not known.

The observed beam spread of the module was nominally ±45°, a number which has been characteristic of the single slit with this deflector geometry. The deflectors (still 0.020 inch tungsten rods) were mounted ±0.060 inch on either side of the slit and 0.025 inch in front of it.

The module was started with a feed pressure of 2.5 inch of Hg, but this was increased to 6 inches and most of the run was with this pressure. There was a filter in the feed line. The first several hours were run with the slit at 15 kv and about 60 microamperes. It was suspected that the slit edges were not wet uniformly, so the high voltage was shut off for 30 seconds to allow the fluid meniscus to move outward. When turned back on, the module reached an operating level of 120 microamperes at 15 kv (and 6 inches Hg feed pressure) and remained at that level for the rest of the experiment. The extractor was run at -1 kv, with 1.5 microamperes current. The deflectors were run at 6 kv, and experienced no drain current.

In an effort to induce the deflector voltages to follow the slit voltage to ground during a time-of-flight pulse, a 500-pf capacitive coupling between the deflectors and the slit was installed. The time constant of this circuit was large enough, however, to noticeably distort the time-of-flight traces. In particular, the ion peak was smoothed out and the low specific charge tail was stretched out. Thus, the time-of-flight results obtained are too low in I_{sp} and too high in flow rate.

The indicated performance of this module was somewhat poorer than expected. The indicated I_{sp} was about 1000 seconds, the thrust 60 micropounds, flow rate 30 micrograms/sec, efficiency 65%, and average specific charge 4000 c/kg. The thrust level was at least equal to the performance of previous single slit runs, corresponding to about 40 micropounds/in.

12.2.4 Run No. 6904-02; 96-Hour Endurance Run

The twin slit module was installed in the NRC 4 foot x 8 foot tank for an endurance run. The module ran for 96 hours before the test was terminated due to excessive extractor and deflector drain, accompanied by excessive arcing.

and degraded efficiency and I_{sp}. The cause was determined to be an over-feeding condition which flooded one of the slits at an early stage, soon 23 to 30 hours into the run. Remarkably, the slit recovered from this condition temporarily, enough so that the performance stayed nominal (1500-sec I_{sp}, 60% efficient) for at least 70 hours. Irreversible damage was done, however, and the performance began to degrade.

A mechanical time-of-flight spark gap pulser was used during the run, replacing the normal thyratron circuit, so that slit voltages in excess of 15 kv could be safely maintained. The slit voltage was coupled to each deflector with a 500-pf capacitor in series with a 0.1 meg resistor. This circuit induced the deflectors to follow the slit to zero voltage during a time-of-flight pulse. The oscilloscope collector current traces showed no evidence of distortion due to this arrangement.

For this run, the deflectors were made of 0.035 inch x 0.020 inch stainless stock, cold rolled from 0.030 inch stainless rod and finished to a round edge. The deflectors were spaced 0.020 inch on either side of the slits and 0.005 inch front of the slit. It was expected that this geometry might improve the uniformity of the extraction field. No improvement in performance was seen, however. In fact, the performance was hampered by this deflector design, if anything.

The slit voltage was run at 15 kv nominal, although some attempt was made to vary this condition, watching the effects. The extractor was run at -1 kv, and the deflectors were run at about +6 kv. The total power input to the slit ranged between 1.5 and 3 watts. The extractor and deflector currents were erratic, but reasonably low for the first 70 hours. After 70 hours, a sharp change took place in the drain current density, accompanied by an increase in deflector arcs. Shortly thereafter, performance began to degrade.

Figures 67 through 73 summarize the performance throughout the run. The efficiency was fairly constant at about 60%.

The nominal beam spread was estimated at $\pm 20°$ throughout the run, though it deteriorated at the last up to $\pm 45°$. At 25 hours, a feed pressure rise flooded the slit and ultimately contributed to its failure. Another

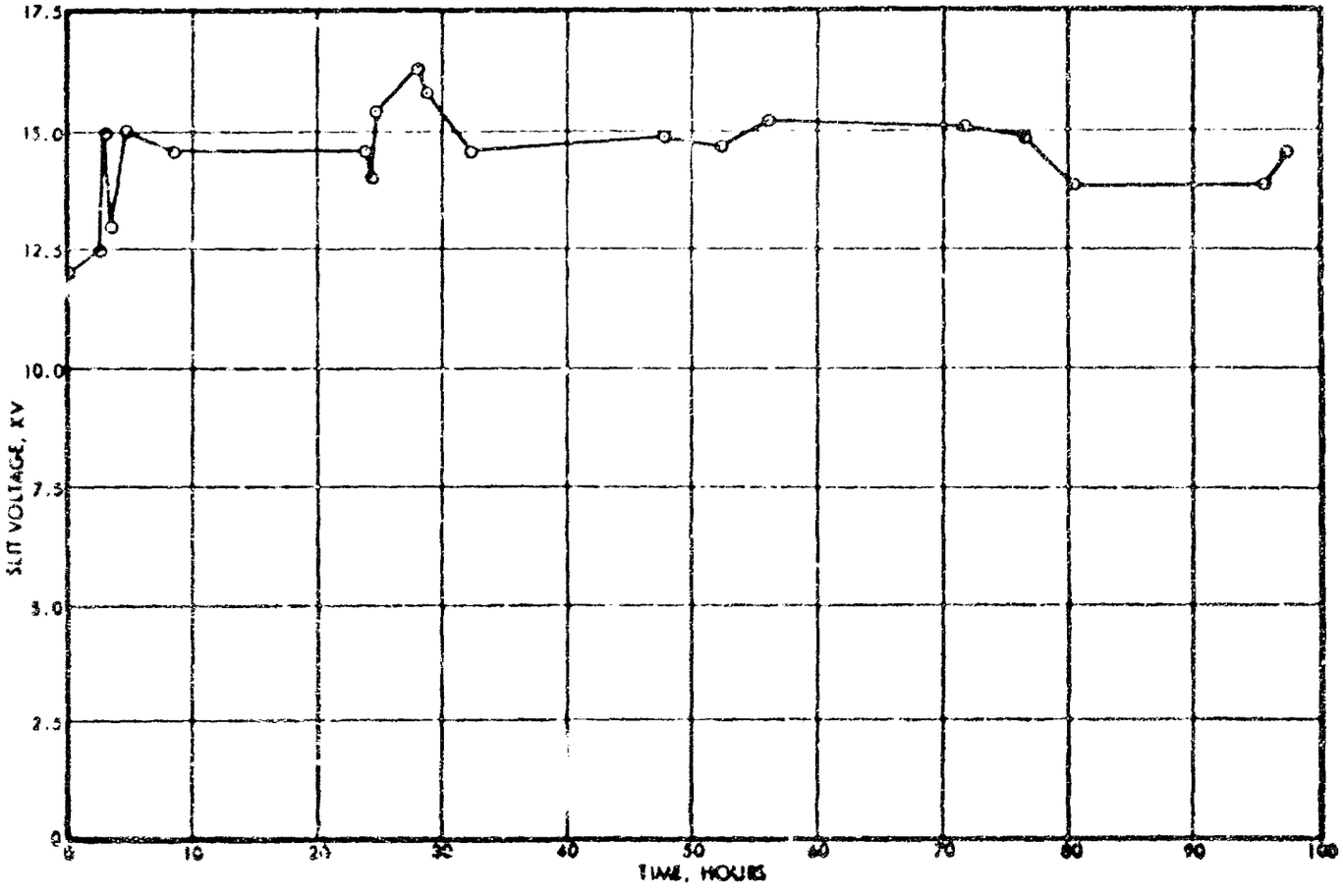

Figure 69. Slit Voltage Versus Time, 96-Hour Endurance Run, Twin Slit

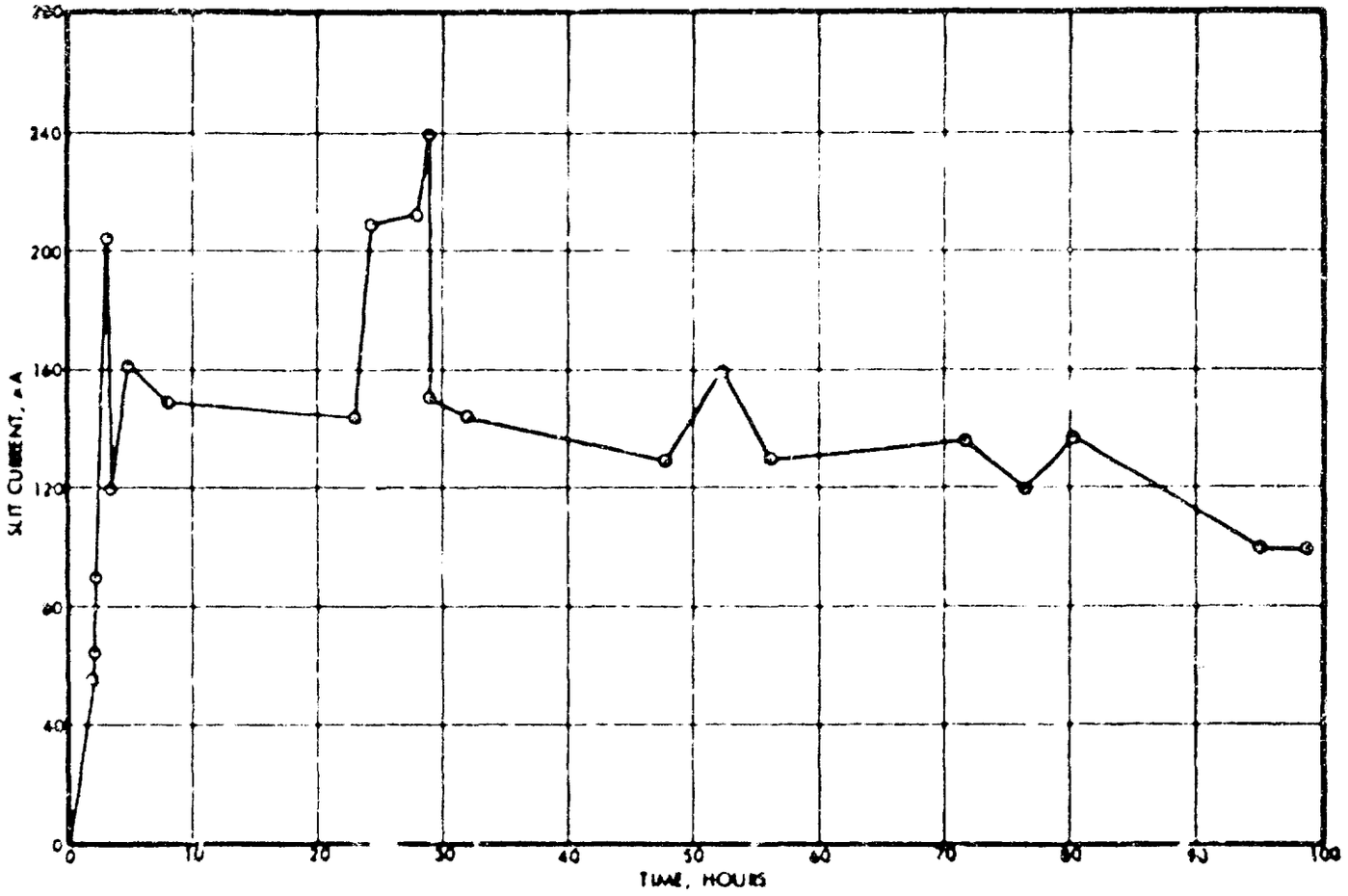

Figure 68. Slit Current Versus Time, 96-Hour Endurance Run, Twin Slit

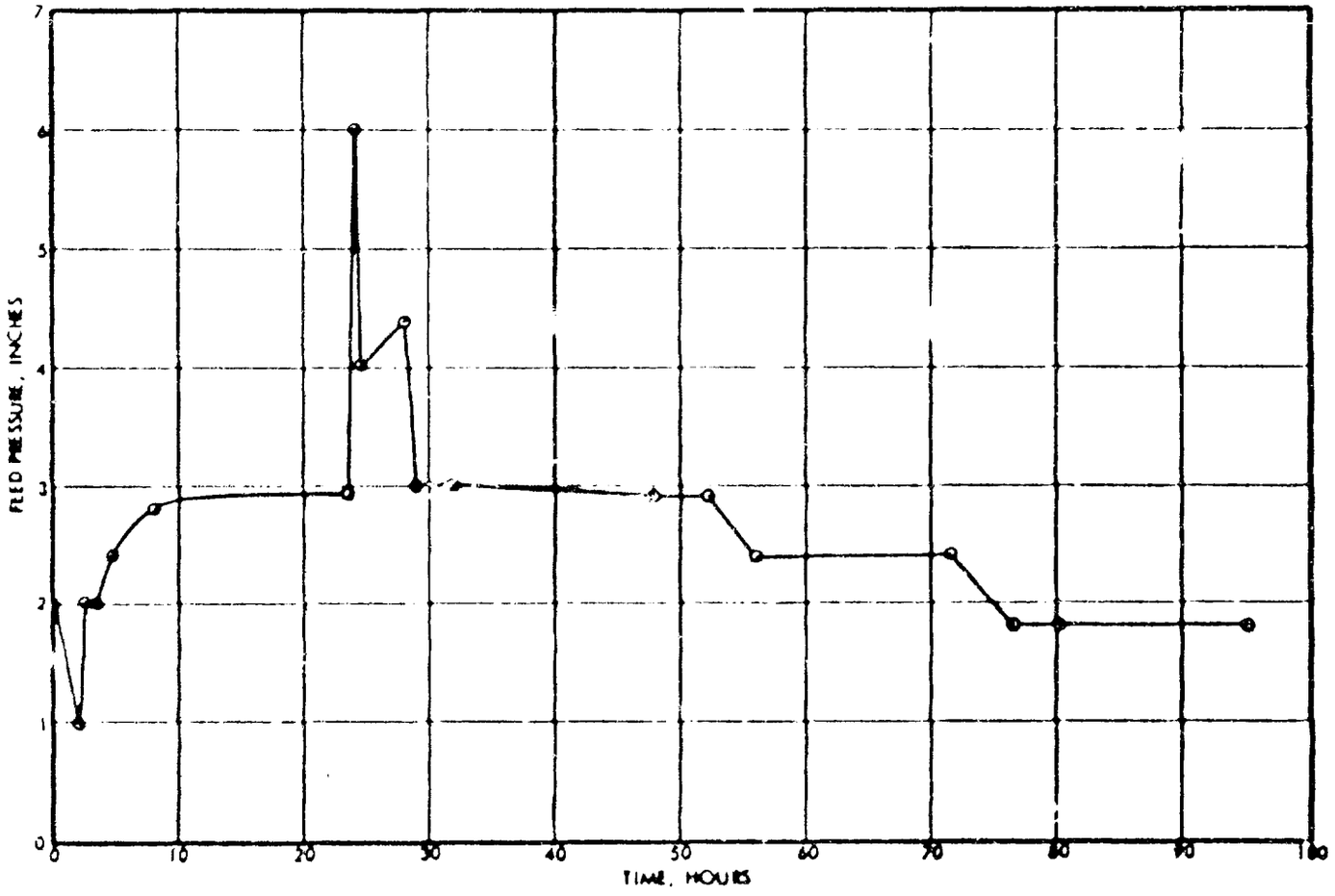

Figure 69. Feed Pressure Versus Time, 96-Hour Endurance Run, Twin Slit

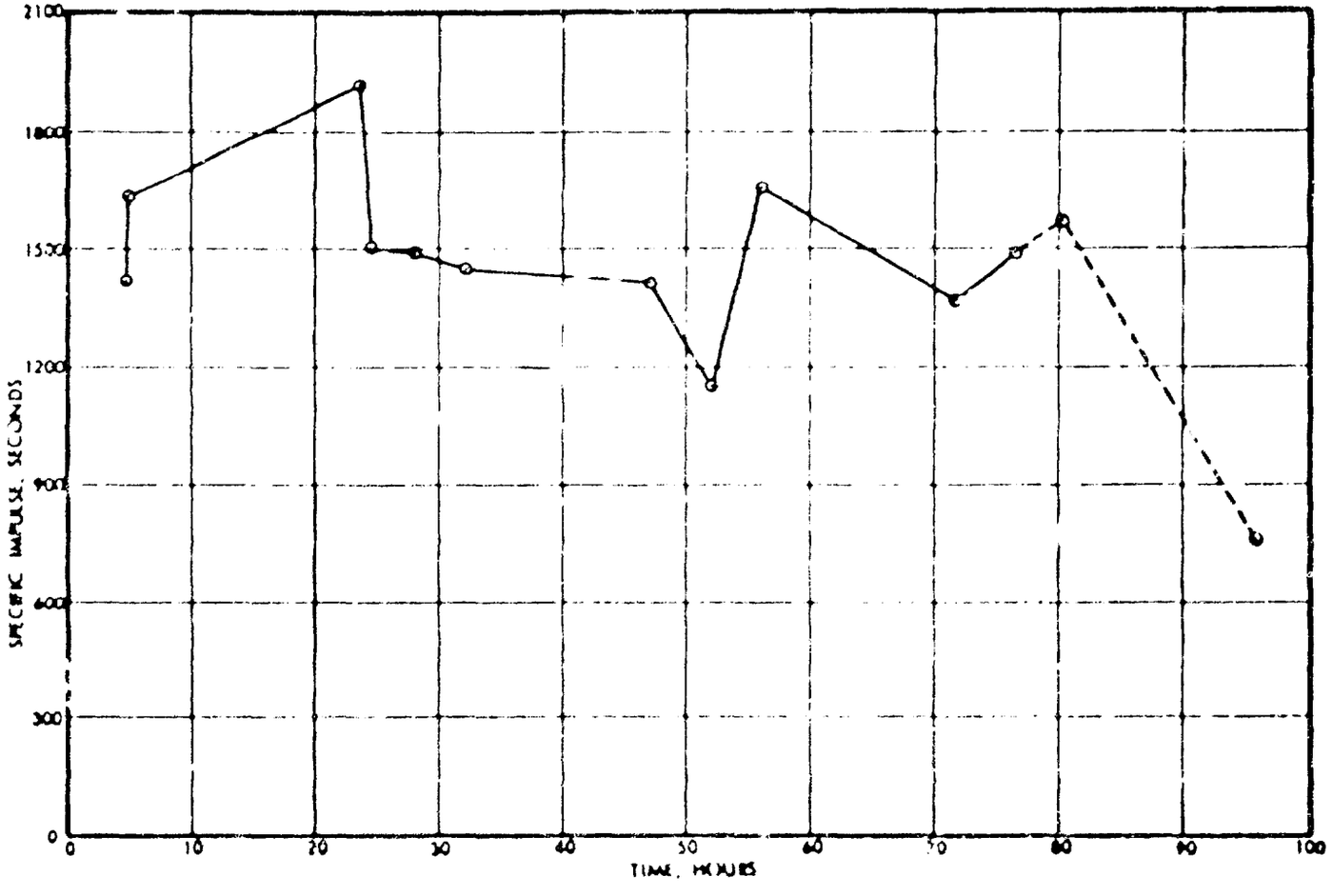

Figure 70. Specific Impulse Versus Time, 96-Hour Endurance Run, Twin Slit

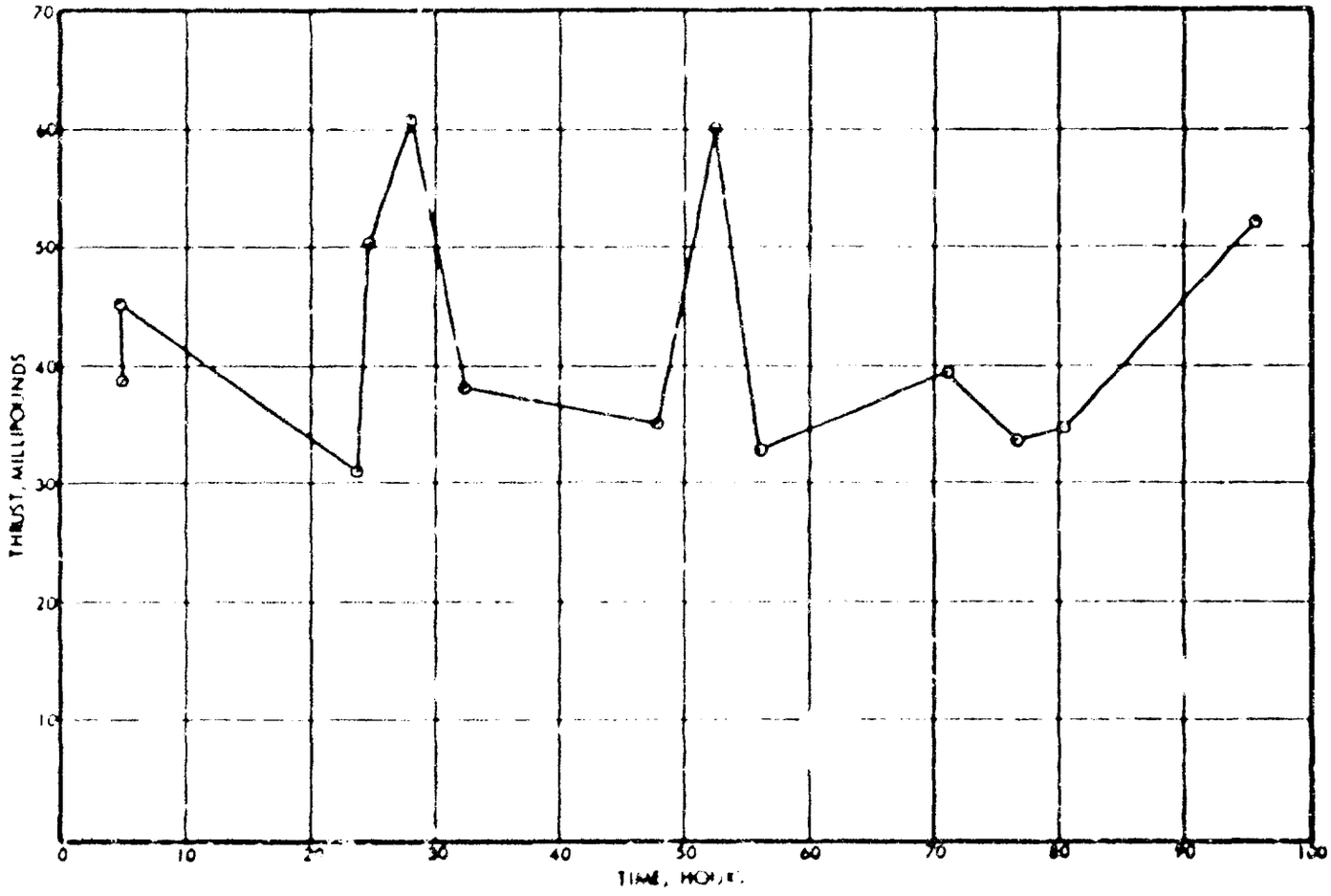

Figure 71. Thrust Versus Time, 96-Hour Endurance Run, Twin Slit

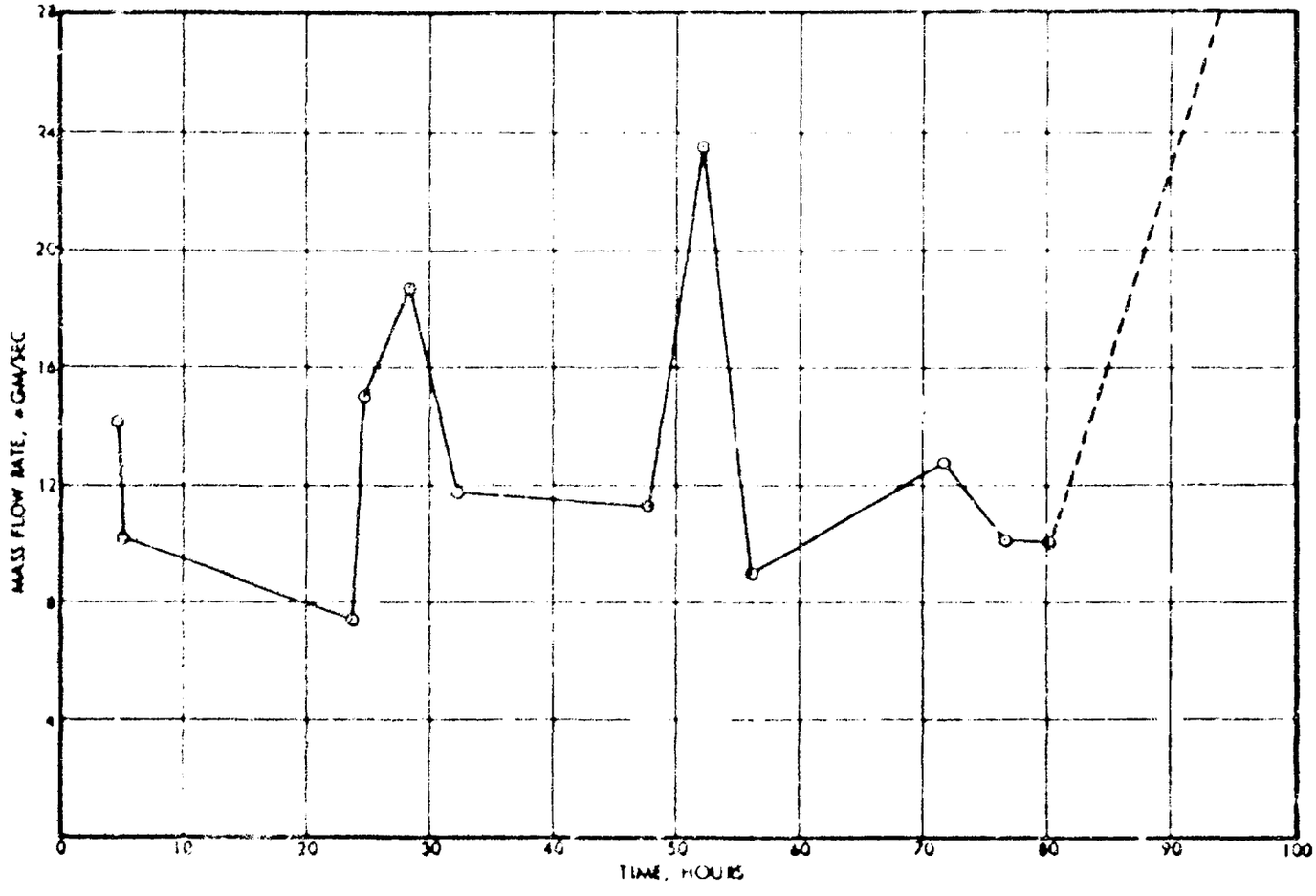

Figure 78. Mass Flow Versus Time, 96-Hour Endurance Run, Twin Slit

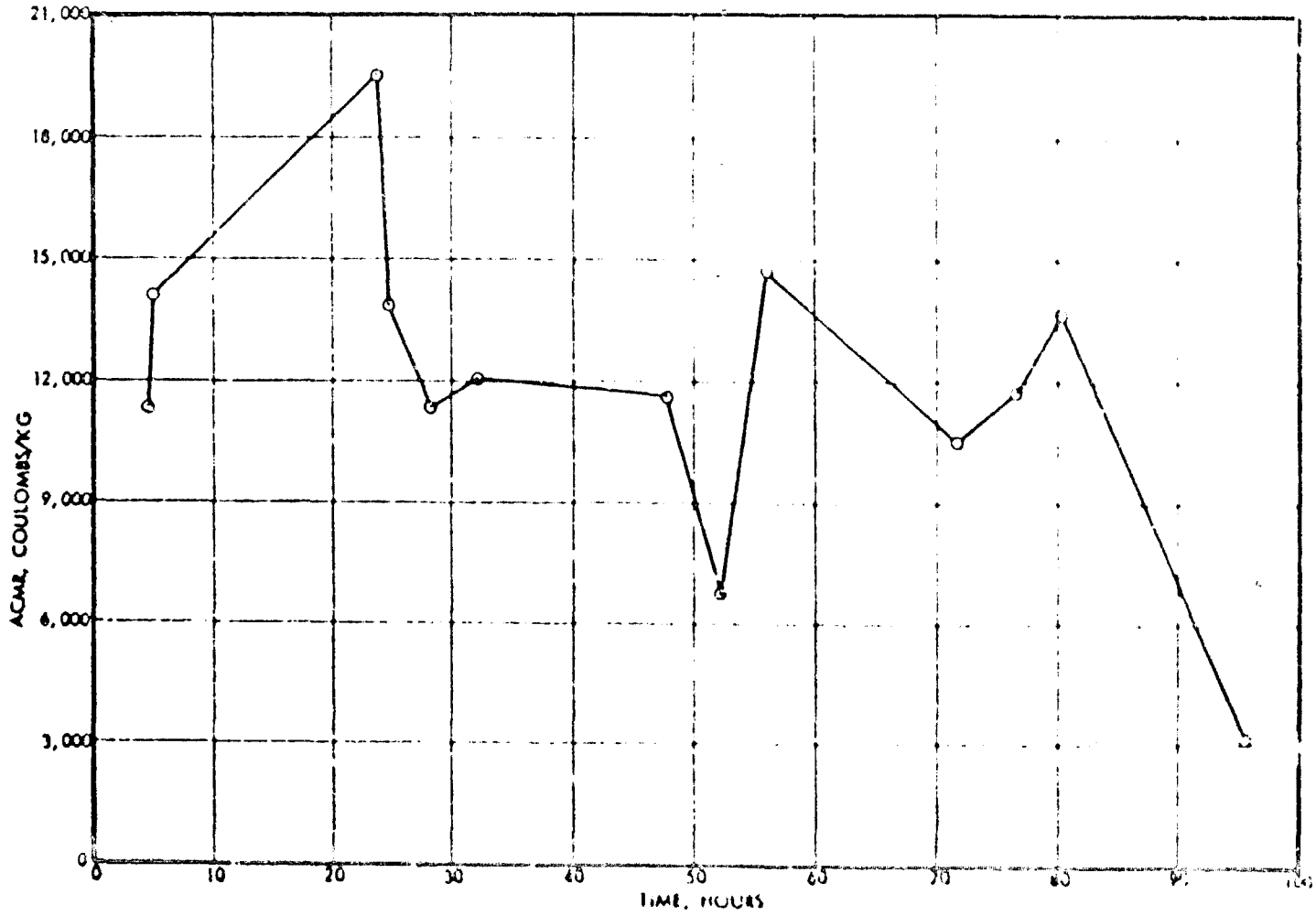

Figure 73. Average Charge to Mass Ratio Versus Time, 96-Hour Endurance Run, Twin Slit

factor which probably contributed to the failure was a relatively large imperfection on one of the slit edges. This spot began to glow very early in the run, and the particular slit it was on behaved worse than the other slit through the run. Most of the drain current went to the deflectors, and after the run was over the deflectors were found to be encrusted with salt. There was also a heavy buildup of tar on the slit edges. Figure 74 shows the extent of the damage to the deflectors and extractor, and Figure 75 shows the slit after the run, after the extractor was removed. There was no evidence of any leakage from the gasket or any breakdown at the deflector holders. The sides of the module were clean.

The salt encrustations on the electrodes were evidence of direct impingement of fluid. This probably occurred first during the flooding at 21 hours, and again toward the end of the run when there was an unexplained rise in the mass flow rate. Other evidence of direct impingement on the deflectors at the end of the run were a very high drain current and a high floating potential on the deflectors when their power supplies were turned off.

The insides of both slits were inspected after the run. The stainless steel surface directly behind the platinum edge was sharply etched in a definite erosion pattern. The platinum itself was unharmed, and so was the epoxy bond between the platinum and stainless. The etching (Figure 76) pattern was characteristic of electrochemical erosion, but also conformed rather closely to the flow pattern of the slit. This led to the conjecture that such erosion was initiated by local nonuniformities in the flow field, or by local imperfections on surfaces.

12.2.5 Run No. 6905-01; 60-Hour Run

The slit edges on the module were refinished, and the deflectors replaced by 0.020-inch rods. These were spaced 0.030 inch on either side of the slit centers, and about 0.010 inch above the slit edges. The module was installed in the NRC 4 foot x 8 foot tank for an endurance test.

As in the previous twin slit run, this run failed by a direct short from slit to deflectors, apparently initiated by deflector impingement. Sixty four hours were logged before the experiment was turned off, although failure occurred some 3 to 4 hours previously. By the second day there was

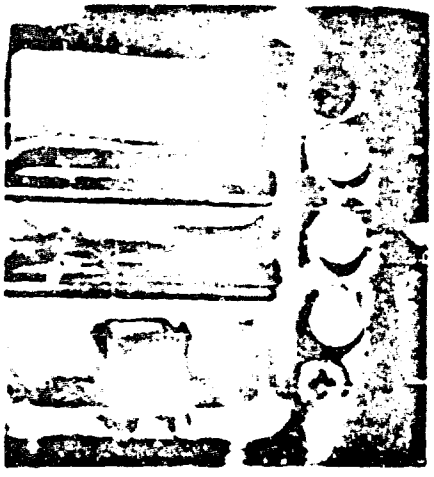

Figure 74. Twin Slit Module After 96-Hour Endurance Run, Showing Damage to Deflectors and Effects of Flooding on Extractor Plate

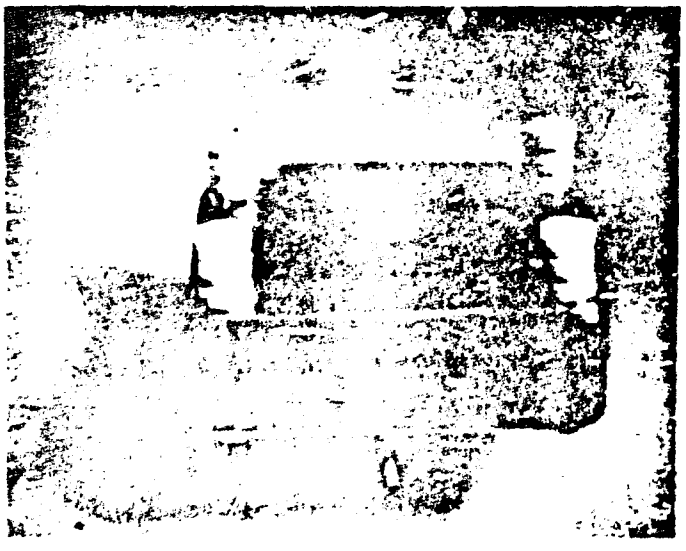

Figure 75. Twin Slit Module, Without Extractor, After 96-Hour Endurance Run

Figure 76. Twin Slit Module After 96-Hour Endurance Run; Inside Edge of One Slit, Showing Erosion Pattern in Stainless

significant deflector drain, although none occurred the first day. The condition continued to deteriorate. It is characteristic of the double slit module that the deflector current shows small fluctuations, even if it is nominally zero. This is in contrast to single slit performance, where under optimum conditions the deflector current is absolutely zero.

The module was operated at 1.9-inches net feed pressure through a 0.8-micron millipore filter. The high voltage was 15 kv, and the current was 120 μamp. Deflector voltages were 6 kv, and the beam was very uniform with a spread of ±20°. A performance problem was evident, however, since the I_{sp} was 1320 seconds and the efficiency was 60 percent. During this first part of the run, the thrust was 24 μlb/in, and the flow rate was 8 μgm/sec/in. The total thrust was 38 μlb.

Later, in an attempt to raise the charge-to-mass ratio, the deflector voltages were dropped to 5 kv. This resulted in an increased current, but the I_{sp} was lower yet — 1285 sec. The efficiency had increased 5 percent, and the thrust increased, but the flow rate had nearly doubled.

Next, an attempt was made to raise the I_{sp} by increasing the slit voltage to 15 kv and dropping the feed pressure to 1.0-inch net. This failed again. The flow rate remained substantially the same, but the I_{sp} dropped still further to 1121 seconds.

These rather discouraging results have at least a hint of a pattern. The results with wider deflector spacing showed steady operation but poor performance (I_{sp} = 1030 seconds). For the last two runs, the deflectors were brought in closer to the slit. This resulted in somewhat higher I_{sp}, but a disposition to fail through excessive deflector drain. Apparently, it is desirable to move the deflectors closer from a performance standpoint, but undesirable from a reliability standpoint.

Inspection of the module after the run showed that direct current paths had formed from the slits to both deflectors through jelled NaI glycerol columns. There was evidence of flooding and tar formation on the slit edges. The edges themselves were not damaged, but the erosion of the stainless steel faces inside the gap, first seen in the previous twin slit run, was even more extensive. It was evident that erosion began at localized spots on the metal, probably where flow was stopped or impeded by an unrelated mechanism. After erosion began, it propagated a fan-like pattern further and further downstream. Some of these patterns extended to the boundary of the platinum; some did not. All stages of growth were observed.

12.2.6 Run 6906-02

The twin slit module was placed in the new 4 foot x 8 foot vacuum chamber with the 24 inch vacuum pump and was run for 115 hours at specific impulse levels in excess of 1500 seconds. Performance was very smooth with practically no arcing, due partly to the improved vacuum (1×10^{-6} to 1.6×10^{-6} torr) and partly to improvements in the slit edges.

The module was prepared for this run with a larger radius, about 0.001 inch, on the slit edges. Wire rods were used for deflectors. The rod diameter was 0.020 inch. The rods were placed 0.018 to 0.020 inch in front of the slit edges, and were spaced 0.070 inch apart. The module was supplied with a radiative heater.

The entire run was made at 15.2 kv slit voltage, -1.6 kv extractor voltage, and 6 kv on each of the deflectors. Figure 77 through 82 give a time history of the varying run parameters. The extractor was drawing a current of 2.0 to 4.0 microamperes from positive secondaries. There was no readable deflector current until very late in the run, at about 94 hours.

The feed pressure and the module heater were used to control the flow rate. No temperature measurements were available to calibrate the effects of the module heater except those made on needle modules. The module was probably running at about room temperature. Over the first 40 hours, the flow rate decreased regularly until settling out to about 60% of its initial value. At 65 hours, it was increased by increasing the heater power and the feed pressure slightly. From then on until about 94 hours, the module ran at about 1800 seconds I_{sp} and 30 µlb per inch thrust.

As the flow rate decreased, from time zero, the average charge-to-mass ratio went from 12,000 c/kg up to about 18,000 c/kg. After the mass flow was raised, Q/M decreased to about 15,000.

At 92 hours the needle current suddenly increased. This was during an unattended weekend period. A few hours later, however, the change was discovered and a 15-microampere drain current to the top deflector was observed. This was the first detected deflector drain. The situation was partially corrected by raising the upper deflector voltage, thus vectoring the beam away from it. The feed pressure was also cut back, and the module heater current lowered, causing a drop in flow rate. By the time 110 hours had passed, the deflector breakdown had almost completely healed, though occasional deflections of about 1/2 microampere were observed.

The run was started at a thrust level of about 48 µlb. Over the first 20 hours, this dropped to 40 µlb as the mass flow rate dropped. These conditions were maintained until 70 hours, when the original thrust level was reestablished. After the deflector breakdown, when the flow rate was cut back, the thrust dropped to its lowest level of 30 µlb. After recovery from the breakdown and immediately before shutdown, an

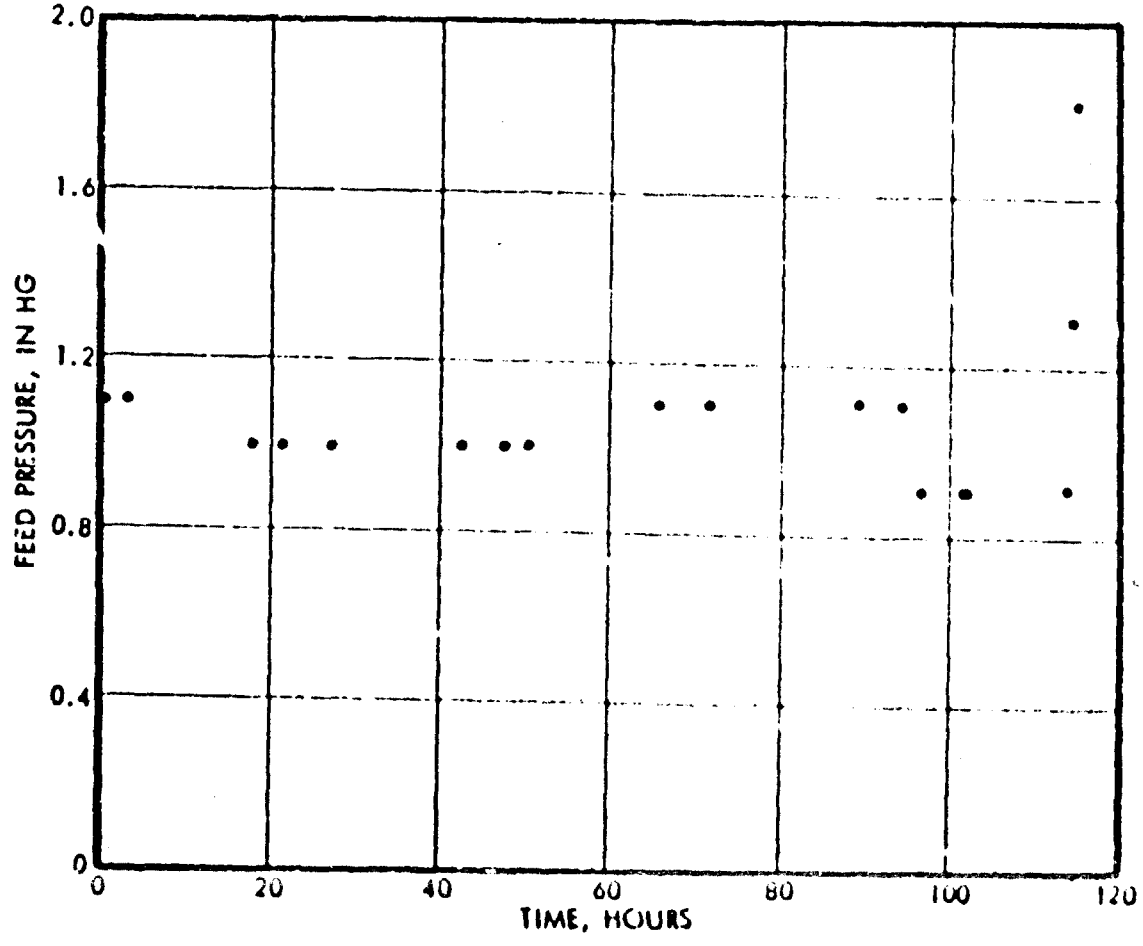

Figure 77. Twin Slit Module, Run 6906-02, Feed Pressure versus Time

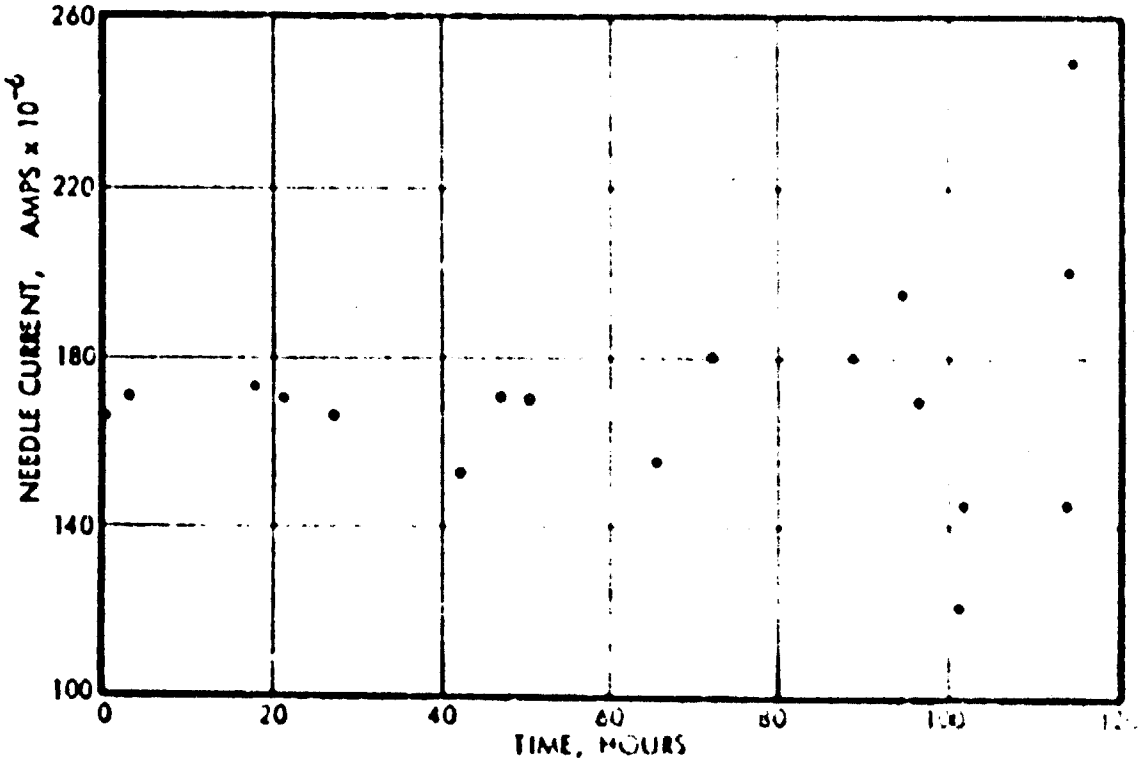

Figure 78. Twin Slit Module, Run 6906-02, Needle Current Vers s Time

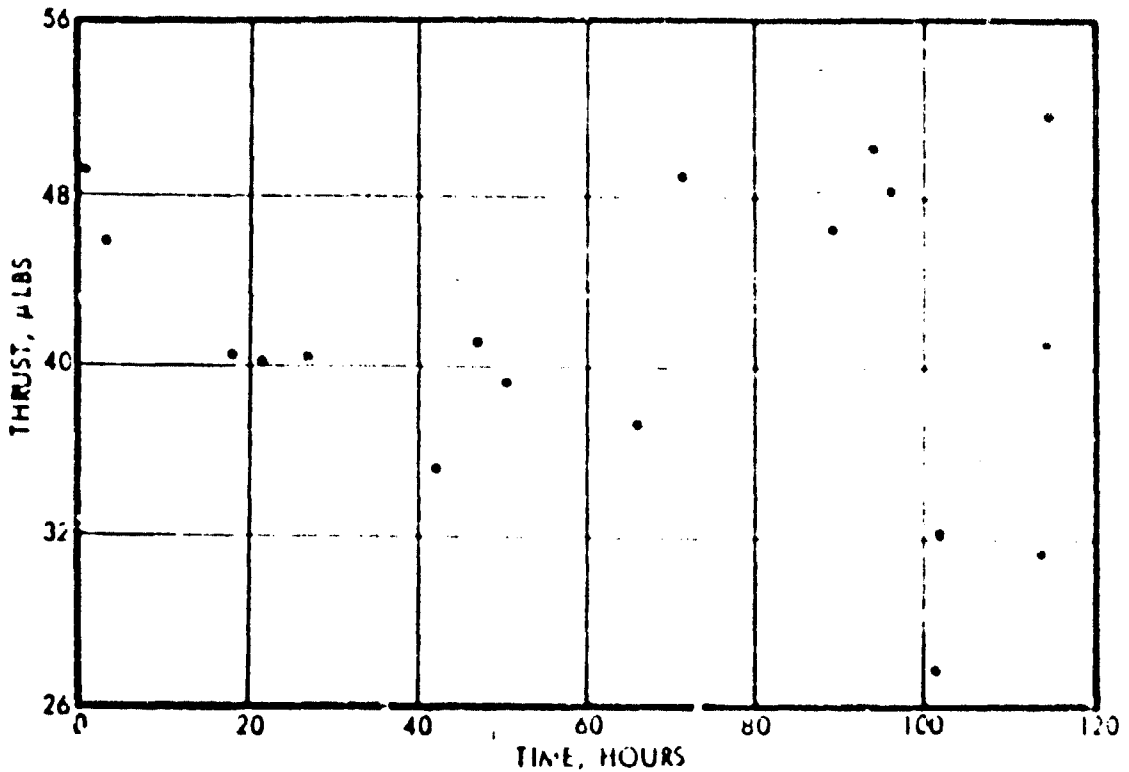

Figure 79. Twin Slit Module, Run 6906-02, Thrust Versus Time

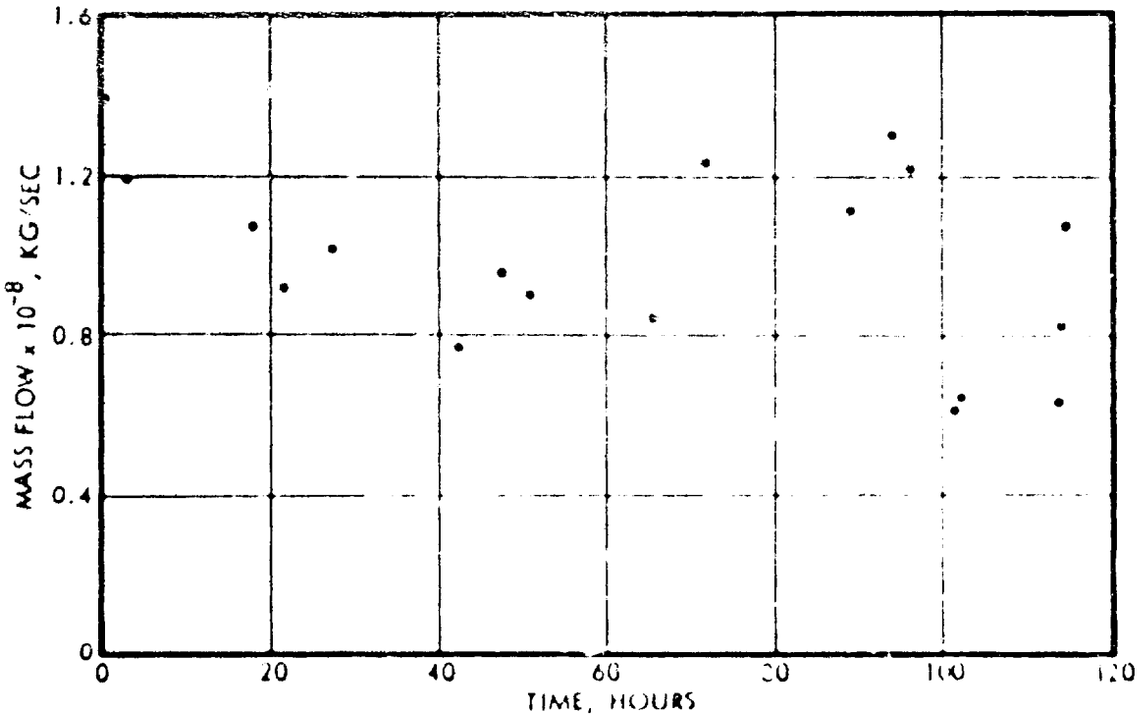

Figure 80. Twin Slit Module, Run 6906-02, Mass Flow Versus Time

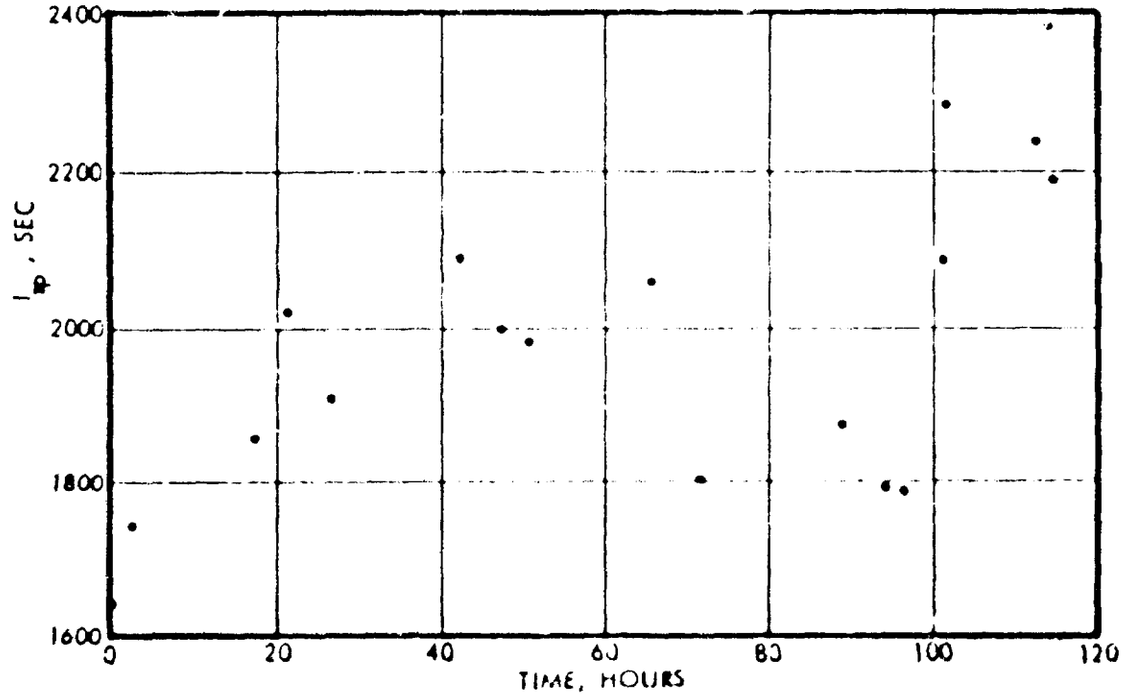

Figure 81. Twin Slit Module, Run 6906-02, I_{sp} Versus Time

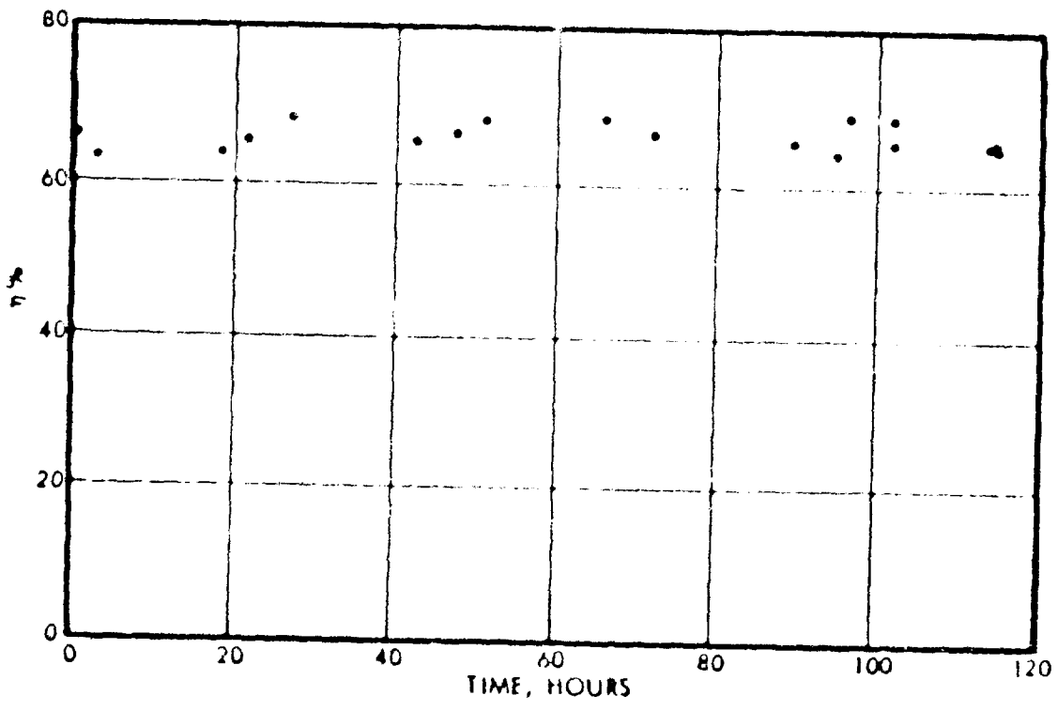

Figure 82. Twin Slit Module, Run 6[illegible]06-02, Efficiency Versus Time (Hunter Beam Efficiencies)

attempt was made to push the thrust level above its original value by increasing the feed pressure. The slit voltage was also increased, but not significantly. The flow rate was sluggish in coming up, and the maximum thrust density achieved was 32 μlb/inch. Arcing to the extractor and deflectors prevented going any higher.

Post-run inspection of the module showed it to be quite clean. The extractor was very clean; the slit edges had grown a few salt crystals, but the flow area was not obstructed. The top deflector had a thin coat of tar in the vicinity of the breakdown.

The beam impingement pattern could be seen clearly on the collector and cold walls. Based on this pattern, the entire beam was contained within an angular spread of ±50°. Visually, the densest part of the beam appeared to lie within the usual ±20° spread.

12.3 ANNULAR SLIT

Work on the annular slit geometry (ASG) was reinitiated late in March, after a lapse of about 5 months. The 1968 work had been done on an old TRW design (Ref. 12-1) consisting of a double-edged annulus with an inner and outer extractor. The results, while promising, were not sufficient to stimulate increased activity, and the project was dropped.

The 1969 effort described here was initially aimed at a cursory investigation of the capabilities of the NASA-Goddard design of the ASG (Ref. 12-2). As the work developed, the apparent potential for a remarkably high thrust-high I_{sp} device with all the important advantages of a needle came as something of a revelation.

By mid-year, it was apparent that high thrust densities were now available. As a matter of course, the ASG was delivering thrust densities which were 30% higher than the highest obtainable with the LSG. This was done at I_{sp} of 1500 seconds or above, with Hunter beam efficiencies equivalent to that of a needle, and with not much more

beam spread than a needle. Further, the unit was soon operated at a thrust of nearly 100 μlb: while not the highest thrust reported, this is the highest we know of at 1500 seconds I_{sp}.

In view of these successes, and in view of the nature of the difficulties with the LSG, steps were taken shortly after July to de-emphasize the LSG and accelerate work on the ASG.

Four problems were recognized as being more or less basic to the ASG:

1) Uneven rim wetting. Never a concern in the LSG, this becomes important here where it significantly affects thrust vector direction. This problem was solved by improved geometry and fabrication techniques.
2) Tar formation. The thick plug at the center of the slit acted as a focus point for energetic electrons. Since it was easily wet with propellant, tar formation was commonly seen here. Several partial solutions were found for this problem.
3) Flow impedance matching was of the same order of difficulty as in the LSG.
4) Beam spread is critically dependent on geometry and rim wetting. At first it was ±20°, but it was brought down to ±10° with geometry improvements. This tolerance is not as reliable as on a needle, since the slit tends to overfeed more easily than a needle.

Several significant technological advances and milestone achievements contributed to the solution of these problems:

1) Improvements in the center plug geometry resulted in reduced beam spread.
2) Improvements in the propellant feed geometry resulted in uniform rim wetting.
3) Remarkably high thrust densities were demonstrated with good performance, as described above.
4) A unit was endurance-tested for 600 hours.
5) A module was built and tested at 100 μlb thrust for 500 hours.
6) A unit was thrust vectored, using standard deflector electrodes, both in one plane and in two orthogonal planes.

The TRW source is 1/8 inch in diameter, and will fit in a 1/4-inch extractor hole. It takes little more space than a conventional needle, and it may be electrostatically vectored as easily as a needle. The basic geometry is a single emitting rim type slit with a concentric centerpiece held at source potential. The propellant forms a meniscus within the 0.002-inch-wide feed gap formed by these two parts. The propellant jets are drawn from the high field region on the emitting rim. Platinum -10% iridium has been used on the emitting surfaces. A platinum -10% iridium slit rim bonded to the shank of the tube, and a platinum -10% iridium center plug have both been incorporated into the ASG.

One might question the propriety of classifying the device as an annular slit. It is actually a large diameter needle with a plug in the hollow center. The purpose of the plug is to provide capillary wetting action to draw propellant to the emitting rim, to increase flow impedance, and to prevent a large propellant meniscus from being exposed to evaporation and backstreaming electron bombardment.

The original "annular slit geometry" nomenclature has to some extent been established in Reference 12-2. In an effort to classify this device separately from the conventional double emitting edge, isolated center extractor, annular slit geometry, other names have been considered. A more descriptive term is "annular needle geometry." However, the term "annular slit geometry" is still commonly used. In this report the references ASG and ANG are used interchangeably.

The emission mechanisms in the annular needle geometry (ANG) have not been studied extensively, but are felt to be similar to those in a small diameter needle. A program of microscopic study would be revealing in this respect.

12.3.1 Early Trials

Three runs were made using the annular slit based upon the NASA-Goddard design (Figure 83). These slits performed reasonably well in the short term, producing at best 25 μlb, 1713 seconds, and 56 percent Hunter beam efficiency for 1.76 watts of power (18 kv and

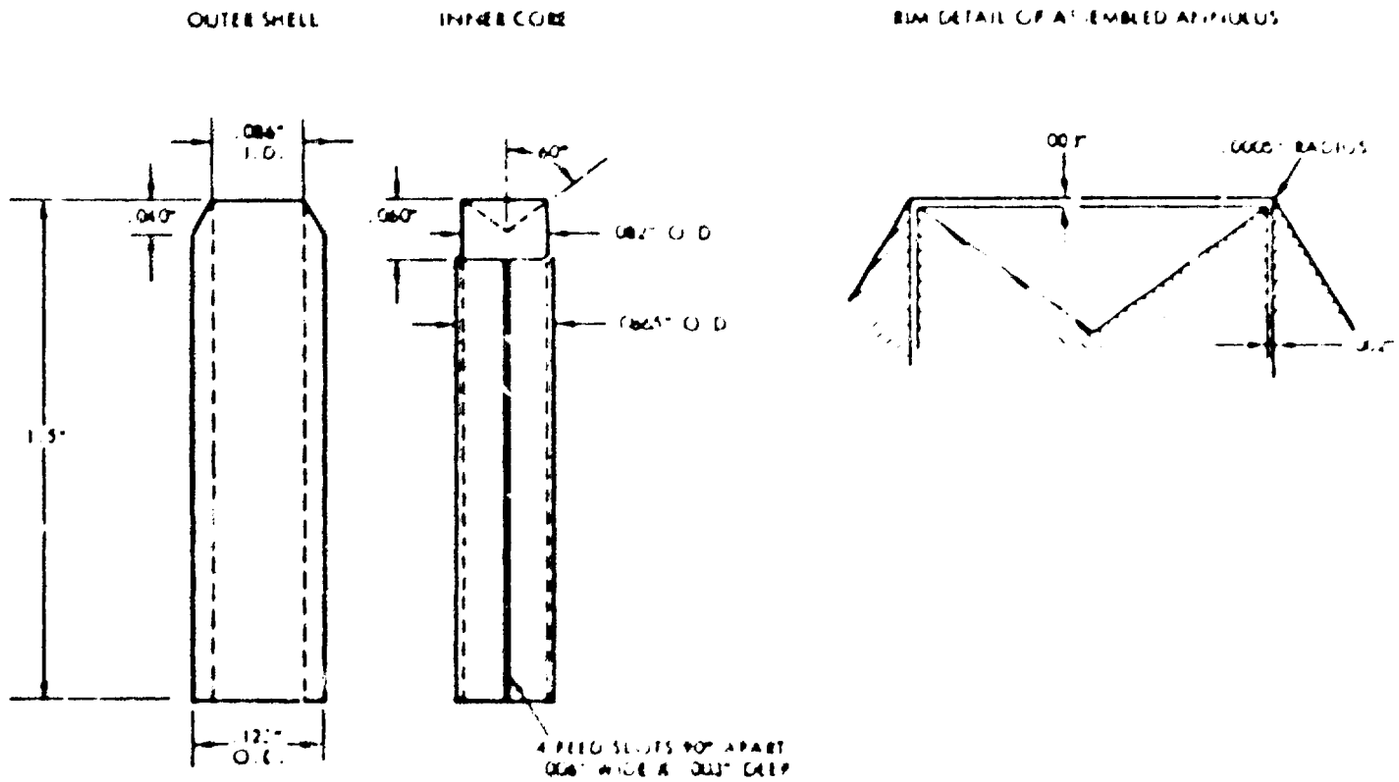

Figure 83. Early Design of Annular Slit

98 amp). The annulus later easily produced between 25 and 50 μlb of thrust at voltages varying from 14 to 17 kv. The major problem in the early runs was electrolytic erosion of the outer stainless steel rim. This problem was eliminated when the slits were made of platinum. Uneven feed distribution along the emitting edge was also a problem. Some of this was caused by non-uniform spacing between the inner and outer parts of the annulus. Other causes were uneven wetting along the emitting rim and the influence of gravity on the shape of the meniscus. More uniform spacing was achieved in early designs by machining a grooved collar with a slightly oversized O.D. The feed grooves permit passage of the propellant to the emitting region 60 mils above the collar (Figure 83). More thorough cleaning procedures eventually improved the wetting.

The fact that electrolytic erosion occurred only on the outer edge of the annulus indicated that this edge was, as expected from the geometry, the site of the emitting jets. Tar formed in the first two runs in the beveled hollow at the top of the inner piece of the annulus. During the third run, a higher negative bias (i.e., -2000 volts versus -1000 volts) was used. Tar did not form during this run (which lasted 24 hours, approximately as long as the other runs), although propellant with a brownish color, indicating a large amount of free iodine, was present in the fluid.

12.3.2 Fabrication of the First Platinum Edges

When the platinum tubing and rod needed to provide the annular slit with erosion resistant edges were received, the platinum tips were made and brazed to stainless steel bodies with 18% Ni, 82% Au filler. The platinum edges were machined to the required shape in the jeweler's lathe.

After fabrication was completed, the slit was carefully cleaned to ensure good wetting by the propellant to improve capillarity around the slit edge.

12.3.3 Run 6206-04, Attempted 100 Hours

The annular slit with platinum emitting edges was run for 67.5 hours until a leak in the feed line terminated the run. Performance was excellent and the platinum edges had no indication of erosion. The annulus emitted around the entire rim, indicating good wetting. The relatively high efficiencies, > 73%, indicated uniform feed and capillarity around the rim. Figure 54 shows several TOF's taken during the run.

The goal for this run was an I_{sp} of > 1500 seconds, a thrust of 12 μlb, and 100 hours running time. The I_{sp} and thrust goals were exceeded and the leak in the Luerlok fitting was the only reason the 100 hours was not attained. There had been no performance degradation during the run and the annulus was in excellent condition at the end of the run (i.e., no erosion or tar).

The first 16.5 hours of operation consisted of overnight idling at 13.5 kv on the annulus, -1.5 kv on the extractor, 0 inch feed pressure, and I_n = 20 μamp. After the necessary operating parameters were determined next morning, i.e., V_n = 15 kv, P = 5.5 inches of Hg, I_n = 50 μamp, the module was then operated for the next 50 hours at greater than 1500 seconds I_{sp}, greater than 12.9 μlb, and greater than 73 percent Hunter beam efficiencies.

12.3.4 Experiments with Geometry

The TRW annular slit geometry consists of an outer tube, 0.125 inch O.D. and 0.086 inch I.D., concentrically bored. The source edge is beveled around the outside to an angle of about 20 degrees. Figure 85 is a 10X magnified photograph of the tip of the slit.

During the course of this work, the centerpiece of the slit underwent several transformations in geometry. Careful experimentation demonstrated that the distance of the centerpiece behind the outer rim critically influenced the beam profile. The slit in Figure 85, an early model, had the centerpiece 5 to 7 mils back of the rim. This resulted in a splayed-out hollow beam with wide half-angle. The centerpiece was then tried at various depths below the rim of the needle. It

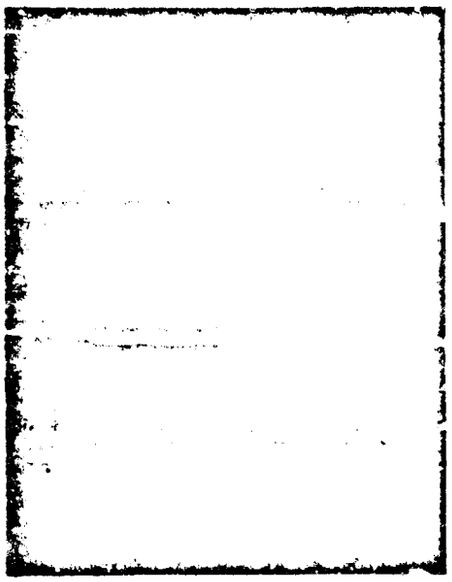

(a) 18 HOURS

V_m = 14.2 kv
I_m = 51 μamp
V_x = -1.6 kv
I_x = 0.1 μamp
I_{sp} = 1870 sec
Thrust = 12.9 μlb
$\dot{m}$ = 0.33×10^{-6} kg/sec
Eff = 75.4%
$\overline{(Q/M)}$ = 13,040 coul/kg

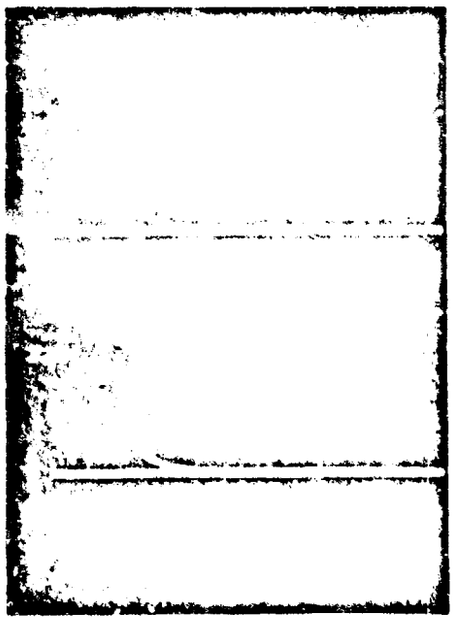

(b) 37 HOURS

V_m = 15 kv
I_m = 52 μamp
V_x = -1.6 kv
I_x = 0.8 μamp
I_{sp} = 1940 sec
Thrust = 13.9 μlb
$\dot{m}$ = 0.32×10^{-6} kg/sec
Eff = 75.4%
$\overline{(Q/M)}$ = 13,040 coul/kg

Figure 84. TOF Information Run 6909-04, Platinum Edged Annular Slit. TOF Length is 60 cm, Sweep Speed 20 μs/cm.

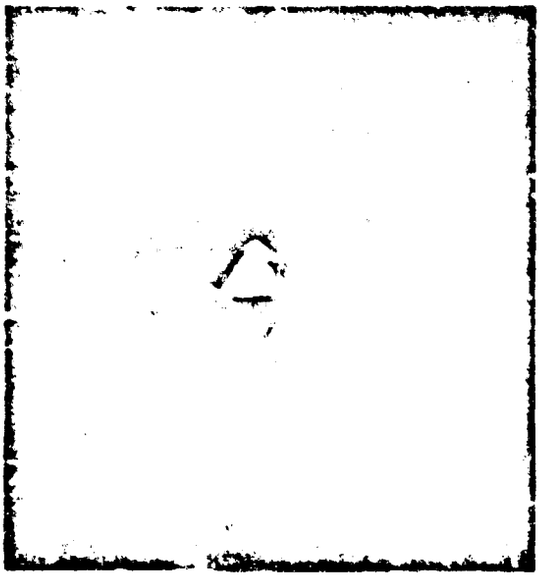

Figure 85. Typical Annular Slit Source, Magnified 10X

was set at depths of 0.005 inch, 0.007 inch and 0.010 inch. The shallowest setting caused an excessively wide beam spread. The inner beam was hollow so that practically no mass was being accelerated straight ahead. The effect of pulling the centerpiece back was to focus the beam, so that at 0.010 inch depth, the beam was highly uniform through the center as observed visually.

The extractor hole size for the ANG is nominally 0.230 inch. A smaller hole, 0.190 inch, was tried with no significant change in performance. Extractor hole size in a needle module is 0.140 inch, and in the LSG the extractor slit width is 0.160 inch.

Nominally, the annular needle is placed in the extractor so that its tip is just even with the outer surface of the extractor. The beam spread is affected by this positioning, and the optimum needle tip position from a focusing standpoint was found to be approximately 0.05 inch behind the extractor face. However, this positioning leads to increased extractor drain and higher breakdown probability.

Several different geometries were tested to determine the effect of geometry on other operating characteristics. An annulus with a slightly rounded emitting edge, 0.001 inch radius, was tried. The operating voltage for this was prohibitively high, above 15 kv. The geometry also produced excessive beam spread. A sharp emitting edge with a narrow bevel around the outside of the rim produced a smoother current and a higher thrust at a lower voltage (12-13 kv).

The centerpiece of the earliest ASG consisted of a straight rod, 0.0865 inch in diameter, with the topmost 0.060 inch turned down to a diameter of 0.082 inch, leaving a 0.002 inch feed gap between the centerpiece and outer tube. Four rectangular feed slots ran the length of the centerpiece, up to the feed gap. This design had two serious drawbacks. The rectangular feed channels were difficult to machine, and the uniformity of feed gap width, i.e., the concentricity of the centerpiece, was very difficult to maintain. The slit also tended to wet first on the rim in the vicinity of the feed channels. It was difficult to achieve uniform wetting over the perimeter. In a later design, the four rectangular feed grooves were replaced with four flats which were simply filed out of the cylinder. These were not entirely satisfactory, since it was difficult to fabricate four such channels with equal flow impedances. When this was not done properly, some sectors of the rim overfed, while others would not wet for long periods of time. The solution to this problem was to machine a small propellant plenum 0.1 inch below the top of the centerpiece, approximately 0.2 inch long and 0.005 inch deep. This plenum offered a low flow resistance reservoir which would fill completely with fluid. The fluid would then feed out of the plenum, uniformly wetting through a 0.002 inch feed gap. This device produced uniform emission around the entire rim within 2 hours after startup.

Figure 86 shows the TRW source design that finally emerged from these experiments. The centerpiece is in two pieces. The top piece, all platinum, is kept short to eliminate the concentricity problem. A 5-mil-deep feed plenum, which uniformly distributes feed pressure around

the perimeter, is machined just below the feed gap. The plenum is filled through four equally spaced channels emanating from a central feed channel. This design has greatly improved the uniformity of propellant wetting around the rim. Impedance control is provided by a single, slightly tapered rod inserted in the back of the unit. Concentricity of this unit is not important. Flow passage is achieved by nonuniformities in the roundness of the rod.

The development of a standard, machine-reproducible method for impedance control is one of remaining problems to be solved for this configuration. Several advances have been made toward the solution of the problem. Devices that have attained some degree of success include a 4-mil I.D. needle flow passage of calibrated length, and also a spring and plug arrangement.

Single slit experiments, mostly conducted with sharp rims (less than 1/4-mil radius), have been most successful in producing uniform, high Q/M beams at relatively low voltage. Later experiments (including the seven-needle module to be discussed) run with slightly rounded source rims resulted in higher voltage and higher I_{sp} for the same Q/M.

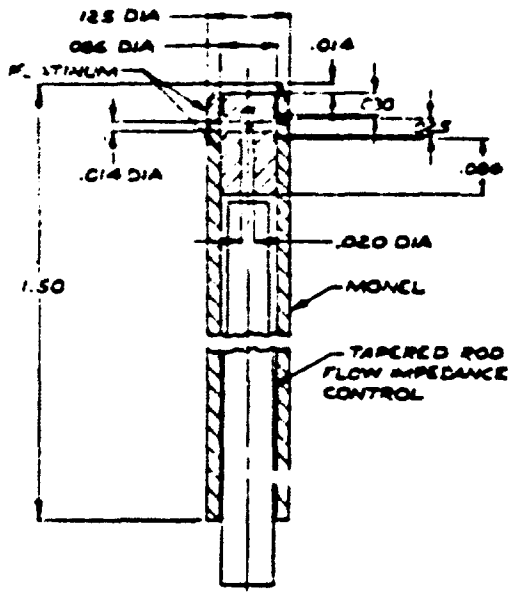

Figure 86. Section Drawing of TRW Annular Slit Design

12.3.5 Thrust Density Considerations

The normal characterization of thrust density for a slit source is in micropounds per linear inch of emitting edge. The linear slit geometry (LSG) has reliably demonstrated 30 to 40 micropounds/inch and has achieved a nominal upper limit of 60 micropounds/inch at which serious reliability problems appear. The LSG has run at this high thrust density only for short periods (4 hours) at a time.

The TRW annular slit geometry (ASG) has an emitting rim diameter of 0.086 inch. Sources of this type have demonstrated thrusts in the neighborhood of 25-30 micropounds in the 1500 sec I_{sp} range, and have achieved thrusts up to 50 micropounds at lower I_{sp} without difficulty. A thrust of 50 micropounds on a diameter of 0.086 inch corresponds to a linear thrust density of 185 micropounds/inch, a number much larger than the thrust densities achieved by linear and double rimmed annular slit devices. This is perhaps an unfair comparison, since it is more meaningful to discuss thrust density per unit area.

The existing technology for clustering needles is easily extended to the ASG. The extractor hole size required is barely more than that of a needle--about 0.250 inch in diameter. Table 12-2 presents a comparison among the needle, linear and annular geometries that leads to the conclusion that the latter gives the highest thrust density capability in the 1500 second I_{sp} range. The standard of comparison is the 36-needle module currently under development at TRW (Section 6). Thrust densities are calculated for both hexagonal and square packing, the former being about 16 percent denser than the latter. The LSG module is assumed to be packed with parallel slits of arbitrary length, with a 0.4-inch nearest-neighbor separation as used on the current TRW double slit module.

The geometries being compared produce I_{sp}'s of 1500 seconds or greater. The needles and ASG operate at Hunter beam efficiencies of 70 percent or more, while the LSG operates between 60 and 70 percent. It should be noted that the thrusts compared are not chosen on an equal basis. For a needle, 3 micropounds is a safe upper limit; for the LSG,

Table 12-2. Thrust Density Comparison for Various Colloid Concepts

Packing Geometry	Needles			Goddard Annuli	
	Hex	Square	LSG	Hex	Square
Nearest Neighbor Distance (in.)	0.250		0.400	0.410	
Packing Density (per sq. in.)	18.5	16	2.5*	7	6
Thrust (μlb. per unit)	3		60*	25	
Thrust Density (μlb/in²)	55	48	150	175	150
Relative Flow Conductance (per unit)	1		9.2*	2.8	
Operating Voltage (kv)	13		18	14	
Current (μamp per unit)	10		200*	70	

*Per linear inch.

60 micropounds/inch is an extreme upper limit; and for the ASG, 25 micropounds is a reliable nominal at 1500 sec I_{sp}. The TRW design has, in fact, been run at 100 μlb. Stark at Goddard reports an upper limit of 300 micropounds, but this is apparently achieved only at the expense of reduced I_{sp} and efficiency. Table 12-3 exemplifies the high thrust data points. The reliability and reproducibility of such high thrusts should be carefully scrutinized. However, by using only 25 μlb for the ASG, we are conservatively comparing what the ASG does with ease against what the LSG does with difficulty.

Table 12-3. Summary of High Thrust Data from TRW and Goddard

Thrust (μlb)	Source Voltage (kv)	Source Current (μamp)	Feed Pressure (in.Hg)	I_{sp} (sec)	Beam Effec. (%)	Mass Flow $\left(\frac{\mu gm}{sec}\right)$	Q/M (c/kgm)
				TRW			
57(1)	14.7	147	15.3	1356	78	19.0	7,600
81.5(2)	15.8	200	18.0	1327	70	27.9	7,170
95.4(2)	15.8	215	23.4	1075	66	40.3	5,340
99(2)	19.0	300	19.0	1500	57	30.0	8,960
				Goddard			
221	18.0	300	5.3	555	50	1.8×10^5	0.82
298				603	59	2.3×10^5	0.98

(1) Run No. 6908-02
(2) Run No. 6908-08
(3) Reference 12-2 (Stark)

The TRW data in Table 12-3 is taken mainly from Run No. 6908-08, which was a short run in NRC 4 feet x 8 feet tank specically for the purpose of testing high thrust performance. They were taken with an early needle, with no feed plenum and four propellant feed flats. None of the operating conditions were maintained for more than 15 minutes. The data in run -08 were taken after the needle had been equipped with deflectors, while the data in run -02, an earlier run, were taken without deflectors.

The Goddard data, while incomplete, are presented for comparison. They represent the highest published thrusts for such a device.

12.3.6 Run 6908-02, 188-Hour Endurance Test

An annular needle source was run unvectored for 188 hours. The purpose of the run was to test endurance and study the effects of parameter variations. This run was the first which was truly demonstrative of the potential capability of the AMG. Table 12-4 is a summary of data from this run. This source was run with a heater. Most of the performance variations are believed due to either the effects of temperature variations on the propellant viscosity and its flow rate, or to the uncontrolled rim wetting condition of the rim. Specific impulse was high and efficiencies were all above 75%. The centerpiece was 0.010 inch behind the rim, and the beam spread more than normal. The extractor held at -1.2 kv. No extractor drain was observed.

Table 12-4. Some Data from Run 6908-02, the 188-Hour Single Needle Endurance Run

Hours	Feed Pressure (in.Hg)	Source Voltage (kv)	Source Current (μamp)	Thrust (μlb)	I_{sp} (sec)	Beam Effic. (%)	Mass Flow $\frac{\mu gm}{sec}$	Q/M (C/kg)
7	10.2	12.8	55	22.0	895	78	6.04	3,400
22	8.7	12.8	83	23.0	1591	76	6.64	12,500
46	9.35	12.9	100	29.6	1602	80	8.38	11,900
143	12.0	14.0	135	44.8	1512	78	13.0	10,000
143	15.3	14.7	147	57.0	1356	78	19.0	7,600
150	10.15	15.8	190	72.1	1560	82	21.0	9,000
150	10.15	17.0	150	55.0	1652	79	15.2	9,700
166	9.75	13.0	100	37.8	1214	77	14.1	10,800

The source edge was observed visually during this run, and propellant jets were identified streaming off the rim. The middle region of the centerpiece was observed to have an active froth or foam during the high thrust periods, and it was inferred that this was due to the action of high energy backstreaming electrons (formed between the potential barrier and annular needles) on seeping glycerol. This was further verified by post-run observation of a hill of tar in the midportion of the centerpiece. The outer region of the centerpiece remained clean. This same condition has been observed on many of the sources, and it is felt that tar formation on the centerpiece is a major problem. In later experiments with various centerpiece geometries, the objective was to keep excess glycerol from straying onto the midportion of the centerpiece. These experiments are described in section 12.3.10.

12.3.7 Runs 6908-07 and 6908-09; Two-Vector-Electrode Research

A single slit source with two vectoring electrodes was fabricated, and preliminary testing was accomplished. Figure 87a. is a view of the extractor-electrode assembly, and Figure 87b. shows a front view of the assembly with the slit source in place. The deflectors were made from stainless tubing with a 0.180-inch I.D. and a 0.010 inch wall thickness. The source used on all vectoring experiments was an intermediate design with the centerpiece 0.014 inch behind the rim and an annular propellant plenum just below the feed gap. The propellant was fed in around the outside of the centerpiece.

The first test, Run No. 6908-07, was made in a small chamber with a 6-inch pump. The source voltage was 12.7 kv and the current was 85 microamperes. The performance was in the neighborhood of 1470 seconds I_{sp}, 23 micropounds thrust, and 70% efficiency. The beam deflection was photographed.

Based on the visible beam limits, the beam showed a nominal spread of ± 10 degrees under all vectoring conditions. Photographs of the beam deflection are shown in Figure 88. The beam was vectored up approximately 8 degrees (Figure 88a) and down approximately 9 degrees (Figure 88c).

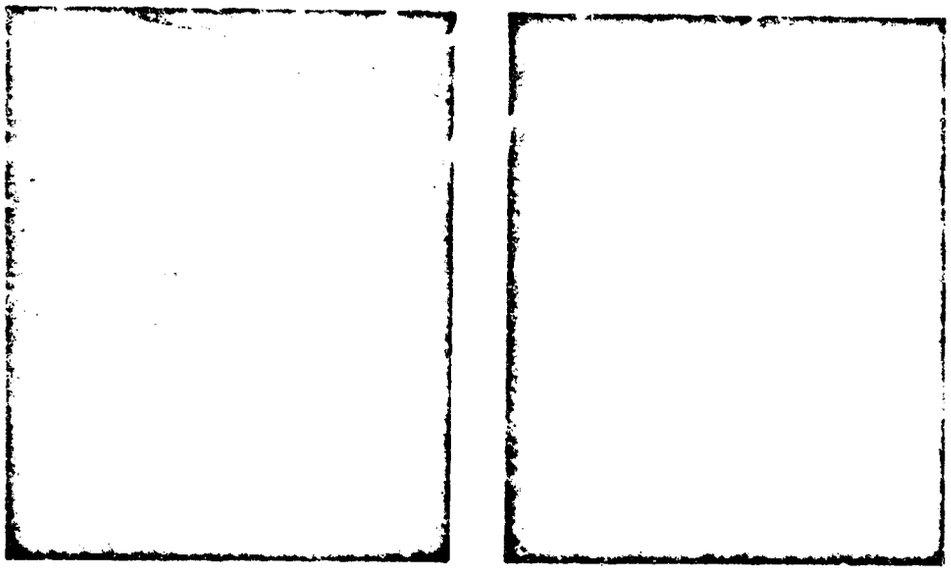

a) Extractor-Electrode Assembly b) Front View with Slit in Place

a) Extractor-Electrode Assembly b) Front View with Slit in Place

Figure 87. Experimental Single Slit with Two Vectoring Electrodes

In the unvectored position, the deflectors were both held at 7 kv. To vector, a voltage differential of 6 kv was applied between the electrodes, indicating a vectoring capability of about 700 volts/degree.

The second test, Run 6908-09, was made in a larger (4 feet x 3 feet) chamber in an attempt to verify the visual data with probe data. The accuracy of the visual data is of course affected by the inability of the analysis process to accurately account for variations in visual beam intensity, and the inexact correspondence of visual beam density to thrust and current density. The accuracy of the probe data is also under question since it was not possible to probe the whole beam in the deflected position. The results show order of magnitude agreement, however. The probe data indicated a somewhat lower deflection capability of 1200 volts/degree.

Table 12-5 summarizes the conditions under which the vectored and unvectored probe measurements were taken. No significant extractor or deflector drains were noted. The two sets of readings were taken within an hour of each other.

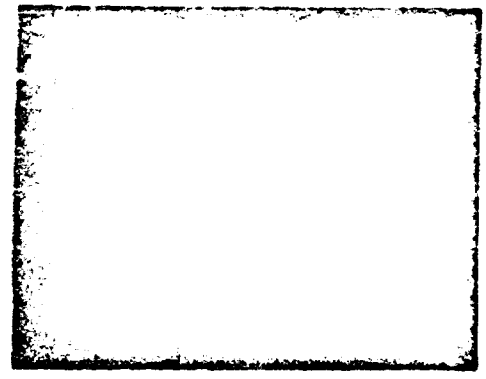

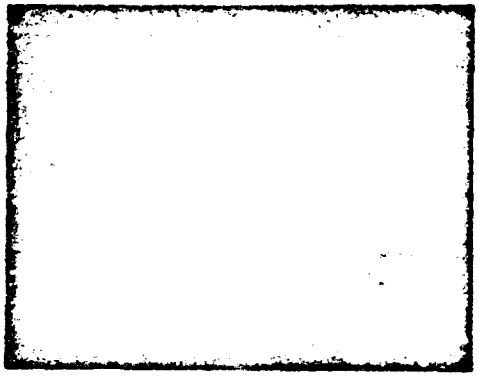

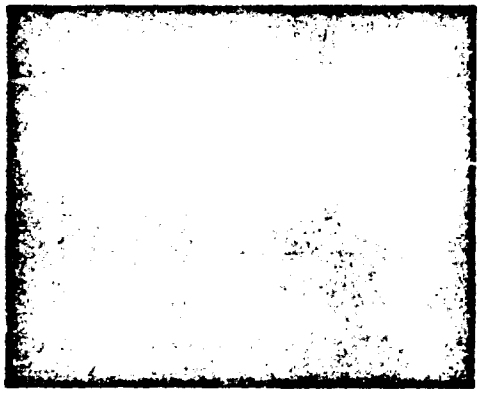

c) Vectored Down

Figure 88. Time Exposures of Beam from Slit with Two Vector Electrodes (Beam Image Partially Reflected in Extractor)

Figure 89 shows the variation of Q/M with angle for the vectored and unvectored beams. In agreement with previous experience, Q/M and I_{sp} are highest at the larger angles (Ref. 12-1) due to the effects of field enhancement. Figure 90 is a composite plot of thrust and current densities for the vectored and unvectored beams.

Figure 89 and 90 each show beam asymmetry probably caused by non-uniform wetting. This was almost certainly due to gravitational effects, since the lower part of the beam apparently had a higher mass flow and low Q/M. This data was, in fact, the first solid evidence that gravitational effects produced asymmetries. The centroids in Figure 90 show a total thrust deflection of about 5 degrees. The thrust curve for the vectored beam had to be extrapolated rather arbitrarily for the large positive angles, and this represents a source of error. The current density data indicate a total beam spread of $\pm 18°$, about twice that observed visually. There is, however, a fair correlation between observed current and thrust densities.

Table 12-6 summarizes the other important time-of-flight parameters as a function of angle.

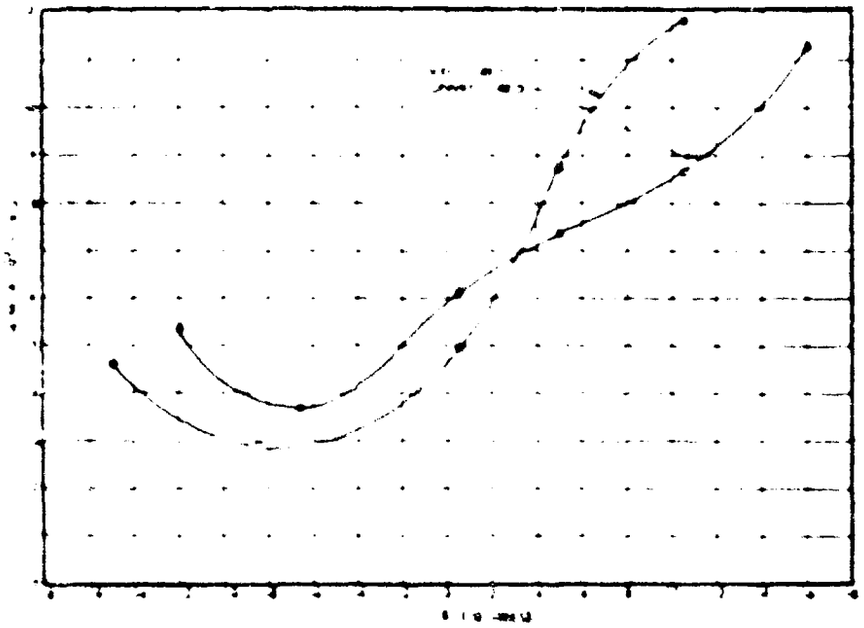

Figure 89. Average Q/M Versus Angle: Probe Measurements from Slit with Two Vector Electrodes

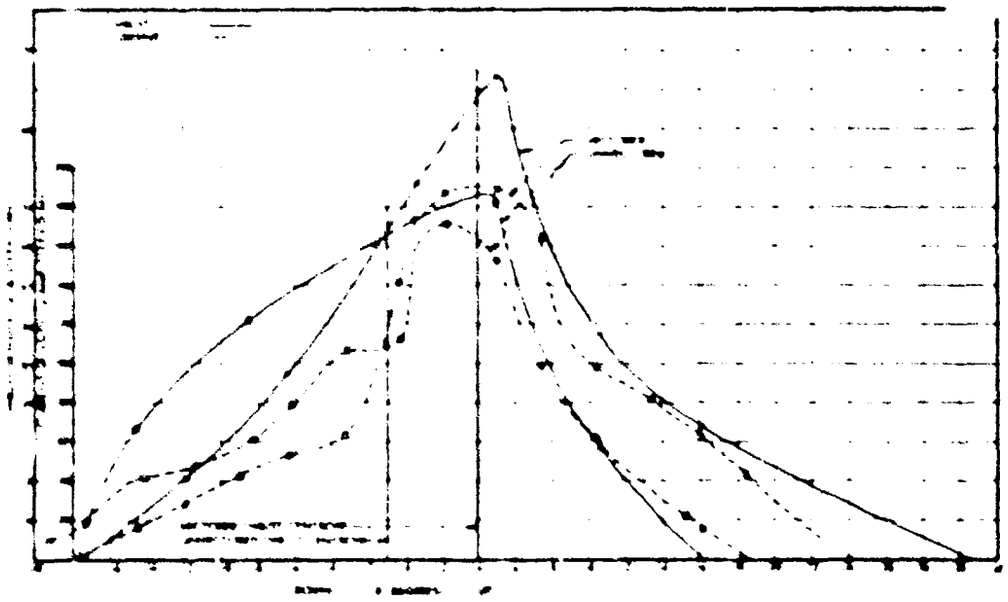

Figure 90. Composite Plot of Thrust and Current Densities; Probe Measurements of Two-Electrode Vectored Slit

Table 12-5. Summary of Probed Beam Conditions for Vectored Slit*

	Unvectored	Vectored
Feed Pressure (in.Hg)	8.9	8.05
Slit Voltage (kv)	13.3	13.3
Slit Current (microamps)	77.0	80.0
Upper Deflector Voltage (kv)	6.6	3.5
Lower Deflector Voltage (kv)	6.6	9.4
Extractor Voltage (kv)	-1.8	-1.8
Thrust (micropounds	34.2	32.0
Mass Flow (microgm/sec)	14.2	12.3
I_{sp} (sec)	1090	1183
Efficiency (percent)	82.0	78.0
Q/M (coul/kg)	4,290	6,503

Table 12-6. TOF Summary for Vectored and Unvectored Beam Profiles, -5° Shift in Thrust Centroids

	Angle (deg)	Current* Density	Thrust* Density	I_{sp} (sec)	Q/M (c/Kg)	Efficiency (percent)
	-14.7	41.8	19.77	913	4560	71
	- 8.5	60.7	36.6	806	2958	79
Unvectored	0.5	111.9	51.9	1042	4946	79
	5.0	152.0	54.1	1421	8782	83
	10.6	60.8	17.0	1533	11855	72
	-12.0	28.3	12.3	1043	5333	74
	- 6.5	53.4	28.3	902	3715	79
	0.67	141.8	57.8	1140	6141	76
Vectored	5.0	188.0	73.9	1304	7340	84
	10.5	98.4	34.7	1383	8644	80
	16.0	62.3	20.1	1555	11375	77

*Microampere/steradian and micropounds/steradian.

During Run 6908-09, some preliminary performance mapping of the annulus with vectoring electrodes was also accomplished. The results are shown in Figures 91 and 92. An extrapolation of the data in Figure 91 indicates that a 25-micropound, 1500-second operating point may be found at a feed pressure near 5 inches and a source voltage near 14 kv. This point became the basis for a standard design of a 25-micropound source. The vectored source used here had two deflector electrodes, but the geometry was not much different from that of a source with three deflector electrodes, to be discussed below.

During the performance mapping of the single vectored annulus, the extractor was run constantly at -1.75 kv. Some extractor drain was observed, but always less than 3 microamperes. There were no significant current drains to the vectoring electrodes.

12.3.8 Run 6909-01; Three-Vector-Electrode Research

The concept of using three vector electrodes is a unique one which seems particularly well adapted to the AMC. In the first place, the slit source is large enough (1/8-inch diameter) to accommodate three electrodes around its perimeter without serious fabrication or assembly tolerance problems. Secondly, the use of three vectoring electrodes is consistent with the use of a hexagonal packing geometry in a module.

The hexagonal close-packed geometry has three principal axes which lie symmetrically at angles of 60° from each other. Along these axes lie rows of sources spaced at the nearest neighbor distance. Between each row there is enough room to run a vector electrode support rod for all the sources in an adjacent row. The support rods for each of the three principal axes must lie at different levels to avoid interference with each other.

A three-electrode vectoring scheme was tried on a single slit source. Figure 93. shows the arrangement of the vector electrodes in the extractor hole. The slit used was the same as that of the two-electrode study and the dimensions of the vectoring electrode cylinder were also the same.

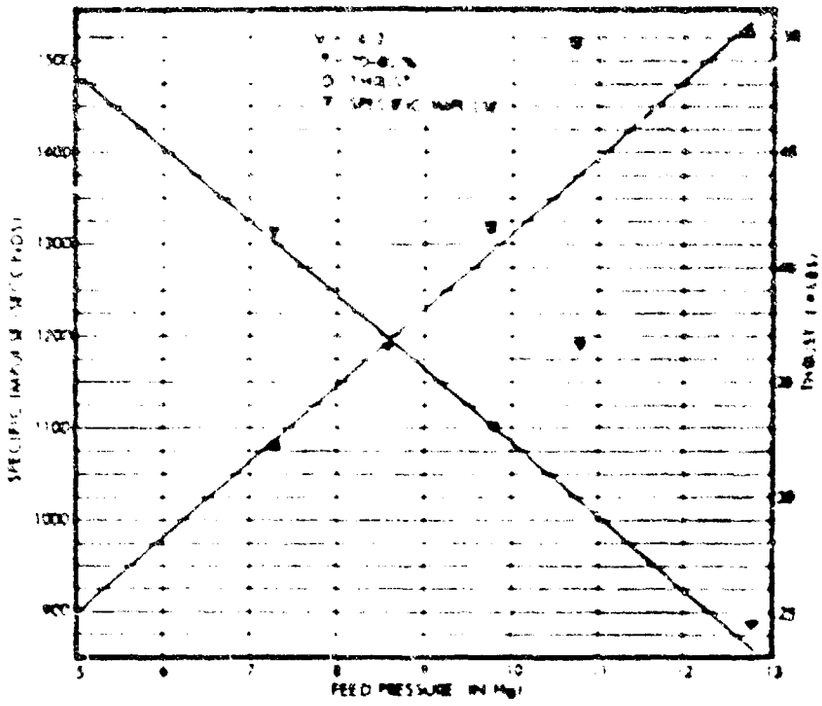

Figure 91. Thrust and I_{sp} as a Function of Feed Pressure for Constant Source Voltage; Vectored Single Slit

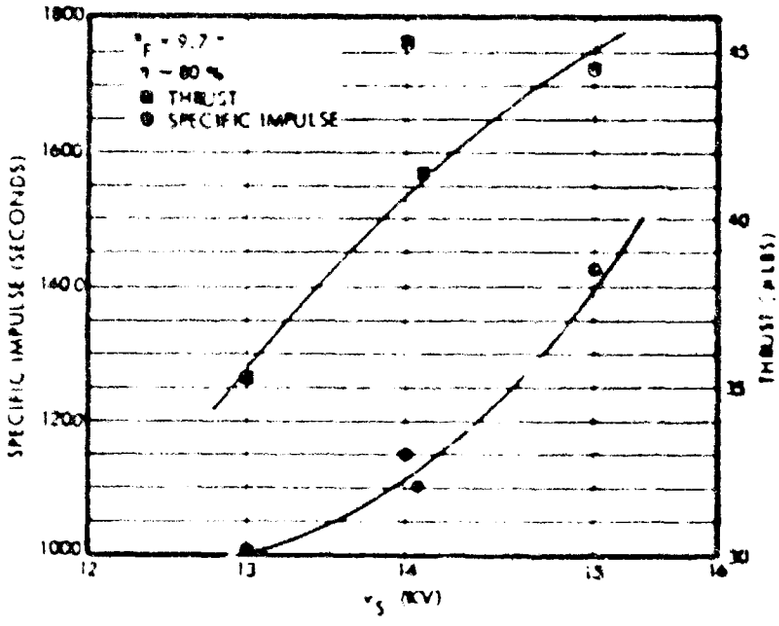

Figure 92. Thrust and I_{sp} as a Function of Source Voltage for Constant Feed Pressure; Vectored Single Slit

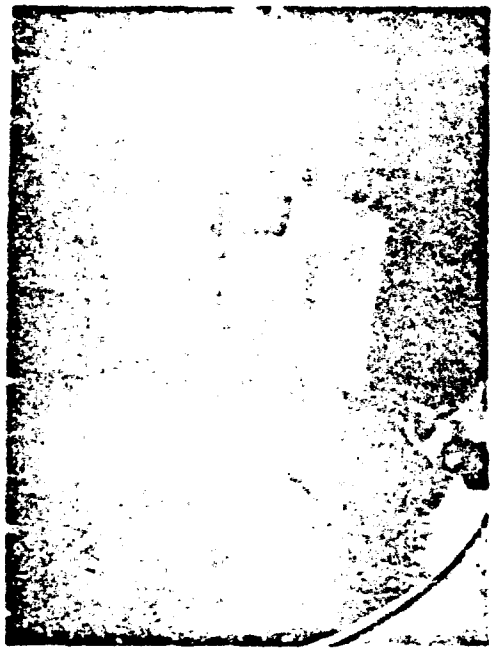

a. Extractor-Vector Electrode Assembly from Rear

b. Front View, with Slit in Place

Figure 93. Experimental Single Slit with Three Vectoring Electrodes

This slit was run in the 4 ft x 8 ft test chamber, successfully thrust vectored in one plane, and the beam was photographed (Figure [illegible]). The slit performance closely matched the data found for the two-vector-electrode single slit. Based on the visual evidence of the photographs, the nominal beam spread from this source was from 9 to 12 degrees. The beam vectored up at an angle of 6 degrees, and down at an angle of 8 degrees.

The vectoring electrodes were oriented with the gaps at 0, 120 and 240 degrees, with zero degrees being straight up. Thus one vector electrode covered the bottom and two the top. The upward vectored beam was accomplished with the two top electrodes at 1 kv, and the bottom electrode at 11 kv. The downward vectored beam was run with 9 kv on the two top electrodes and 3 kv on the bottom. In the worst case the deflection voltage was 10 kv, giving almost 1700 volts/degree. It was easier to vector downward, with a voltage differential of 6 kv and a vectoring capability of 750 volts/degree. This might be expected because of the asymmetrical mechanism by which the beam was vectored. Again, no significant drain currents were observed to any of the deflector electrodes or the extractor. The undeflected beam was run with the vector electrodes at 6 kv.

These pictures were made while operating at a source voltage of 14.4 kv, a current of 95-100 microamperes, and a feed pressure of [illegible] inches. The I_{sp} was nominally 1500 seconds, thrust 28 micropounds, and mass utilization efficiency 70%.

12.3.9 Seven Source Module; 500-Hour Test

Seven individual slit sources of the most recent design were fabricated and impedance tested. The average impedance was equivalent to about six needles per source, and the impedance match was good to only about 12%. It is felt that with more care and better methods, much better impedance matches could be obtained, but it is not certain what allowable tolerances for impedance matching are on sources of this size. Also, the impedance chosen here was rather low, since the sources were being designed for high thrust purposes. Testing of the module showed that a higher impedance would probably be desirable (something of the order of three equivalent needles).

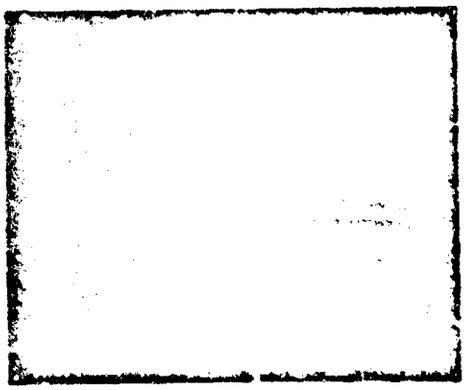

a. Vectored Up: Top Electrodes at 1 kv; Bottom Electrode at 11 kv

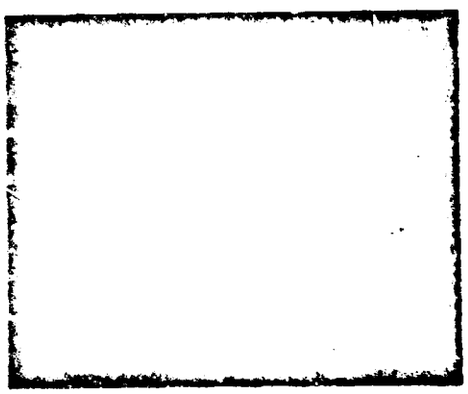

b. Vectored Down: Top Electrodes at 9 kv; Bottom Electrode at 3 kv

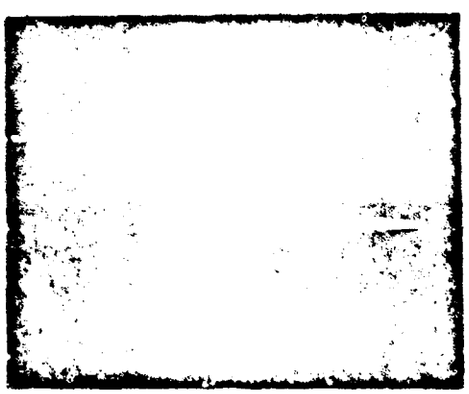

c. Unvectored: All Electrodes at 6 kv

Figure 94. Time Exposures of Beam from Slit with Three Vectoring Electrodes (Thrust: 2 mlb; I_{sp}: 1500 sec; Beam Efficiency: 76 percent)

The seven sources were installed in an existing needle module plenum which was modified for the purpose. They were installed in a hexagonal pattern with an extractor hole diameter of 0.230 inch and a nearest neighbor spacing of 0.410 inch. The module was unvectored (Figure 95).

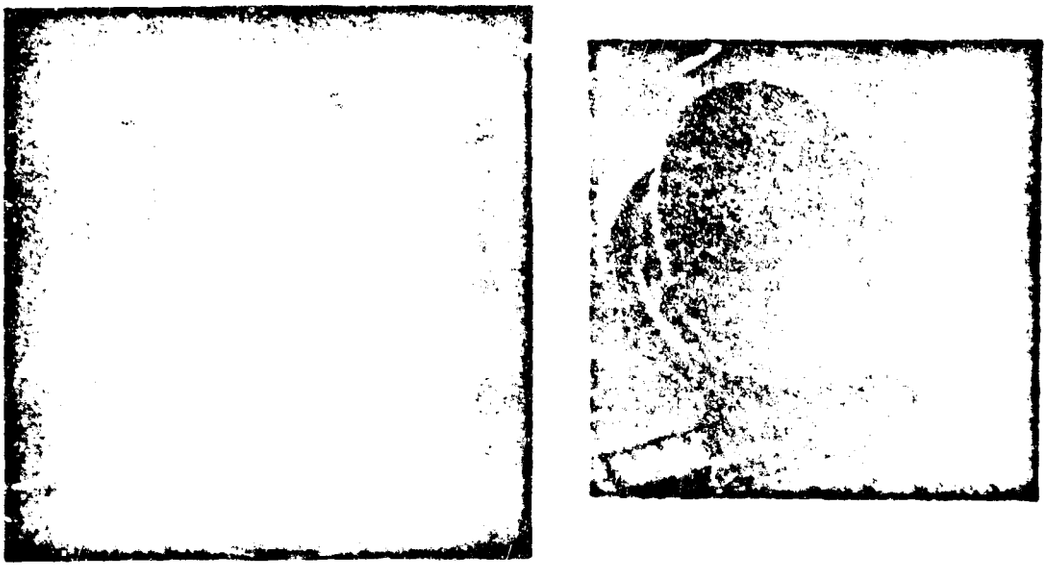

Figure 95. Experimental Seven Slit Module, Unvectored

The module was tested briefly in the 4 feet x 8 foot facility. The highest performance achieved is summarized in Table 12-7 The 1-milliampere current was the limit of the system's measurement capability. The 387-micropound thrust results in a thrust per needle of 55 micropounds. Backstreaming electron current, source extractor breakdown and gas generation were all problems which were minimized but not removed by keeping the extractor at a high negative voltage. The center source, in particular, was a source of trouble, just as has been experienced in the past with hexagonal needle geometries. It acted as a focus point for backstreaming electron current. Its performance was very erratic and it was the cause of much of the source-extractor breakdown. The run was terminated after approximately 2 hours.

Table 12-7. Performance of Seven Slit Module

Source Voltage = 14.2 kv	Thrust = 387 micropounds
Source Current = 1 Ma	Specific Impulse = 1333 sec
Extractor Voltage = -4 kv	Hunter Beam Efficiency = 79%
Extractor Current = 25 μamp	Mass Flow Rate = 132 μgm/sec
Feed Pressure = 3 in. Hg	Average Q/M = 7582 c/kg

Post-run examination showed all needles undamaged, but the familiar traces of tar appeared on the centerpiece. Tar buildup on the center source had already progressed significantly.

The seven-needle module was then operated with only the six outer needles emitting. The center needle was plugged up with wax because of its being the source of much arcing and beam disruption.

The module was installed in the 4 by 8 foot chamber (10 inch diffusion pump). It was operated with a standard NaI glycerol propellant solution, and a time-of-flight log was kept. The time-of-flight distance was 1.92 meters. The collector was run grounded, with a -22 volt suppressor grid and a +12 volt screen grid in front of it. The run lasted 506 hours, when it was voluntarily terminated so that the needles could be examined, and the chamber could be released for other experiments.

Table 12-8 gives a summary of the time-of-flight data collected for this run. The high and low values are extremes, and in most cases are not truly representative of the scatter of the data. The latter was approximately 5-10%, depending on the parameter. Beam and extractor voltages, for example, were quite tight, while feed pressure was loose in scatter. All time-of-flight parameters were fairly loose except beam efficiency.

The data showed a trend, which is illustrated in the table by giving a median, or nominal, for three different periods of the run; the beginning, the middle and the end. The medians were not obtained by analysis, but rather were chosen by eyeball judgement, after careful scrutiny. They indicate a lowering of performance as time goes on. This was confirmed to be due to the presence of tar build-up on the center plugs of the needles.

All six annular needles had "stalagmites" of tar build-up on the center plugs. At least one or two appeared to have reached a height of 1/32 inch, approaching the height of the needle rim where it could significantly modify the field. The extractor had a layer of brown, copper-like substance on it, which began to absorb water vapor after about 2 hours in the atmosphere. It was surmised that the coating contained glycerol.

Table 12-8

Six Annular Needle Module, 500 Hour Run, Time-of-Flight Summary.
Thrust and Flow Rate are Uncorrected for Efficiency and Energy Loss.

Parameter	High	Low	Median		
			1st 150 hrs.	150-350 hrs.	350-500 hrs.
HI Voltage (kv)	14.7	13.0	13.2	13.8	14.3
Beam Current (μamp)	550	150	420	400	365
Feed Pressure (in Hg)	6.8	1.6	2.0	2.3	2.6
Extractor Voltage (kv)	-3.0	2.0	-2.1	-2.5	-2.7
Extractor Current (μamp)	2.2	0	.75	1.5	1.7
Chamber pressure x 10^{-6} torr	4.2	1.5	3.0	3.2	2.8
I_{sp} (sec)	1685	1359	1550	1520	1480
Thrust (μlb)	139	99	120	115	110
Mass Flow (μgm/sec)	44.3	27.6	35.0	36.0	35.0
Thrust Efficiency (%)	74.4	68.8	72	70	69
Average Q/M (coul/μgm)	13,900	9,500	12,000	11,400	10,700

12.3.10 The Tar Formation Problem; 600-Hour Needle Run

When the first annular needles were run, it was observed that the center regions would become covered with a thin layer of glycerol propellant which gradually polymerized into tar. This center layer would foam considerably before becoming polymerized. The foaming was caused by secondary electron bombardment liberating hydrogen gas in the propellant layer. The electrons resulted from interbeam collision processes occuring on the needle side of the negative potential barrier, where it is possible for the electrons to return to the needle. The yellow glow in front of all operating colloid devices is an indication that electrons are being made. The effect on annular needles is greatest because: (1) the current density is much higher, which results in more electrons being liberated; (2) their larger size (relative to the 14-mil needles) means that the

negative potential barrier is further downstream, thus creating a larger volume from which secondary electrons can return to the needle; (3) the large negative potential required to bias the annular slit provides these secondary electrons with more than enough energy to polymerize the glycerol; and (4) the secondary electrons are, by the geometry of the needles, focused towards the center of the annular needle.

An obvious solution to the problem of tar forming in the center of the annular needle is to keep the propellant out of this region. To achieve this, several solutions were tested during September, with varying degrees of success. A promising approach was to drill a 1/32-inch deep hole within the center plug. Drilling such a hole concentric with the plug provided edges which, when properly polished, prevented fluid from reaching the center of the plug. The same design with a Teflon stud filling the 1/32-inch deep hole was also tried. This design (Figure 96) was only a limited success. It was intended that the non-wetting Teflon would keep the propellant away from the center of the plug but the Teflon surface became activated after several hours of operation and started wetting. This activation was probably the result of electrons bombarding the Teflon surface during operation. The Teflon plug was removed prior to the next run. In that run, we relied upon the action of surface tension on the edges of the hole to prevent fluid from penetrating into the center of the plug. This worked well for 2 days at 90 μamp but around the 50th hour of operation the fluid began to penetrate to the center of the plug. Upon removal, microscopic inspection indicated that while the fluid had been kept away from the center during most of the run, there was a gradual buildup of tar at the edge of the 1/32-inch deep hole where the inner meniscus of the fluid was. This tar appeared to act as a wick for propellant, eventually drawing fluid into the center.

Two other approaches were tried, also with limited success. In one, a Teflon hat was placed in the plug to cover the inner meniscus (Figure 97). This design was intended to protect the meniscus region from electron bombardment. It was unsuccessful, however, as the meniscus succeeded in reaching an exposed area on the

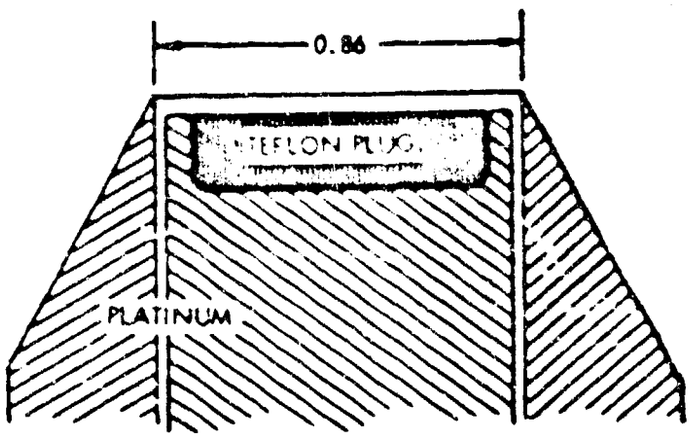

Figure 96. Annular Needle with Teflon Plug Located in Center Piece

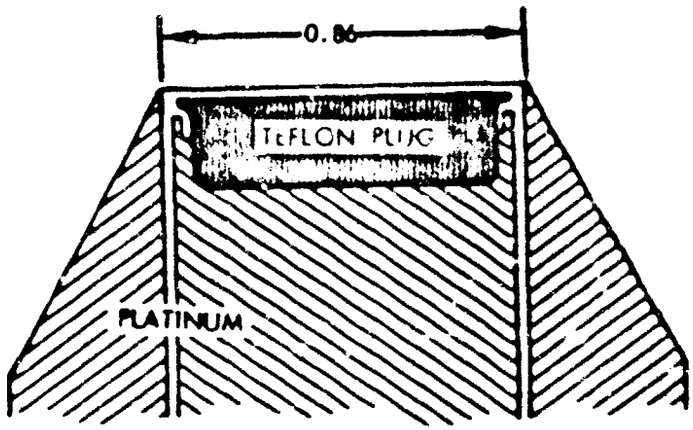

Figure 97. Annular Needle with Teflon Hat to Cover Inner Meniscus

Teflon, probably as a result of non-uniform wetting. Once tar formation was initiated around the edges, the propellant succeeded in climbing onto the activated Teflon surface.

The last approach tried was perhaps the least obvious, and proved to be a good deal more successful than anticipated. This was the simple expedient of letting propellant cover the entire center plug.

In this experiment, an annular needle was operated for 600 hours with little significant tar formation. The run was terminated by a vacuum accident. The thrust was kept between 25 and 35 μ lb, the I_{sp} between 1120 and 1250 seconds. Operating voltages were 12.8 kv on the needle and -1.5 kv on the extractor. The current varied between 65 and 90 μ amp. This needle was designed to operate with the propellant completely covering the center plug, although the feed was still through the concentric space between the center plug and outer wall. The propellant covered the plug to a depth of approximately 15 mils at the shallowest part. After a day of operation, the center region began to bubble occasionally, but remained tar-free and the fluid remained clear. The bubbling suggests that the center region developed a rather high concentration of gas due to electron bombardment because of a lack of fresh propellant flow into this region. Despite this stagnant condition in the center, there was enough transport of propellant out of this region to prevent the buildup of tar. There was a tar buildup on the outer rim of the needle, but it was not nearly as large as the amount produced in the center of the needles during the 500-hour run with the six-needle module.

Secondary electrons bombarding the needle come from the extractor and from the beam itself due to charge exchange and beam particle interactions occurring within the potential barrier.

The electrons produced within the beam can be reduced in number by using a smaller extractor hole which reduces the volume of space producing these electrons by moving the potential barrier closer to the needle tip. Cutting away some of the outside material on the shank of the needle will have a similar effect (the emitting rim was 89 mils in diameter but the shank of the annulus was 115 mils). Another technique which could be used is reshaping the extractor hole so that only a minimal amount of the surface struck by the ions is

in a position that will permit secondary electrons to have a trajectory which will let them strike the needle. Such an extractor would have a flat upper surface flush with the needle rim and a knife edge on the extractor hole with just enough radius to eliminate electron emission.

Operating the center of the annular needle filled with propellant increases the amount of propellant evaporating as the needle diameter is increased. The mass evaporated from the annular needle is as follows:

12.3.11 Evaporated Mass Fraction

Evaporation rate of glycerine at 24°C ($P = 2.8 \times 10^{-4}$ torr) is given by

$$E = \frac{PM}{N(2\pi mkt)^{1/2}} = 9 \times 10^{-6} \text{ gm/cm}^2 \text{ sec}$$

where

P	= pressure	m	= the mass of the evaporating atom
N	= Avogadro's number	K	= Boltzmann's constant
M	= gram molecular weight	T	= the absolute temperature.

Since the diameter of the annulus is 0.039 inch, the hemispherical surface emitting area is $S = 2\pi r^2 = 0.08 \text{ cm}^2$.

The evaporating mass $= E \times S = 7.2 \times 10^{-7}$ gm/sec.

The percentage of mass evaporated compared to that carried by the beam is 9.5%, assuming 25 μ lb @ 1500 seconds requires 7.5×10^{-6} gm/cm^2 sec. The presence of NaI in the propellant depresses the vapor pressure, according to Raoult's Law, from 1/3 to 1/8 (depending upon whether the NaI completely dissociates). In addition, there may be a further drop in the evaporation rate if a higher concentration of NaI exists at the surface because of the glycerine evaporation. Tests on the amount of propellant evaporation versus time can be made to study this effect. It has also been reported in the literature that the actual evaporation rate of glycerine into a vacuum is actually 0.05 that predicted by kinetic theory. We are, however, suspicious of that statement and feel it needs further experimental verification.

12.3.12 Thrust Vectoring; 6-Needle Annular Module

A module consisting of a vectorable linear array of six annular needles was fabricated and tested during October. A photograph of the module is shown in Figure 98 and Figure 99. The module was operated for 24 hours, during which time the beam was vectored over a range of 14 degrees ($\pm 7^{\circ}$) at thrusts of 150 μ lb for a 1330-second I_{sp} beam. For this thrust, I_{sp}, and deflection the needle voltage was 14.5 kv, the needle current 600 μ amp, and the deflector voltages 10 and 7 kv. The run was terminated because two of the 6 needles (No. 5 and No. 6) could not be made to emit properly. These needles appeared to be plugged up and almost all of the current was emitted from the other 4 needles. These particular needles became plugged up several times during pre-run impedance measurements. The back flushing apparently did not completely clean out the interiors and the propellant entrained the remaining particles and returned them to where the previous blockage had occurred.

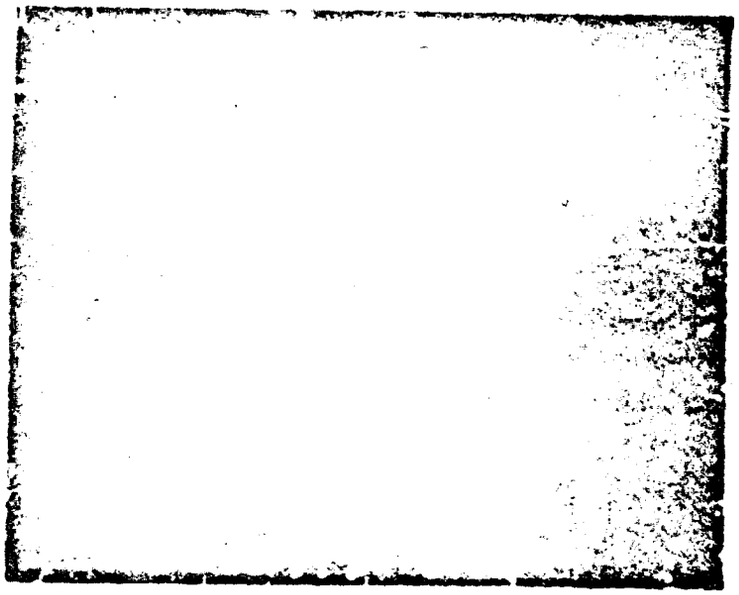

Figure 98. Top View Looking Down on Extractor Deflector Electrodes, and Annular Needles of 120 μlb Thrust Vectorable Module.

Figure 99. Side View of 120 μlb Thrust Vectorable Module

REFERENCES

12-1 M. Huberman and P. Kidd, "Charged Particle Electrostatic Thrusters," AFAPL-TR-69-14, March 1969.

12-2 Kenneth W. Stark, "Design and Development of an Annular Slit Colloid Thruster," AIAA paper No. 69-287, 7th Electrical Propulsion Conference, Williamsburg, Va., March 1969.

APPENDIX A

IES Converter Operation

Figure A-1a illustrates the basic IES circuit, supplying a load resistance, R. The energy-storage inductor, L, has a linear flux versus MMF characteristic with a slope, K. It has a primary winding, N_1, and a secondary winding, N_2, with magnetizing inductances $L_1 = KN_1^2$ and $L_2 = KN_2^2$, respectively. The transistor switch, Q, is externally controlled to turn on and off cyclically within a time period, T. A steady-state operating cycle of this circuit, with input voltage e_{in} and output voltage e_o can be described as follows.

During the time interval T_{on}, the transistor is switched on by the base drive circuit and the current i_1 in N_1 causes the inductor to absorb energy from the input source. Meanwhile, diode CR blocks any current in N_2. Thus, a given quantity of energy is stored in the inductor during T_{on}. When Q is turned off, the MMF continuity demanded by the inductor causes i_2 to flow immediately through the diode to charge the filter capacitor, C, and load, R. The energy stored in the inductor during T_{on} is thus released to C and R during T_{off}.

Figure A-1b illustrates the circuit waveforms during one steady-state operating cycle, assuming ideal components in Figure A-1a. Voltage $e_1 = e_{in}$ across N_1 during T_{on}, causes i_1 to increase from i_a to i_b at a constant rate e_{in}/KN_1^2, while i_2 is 0 in N_2. At the end of T_{on}, the continuous MMF acting on the inductor causes $i_2 = N_1 i_b/N_2$ to start flowing in N_2 and decreasing at a constant rate e_o/KN_2^2. During this time interval T_{off}, $i_1 = 0$. Since the increase of MMF, $N_1 \Delta i_1$, during T_{on}, should be identical to the decrease in MMF during T_{off} for steady-state operation,

$$N_1 T_{on} \left(e_{in}/KN_1^2\right) = N_2 T_{off} \left(e_o/KN_2^2\right) \qquad (A.1)$$

from which

$$\frac{e_o}{e_{in}} = \frac{N_2}{N_1} \frac{T_{on}}{T_{off}} \qquad (A.2)$$

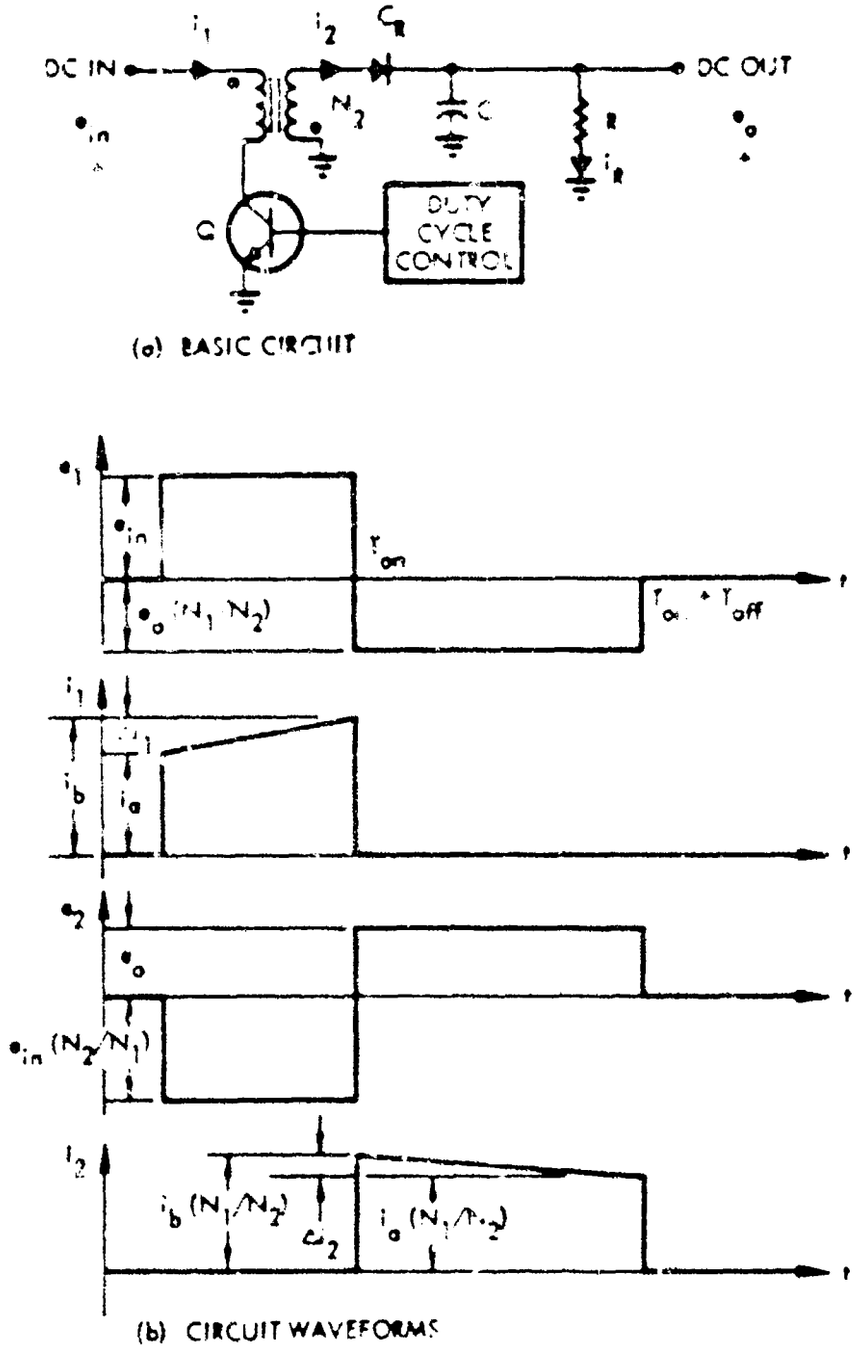

Figure A-1. Basic Concept of IES Circuit

Thus, despite a variation in input voltage, a constant output voltage can be maintained by controlling the ratio T_{on}/T_{off} with the base drive circuit.

Figure A-2 shows the circuit waveforms before and after the occurrence of an output short at $t = t_1$ when the power transistor Q is conducting. Current i_1 does not increase abruptly, as Q sees only the inductor with inductance L_1 and not the short circuit in the output. While $E_1 T_{on} \Delta i_1 = E_2 T_{off} \Delta i_2$ for each cycle before the short condition, $E_1 T_{on} \Delta i_1 > E_2 T_{off} \Delta i_2 = 0$ after $t = t_1$ as the output voltage becomes 0 during T_{off}. Therefore, the current level of i_1 is steadily increased on each succeeding cycle. The system can be shut down by a current-sensing circuit (for example, after the fourth cycle as indicated in Figure A-2) so as not to allow the energy-storage inductor to go into saturation and cause a current surge in Q. The stored energy of the inductor goes to 0 following system shutdown, and the arc is extinguished. When power is turned on again after the removal of the short circuit, the input current and the output voltage gradually build up to their respective steady-state values resulting in a soft turn-on. Thus, during either a startup or a severe output short, no power conditioning component is subjected to excessive stress from voltage or current transients. This is in contrast to the more conventional designs where heavy in-rush current may occur during startup and an output short is reflected back to the power source within a half-cycle of the operating frequency. This immunity of the power components in the "energy ladling" circuit to high-voltage and/or high-current transients greatly enhances the system reliability.

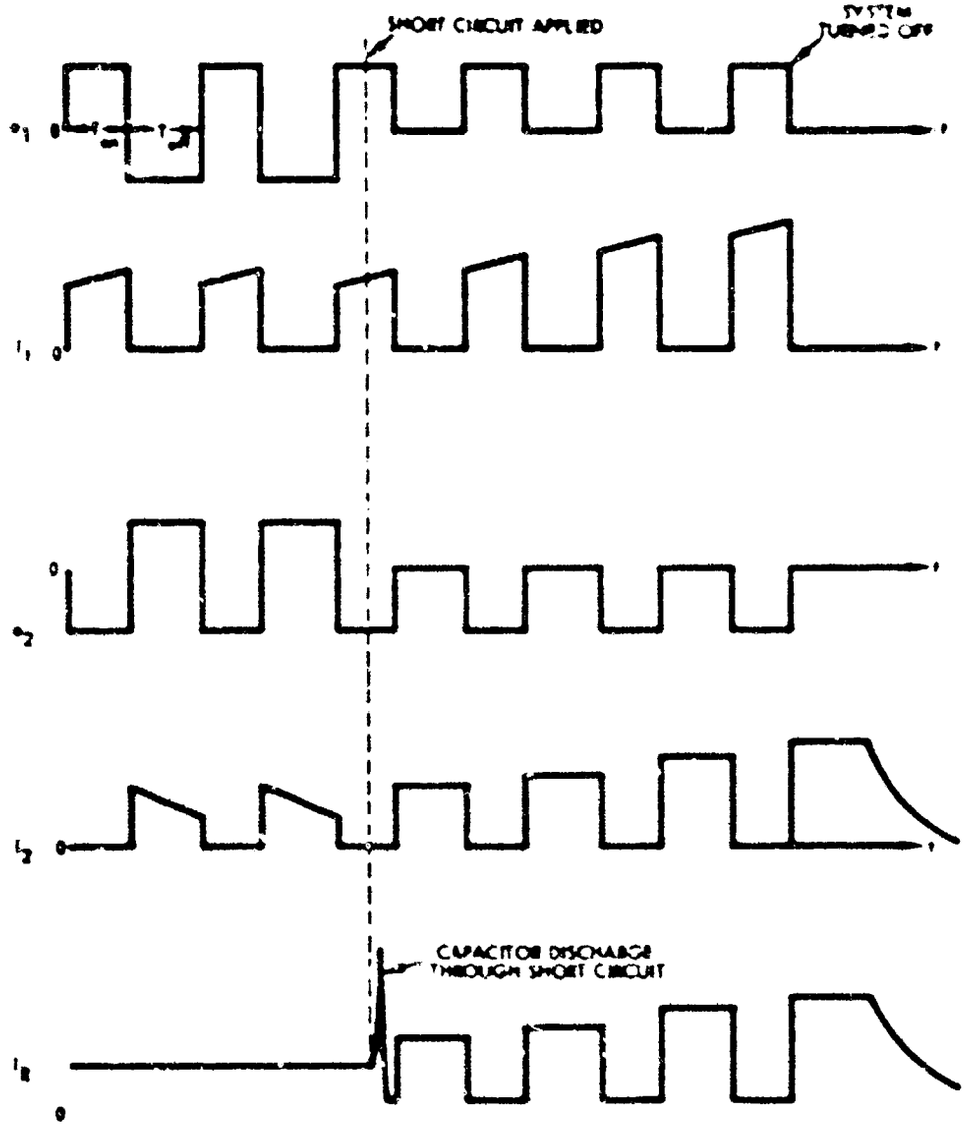

Figure A-2. Circuit Waveforms During Output Short

Unclassified

DOCUMENT CONTROL DATA - R & D

The Systems The Space Park Redondo Beach, California	Unclassified

Charged Droplet Electrostatic Thruster Systems

Technical Report, January 1, 1969 to January 30, 1970.

Haywood Shelton, Charles W. Lear, Phillip W. Kidd, Marshall N. Huberman, Bertrand F. Farber, Walter F. Krieve

March 1970	245	
F33615-69-C-1254		
	AFAPL-TR-70-31	

Copies of this report should not be returned unless return is required by security considerations, contractual obligations, or notice on a specific document.

	Air Force Aero Propulsion Laboratory Air Force Systems Command Wright-Patterson Air Force Base, Ohio

A program to develop and advance the technology needed for practical colloid propulsion flight system is described. A 100-micropound, 1500-second specific impulse, vectorable colloid thruster concept has been developed and tested. Several neutralizer concepts and their interactions with the colloid beam plasma potential are discussed.

Direct thrust measurements have been correlated with time-of-flight calculations for various 100-micropound colloid thruster concepts. Several propellants, including liquid metals, have been investigated. The feasibility of pulsed and AC colloid propulsion has been investigated. Various single-needle colloid experiments were performed.

A preliminary power conditioning approach for a 1-millipound, orthogonally thrust vectorable colloid system has been developed. The anticipated effects of synchronous orbit solar radiation on needle operating temperature have been examined.

DD FORM 1473

Unclassified
Security Classification

Unclassified

[illegible]	[illegible]		[illegible]		[illegible]	
	[illegible]	[illegible]	[illegible]	[illegible]	[illegible]	[illegible]
Electric Propulsion Colloid Propulsion Microthruster Technology						

Unclassified
Security Classification